UNIVERSITY OF STRATHCLYDE

DEPARTMENT OF MECHANICAL AND AEROSPACE ENGINEERING

Compressive Mechanical Behaviour of Nitinol Wires used in Aortic Stent Grafts

Ana Sofia De Freitas Alves

A thesis presented in fulfilment of the requirements of the

Degree of Doctor of Philosophy

2021

Declaration

This thesis is the result of the author's original research. It has been composed by the author and has not been previously submitted for examination which has led to the award of a degree.'

Signed:

Date:

Acknowledgements

I would like to start by thanking Dr Marcus Wheel and Prof David Nash for their supervision, guidance, and patience during my PhD studies.

Thank you to Dr Robbie Brodie from Terumo Aortic for his support and guidance. Thanks to Alexandros Boukis for his help during in testing and analysis and whose input and assistance have been of great value.

I would like to thank Dr Paulo Tavares and Dr André Cavaleiro at INEGI – Institute of Science and Innovation in Mechanical and Industrial Engineering in Portugal and Dr Alastair Wark from department of Pure and Applied Chemistry from University of Strathclyde for their help during the preparation of my samples. I am also very grateful to Prof Aaron Stebner from Colorado School of Mines, USA for his valuable help and support on the numerical part.

To my friends and colleagues from the Department of Mechanical and Aerospace at University of Strathclyde a special thanks to Dr Emma Henderson for her friendship and all the opportunities she gave me during my PhD studies, to Misael Pimentel, Faidon Kyriakou, Joana Fidalgo, Thomas Burel and Ferdin Saga for their warming welcome and friendship.

To my lifetime friends Ana Mota and Diana Tavares, I want to thank them for their unconditional friendship and support that helped me go through the distance from home. I also would like to thank to Sofia Pimenta for always being there for me during the good and bad times of my PhD and for becoming my confident and dearest friend in Glasgow. To my friends in Glasgow, Martin Prostredny, Carla Ferreira, Daria Stoliarskaia, Ruben Rosario, Scott Davidson, Joao Gregorio, Wenhan Cao, Carlotta Mendez and Paul Duncan for making me feel at home.

Thank you, Steven Black, for all your support, patience and love that helped me keep going throughout this long process.

Finalmente, um agradecimento especial aos meus pais por terem feito os possiveis e impossiveis para eu estar onde estou, sem voces nada disto seria possivel, obrigada por me terem dado a forca necessaria para lutar pelos meus objectivos e por estarem sempre presentes quando eu mais precisei. Um especial obrigado a minha irma, a minha sobrinha Mariana e aos meus sobrinhos Francisco e Gustavo por toda a alegria e risos que sempre me proporcionaram

Abstract

The Anaconda endovascular stent graft is a medical device designed to treat abdominal aortic aneurysms, composed of a nitinol wire structure and a fabric graft. The graft is required to undergo significant deformations before and after the implementation of the device. This thesis addresses the material characterization of thin nitinol wire taking advantage of the test methods already established for tensile and compressive behaviour, mainly focussing on the compressive response. The tensile behaviour here presented consists of a preliminary study of the localised deformation on nitinol wire.

The mechanical characterization of the wire under compression starts with the implementation of digital image correlation (DIC) technique to measure the sample strain field. The compressive test method was found to be unsuitable for compressive loading, where it was not possible to replicate the compressive tests, validate the DIC technique and does not hold the sample securely during the compressive test. This finding led to a complete change of the research goals and paved the way for the development of a test method for fine nitinol wire.

A compressive test method is therefore proposed, which is shown to be valid under compressive loading and for obtaining the compressive material parameters as input to the numerical models. A parametric study was undertaken to understand the optimum ratio between the length and diameter of the sample. An attempt at using this method in a temperature-controlled environment is also presented.

The application of the Auricchio constitutive model, implemented in the finite element software Abaqus, is considered. A comparison with an alternative non-commercial model is also studied and reported along with some suggested improvements. This results in better prediction of the asymmetric behaviour of nitinol wire under compressive and tensile loading and is shown to be very promising in physically representing the bending behaviour of nitinol wire.

Aos meus pais,

Mariana, Francisco e Gustavo

Contents

List of Figures

List of Tables

Nomenclature

AAA	Abdominal Aortic Aneurysm
AMRL	Advanced Materials Research Laboratory
DIC	Digital Image Correlation
EVAR	Endovascular Aortic Aneurysm Repair
FE	Finite Element
FEA	Finite Element Analysis
FOV	Field of View
NiTi#1	Binary Nitinol material supplied by Fort Wayne Metals
SEM	Scattered Electron Microscopy
SMA	Shape Memory Alloy
SME	Shape Memory Effect
wt%	weight percentage of Nickel or Titanium in Nitinol

Chapter 1 Introduction

1.1 Context

Nitinol is a shape memory alloy (SMA) that is part of the class of shape memory materials (SMMs). It was first discovered at the now disestablished Naval Ordnance Laboratory, located in Maryland, United States and, as the name indicates, it is an alloy composed by nickel and titanium. SMAs attracted a large attention due to their particular characteristics of superelasticity and shape memory effect. Nitinol is an alloy used in a wide range of applications and, mainly due to its biocompatibility, it is extensively used in biomedical applications. Endovascular stents graft are one of the fields where nitinol is commonly used within the medical device industry.

An endovascular stent graft is a medical implant that consists of a fabric tube supported by several nitinol wire rings that are used to reinforce a weak spot in the aorta. The less-invasive application of an endovascular stent graft forces the stent to undergo several states of deformation when is compressed inside the deployment device and after it expands during deployment. The ability of nitinol, to superelastically bend without permanent deformation during these stages, makes it the preferred material to be used in endovascular stent grafts.

The Anaconda stent graft is the chosen device used as the case study in the current work to understand the bending behaviour of nitinol wire. The Anaconda stent graft is developed and manufactured by Terumo Aortic and is designed to treat Abdominal Aortic Aneurysms (AAA). The structure of the Anaconda device design is composed of a patented ring stent design that takes advantage of the nitinol superelastic characteristics under high bending deformation during the deployment of the device. Further details of this device are described in section 2.1 of Chapter 2. In order to better understand the mechanical behaviour of nitinol wire and optimise the Anaconda stent graft, Terumo Aortic has a long-time collaborative relationship with the University of Strathclyde. This

work includes the characterization of the bending behaviour of nitinol wire to subsequently improve the design of this device.

When a structure is deformed in bending, the material undergoes both compression (towards its inner bend surface) and tension (towards its outer bend surface) deformation. Thus, to characterize the bending behaviour of nitinol wire it is important to also characterize the wire under uniaxial tensile and compressive loading.

During mechanical characterization of a material, tension is the most common test performed to understand the basic properties of it. Therefore, tensile testing on superelastic nitinol wire is very common to find in the literature, with several different studies published regarding the mechanical response of nitinol. In fact, a standard testing method for tension is also available - ASTM F2516-14 [1]. In more recent work, Boukis [2] published an extensive study of nitinol wire under tensile loading at high-strain deformation. This work was sponsored by Terumo Aortic – part of the long-term collaboration with University of Strathclyde, where Boukis used the company internal procedure for tensile testing available at Terumo Aortic laboratories.

Similar to the tensile response, characterization of the bending behaviour of nitinol is also available in the literature. Brodie [3] extensively studied the bending behaviour of nitinol wire where a test method for bending was developed allowing the characterization of the wire's load-history dependent bending response. A full-field strain measurement of thin nitinol wire in bending was also presented in his work that allowed insights of the tension-compression asymmetry and localised deformation in bending. This work is also part of the collaboration between Terumo Aortic and University of Strathclyde.

Nevertheless, compressive testing of nitinol wire under large strain deformations is an ongoing challenge where there is also no standard method test available. The literature is also scarce for this type of loading with very few studies published that can be used to improve the designing of the medical devices. Currently the device designers of Terumo Aortic have very little information on compressive stress-strain data for the specification of nitinol with most of the mechanical properties' specifications being currently based on

tensile properties, thus creating the need for characterizing the superelastic nitinol wire under compressive loading, relevant to the application of stent graft components design.

Understanding fully the mechanical behaviour of superelastic nitinol wire is also important when improving the design of the medical devices when using Finite Element Analysis (FEA) tools. Although some constitutive models for nitinol are available in commercial software packages such as Abaqus, they still require numerous input of parameters obtained experimentally. To have a significant improvement of these numerical models, it is important to have a set of experimental data to validate the models under different modes of deformation.

1.2 Objectives

The main objective of the present work is to develop a compression test method able to study the compressive behaviour of superelastic nitinol wire used for self-expanding stent grafts. This method will improve the understanding of the nitinol wire under compressive loading at high strain deformation to subsequently improve the analysis and optimization of stent graft medical device design.

The experimental parameters obtained from the compression test method developed are thereafter implemented in the FEA models, to have a better understanding of their limitations under compression loading, most notably of the constitutive model available within Abaqus commercial FE software. A non-commercial numerical model [4] will also be studied and compared with previous numerical results.

1.3 Layout

Chapter 2 contains the background to the research. This chapter explains the application and design of a stent graft using the Terumo Aortic Anaconda device as a case study. It also explains the mechanical behaviour of nitinol, describing the different phases and transformations that nitinol undergoes. This will show the reader the importance of studying nitinol and introduce the reader to the phenomena and terminology that will be

used throughout this work. Finally, this chapter specifies the particular material used during the experimental work.

The Literature Review in Chapter 3 focuses on the mechanical characterization of nitinol, investigating all the major experimental considerations, looking at how previous investigators have approached tensile, compressive and some bending testing. The results presented by previous investigators are used as quantitative information of the material behaviour. This chapter concludes with a brief description of the constitutive modelling of nitinol for FEA, focusing on two different models, one widely used in industry for the design of stent devices and a non-commercially implemented model.

Preliminary tensile tests are presented in Chapter 4 to study the localised deformation versus the global deformation of nitinol wire as well as the influence of different grips when testing nitinol wire in tension. The testing machine available at Terumo Aortic laboratories proved suitable for providing valid tensile tests so these preliminary tests served to get acquainted with this machine, the testing protocols of Terumo Aortic and also to demonstrate localised deformation of nitinol as described in Chapter 3.

Chapter 5 reports on the initial uniaxial compressive testing on nitinol based on previous work. The main goal for this chapter is to reproduce the results obtained on the previous work as well to improve the test method by adding a technique able to obtain the full strain field of the sample during the compressive test as well as finding the best technique to control the temperature. This chapter explains how and why it was unable to reproduce the previous results leading to a different approach of compressive testing of wire.

Chapter 6 describes how the new test method that uses a conventional testing machine is developed. This chapter outlines all the iterations and changes made to the test set up needed to obtain a repeatable test method. The machine available at Terumo Aortic was part of the test method iteration, however, when the machine is subsequently used to perform the compressive tests, the results became less reproducible because of the machine stiffness and the tensile-compressive asymmetry exhibited by nitinol. For the

final iteration, preliminary compressive tests were performed to validate the method using previous results for comparison.

In Chapter 7, a more comprehensive compressive testing programme is discussed. Here, different studies are presented taking in consideration the effect of the sample length on the compressive response and the effect of temperature. This chapter describes the best sample length to test nitinol wire under compressive loading.

The FEA models are presented in Chapter 8, where the experimental data from Chapter 7 is used to parameterise, the numerical models presented in this chapter. Two different FEA constitutive models are presented in this chapter, namely the Auricchio model, a commercially implemented model widely used in the design of stent grafts, and a model developed by Kelly and Stebner, this latter model being tested by the developer, with the experimental data being shared. The final results are compared against the experimental results to validate the models and identify which model better represents the behaviour of nitinol wire under compressive loading.

Finally, Chapter 9 presents the main conclusions of this work and proposes recommendations for future studies.

Chapter 2 Background

Anaconda is a customisable stent graft system used to repair abdominal aortic aneurysm (AAA) that is produced at Terumo Aortic in Glasgow, Scotland. This device is customisable to each patient's individual anatomy, meeting their specific needs. The keyword 'customisable' makes this device more challenging to develop due to the various specifications, inherent to a custom design, such as different sizes/diameter, number of nitinol rings, and so forth, that need to take in to account different physical variations. This device consists of multiple nitinol rings connected through a tubular graft material. The main importance of studying this device is to assess the behaviour of the system over its life cycle and the deformations/steps that the device is subjected to, from the compression of the device which allows it to fit in the delivery system to the expansion when it is release inside the aorta. During this deformation, the nitinol wire rings suffer high strains under tension, compression, bending and torsion. Therefore, it is very important to study nitinol wire under these complex loadings to improve the design of this device.

The design of this device is based on computational simulation, where the prototypes are studied using finite element (FE) modelling based on numerical deformation models and constitutive equations. These constitutive equations are fed by mechanical properties obtained through extensive experimental tests. Different experimental tests are performed on the wire by means of model validation to understand its behaviour under complex loading that include tensile testing, compressive testing, bending, torsion and fatigue testing. In the past, the testing of very small diameter nitinol wire has been extremely challenging and has resulted in the need for the present work.

It is in the experimental tests that this work is focussed, compressive loading is the least understood from an experimental perspective leading to a lack of identified compressive parameters required in the constitutive models. The core of this work goes through the development of a reproducible compression test able to identify the constitutive

parameters associated with this loading that can then be used in the numerical models to improve the FE modelling of the Anaconda device.

This chapter describes the practical application that is behind the study of nitinol wire and the necessity to provide a full material characterisation of nitinol. Therefore, the application of this work is presented in this chapter as follows:

- Application and design of the Anaconda stent graft device developed by Terumo Aortic – Case study used for stent graft device;
- The material specifications of nitinol;
- Characteristics of the nitinol used during this work.

This is important to understand how the following literature review is structured, giving the reader the necessary information about previous investigations made and justifying the methodology proposed and developed throughout this work.

2.1 Background

Abdominal aortic aneurysm (AAA) is a balloon-like swelling that appears in the aorta, the main blood vessel that runs from the heart through the chest and abdomen [5] that can be treated by the Anaconda device. An aneurysm is caused by the weakening of the vessel walls and if unnoticed there is a great danger of rupture to the vessel, leading to death within minutes. It is estimated that 1 in 20 men in Scotland, aged over 65 suffers from AAA. Usually there are no obvious symptoms and it is more prevalent in men. [6]

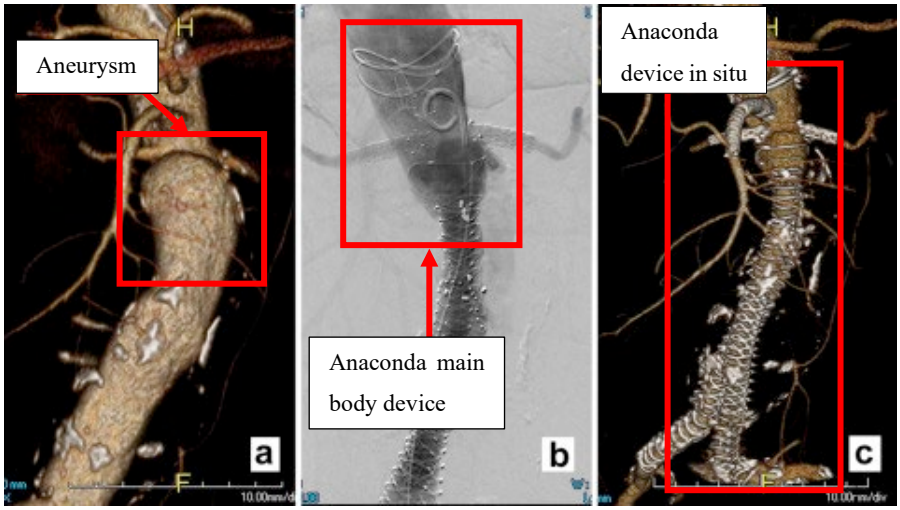

Figure 2.1 – CTA three-dimensional reconstruction; a) short-necked aneurysm; b) angiogram showing patent target vessels and a small type I end leak; c) 3D CTA reconstruction of the 1-month follow-up showing the endograft in situ. [7]

Anaconda, a self-expendable customised stent graft system developed by Terumo Aortic based in Glasgow, UK, is composed of three different parts, a main body and two iliac legs made of multiple nitinol wire ring stents combined with woven polyester tubular graft material. The stent is placed inside the vessel, above the aneurysm region, sealing the artery and conducting the blood through the polyester graft material and is inserted inside the body through a less-invasive surgery called Endovascular aortic aneurysm repair (EVAR). Figure 2.1 shows before and after the implantation of the Anaconda device using computed tomography angiography (CTA). In Figure 2.1.a) it is possible to observe the aneurysm in the vessel and c) a 3D reconstruction CTA one month after the implementation where the aneurysm had resolved spontaneously.

Figure 2.2 shows a schematic image of an Anaconda device deployed in an aneurysm. It is composed of three different parts; the main body and the top stent, consisting of a dual-ring stent that provides the sealing against the wall which is anchored in the healthy walls by four nitinol hooks, preventing the device from moving after deployment. The main body has two bifurcated legs at the bottom where the iliac legs are deployed after and docked to them. The stent expands in the aneurysm area, maintained in place by the hooks.

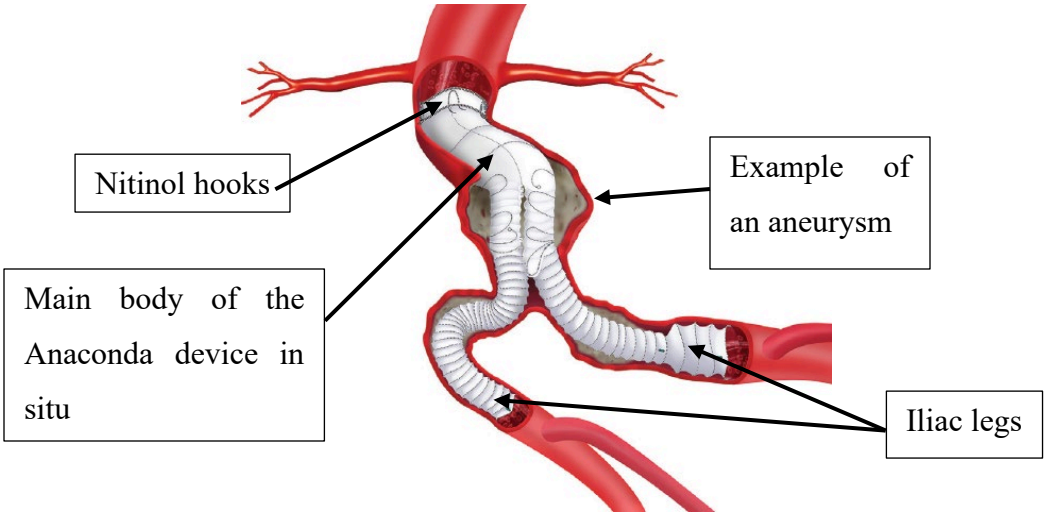

Figure 2.2 – The Terumo Aortic Anaconda device deployed. [8]

One of the main advantages of the Anaconda device is that it does not require any open surgery to be implanted, it is deployed using a delivery system (Figure 2.3). This system consists of a small tube/catheter, where the main body tube has a diameter between 6.8 to 7.5mm. The stent is pre-compressed inside the delivery system and introduced inside the body through the artery in the groin. Figure 2.4 shows the delivery system and how it works within the damaged vessel area, where it can also be repositioned after deployment. The delivery system docks the main body initially. Once the main body is positioned correctly, the delivery system adds the first iliac leg. The legs are fully supported with independent nitinol ring stents. The first leg is put in place using a magnetic system and it connects to the main body via four hooks. The second leg is added after, guided by the delivery system of the main body and similar to the other parts, it docks to the main body using four nitinol hooks.[7], [9][10] In appendix A is possible to see a sequence of images of the Anaconda device being deployed.

Figure 2.3 – Unsheathed Anaconda body device on its delivery system [3]

The metal body used within the stent needs to reach very high compressive strains and be able to expand to the original shape without any permanent deformation. Figure 2.3 – Unsheathed Anaconda body device on its delivery system [3]Figure 2.3 shows the delivery system with the Anaconda body exposed, where it is possible to visualise the deformation that the body is subjected when placed on the sheath. Depending on the size, the Anaconda body outer diameter ranges between 21.5 to 34 mm where, as mentioned previously, the sheath of the delivery system has a diameter of 6.8 to 7.5 mm. The reason nitinol is the most common metal used in mechanical medical devices, specifically stents, is due to its flexibility - up to 20 times greater than stainless steel and to its biocompatibility. [11] This flexibility improves the deployment of the medical device, however, due to this it is very important to understand the behaviour of nitinol when subjected to high strain deformations.

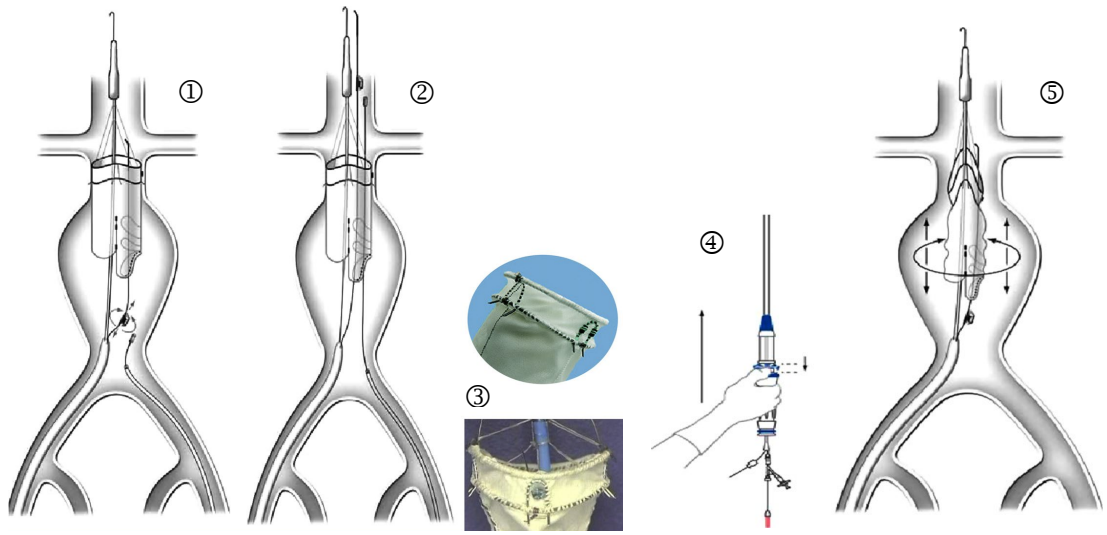

Figure 2.4 – The Anaconda device in three-pieces endovascular device; a) ① Anchored of the main body onto the vessel wall; ② connection of the 2 iliac legs to the main body; ③ Close up of the main body hooks; b) ④ Delivery device that controls the deployment allowing multiple rotational, proximal and distal repositioning as seen in ⑤. [9]

To better understand the requirements of nitinol wire in stent graft devices, it is important to consider the Product Life Cycle of a device. The main steps in the Product Life Cycle of the Anaconda device described focus on the ring stent and consist of:

1. **Device manufacture at room temperature (RT) –** nitinol wire is wound into ring bundle with multiple wire turns and sewn onto fabric. Ring wire in bending with maximum strain < initial elastic limit.
2. **Device assembly to delivery system at RT –** Rings are deformed into saddle shape by attachment to delivery system. At this stage the wire bends with maximum strain > initial elastic limit, causing material to change phase (max ε >1.2% in tension and compression)
3. **Device compaction in sheath at RT –** The rings are compacted into sheath via funnel, the wire bends at peal and valley regions with a maximum strain beyond loading transformation plateaux (>7.5% tension, >4% compression).
4. **Product sterilization (RT to 53˚C and back to RT) –** stresses increase in strained area due to temperature increase and consequent decrease when temperature returned to RT.

5. **Endovascular delivery of compacted device to implant site at body temperature (37˚C) –** similar to sterilization phase, stresses increase in strained areas due to temperature increase from RT to body temperature.
6. **Unsheathing of device at implant site (37˚C) –** wire at peak and valley positions rapidly reduces its bend curvature as ring expands.
7. **Repositioning of device by collapse / reopen (37˚C) –** rings collapse back to steep saddle shape and the material loads with maximum strains beyond initial elastic limit, causing material change phase (max ε>1.2% in tension and compression). Re-opening of the ring will unload the material
8. **Release of device from delivery system, at implant site (37˚C) –** wire continues to unload until the ring contacts the vessel walls.
9. **Long term implantation with excluded aneurysm and pulsatile blood pressure loading (37˚C) –** ring is cyclically loaded and unloaded in bending with small $\Delta\varepsilon$ levels about a mean strain.

When looking at the Anaconda device, the nitinol supporting structure reaches large bending strains when it is compressed inside the delivery device, these being recovered when it expanded to its original shape inside the aorta. Therefore, there is an increased need to study nitinol wire under complex loadings and be able to reproduce them in FEA software used for device design. Currently nitinol wire has been extensively studied under tensile loading, bending and torsion but there is still a lack of information when it comes to compressive loading in wire.

2.2 Mechanical Behaviour of Nitinol

The shape memory effect (SME) is the ability of some materials to shift their phase, where their crystal structure can be reorganized. In practice, these materials have the capacity to restore their original shape after a change in temperature. This property can be found in different materials like alloys, ceramics or polymers. [12] The functional effects that make materials with SME more extraordinary than other materials are pseudoelasticity, one-way memory effect and two-way memory effect, all illustrated in Figure 2.5.

Pseudoelasticity is when the mechanical deformation is higher than the martensitic start stress (σ^{Ms}), with a force (F) being applied to the material, and the material has the ability to recover this strain back following a different path when unloading as shown in Figure 2.5.a). Thus, this effect in shape memory alloys (SMA) exhibits a hysteresis loop during the stress-strain cycle and is observed at high temperatures (austenitic finish temperature (Af) < Temperature (T)). The one-way shape memory effect happens by heating a cold deformed SMA above its temperature of transition, this is the effect that gives these generic materials the name of shape memory alloys. In other words, when at a cold temperature an SMA material that is apparently permanently deformed by a mechanical process, then when heated returns to its original shape, as illustrated in Figure 2.5b). The transition temperature is different for different SMAs. Similar to one-way memory effect, the two-way memory effect also changes the material to its original shape when heated above its high characteristic temperature, but also changes the shape of the material at cold temperature, in this case when its lower characteristic temperature is achieved. This effect only occurs after a special thermomechanical treatment (TMT) is applied to the material, this effect is illustrated in Figure 2.5 c).[13][14]

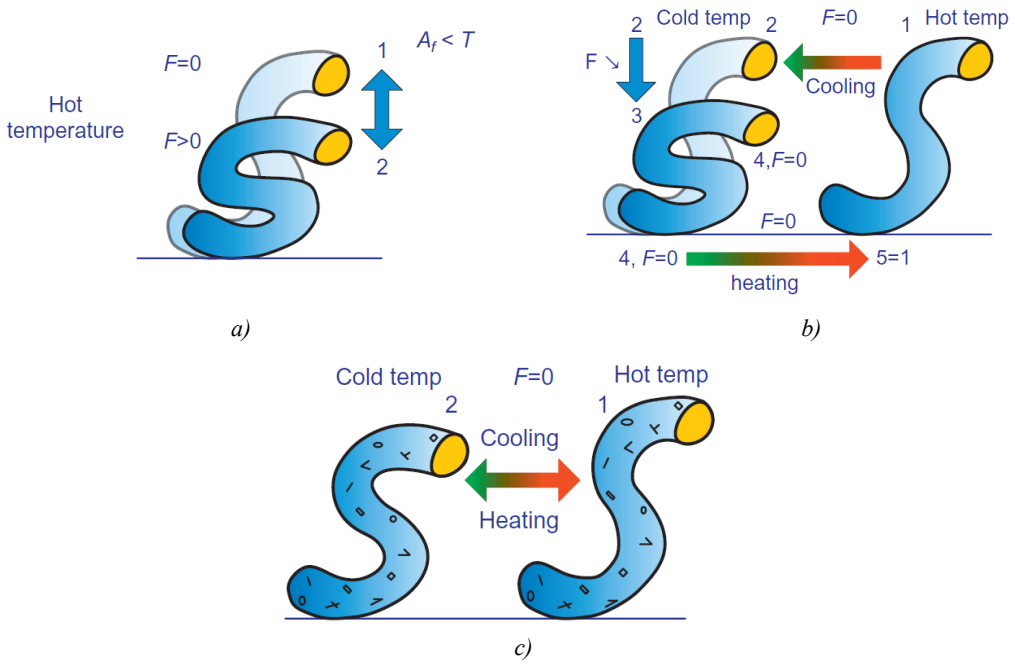

Figure 2.5 – Illustration of the basic shape memory effect; a) Pseudoelasticity; b) One-way memory effect; c) Two-way memory effect. [13]

Nitinol is a SMA widely used in several practical applications due to its superelasticity and memory effect. [15] The Nickel-Titanium alloy (Nickel Titanium Naval Ordnance Laboratory) was first discovered by William J. Buehler in 1959 at Naval Ordnance Laboratory, in Maryland and later developed by Buehler and Frederick E. Wang and, as the name suggests, is an alloy composed of Nickel and Titanium. [16][17]

Nitinol presents two different phases each with different crystal structure, austenite (A) at high temperatures and martensite (M) at lower temperatures. The structural differences between these phases are a highly ordered crystal structure in austenite and on the other hand a more disordered crystal structure found in martensite. More detail of nitinol mechanical effects and structure will be presented later in this chapter.

Currently nitinol has a wide range of applications including aerospace, automotive, robotics and biomedical. The first application of nitinol was aerospace, a 'Shrink-to-fit' pipe coupler used on the F-14 jet fighter. Later it started to be used in biomedical applications, first in orthodontic bridges wires, then in orthopaedic surgery and finally in cardiovascular surgery, this last is the field in medicine where the implementation of nitinol is extensively used, mainly due to its flexibility and its biocompatibility. [16]

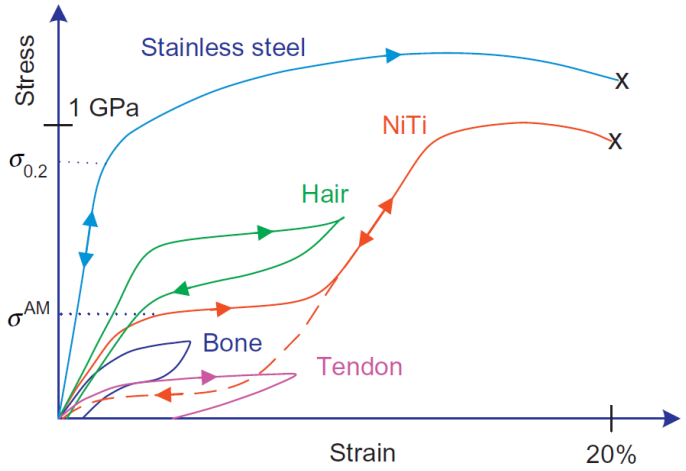

Figure 2.6 – Comparison of the Stress-Strain response of nitinol, stainless steel and biomaterials. [13]

Nitinol is widely used in medicine mainly to its biocompatibility. Figure 2.6 compares the mechanical behaviour of nitinol with other biological materials and stainless steel, where it is possible to see the similarity of the elastic properties of nitinol to natural biomaterials, and the differences to stainless steel's typical response. [13]

2.2.1 Martensitic Transformation

The shape memory effect is based on the ability the material has to easily transform to and from martensite, but at the same time, understanding the details of martensitic changes can be very complex. So, understanding the basic principles of martensite behaviour is essential to understand the engineering aspects of the shape memory effect. [18]

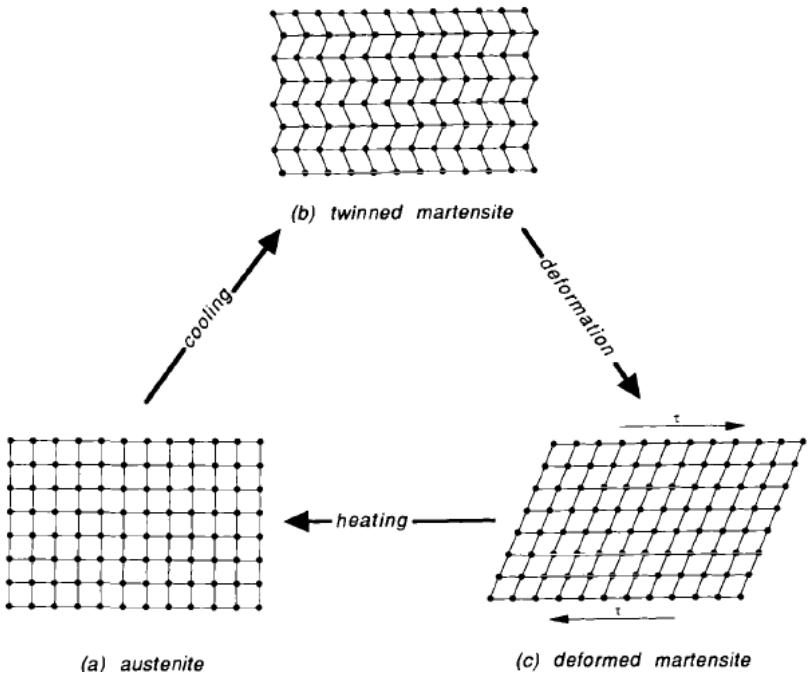

Figure 2.7 – Lattice changes within the shape memory process. [18]

As mentioned before, nitinol is composed of two different phases where each of them has its specific lattice. At high temperatures the phase present is austenite (A) that has a body centred cubic (BCC) structure and at low temperatures the phase present is martensite (M) composed of a monoclinic lattice. The transformation between the structures happens

when the atoms move by shear lattice distortion, known as the martensitic transformation. This transformation can take two different orientation direction - *variant*, twinned martensite and detwinned martensite where in both cases a new martensitic structure is created. Twinned is usually formed due to thermal loading, where it accommodates shape changes during the transformation. On the other hand, detwinned martensite is formed when mechanical stress is applied, where the orientation from one variant to other changes according to the direction of the applied stress. Figure 2.7 shows the three different lattices present in nitinol [17]–[20]

As seen in Figure 2.8, upon cooling with no applied load, the lattice changes from austenite to twinned martensite (forward transformation) below the martensitic start temperature (M_s) and the transformation is completed at the martensitic finish temperature (M_f) with a negligible macroscopic shape change in the material. When heating the material from the martensitic phase, the lattice transforms back to austenite (reverse transformation) starting the transformation at the austenitic start temperature (A_s) and at the austenitic finish temperature (A_f) the transformation is complete. Note that martensitic transformation is associated with a hysteresis, this being created by the fact that the transformation temperatures are different when heating and cooling. [18], [20]

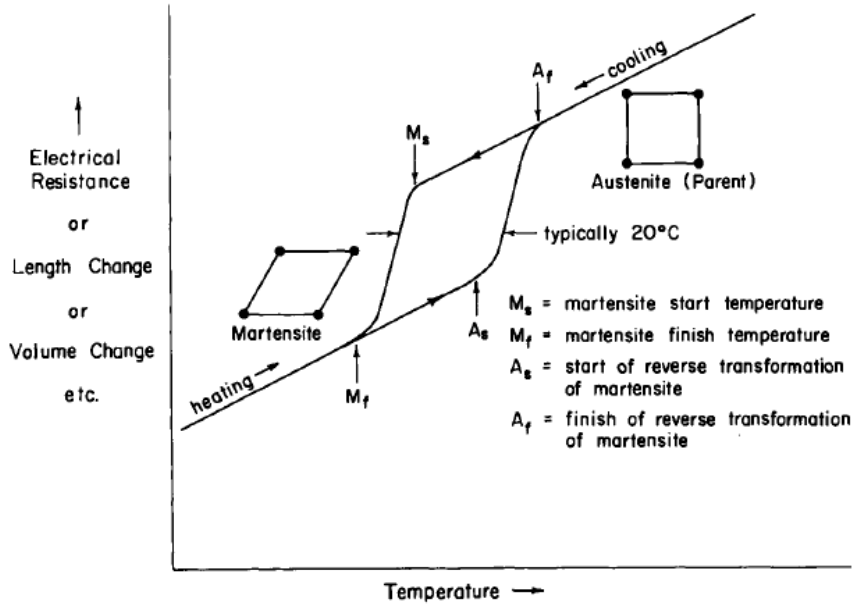

Figure 2.8 – Hypothetical response of property change versus. temperature for a martensitic transformation. [18]

2.2.1.1 R-Phase

An intermediate phase can be found during the transformation between austenite and martensite (during cooling), creating a rhombohedral phase, also known as the R-phase. This phase creates a hysteresis that is associated with small temperature change, i.e., 1.5°C. This transformation occurs between Rs (R-phase start temperature) and Rf (R-phase finish temperature), similar to the martensitic transformation, and a new lattice is created by changing the angle of the cube edges by distortion while the temperature decreases. In Figure 2.9 it is possible to compare the R-phase crystal structure with both martensite and austenite crystal structures.

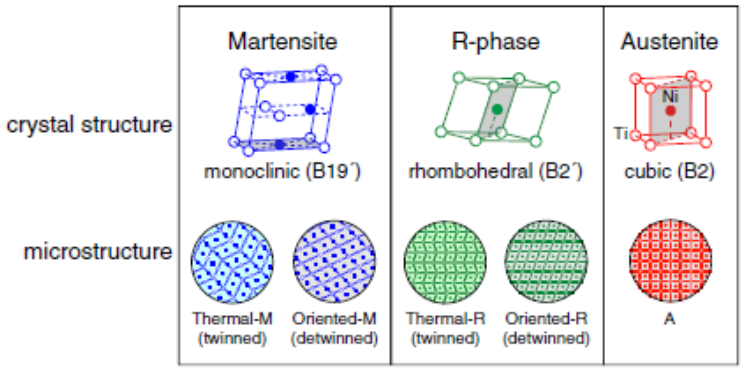

Figure 2.9 – Illustration of the different phases and respective crystal structures in nitinol with R-phase included. [21]

This transition is very useful for thermal actuator applications due to occurring over very small changes in temperature. [18]

2.2.2 Shape memory effect

The shape memory effect is associated with thermal induced phase transformation and it happens when a mechanical load is applied on twined martensite transforming it into detwinned martensite, this load needs to be high enough to start the transformation, higher than the *detwinned start stress* (σ_s). This process results in a macroscopic change in the material, where it retains the deformed configuration after the load is released. An increase of the temperature of the SMA higher than A_f will reverse the phase transformation, from detwinned martensite to austenite, leading to a complete shape recovery. The formation of twinned martensite when the temperature cools back to a temperature below M_f, has no associated shape change. The process thus described is called the *Shape Memory Effect* (SME) (Figure 2.10a) and Figure 2.10 b)).

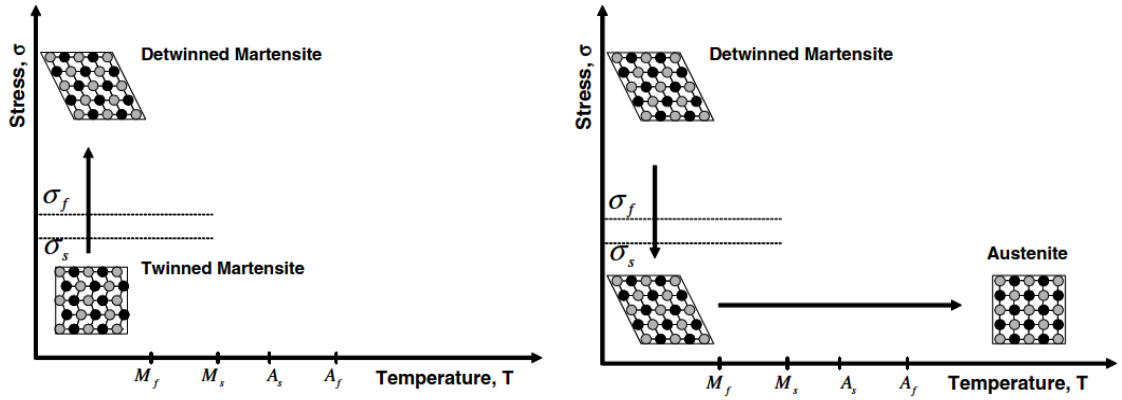

Figure 2.10 – Schematic of shape memory effect of an SMA a) detwinning of the material with applied stress; b) unloading and subsequent heating to austenite with no load applied. [20]

A direct formation of detwinned martensite can be obtain when the material is cooled to the austenitic phase and a mechanical load higher than σ_s applied (Figure 2.11). This transformation produces a shape change in the material, where reheating the material with the load being applied results in shape recovery. [18], [20]

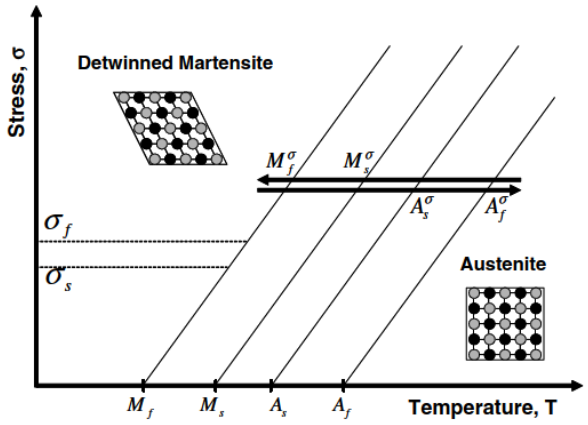

Figure 2.11 – Temperature-induced phase transformation path. [20]

2.2.3 Pseudoelasticity / Superelasticity

The SMA transformation can also be observed when a mechanical load is applied at constant temperature (Figure 2.12). When a very high load is applied to the material in the

austenite phase it can transform to fully detwinned martensite. A fully shape recovery is observed when unloading back to austinite if the temperature of the material is above A_f. This behaviour observed in the material is called the pseudoelastic effect or superelasticity.

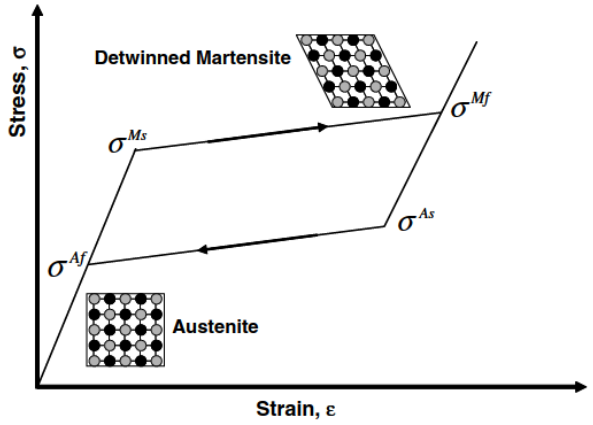

Figure 2.12 – Pseudoelasticity in a stress-strain diagram [20]

The macroscopic shape change under superelasticity is shown in Figure 2.12 in a stress-strain diagram. It is possible to see where the martensite transformation stress levels start and finish, σ^{Ms} and σ^{Mf} respectively. During the unloading, similarly to loading, the reverse transformation occurs when the transformation stress levels are between σ^{As} and σ^{Af}.

The detwinned martensite formed from austenite due to the applied stress is called stress-induced martensite (SIM) and results from many thermomechanical loading paths.

2.2.4 Two-way Shape Memory Effect

The two-way shape memory effect (TWSME) is when an SMA has mechanical load applied but under a cyclic thermal load, in other words, is subjected to a repeated thermomechanical cycling along a specific loading path (training SMA). By applying a loading repeatedly in the material that follows a cyclic mechanical or thermal path it causes the hysteresis response to stabilise, saturating the inelastic strain, a process described as training the SMA. Looking at the example in Figure 2.13, a cyclic mechanical

loading is applied in an SMA during its pseudoelastic regime, where in the first cycle there is an irrecoverable strain and then in each subsequent cycle permanent strain is gradually accumulated which tends to stabilise towards the final cycle. [20]

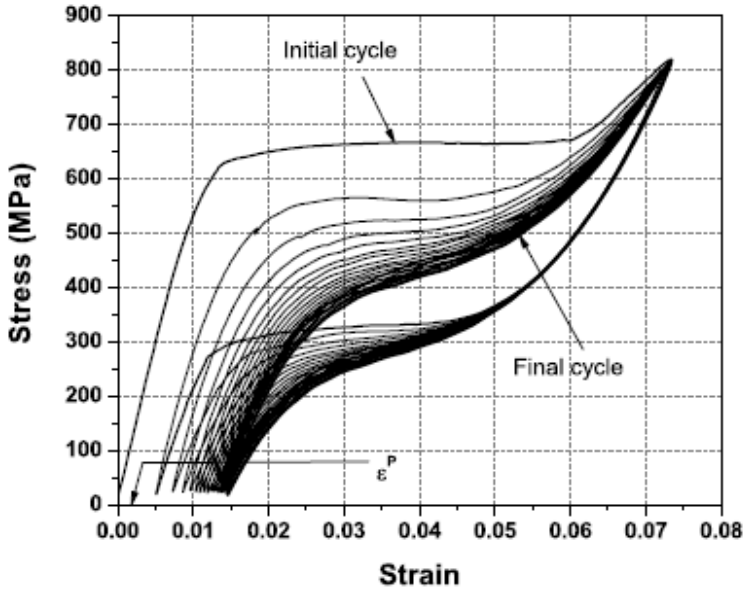

Figure 2.13 –Cycle effect in a pseudoelastic response of a nitinol wire. [20]

2.3 NiTi#1

The nitinol used in the Anaconda device is manufactured by Fort Wayne Metals – Type NiTi#1 composed by 55.94 wt% of Nickel and the rest of Titanium (≈44 wt%), with an A_f of 14.10˚C.

The diameters of the wire used in the device are of 0.22mm and 0.45mm. For this work a specific wire of 1mm diameter was manufactured to perform the compression tests. The samples were cut using the electrical discharge machining (EDM) technique. Material machining was performed by Glenhead Engineering – Scotland, UK and the material was used as received for the experimental work.

3.1 Mechanical characterization of Nitinol

Understanding the mechanical response of superelastic nitinol under different loadings is fundamental to better comprehend the thermomechanical constitutive response and to further improve the behaviour of self-expanding stent structures. Since there is a general lack of information on the mechanical response of nitinol when under uniaxial compression loading, a literature review was conducted to collect previous investigations into the mechanical behaviour of nitinol mainly under this loading. (Note that this literature review will discuss both tensile and compressive loading and will touch on some ideas of bending, but the torsional response of nitinol is beyond the scope of this work). This literature review is aimed at improving material characterization on Terumo Aortic nitinol wire therefore it was conducted with four major objectives in mind:

- Understand the behaviour of nitinol wire under tensile loading;
- Identify how to perform repeatable mechanical characterization testing in small diameter superelastic nitinol wires in compressive loading;
- Understand the behaviour of small nitinol wire under compression loading;
- Acquire knowledge on FEA-implemented constitutive models usually used during the design of superelastic nitinol components taking further account of the response under compression loading.

3.1.1 Tension

Tension is by far the most used test to characterize materials due to its simplicity and the amount of information given during the test, it consists basically of a sample fixed at both ends and a pulling force is applied to one end and the other end maintained fixed. Several standards, such as the ASTM-F2516-14 [1], have been created providing recommendations and guidelines to engineers when conducting tensile tests. Looking at nitinol, understanding the behaviour under tension is also important when understanding

the thermomechanical constitutive response because this is how most of the constitutive parameters are obtained. Several researchers have investigated different aspects of nitinol response under tensile deformation such as temperature sensitivity, load history effects and load rate effects.

Since this work focuses more on compressive testing, this literature review will go over the stress-strain response of nitinol wire under tensile loading, comparing in the following sections the temperature sensitivity and later the localized transformation.

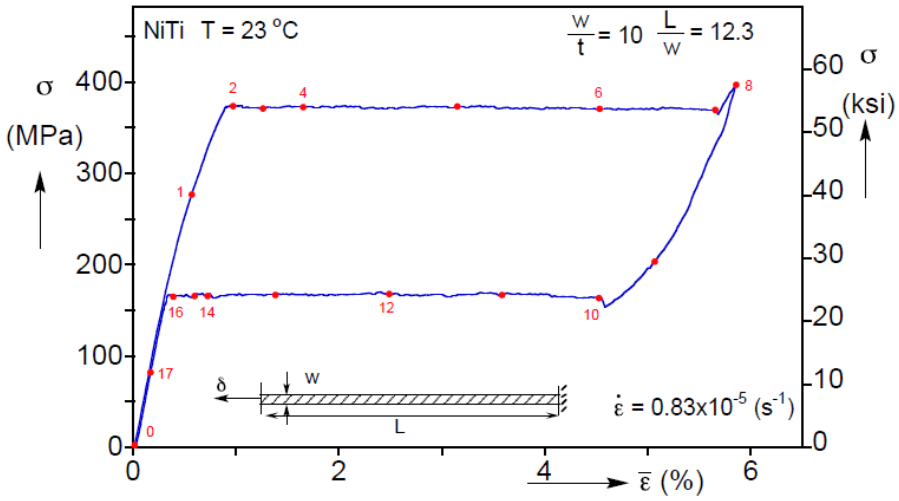

Figure 3.1 – Example of stress-strain response on nitinol expected during tensile loading of a strip at room temperature. [22]

Figure 3.1 shows the stress-strain curve for a nitinol strip under tensile force obtained by Jiang et al. [22] to study the evolution of phase transformation. The test was performed at room temperature of 23°C and represents a common response of nitinol under tensile force. The curve displays a closed pseudoelastic hysteresis, described previously. The curve starts with a linear elastic response that goes up to point 2 in the figure, a distinct plateau, the 'upper plateau' then starts. This plateau indicates the forward transformation, from austenite to detwinned martensite, and is associated with a material instability. The loading transformation finishes at point 7. Point 8 is when the specimen starts unloading. The unloading starts with a homogeneous deformation until point 10, where the lower

plateau starts. This plateau refers to the reverse transformation, where the material transforms back to austenite from detwinned martensite. The transformation finishes at point 16 where the specimen is fully transformed back to austenite. The specimen then unloads homogeneously with similar stiffness as during loading, down to point 0.

3.1.2 Compression

When performing material characterization, compression testing appears as one of the fundamental tests. This test is vital to understand the behaviour of the material under compressive loading mainly when asymmetry is present between tensile and compressive loading. Although the concept of the compression test is quite simple, it has several associated difficulties such as buckling, or barrelling and the modes of deformation are highly dependent on the sample geometry and friction on the contact surface. Therefore, it is important to maintain the initial alignment during the test, and also ensure that the sample ends are perpendicular to the wire axis.

To characterize nitinol used in medical device stents, the challenge increases when looking at testing under compressive loading due to the difficulty of testing fine wire in compression when subject to large superelastic strains. The literature available for fine nitinol wire under compressive loading is very limited and will be reviewed below. Considering the available literature, it can be divided in two different approaches. In the first approach the compression tests are performed with the incorporation of alignment supports and the second approach uses no support.

Orgéas et al [23], [24] studied the tension-compression asymmetry of nitinol alloy and the stress-induced martensitic transformations in isothermal shear, tension and compression. To test nitinol under compressive loading an anti-buckling device was used to test dog bone shaped sheet with dimensions of 40 mm x 5,6 mm x 2,7 mm (L x W x T) and with Af=55°C. The specimen was heat treated to improve the superelastic characteristics. The compression tests were performed with at low strain rate (10^{-3} /s), the test temperature was between -30°C and +100°C and samples compressed up to a nominal 8% strain with actual measured deformation of 6% strain. Although the specimen used here was neither

obtained from wire nor cylindrically shaped, it was possible to identify the asymmetry presented in nitinol.

Considering cylindrical specimens in particular, Bechle et al. [25] and Jiang et al. [22] tested nitinol tube to study buckling and localized deformation during compressive testing. A support fixture was used to guide the specimen, minimizing buckling effects along the test length. A tube with a diameter of 6,35 mm and a wall thickness of 0,25 mm was used with a total length of 40,6mm and a working length of 20,3 mm. The ratio between length and diameter is of approximately 3, the tested temperatures of the specimen were 13°C, 23°C, 33°C and 43°C and digital image correlation (DIC) techniques were applied to monitor the evolution of strain along the specimen during loading and unloading. The temperature was controlled by a water circuit passing inside the tube. Buckling of the specimen was observed due to the higher ratio of the tube diameter to the wall thickness.

Siddons et al. [26] tested nitinol tube under tensile and compressive loading in the superelastic regime. Again, the specimens were placed in a specific support to avoid buckling during loading. A superelastic tube (A_f of -8.5°C) with an outer diameter of 3.175 ± 0.025 mm a wall thickness of 0.335 ± 0.025 mm, a total length of 42 mm and a free length of 7 mm (between grips) was tested. The test temperatures were 19°C and 37°C, with up to 100 loading cycles applied and samples deformed up to 2.5 mm (6% strain). Asymmetry between tension and compression was observed and the stress-strain curves changed in the first cycle but stabilized after approximately 40 cycles.

Similar to Siddons [26], Reedlunn et al. [27] also tested nitinol tubes under tension, compression and bending to study the localized deformation during phase transformation. During compressive testing, a set up with custom-designed fixtures was used along with a DIC technique to monitor the local strain field and reduce the grip effects. An as received tube specimen was used with an outer diameter of 3.176 mm and a wall thickness of 0.3175 mm. The total length of the specimen was 41.59 mm and the free length during the test was 9.38 mm. DIC was effectively used as an extensometer to monitor the strain field during loading/unloading and the gauge length (GL) used was 5.33 mm. The test was

performed at room temperature and the sample deformed up to 4% strain. Again, asymmetry was observed when comparing the compressive stress-strain curve with the tensile one and no localized transformation was identified during compressive loading.

Turning now to testing wire samples under compression, Henderson et al. [28] proposed a new approach. Wires with nominal diameter of 1, 1.8 and 2.4 mm were tested in the superelastic regime using the holder shown in Figure 3.2 to avoid buckling during the test. The total length of the specimens was 21.5, 37.8 and 48.4 mm with a free length of 1, 1.8, and 2.4 mm, respectively. Specimens were deformed up to 4% strain for 50 cycles at a temperature of A_f + 30°C. This method presented good results under compression loading for fine wire.

Later, Brodie [3] used the same method to characterize stress-strain response up to 6% compressive strain at room temperature, characterize the stress-strain response at different temperatures, investigate the effect of three load-unload cycles to 6% compressive strain and investigate the effect of loading history on the unloading stress-strain path in compression at 37˚C. For all uniaxial compression test results presented in his work, the stress-strain curves presented a vertical drop in stress when changing from loading to unloading. This was assumed to be a result of frictional forces in the wire holders. To obtain the true material response to compressive loading Brodie developed a different compressive test method without any supports, explained more in detail further in this literature review.

For the second approach to compression testing, where no supports are used to maintain alignment during the test, the available literature suggests both the use of bulk samples and cylindrical specimens with a lower ratio of length to diameter. Also, different strain rate testing has been suggested by some authors. Furthermore, when testing nitinol wire in compression with no supports restraining the sample, extra care needs to be taken from a safety perspective due to the risk of the sample jumping out of the support during the test.

Elibol et al. [29] compared the stress-induced martensitic transformation under uniaxial tension, compression and compression-shear loading in the superelastic regime. For the compression tests, specimen of 9 mm diameter and 9 mm length (L/D=1) were used and at the end surfaces (in contact with the platens) lubricant was applied to reduce friction effects. The specimen was deformed up to 3% strain and the strain field was measured using an optical DIC technique.

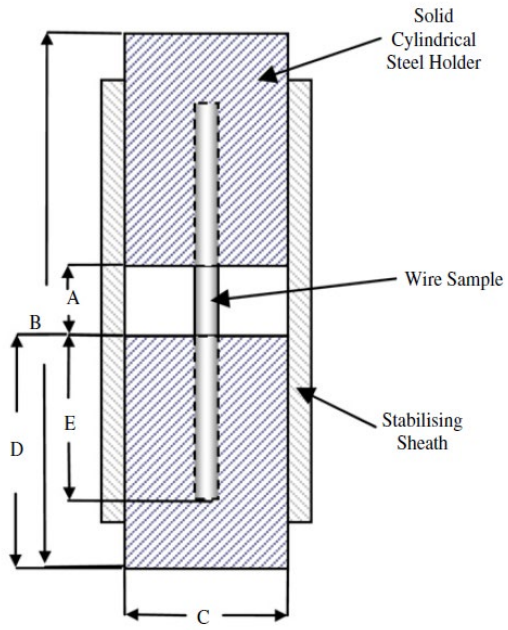

Figure 3.2 – Compression test holder for nitinol wire. [28]

Jalaeefar et al. [30] compared the mechanical properties of nitinol with structural steel. For the compression tests, specimens with a diameter of 8 mm and 12 mm long were used with L/D = 1.5 to avoid buckling effects during the loading. The specimens were deformed until final rupture, which in nitinol was equivalent to approximately 37% strain.

Both Xie et al. [31] and Liu et al. [32] studied the asymmetry of the stress-strain curves of nitinol under tension and compression. To study under compressive loading, specimens

with a diameter of 6.7 mm and a length of between 10 and 20 mm were used and tested at room temperature. Lubricant was placed on the loading surfaces to reduce friction forces and a linear variable differential transformer (LVDT) was used to measure the strain field in the test. The specimens were subjected to 50 loading cycles and maximum strains of 1%, 2% and 4% were applied. Eventually, it was concluded that the specimens subjected to compressive loading were quickly strain-hardened and no stress-plateau was visible on the stress-strain curves for compression, suggesting that the reorientation process of the martensite takes place more easily under tensile than compressive loading.

Saigal et al. [33] wanted to study the compression of "bulk" sized nitinol as well as the tension-compression asymmetry and compare the results with the available literature for tubing and wire devices. The specimens used had a diameter of 6.73 mm and a length of 13 mm, having a ratio L/D of 1.9. The compression test was performed at temperature of 50°C and the main conclusion was that compressive strength levels were much higher than tensile strength levels.

While discussing testing nitinol under compression loading, Chen et al. [34], Nemat-Nasser et al. [35]–[37] and Adharapurapu et al. [38] focused on studying nitinol at high strain rates using a split Hopkinson pressure bar (SHPB). Chen et al. [34] tested at room temperature with cylindrical specimens of 7.94 mm diameter and 8.10 mm long. Nemat-Nasser et al. [35]–[37] on the other hand tested cylindrical specimens with a diameter of 4.5 mm and 5 mm long with polished ends to reduce friction. Finally, Adharapurapu et al.[38] used cold-rolled nitinol with diameter of 12.7 mm. In conclusion, all authors demonstrated that the compressive stress-strain behaviour depends on the strain rate. Furthermore, both Nemat-Nasser et al. [37] and Adharapurapu et al. [38] also studied the effect of temperature with high strain rates where it was concluded that the behaviour of nitinol under compressive loading has a stronger sensitivity to temperature than to strain rate.

Increasing the L/D ratio of the specimens, Zhang et al. [39] tested at room temperature cylindrical specimens of 3.5 mm diameter and with a L/D of 3 to minimize the end effect

and prevent buckling. The compression strain tested was of 4.2% with lubricant applied on the ends. An infrared camera was used to measure the specimen temperature.

Šittner et al. [40] tested wire to study the Young's Modulus in the martensite phase. The test was designed to question the previous results regarding Young's modulus which suggested that in the compression of wire the modulus of the stress-induced martensite should be higher that the austenite modulus. The setup used in the experimental compression test was based on a standard compression method using a wire diameter of 1.78 mm and 3.53 mm long with heat treatment. Temperature during the test was 60°C and the compressive strain was up to 5%. DIC was used during the test to measure the strain field.

More recently, Brodie [3] and Boukis [2] improved the compression testing approach used by Henderson [28]. This new testing focused on elimination of the friction forces reported when using Henderson's method. Initial feasibility of this approach was performed by Brodie in collaboration with Boukis. This new approach is a scaled-down version of the large diameter sample, bulk materials used by previous investigators presented above in this section. It used the Deben Microtest 2000 (Figure 3.3.a)) in-situ loading equipment within a Scattered Electron Microscopy (SEM). The SEM used in this setup was a Hitachi Scanning Electron Microscope S-3700N. A specific miniature sample was created for this test taking in account a suitable L/D ratio to avoid buckling, using wire diameter of 1 mm and 3 mm long produced by EDM machining to ensure that the ends of the sample are perpendicular to the wire axis. The sample is placed horizontally as shown in Figure 3.3.b), contrary to all the compression tests described previously. The test was performed at room temperature (23°C) and lubricant was used on the sample ends to allow lateral expansion. Specific compression platens were manufactured and heat-treated to have a harder surface, thereby avoiding indentation by the sample during loading. The displacement used was equivalent to 6% nominal strain as shown in Figure 3.4.

Figure 3.4 shows the compressive stress-strain response commonly obtained in nitinol. Analysing the curve for up to 6% strain, linear elastic behaviour is exhibited up to

approximately 0.02 true strain. In compression unlike tensile loading, the stress-strain curve does not exhibit a flat upper loading plateau, rather, this 'plateau' or inflection has a stress increase of approx. 200 MPa between 0.02 and 0.04 true strain. Beyond 0.04 true strain a second linear response is exhibited up to 0.06 true strain, attributed to deformation by martensite elasticity. During unloading, a linear response is displayed and goes up to approx. 0.04 true strain where the unloading plateau starts. Again, the plateau presented in the stress-strain curves under compression loading during unloading is not flat but exhibits a decrease of true stress along with the true strain throughout the phase change from martensite to austenite. A final linear unloading is exhibited closing the cycle or loop this way. Thus, the hysteresis as described in section 2.2.1 for tension is also observed when nitinol is subject to compressive loading and unloading.

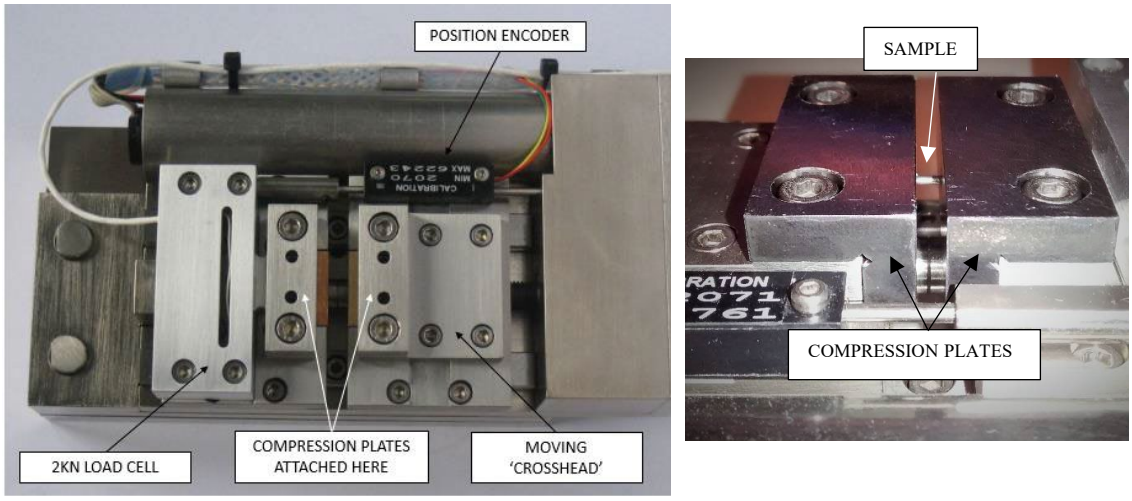

a) *b)*

Figure 3.3 – Compression test setup for nitinol wire without holders; a) Detail of the setup; b) Sample placed between platens. [2], [3]

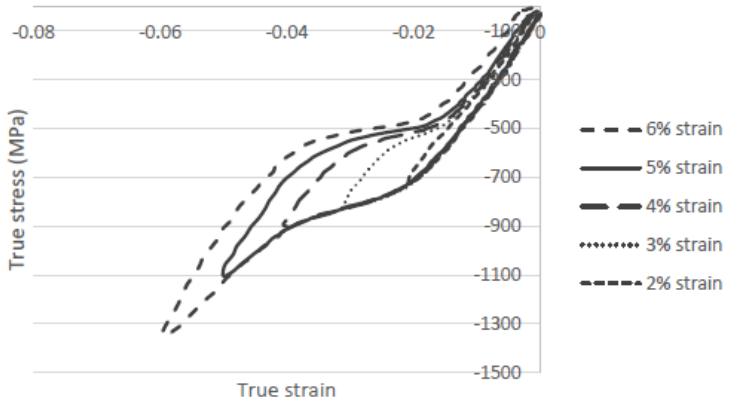

Figure 3.4 – Compression stress-strain response for nitinol. [2]

As explained previously, the stress-strain response obtained during compressive loading does not show a plateau like the one observed during the response for tensile testing, nevertheless, to keep the same terminology as the literature available for compressive testing on nitinol, plateau will be used in this work to describe the inflection observed during compressive loading.

3.1.3 Asymmetry

Comparing the stress-strain response for tension seen in Figure 3.1 and compression in Figure 3.4 it is possible to observe the asymmetry of nitinol. Although the quantitative values differ substantially, the qualitative comparison between tension and compression is more consistent. In both responses a linear elastic response is evident as well as an upper and lower 'plateau'. Bucsek et al. [41] considered the myths and truths of nitinol mechanics regarding the tension-compression asymmetry, where they identify as true:

> '*The truth is martensite crystals may be more compliant, equally stiff, or stiffer than austenite crystals, depending on the orientation of the loading direction with respect to the unit cells.'*
>
> *'The Young's Modulus of polycrystalline nitinol is not a fixed number – it changes with both processing and in operando deformations. Nitinol*

martensite prefers to behave stiffer under compressive loads and more compliant under tensile loads.'

When Reedlunn et al. [27] studied tension, compression and bending on nitinol tubes, they also evidenced the asymmetry between tensile and compressive loading, Figure 3.5

Looking at the lower graph from Figure 3.5 and analysing the response from test C1 and T1 (interrupted line), during loading the initial modulus in compression is a straight line that goes up to approx. 1% strain and in tension the line is almost straight up to 1% with a slight change in the slope at 0.5%. This slight curvature in the elastic modulus in tension is often referred to as the evidence of the R-phase. Above 1% strain the transformation of austenite to martensite starts both in tension and compression but with the critical stress being much higher in compression at approximately 600 MPa against 400 MPa in tension. The plateau in tension is flat and reaches 6% strain, on the other hand, in compression the plateau displays a positive slope and is much smaller than in tension, up to 3.5% strain approx. After 3.5% there is the formation of another linear increase of stress with a steeper slope, similar to the initial modulus, that goes up to 4% strain. This indicates that deformation is not affected by the phase transformation but by martensite elasticity.

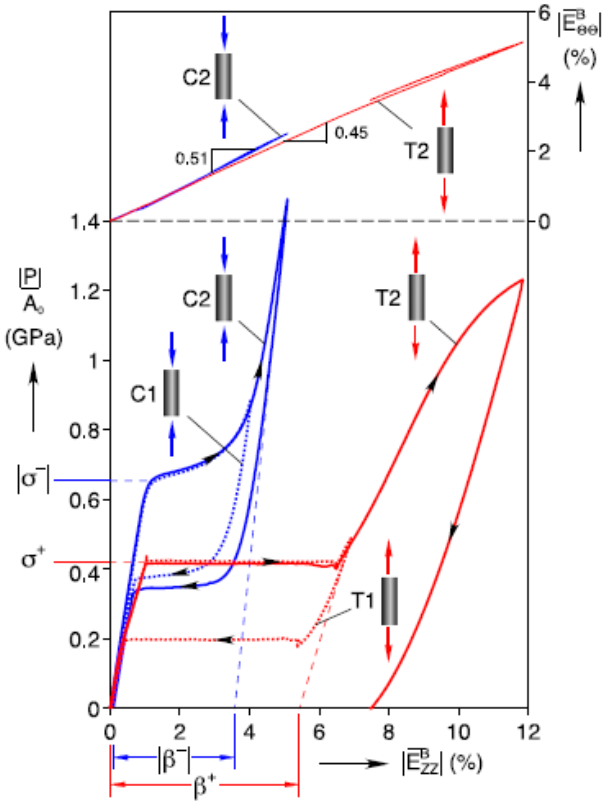

Figure 3.5 – Comparison of tension and compression response. [27]

Considering now unloading, there is another unload modulus, like the loading, both for compression and tension. This modulus is continuous down to approx. 3.5% strain in compression where the reverse transformation then starts with the creation of the plateau. Similar to loading, this plateau has a slope, where the stress decreases with decreasing strain, contrary to tensile unloading, where a flat plateau is observed. The unloading plateau in compression occurs at higher stress values when compared with the tensile response and both finish approximately at 0.5% strain. Below this point, both tension and compression have a linear elastic response finishing at 0% strain, where the material is fully austenite.

Henderson et al. [28] also studied the tension-compression asymmetry on nitinol but in this case for wire. The results obtained are the same as Reedlunn, where the stresses are

higher in compression than in tension. This asymmetry is attributed to the low crystallographic symmetry of the martensite structure [24], validating also the truths described by Bucsek et al [41].

Reedlunn et al. [27] also tested new samples under compression and tension for higher strains, Figure 3.5 specimen C2 and T2. Both follow the same path during loading. During unloading, in tension there is a small deviation in T2, this being caused by the high strain where a significant plastic deformation occurs leading to the non-closure of the loop with a residual strain of 7.49 %. In compression the unloading in both experiments have similar strain fields.

3.1.3.1 Localization

Shaw and Kyriakides [19] studied the difference between the local and global deformation during tensile testing in wire. In results shown in Figure 3.6 they compare the stress-strain curve obtained through the machine displacement and the mini extensometer. Figure 3.6.a) shows there is a difference between the two curves due to the slip in the grips when pulling. This slipping in the grips happens during the transformation, when the martensite transformation starts it causes an increase in the stiffness of the material, this way increasing the stress in the elastic deformation.

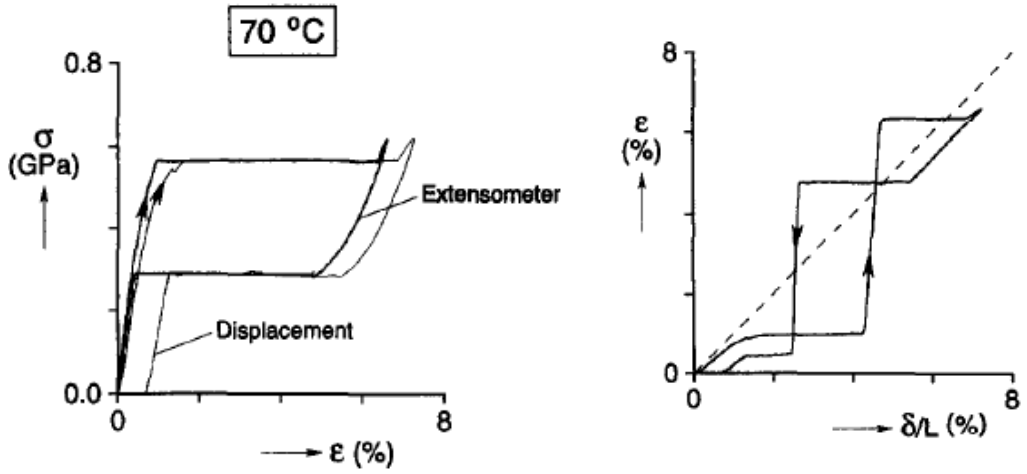

a) *b)*

Figure 3.6 – Comparison of global and local responses at 70˚C; a) Stress-strain response; b) local strain vs end deflection. [19]

It is important to understand how local transformation occurs compared with global transformation to avoid errors and to understand the associated physical mechanisms thereby improving the modelling parameters.

Comparing the local deformation from the extensometer with the total deformation (Figure 3.6.b)) is possible to see that in the initial elastic deformation both local and global strain are in accordance, until martensite starts transforming ($\varepsilon \approx 1\%$). From this point forward the local strain stops growing while the global strain keeps increasing, meaning that the transformation is occurring in a different part of the specimen or there is slipping. At $(\delta/L) \approx 4.5\%$ the local strain increases abruptly up to $\varepsilon \approx 6.5\%$, this means that the material within the gauge length of the mini extensometer has transformed to martensite. During unloading the initial part again shows both strains in accordance, this recovered deformation is elastic deformation from detwinned martensite. Similar to loading, globally the specimen is deforming but not within the extensometer gauge length, then abruptly, the deformation due to the reverse transformation is localised within the gauge length. The final elastic unloading is again the same for both local and global deformation. Through this experiment it is possible to conclude and initially understand how the transformation occurs locally along the sample for tensile loading in nitinol wire.

Following this, Shaw performed the same experiment but with four mini extensometers placed in different parts of the wire along with a thermocouple, as explained in Figure 3.7, to understand the evolution of the stress-induced transformation.

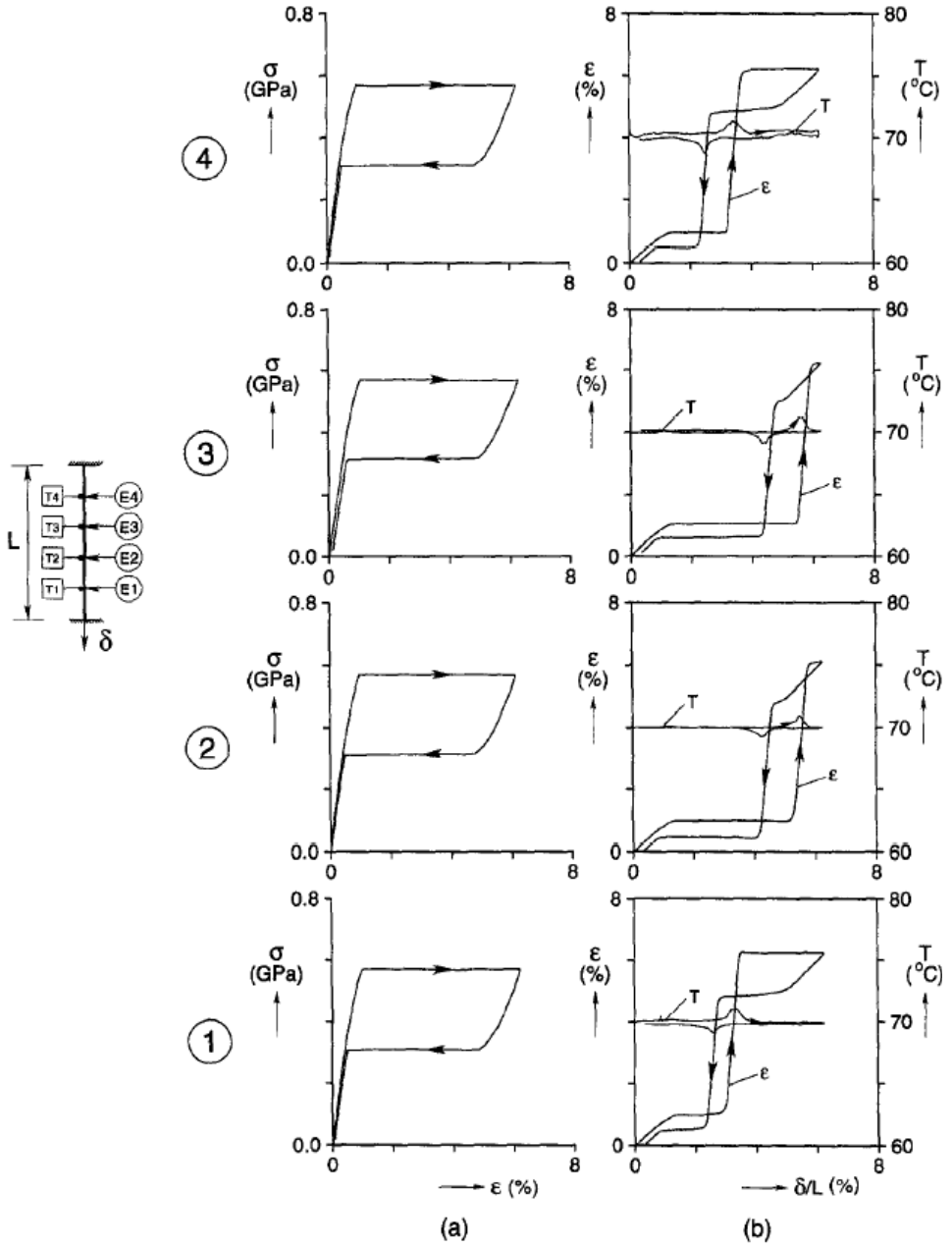

Figure 3.7 – a) Local stress-strain responses at different positions in the wire; b) corresponding strain and temperature histories. [19]

From this study it is possible to detect four different transformations happening at different times. During loading the transformation starts at **1** followed immediately after by **4**, later the transformation happens at **2** and finishes at **3**. This demonstrates that martensite starts

transforming near the grips and propagates towards the centre. Unloading starts at **3** followed by **2**, then at **1** and finishes at **4**.

Also, with the thermocouples it was possible to see at each location that the temperature changes when the transformation is occurring, creating peaks in temperature. This demonstrates the materials sensitivity to temperature.

Ultimately, Shaw and Kyriakides concluded that the transformation stress along with the mechanical response are very sensitive not only to temperature but also strain range and thermomechanical history.

Both Reedlunn et al. [27] and Bechle et al. [25] also analysed, but with the benefit of DIC techniques, the strain field during tension and compression. The stress-strain curves for tension and compression are presented in Figure 3.9 where the circled numbers correspond to the strain field images obtained through DIC, red numbers correspond to tension with the strain field in Figure 3.10 and the blue numbers to compression with the strain field in Figure 3.11.

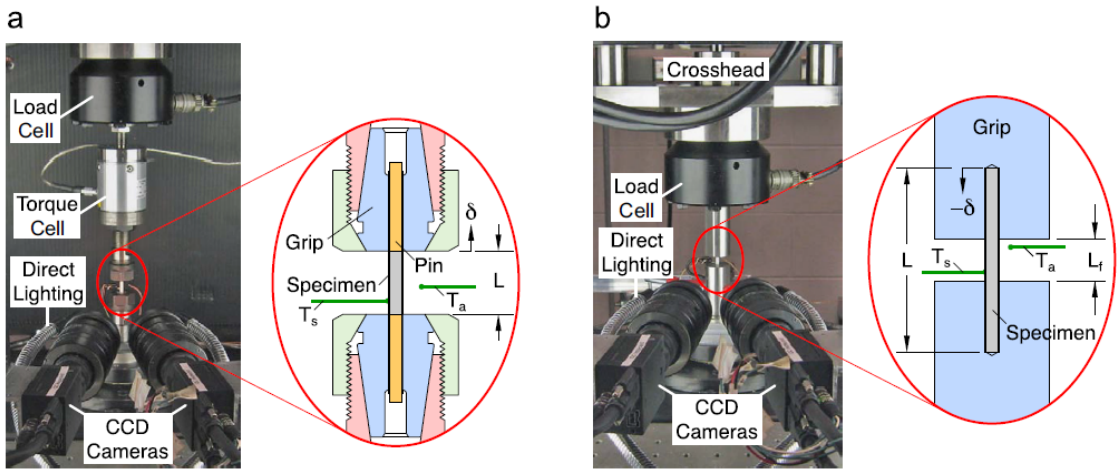

Figure 3.8 – Photographs of uniaxial setups and schematics of grips (to scale): a) tension setup; b) compression setup [27]

In Figure 3.8 it is possible to observe the test setup used by Reedlunn [27] for both tension and compression test. From the figure it is possible to see that in for tension, the nitinol tube was held by collet holders. For compression, the nitinol tube was held using steel cylinders, each with a 3.20 mm diameter with a 15.9 mm hole, the specimens were coated with light oil to help the specimen slide freely inside the compression grips.

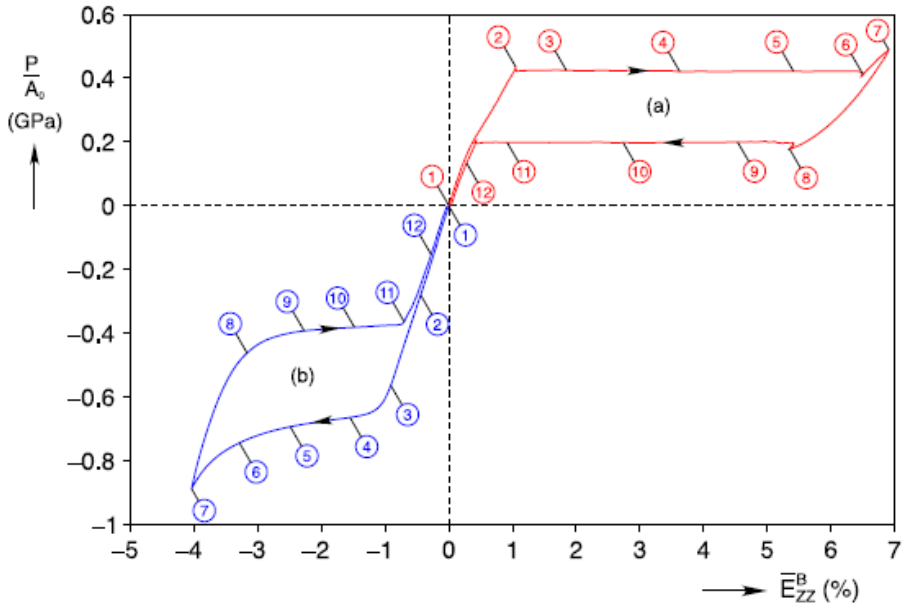

Figure 3.9 – Stress-strain responses of tube specimens at room temperature during a) tension and b) compression. [27]

Comparing the evolving strain fields in Figure 3.10 and Figure 3.11, initially it is clear that there is a localized transformation under tensile forces contrary to what is seen for compression.

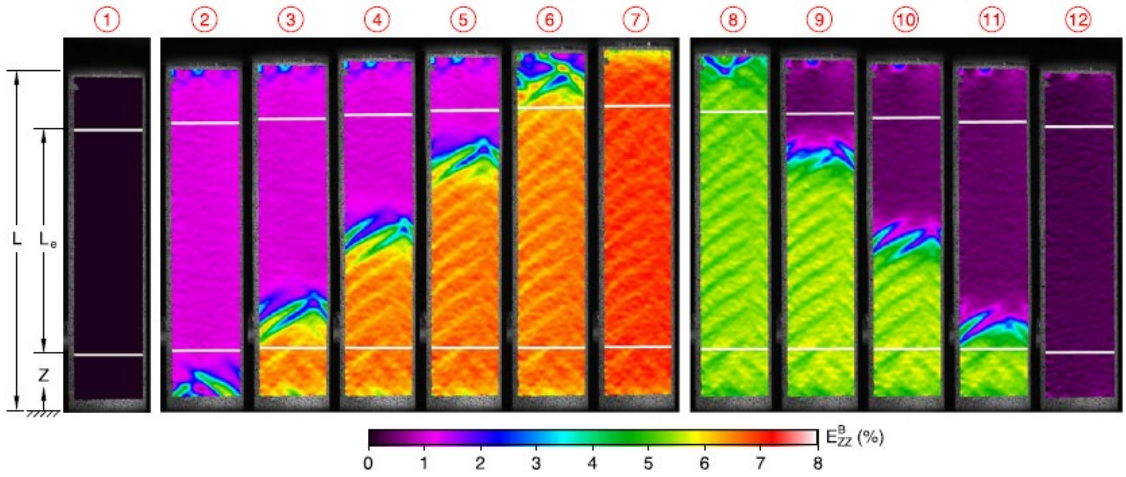

Figure 3.10 –Tension experiment with axial strain field images from DIC at times labeled in Fig. 3.8.a). [27]

The strain fields shown in Figure 3.10 are related to the tube specimen, detected by DIC where the circular numbers in red correspond to the numbers presented in Figure 3.8 for tension. The white lines in the strain field represent the DIC extensometer gauge length. Image **1** refers to the start of the test with zero forces applied. Images **2** – **6** show a propagating transformation front with increasing applied force, this is during transformation $A \rightarrow M^{+}$, from the lower grip to the upper during the load plateau. In image **7** the specimen is fully transformed in Martensite, at maximum strain. Images **8 – 11** represent the unloading plateau, and shows the transformation propagation from the upper grip to the lower grip that is the $M^{+} \rightarrow A$. Finally, in image **12** the transformation is complete with a very small residual stress, indicating almost perfect superelasticity with no permanent residual deformation. The white lines in the strain field represent the DIC extensometer gauge length. When analysing the strain field images, is possible to identify on image **2**, **6** and **8** that the grips have influence on front, where the front near the grips is altered when comparing to the images **3 - 5** and **9 – 11**.

When analysing the strain fields under uniaxial compression, Figure 3.11, it is clearly seen that contrary to what was observed during tension, there is no distinct transformation when looking at deformation under this load.

The forward transformation goes from image **2 – 6** where the strain field is almost homogeneous. From image **8 – 12**, during the reverse transformation, the strain field is again quite uniform, with the exception of image **10**, that the author justified as the tube buckling. In this situation, the grip strain measurement was contaminated by the specimen settling into the grips, grip compliance and small friction between the specimen and the grips, therefore, the chosen gage length was not the grip strain but the black lines seen on image **1**.

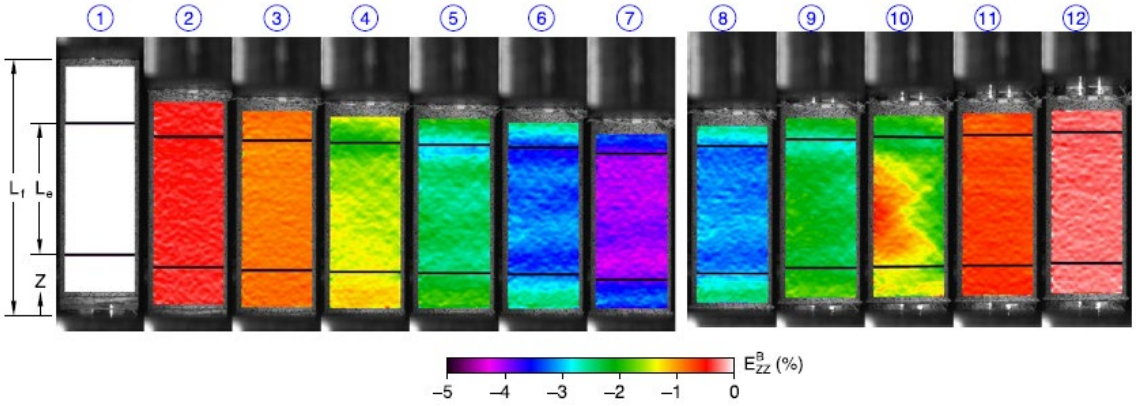

Figure 3.11 – Compression experiment with axial strain field images from DIC at times labeled in Fig. 3.8.b). [27]

A similar study was made by Bechle and Kyriakides [25] where they tested the tension-compression asymmetry in nitinol tubes. In Figure 3.12 it is possible to observe the setups used for tension and compression test. Figure 3.13 shows the stress-strain curve during tensile loading and the respective strain field obtained through DIC technique.

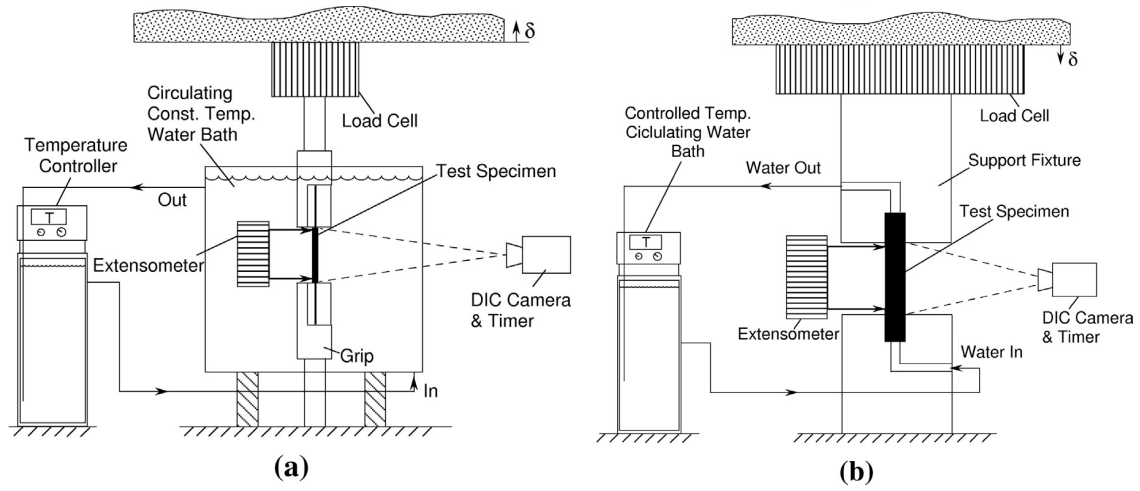

Figure 3.12 – Custom experimental setups for isothermal a) tension and b) compression test on tubes. [25]

Analysing the strain field in tension in Figure 3.13.a), during loading, austenite deforms elastically and homogeneously as shown in image **1**. The material starts transforming into the martensitic phase at just under 400 MPa. In this image, it is possible to see that martensite nucleates at one of the gripped ends, this is due to the apparent stress concentration, this phase change results in local macroscopic deformation as seen in image **2**. With the increase of the elongation, the martensitic phase keeps propagating, from left to right (images **3 – 6**) corresponding to the start and end of the upper stress plateau. Due to the circular geometry of the specimen, the nucleation front has a shape of a spiral, images **3** and **4**.

In image **5**, around halfway through the transformation in the specimen, martensite starts nucleation in the opposite grip. (images **5** and **6**). The two fronts propagate towards each other, and in image **8**, just before the transformation finishes, there is a drop in stress (point **8** in the stress-strain curve) caused by the interaction of both fronts. From image **8** to **9** the transformation is complete, comprised of fully detwinned martensite and uniform.

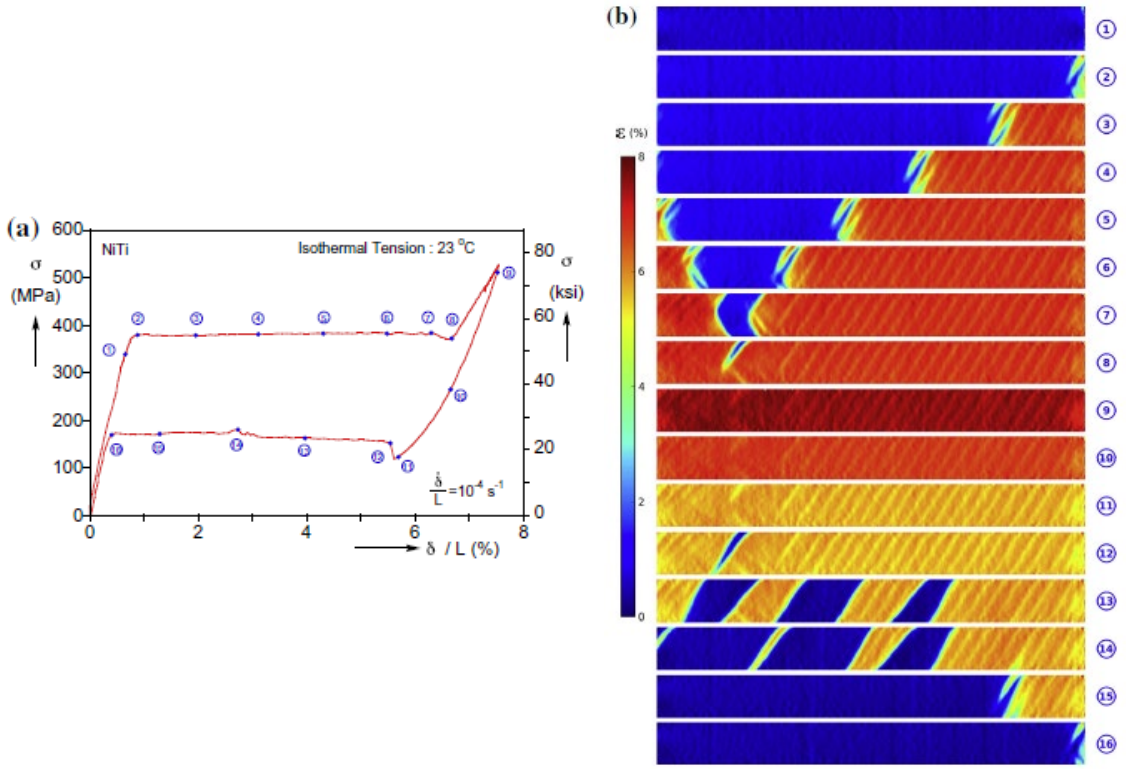

Figure 3.13 – a) Pseudoelastic tensile stress-strain response of NiTi tube at 23°C; b) Axial strain field from DIC with corresponding numbers to the tensile response [25]

During unloading, the strain field is slightly different. The deformation is homogeneous in image **10** and **11** then in image **12** martensite becomes unstable and start transforming back to austenite, the nucleation starts in the same location of the previous termination of the A → M transformation, with an increase in stress. During unloading, the transformation front is a single helical band, image **13**, during this transformation the stress increases gradually up to point **14**. At this point, image **14**, the left front reaches the grip, previously responsible for the nucleation recorded. From image **14** to **15** a single front propagates to the grip on the right side. Finally, at image **16** the reverse transformation is complete.

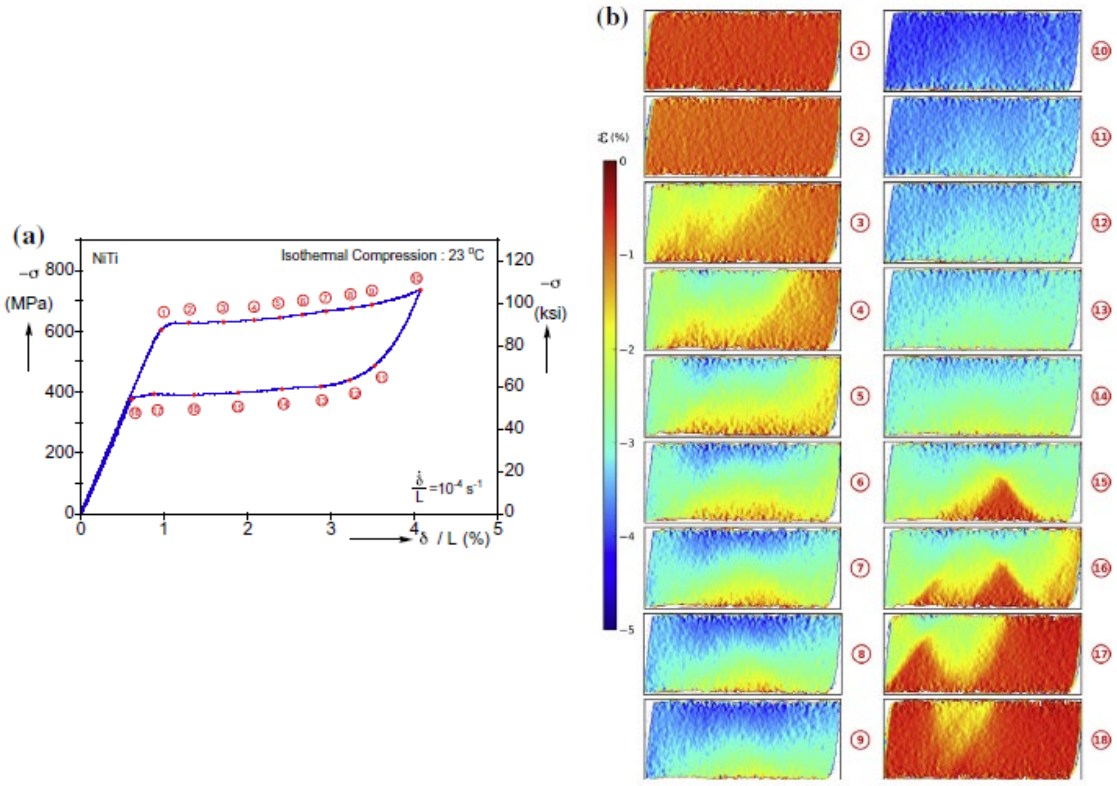

Figure 3.14 –) Pseudoelastic compressive stress-strain response of NiTi tube at 23°C; b) Axial strain field from DIC with corresponding numbers to the compressive response [25]

When under compressive loading, and similar to the Reedlunn results, the strain fields observed from DIC show a more homogeneous transformation with no localization in Figure 3.14. From image **3** to **8** the strain field has exhibited some deformation. This deformation indicates that the specimen is undergoing some bending during loading. Upon unloading, the deformation remains homogeneous until image **14**. Again, a strain gradient is visible in the specimen, image **15** and **16**, this gradient is associated with bending occurring during unloading. In image **18** the transformation is complete, and the deformation is uniform.

The reason why tension exhibits strain localization and compression not, is still a long-standing open scientific question. One plausible explanation to the asymmetry on nitinol is due to differences in detwinning strain and critically resolved shear stresses (Schimd

factors) caused by crystallographic texture. In other words, Mao et al. [42], while using electron backscatter diffraction in nitinol tubes, found that grains aligned for tension had a distribution of Schmid factors within ±8.7%, while grains aligned for compression varied by ±20%. They argued that a narrow distribution of Schmid factors leads to an autocatalytic effect, where when one grain transformation causes the surrounding grains to transform, leading to a macroscopic front. On the other hand, a large distribution of Schmid factors, implies that transformation is less likely to spread to surrounding grains without a large increase in stress, leading to a more diffuse transformation.

In conclusion, when it comes to tensile testing, extra attention needs to be taken into account during strain measurement and that the nitinol mechanical response also depends on geometry. As mentioned by Bechle, [25]due to the circular geometry of the tubular sample, the nucleation front of martensite transformation on Figure 3.13 is in the form of a multi-pronged spiral. When looking at the length dependence, no information is available in the literature that suggests a size dependence when characterising nitinol wire under tensile loading.

On the other hand, it is possible to see that martensite transformation appears to be more homogeneous during compressive loading and this is possibly due to the need of a large increase in stress for a single grain to cause transformation to the surrounding grains. When understanding the sample size dependence of the mechanical characterization of nitinol in compression, no information is available in the literature, suggesting that there is no size dependence.

3.1.3.2 Effect of temperature

Understanding how the temperature affects nitinol mechanical response is also important when characterizing the material to be used in medical devices.

Duerig et al. [43] studied transformation temperatures in nitinol wire used in medical devices under tensile loading. Figure 3.15 shows the forward transformation at different temperatures, ranging between -80°C and 80°C, where is possible to see how the stress-

strain response changes with temperature. As the temperature increases, the upper plateau occurs at higher stress values.

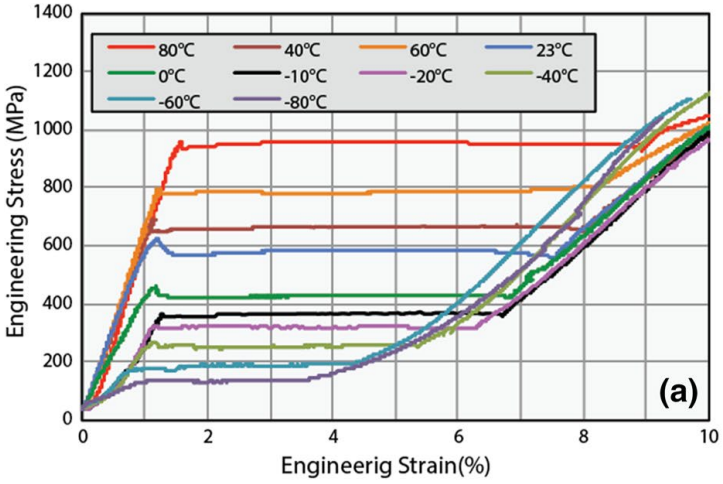

Figure 3.15 – Loading curves at various temperatures during tensile loading [43]

Looking at the response in compression, as tested by Bechle et al. [25], with increasing temperature, the stress at the transformation start is higher.

The stress-strain response in nitinol is thus highly dependent on temperature during the test for tensile and compressive loading. Heat treatment and ageing also have an effect on the response of nitinol wire and it is therefore important to take test temperature into account when testing nitinol wire for medical devices as well as the local in-situ temperature.

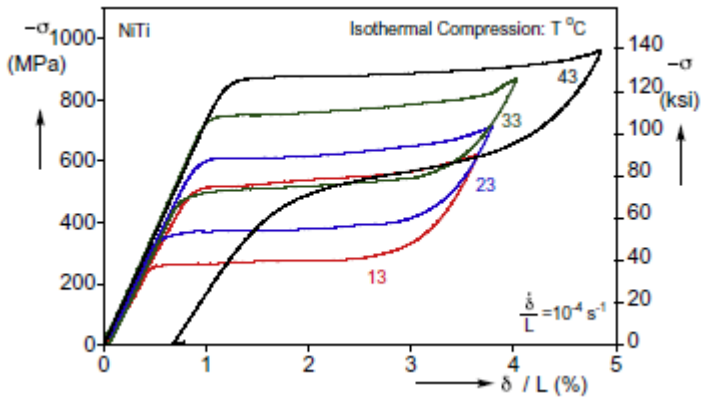

Figure 3.16 – Compressive stress-strain response of NiTi tube at different temperatures [25]

3.1.4 3-Point Bend testing

When designing endovascular stent graft devices, it is important to understand how the nitinol wire component of the device behaves under bending deformations. Thus, it is important to have a better understanding of the material in-service behaviour, since the more prevalent deformation in the Anaconda stent graft device is bending both when it is compacted to enter in the delivery system and later in-service. Testing nitinol wire under bending deformation is important to obtain the experimental data to be used later in FEA simulations of the nitinol stent graft, in which 3-point bending is the favoured type of bend test. In this test the force is applied in the midpoint of the sample which is placed on two supports. This section will briefly describe the latest work of Brodie [3] and Boukis [2] related to 3-point bending on nitinol wire.

Both Brodie [3] and Boukis [2] work focused on testing nitinol wire using a 3-point bend testing setup where they study the temperature sensitivity, load rate effects and cyclic behaviour. Brodie [3] tested wire of 0.14 mm and 0.45 mm diameter. For each diameter, a different setup was used. With the smaller diameter wire (0.14 mm), supports with a diameter of 1.3 mm were used along with a span of 6 mm. For the larger diameter, the supports used have a diameter of 4 mm with a span of 20 mm. The test was displacement controlled using maximum deflections of 3, 5 and 10 mm. Later, Boukis [2] used a similar

setup to test 0.45 mm and 1 mm diameter wire. Supports with a diameter of 1.3 mm were used on both wires, with a span of 20 mm. The test was also controlled by displacement where 2.5 mm and 6 mm maximum deflection were applied. Both Brodie and Boukis tested the wire at 22°C in air and 37°C in a water bath.

Figure 3.17 shows a typical response of a single load-unload cycle for 3-point bending of 0.45 mm diameter wire at 23˚C. During 3-point bending, it is important to understand the force throughout the bending, therefore the response is given in load-deflection, as seen in Figure 3.17. Analysing the load-deflection response for 10 mm deflection presented in the figure, it is possible to understand that during loading the curve initially shows a linear elastic bending stiffness, the material is in its austenitic phase. At approximately 3.5 mm deflection, the initiation of a small load plateau is visible up to 5 mm deflection. During this load plateau, the material goes through Stress-Induced Martensite (SIM) phase transformation at a near-constant stress. After the plateau, the curve shows an apparently negative stiffness up to the maximum 9.8 mm deflection. During unloading, it is possible to see the increasing of the force until 5 mm deflection, showing the load-deflection hysteresis. The reverse of the phase transformation is visible at the unloading plateau below 5 mm deflection until 2.8 mm deflection. At this point the curve shows the unloading linear stiffness associated with the austenitic phase.

Since 3-point bend testing is not part of the objectives proposed for this work, 3-point bend will not be study experimentally. This type of deformation is crucial when designing stent graft devices, so only a brief description of the previous work is made in this report. Other researchers have also tested nitinol wire during bending deformation, where Reedlunn et al. [27] tested superelastic nitinol tube at 4-point bending at 23˚C where the results for ‘normalised moment’ vs ‘dimensionless curvature’ are shown. Pelton et al. [44] preformed both 3 and 4-point bending on nitinol wire for 1.5 mm diameter with a 20 mm span between supports and De La Flor et al. [45] preformed experimental cantilever bending testing on 1 diameter mm nitinol wire and 60 mm long.

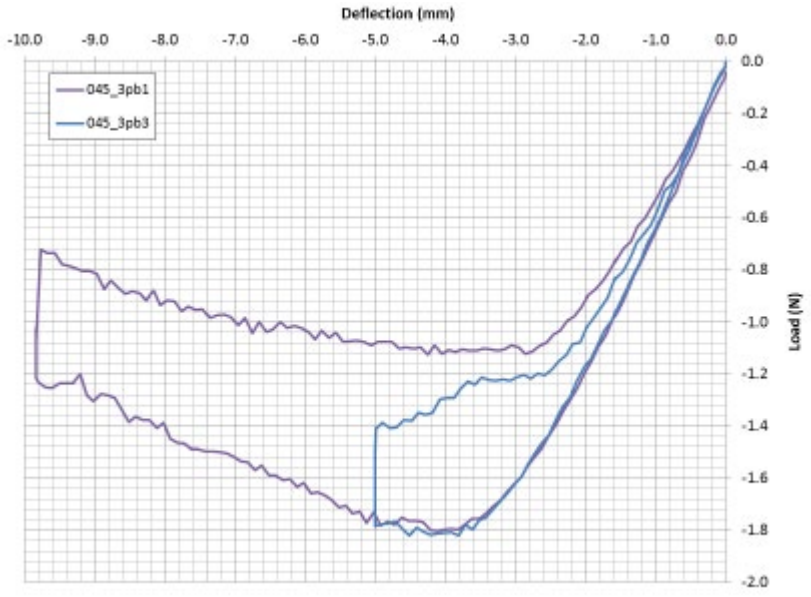

Figure 3.17 – Typical response of single load-unload cycle for 3-point bending of 0.45 mm wire at 23˚For the C obtained from Brodie [3]

This topic is described further during the numerical modelling part, where the inclusion of the compression experimental data will be combined along with the previous tensile data to improve the numerical models available and thereby be implemented in designing endovascular stent graft devices, more specifically the Anaconda device.

3.2 Constitutive Models

FEA has become a fundamental tool in the development, design, and optimization of medical devices, thereby reducing the number of physical prototypes and associated experimental testing of them. Constitutive models for shape memory alloys are nowadays used to analyse reasonably complicated devices under complex thermomechanical loading history.

Constitutive models are mathematical simplifications of complex physical behaviour where the constitutive equations are *complementary equations to the balance and kinematic equations* [46] and they are fundamental in the mechanical analysis of

engineering materials and structures. In the last few decades the atypical behaviour of SMA has motivated the development of models capable of representing the physical mechanism behind the martensitic transformation. [47]

As Figure 3.18 suggests, the models used in SMA can be split in three main approaches, microscopic thermodynamic models, micro-macro models and finally macroscopic models. Microscopic models [47]–[49] are at the level of lattice or crystal-grain of SMA and look at phase nucleation, interface motion or martensite twin growth and are based on two different theories, the Ginzburg-Landau theory, and molecular dynamics. This approach is impractical for structural simulations due to the high computational cost.

Micro-macro models [47], [50]–[54], at micro or meso scales, use the micromechanics to describe the behaviour of the material. To develop these models requires the use of observable variables (OVs), usually consisting of temperature (T) and external stress (σ) or strain (ε), and internal variables (IVs) that consist of volume fraction (ξ) of martensite and mean transformation strain (MTS). Within micro-macro models the two most common approaches used are micromechanics and micro-plane/micro-sphere models.

Finally, the macroscopic models use phenomenological considerations, simplified micro-macro thermodynamics or direct experimental data fitting to describe the behaviour of polycrystalline SMA. They are based on the theory of plasticity or derived from thermodynamic potentials. Due to the computational efficiency, macroscopic models are the most practical option in engineering to design and analyse the structure of mechanical components. For nitinol, several models were developed that capture the effects of superelasticity but only two are readily available in commercial FEA software packages, these are Auricchio and Taylor model [55], [56] and Lagoudas model [57]. Auricchio model is currently the model widely used in the design of superelastic nitinol components within the medical device industry. As an in-built Abaqus model, this model has been verified and validated as a suitable constitutive model for superelastic nitinol. The simplicity of input parameters of the Auricchio model as an in-built user material makes the Auricchio model accessible to a wide user base [58][59].

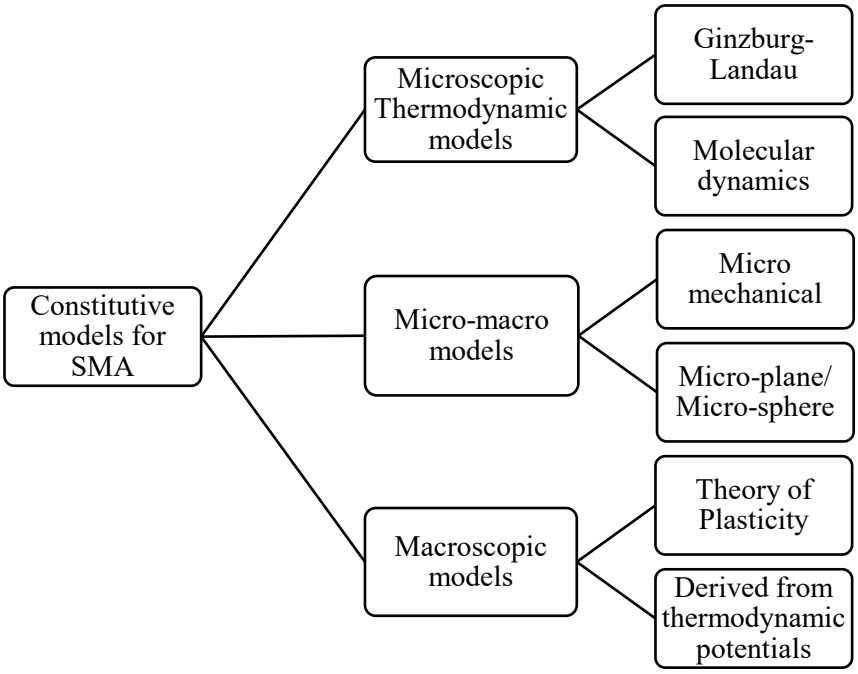

Figure 3.18 – Overview of constitutive modelling approaches for shape memory alloys

Within the scope of this work only the Auricchio model will be discussed because it is the model available in Abaqus, a commercial FEA software. Therefore, it will be the one used for FEA of superelastic nitinol wire loaded in compression, as will be presented in Chapter 7. Abaqus is the preferred software for designing the stent graft medical device, it is also the software used by Terumo Aortic. Therefore, it is the selected software to use in this work, taking advantage of the previous work available during the designing of the Anaconda device. The model available in this software is the Auricchio model, albeit an older version of this model, meaning that some alterations to the model are necessary to obtain a more accurate response to nitinol under compressive loading. A brief explanation of the model will be presented in this section as well as its limitations, identified by the previous work of Brodie [3] and Boukis [2]. Finally, the model developed by Kelly et al. [4] will be use to compare the response of two different models, so a brief description this work will also be mentioned in this literature review.

3.2.1 Auricchio and Taylor in Abaqus

In 1997, Auricchio et al. [55] proposed the development of computational tools for SMA by exploring the applicability of generalised plasticity [60]. The main goals of this work were:

1. Development of constitutive models able to reproduce superelastic behaviour;
2. Implementation of the models in finite element settings;
3. Demonstrate the viability of the models by simulating some applications using finite element software.

Initially a 1D model was developed [61] capable of reproducing the superelastic effect for this state of stress. This model uses two control variables (uniaxial stress [σ] and relative temperature [T]) and one internal variable (single-variant martensite fraction [ξ_S] or austenite fraction [ξ_A]). The production of single-variant martensite is activated by stress increase, temperature increase or the proper combination of both. The full 3D model is a generalization of the 1D model where this model uses three control variables (Stress [τ], Temperature [T] and transformation strain [ε^{tr}]). As internal variables, the 3D model uses two (scale transformation strain [u] and single-variant martensite [ξ_S]). This model considers three phase transformations, austenite to single-variant martensite (A $\rightarrow$ S), single-variant martensite to austenite (A $\rightarrow$ S) and single variant-martensite reorientation (S $\rightarrow$ S). Later the model was improved, allowing different elastic properties for different phases of austenite and martensite [62]. A refined version of the model as well as an efficient algorithm for FE implementation is presented in [63]. Rebelo et al. [64], [65] implemented the 'Auricchio-Taylor' model in Abaqus using a user-defined material subroutine (UMAT for Abaqus/Standard and VUMAT for Abaqus/Explicit). [66]

A more detailed description of the Auricchio model is not within the scope of this work but a complete understanding along with associated equations and evolution of the model is available in the following references [55], [56], [63], [67]–[73].

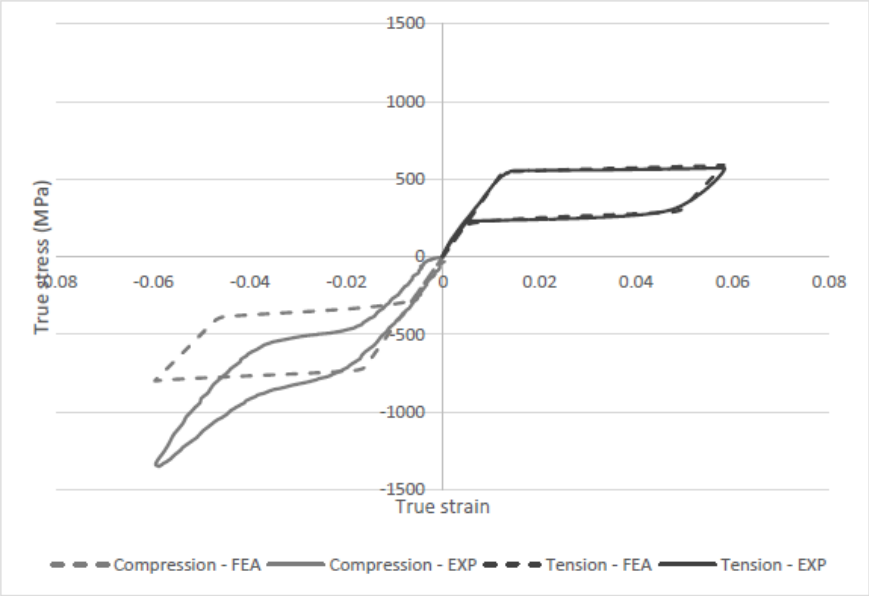

Figure 3.19 – Boukis comparing numerical and experimental response of 1 mm nitinol wire subjected to 6% strain in tension and compression, at 22˚C. [2]

Focusing on the scope of this work, previously Brodie [3] and Boukis [2] studied the capabilities and limitations of the Auricchio model in Abaqus by simulating nitinol wire under different loadings using parameters obtained experimentally. Boukis [2] produced a model capable of studying nitinol wire under tension, compression, 3-point bending and torsion, with the parameters being obtained from previous experiments and the same set of parameters used for simulating the four different loadings. When studying the tension-compression asymmetry, he observed some asymmetry in the model response but when comparing with the experimental response, the asymmetry between tensile and compressive loading is much more pronounced, concluding that the model is very limited when it comes to compressive loading. Figure 3.19 presents some of the numerical results obtained by Boukis for tension and compression.

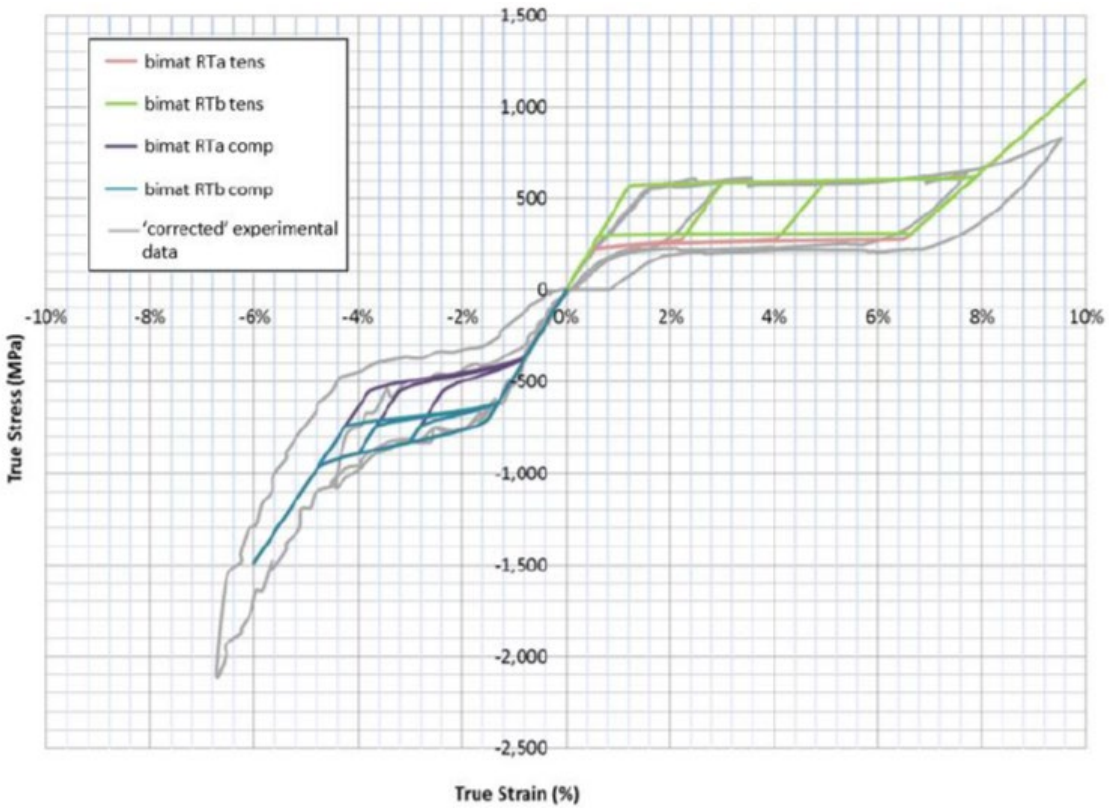

Figure 3.20 – Brodie comparing numerical and experimental response of 1 mm nitinol wire subjected to 6% strain in tension and compression, at 22˚C

On the other hand, Brodie [3] calibrated different UMAT for uniaxial tension and compression, in an attempt to improve the response in compression. Using the respective parameters obtained from experiments for each UMAT, the numerical response obtained for compression loading was closer to the experimental response. When simulating the bending response, Brodie [3] combined the two UMAT, for tensile and compressive loading, to have a bending response closer to the experimental results. Figure 3.20 presents some of the numerical results obtained by Brodie for tension and compression.

This work is based on the findings and associated limitations obtained from Brodie and Boukis and focuses on studying different approaches of the numerical response under compressive loading that can then be applied in a bending simulation.

3.2.2 Kelly and Stebner model

Kelly et al. [4] presented a phenomenological model that describes the macroscopic elastic and transformation behaviour of polycrystalline SMA. The work is based on the framework developed by Sadjadpour et al. [53], [74] albeit with a distinction between the initiation and saturation mechanism. It also follows a formulation for transformation surfaces introduced by Cazacu et al. [75] that describe anisotropic and asymmetric plastic yield surfaces, capturing the asymmetry and processing-induced material anisotropy of SMA transformation. Furthermore, this model is able to distinguish accommodated and orientated martensite, similar to Panico et al. [76] and Chemisky et al. [77]. The model is rate-independent, assuming that at the slow loading rates the kinetics are rate-independent. Rate effects from thermal energy enter in the energy balance. In dynamic situations, the model can be changed to take in account rate effects. Finally, this model ignores the R-phase, due to the small transformation strain involved.

In short, Kelly et al. [4] developed a macroscopic constitutive model of SMA capable of describing:

- Thermal and stress-induced transformation;
- Initiation, reorientation and saturation of martensite under several conditions;
- The difference between various loading modes including tension-compression-shear asymmetry and material anisotropy.

Although various aspects of this model are based on micromechanics, it can be easily and efficiently implemented into engineering design tools like commercial finite element software. A more detailed understanding of this model can be found in [4]

3.3 Summary of Research Priorities from Literature Review

This Literature review highlights some gaps in the knowledge of testing nitinol wire for medical devices particularly in compression, which this research seeks to address in order

to give important insights into superelastic nitinol wire characterisation applicable to stent graft design. These research priorities are listed below:

- The current work aims to take a step forward in compression testing of nitinol wire, using as a base the previous work of Brodie [3] and Boukis [2] at the University of Strathclyde. It thus focuses on testing the wire at different temperatures and obtaining the strain field of the specimen during compressive loading.
- Standardize the compression test for fine wire, examining the repeatability of the test and expanding the test to different materials.
- Improve the existing FEA-based nitinol constitutive model under compression loading, by studying different approaches to the Auricchio model available in Abaqus;
- Compare the response forecast by the Auricchio constitutive model with a different constitutive model.

Chapter 4
Strain Localization Effects During Tensile Loading

4.1 Background

Tensile testing on nitinol wire is widely available on the literature and it is also known of the strain localization of nitinol in uniaxial tension. On the other hand, when looking at compression loading, very little information is available in the literature and no strain localization has been identified under compressive loading. In an attempt to better understand the behaviour of nitinol, a strain localization study is presented in this chapter that replicates the study performed by Shaw and Kyriakides [19] and compared with a similar study presented by Bechle [25] and Reedlunn [27] using DIC techniques to monitor the strain localization. The work presented in this chapter is also to complement the test program presented by Boukis [2] and to gain confidence further along in Chapter 7, when understanding the compressive behaviour of nitinol wire by analysing the strain localization presented on nitinol under tensile loading.

The study presented in this chapter focus on tensile loading in particular interest to on obtaining the strain history plots presented by Shaw and Kyriakides [19] in Figure 3.7 that shows the local strain against the global strain calculated from grip displacement. This study was performed using the Boukis [2] tensile testing methodology and aims to understand how the stress-strain response alters on changing the value of the gauge length (GL) of the extensometer as well as its position on the wire under test.

In this chapter, a study on how the grips influence the tensile test is also conducted. This study looks at the current standards used for nitinol tensile testing, with the purpose of improving these when studying the local deformation.

4.2 Objectives

Based on Boukis' previous work on tensile testing of nitinol wire and understanding of how localised deformation occurs in nitinol wires, the work presented in this chapter has as the main objectives to:

- Identify strain localization on tensile tests using nitinol wire.
- Understand how the grips influence the response;
- Acquire experience in operating the Terumo Aortic testing machine and in interpreting the data it provides;
- Induction to the Terumo Aortic installations and procedures.

4.3 Methodology and results

The methodology used for tensile tests was the same as that developed by Boukis [2], and based on the standard test method ASTM F2516-14 [1]. The material used for tensile testing was the same as detailed in section 2.3, that is, nitinol wire with 0.22 mm diameter, but the sample length of the wire was changed as necessary.

In this section, three different studies were conducted. The first was a preliminary study to see how the local and global deformation change by altering the GL of the sample. The second study consisted of placing the GL at different locations along the wire to see the evolution of the local and the global deformation. Finally, the third study consisted of understanding how the grips influence the local and global deformation response.

The tensile tests were all performed on the testing facilities available at Terumo Aortic and for all the studies, the testing machine used was an Instron 5965 tensile testing machine equipped with an Instron 3119-600 environmental chamber. The machine was fitted with a 2 kN load cell. Specific pneumatic grips were used to restrain the wire ends. The wire was wrapped around horn-like pneumatic cord grips as seen in the schematic diagram presented in Figure 4.4 a). The grip displacement is monitored by the machine and the video extensometer detects the deformation within the GL. This extensometer used was Instron AVE2 non-contact video extensometer. The video extensometer detected

the active GL by tracking two markers that were manually placed along the wire. The test was displacement controlled with the imposed maximum nominal strain of 6%. During the first study, two temperatures were used. Since the first tests were primarily aimed at understanding what type of results it was possible to obtain, they were performed at a controlled temperature of just 30˚C because of the extra time the environmental chamber would take to achieve the 37˚C. All subsequent tests were performed at a controlled temperature of 37˚C.

The results presented in this section were obtained directly using the raw data in the .csv file provided by the machine for each test. The .csv file obtained from the machine contains the information about the strain (%) measured by the video extensometer, the displacement (mm) measured by the machine, the force (N) detected by the load cell and the equivalent tensile stress (MPa) calculated by the software using the user inputs provided at the beginning of each test.

4.3.1 Preliminary study

This preliminary study consisted of trying to understand how changing the GL of the sample would influence the response of the local versus global deformation. For this, as presented in Table 4.1, four different tests were made, changing both the overall length and the GL of the test, as depicted in the schematic shown in Figure 4.1. For this study, two different overall lengths were used. The overall length, as shown in Figure 4.1, is the distance between the grips, where the wire is fixed. The lengths used were, 110 mm and 55 mm. Tests were performed at a controlled temperature of 30˚C, since these were only preliminary tests, with the temperature of 30˚C rather than 37˚C being chosen due to limitations in time. For each overall length, two different GL were tested, one closer to the overall length to understand the deformation on most of the specimen and other smaller to observe if the local deformation changed. Both GL were placed at the centre of the wire. All tests were loaded up to 6% maximum nominal tensile strain and the GL for each overall length are listed in Table 4.1, as well as the temperature of each test.

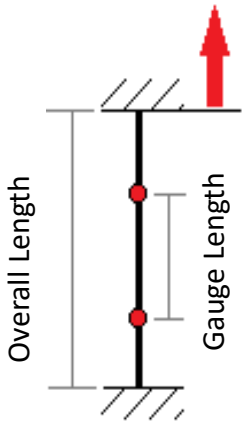

Figure 4.1 – Tensile test scheme of the overall length (OL) and gauge length (GL).

From Figure 4.2 it is possible to observe the results obtained from the preliminary tests. Figure 4.2 a) shows the tensile stress-strain curve obtained from each test and Figure 4.2 b) shows plots of the local strain versus global displacement. The local strain is obtained from the deformation measured with the video extensometer and the global displacement corresponds to the applied end displacement obtained from the machine.

Table 4.1 – List of the preliminary tests at 30˚C.

Test	Sample name	Overall L (mm)	Gauge L (mm)	Temperature (°C)
1	OL110_GL96	110	96.898	31.5
2	OL55_GL45	55	45.136	30.9
3	OL110_GL38	110	38.7	32
4	OL55_GL18	55	18.318	31.4

From Figure 4.2 a) it is possible to see the tensile stress-strain curve are as expected for nitinol wire. The curve has a sharp rise in stress at the beginning corresponding to the austenitic linear elastic behaviour, followed by an upper plateau where phase transformation occurs, until it reaches 6% strain. On unloading, the hysteresis is visible with a drop of the stress level to 300 MPa followed by the lower plateau where the material

transforms back to the austenitic phase, finishing with a closed loop, with no apparent residual strain.

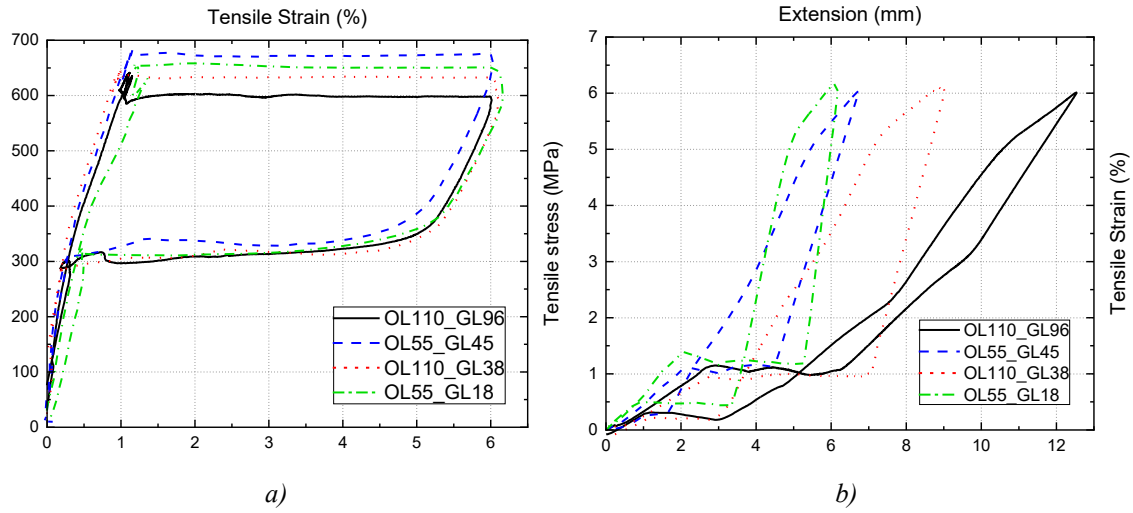

Figure 4.2 – Preliminary tensile test result detailed in Table 4.1s; a) Tensile stress-strain curve at 30˚C; b) Local strain versus global deformation plot for tensile loading.

With Figure 4.2 b) it is possible to understand when the deformation is inhomogeneous, plotting the local strain (Tensile strain in %) versus global displacement (Extension in mm) for each test. It is possible to see that for all curves, a straight line traced at approximately 45˚ during the initial elastic section (approximately up to 2 mm deformation), suggesting that the local and global measurements are in agreement. When the martensite nucleates (Tensile strain ≈ 1%), it is seen that the local strain stops evolving even though the specimen continues to stretch, implying that the transformation is happening elsewhere in the specimen, outside the GL. Between 5 and 6 mm of deformation, the local strain shows a more sudden increase, up to 6%, indicating that at this point the material within the GL has fully transformed to martensite. At 6% strain, the unloading of the specimen begins. The drop seen in local strain indicates the material is changing back to austenite, this is a more homogeneous deformation when compared to loading. At approximately 3 mm of deformation, the material sees another static period until all the specimen is fully transformed back to austenite. The final elastic unloading

again follows a 45˚ line, where the local and global deformation are aligned until it is fully unloaded with no residual deformation.

After analysing the general local strain versus global deformation response and looking at the four different curves presented in Figure 4.2 b), it is possible to conclude that, by changing the GL of the sample, the local transformation differs. When the GL is closer to the grips, the local deformation is more reflective of the global deformation (continuous line and dotted line), detecting most of the deformation in the specimen. When the GL is smaller, dashed line and dashed – dotted line, although the strain deformation is the same, the extensometer only detects part of the deformation imposed on the specimen.

After concluding the preliminary tests and possibly to identify the local deformation, two further tests were performed to validate the results. Detail of the tests can be found in Table 4.2 and Figure 4.4 a) and b). The main purpose of this second set was to test the nitinol wire according to the standard test method ASTM F2516-14 [1] by using the total length of 130 mm and at the working temperature of 37˚C of the Anaconda stent graft medical device. The schematic can be found in Figure 4.4 a).

Table 4.2 – List of the preliminary tests 2 at 37˚C.

Test	**Sample name**	**Overall L (mm)**	**Gauge L (mm)**	**Temperature (°C)**
1	OL130_GL130	130	130	37
2	OL130_GL110	130	110	37

Like in Figure 4.2 b), in Figure 4.3 b) the difference on the inclination between the blue line and the red dotted line, is due to the GL on the red dotted line being smaller than the OL, meaning that the deformation is occurring outside the extensometer gauge length.

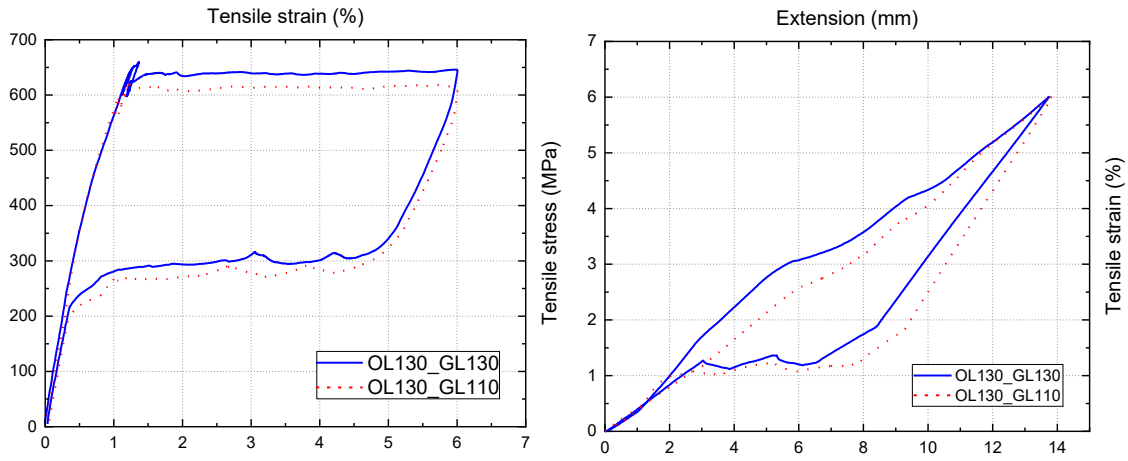

a) *b)*

Figure 4.3 – Preliminary tensile tests 2 results detailed in Table 4.2; a) Tensile stress-strain curve at 37˚C; b) Local strain versus global deformation plot for tensile loading.

4.3.2 Study 2 – Localised tests

The second study consisted of analysing how the deformation within the wire sample evolved, in other words, understand where the transformation initiated on the wire during the tensile test and how it propagated. For that, the total length of the wire was divided into three and three different tests were performed, as presented on Figure 4.4 c), using a different sample for each test. Each test had a total length of 130 mm and the video extensometer had a GL of 43 mm approximately and for each test the GL was placed in one of the three different locations along the wire, at the bottom, centre and top of the specimen, as outlined on Figure 4.4 c).

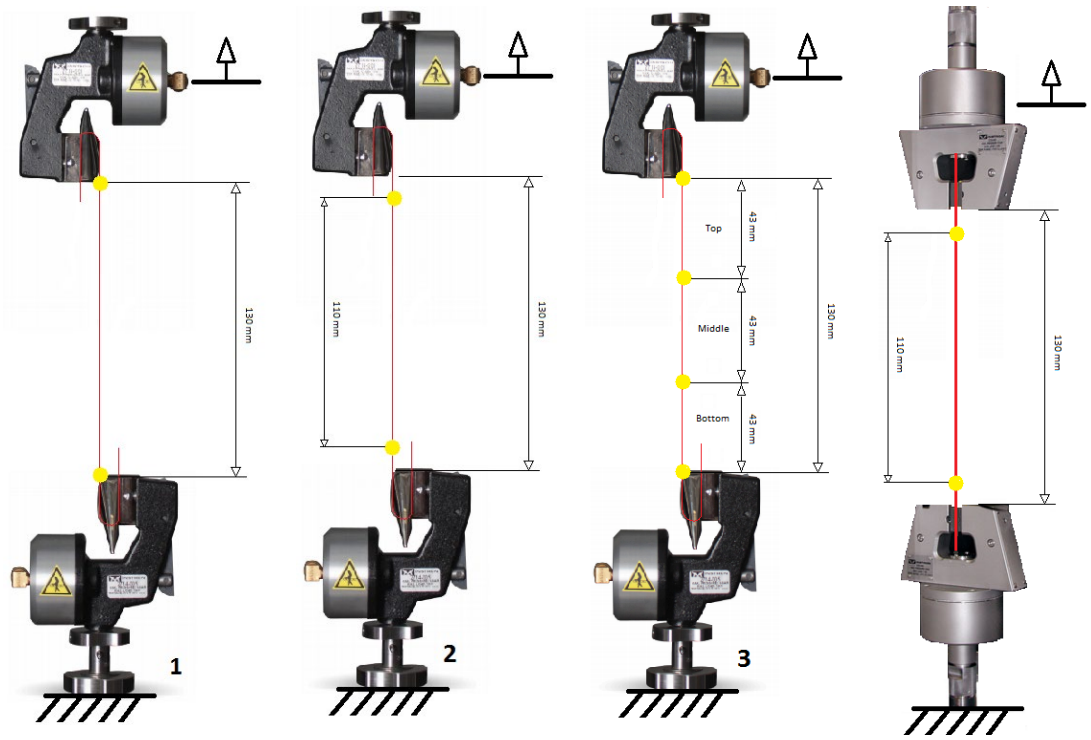

a) b) c) d)

Figure 4.4 – Scheme of the different setups used during tensile testing programme presented on this work.

Table 4.3 – Detail of the localised tests using the same GL at different locations of the sample at 37˚C

Test	Overall L (mm)	Gauge L (mm)	Temperature (°C)	Position of GL
1	130	43	37	Top
2	130	43	37	Centre
3	130	43	37	Bottom

For these tests, the 130 mm sample length was chosen in accordance with the standard and the testing temperature of 37˚C was chosen to reflect the working temperature of the Anaconda device.

Looking at Figure 4.5, it possible to see the local deformation of the nitinol wire when subject to tensile loading with the GL positioned at different places along the specimen.

From the figure, the blue dashed line represents the deformation at the bottom of the specimen, the black continuous line represents the deformation at the top of the specimen and the red dotted line represent the deformation at the centre of the specimen.

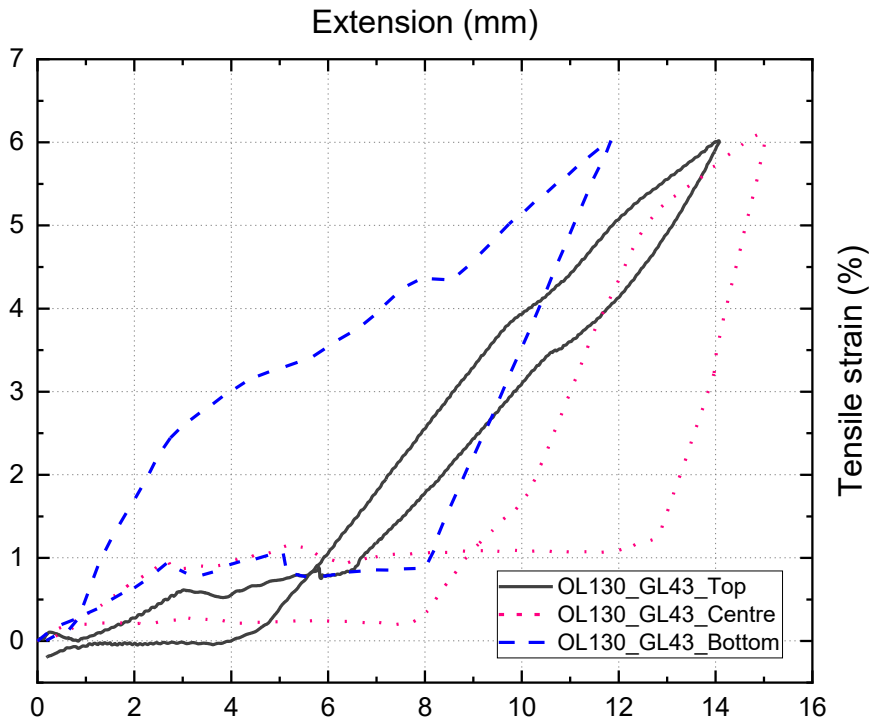

Figure 4.5 – Local strain versus global displacement plot for tensile loading at different positions.

It is possible to observe from the results presented in Figure 4.5 that the transformation starts at the ends of the specimen, starting first at the top, then at the bottom and propagates from both ends until it reaches the centre. This is visible by the static period of no apparent extension in the GL after the initial 45˚ line of austenitic elastic deformation, indicating that the deformation is happening elsewhere in the specimen. This period indicated by the flat line is shorter on the black curve where, after this point, the extensometer once more detects further deformation, followed by the blue line, while the red line only starts recording deformation after 12 mm of global displacement.

Figure 4.6 compares the tensile stress response with the localised deformation response for the test made on the first study, with an OL of 110 mm and GL of 96 mm. Several reference points are placed along both responses to have a better understanding of where the deformation occurs (Figure 4.6 b)) when related to the stress-strain response (Figure 4.6 a)).

Analysing the bullet number on both graphics, it is possible to observe that the initial deformation, from point 0 (initial point) until point ① is homogeneous, meaning that during the austenitic linear elastic behaviour presented on Figure 4.6 a) the sample shows a simultaneous increase in deformation on GL and OL as seen on Figure 4.6 b). Between point ① and ② on Figure 4.6 a) the tensile stress is constant, meaning that martensitic phase is starting to propagate and when looking to the same points on Figure 4.6 b) it is possible to see that the extensometer only detects part of the deformation. Between 2 mm and 6 mm of extension approximately, the tensile strain is constant meaning that the deformation is occurring outside the GL. Then from 6 mm extension until point ② the deformation is homogeneous again and it remains homogeneous until point ④, where the sample reaches the maximum strain and while the martensitic phase propagates.

From point ④ until point ⑥ on Figure 4.6 a) the unloading starts with a homogeneous deformation followed with the reverse transformation along the lower plateau until point ⑨. Now looking at the localised deformation, Figure 4.6 b) shows a homogeneous deformation from point ④ until point ⑨. This indicates that during the reverse transformation the deformation occurs within the GL. The specimen unloads homogeneously from point ⑨ until 0 on Figure 4.6 a) and when comparing with Figure 4.6 b) it is visible that the tensile strain is constant between 3 mm and 1 mm of extension meaning that the unloading deformation is occurring outside the GL.

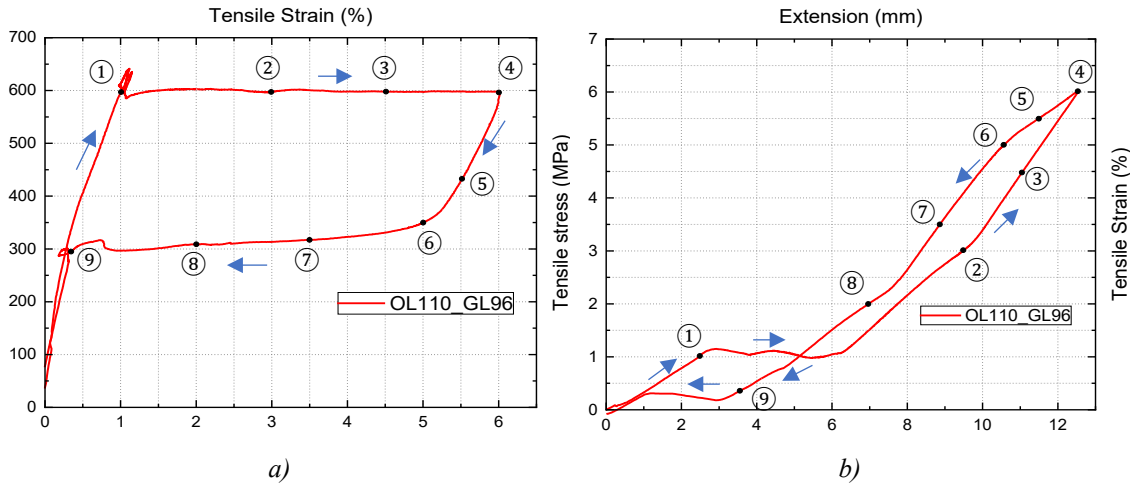

Figure 4.6 – a) Stress-strain response under tensile loading for sample with OL of 110 mm and GL of 96 mm presented in Table 4.1; b) Respective local strain versus global displacement plot with numbered bullet numbers corresponding with the stress-strain response.

After analysing Figure 4.6 a) and b) it is possible to confirm that the deformation along the nitinol wire is not homogeneous during a tensile deformation but since the extensometer in this case is close to the OL it is not possible to see when and where the deformation starts and how it propagates. Thus, it was important to test the tensile deformation with the extensometer placed in different locations along the sample, as shown in this second study, Figure 4.5. Figure 4.7 does the same analyse as Figure 4.6 but in this case comparing the stress-strain response of each test with the localised deformation obtained in Figure 4.5.

Looking at the stress-strain response presented for the three different tests on Figure 4.7 a), c) and e) it is possible to see that the response is similar between the three tests, where the upper plateau occurs around a maximum tensile stress between 500 and 600 MPa, the maximum strain is 6 % and the lower plateau occurs between 300 MPa and 200 MPa. Looking at the deformation on Figure 4.7 b) the deformation is homogeneous from the origin until point ①. From point ① to point ② the extensometer detects no deformation, with tensile strain constant while the sample has an extension of approximately 2 mm, meaning this deformation is occurring outside the GL. Between these points a small stress overshoot on the stress-strain response (Figure 4.7 a)) is also visible. This stress overshoot

is visible also in Figure 4.6 a) and Figure 4.7 c) and e) and according to Boukis' [2] work it indicates the presence of R-phase, which after this phase the deformation follows a linear path from point ② until point ⑤ in Figure 4.7 b), equivalent to the upper plateau in Figure 4.7 a).

Comparing now Figure 4.7 b), d) and f) it is possible to have a better understanding of when and how the martensite transformation occurs. The point ② for Figure 4.7 b) and ① for Figure 4.7 d) and f) is where the deformation starts being homogenous until 6% strain meaning that the extension measured by the cross-head is also detected by the extensometer and it is also equivalent to the beginning of the upper plateau on the respective stress-strain response. It is also possible to see that these points happen at different values of extension, where the deformation is first detected by top extensometer, at 7 mm of extension approximately, followed by the bottom extensometer at 8 mm of extension and lastly by the centre extensometer, at 13 mm of extension approximately.

When looking at unloading, follows a similar path, where the central extensometer is the first to stop detecting any deformation with an extension of 8 mm (point ⑧ in Figure 4.7 d)) followed by the top extensometer with an extension of 4 mm (point ⑨ in Figure 4.7 b)) and finishing with the bottom extensometer at 2 mm of extension approximately (point ⑨ in Figure 4.7 f)).

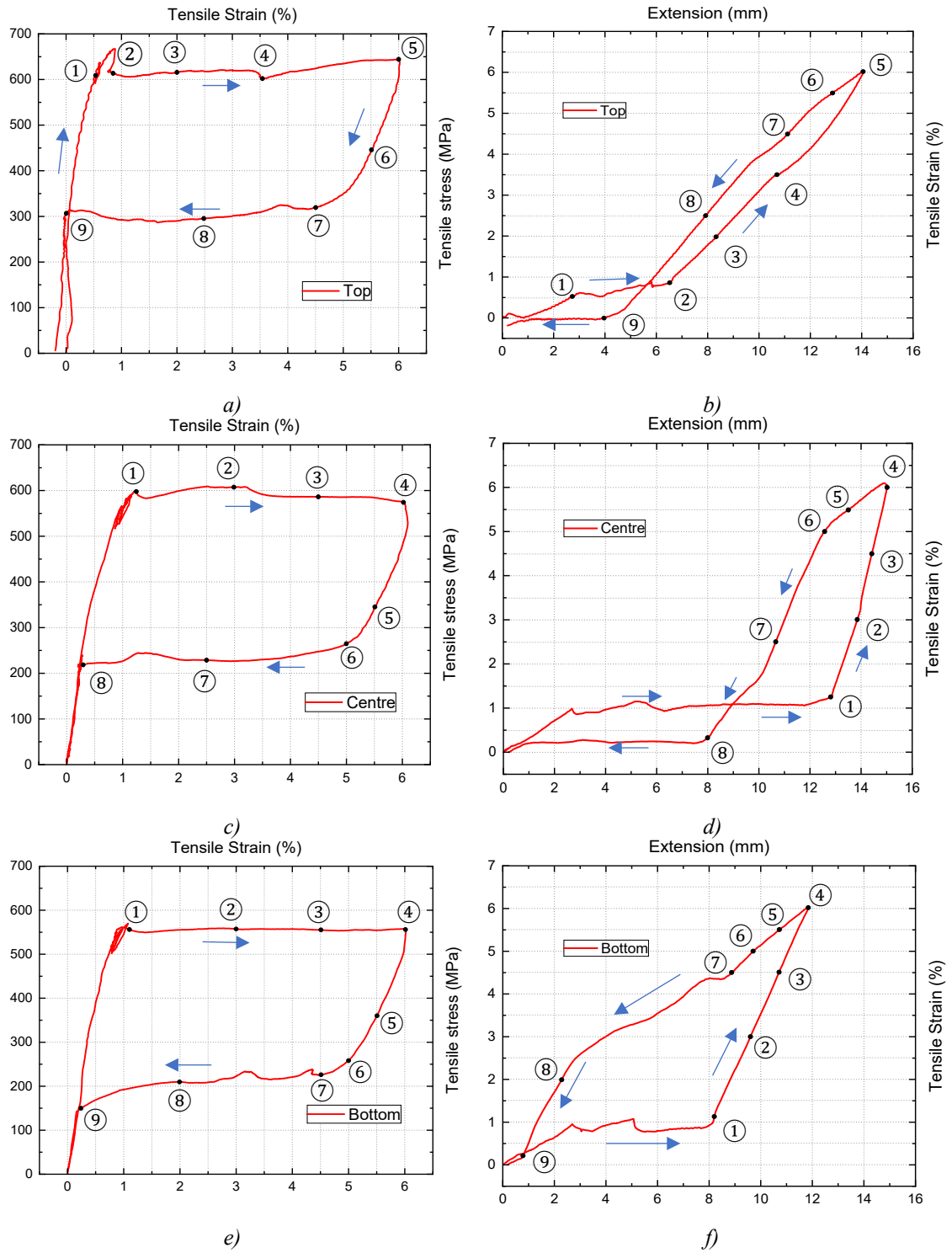

Figure 4.7– Stress-strain response under tensile loading for sample with OL of 130 mm and a) GL of 43 mm placed at the top of the sample; c) GL of 43 mm placed at the centre of the sample; e) GL pf 43 mm places at the bottom of the sample. Respective local strain versus global displacement plot with numbered bullet numbers corresponding with the stress-strain response with the extensometer placed at the b) top of the sample; d) centre of the sample; f) bottom of the sample.

The schematic image in Figure 4.8 represents the martensitic transformation along the nitinol wire under tensile loading. This scheme is just indicative to have a better understanding of how the transformation occurs based on the deformation measured by the three different extensometer placements from scheme in Figure 4.4 c) and the results presented in Figure 4.7. The bullet numbers presented in this scheme are not related to any of the results presented previously, blue colour represents the austenitic phase and orange the martensitic phase. From the scheme it is possible to see that the martensitic transformation nucleates first at the top of the sample, near the upper grip and start propagating towards the centre on number ①. Then on number ②, the transformation starts on the other end of the sample at the bottom and again propagates towards the centre of the sample until both fronts meet around the centre on the sample, as shown in scheme ④. In number ④ the wire is not fully transformed into martensite because from the stress-strain response presented previously the tensile loading stops during the upper plateau. During unloading the phase transformation nucleates towards the ends of the sample, in this case finishing at the bottom end, as presented in point ⑥. From this figure it is important to understand that the transformation starts at both the edges of the sample propagating towards the centre.

As seen on section 3.1.3 , the initiation of the martensitic nucleation initiates at the edges (near the grips) of the sample due to the stress concentration caused by the grips. Since DIC was not used in this study to obtain the field strains, it is unclear if the phase transformation initiates at the bottom or top edge.

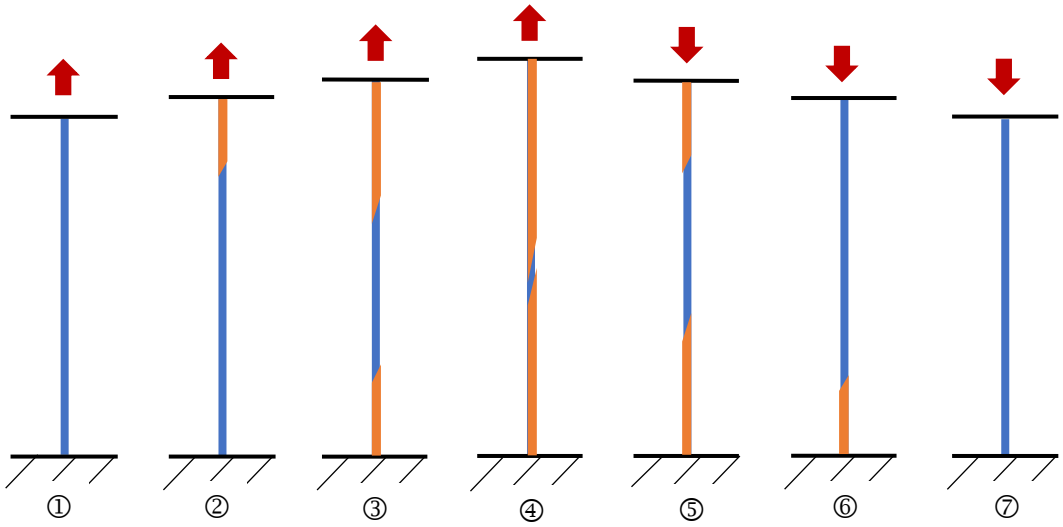

Figure 4.8 – Scheme of how the martensitic transformation propagates along the nitinol wire under tensile loading. Blue colour represents the austenitic phase and orange colour the martensitic phase.

A similar study is presented in section 3.1.2.1 by Shaw and Kyriakides [19], where smaller extensometers were placed along the sample under tensile loading to study the local versus global displacement.

When comparing to other studies presented in section 3.1.2.1 Reedlunn [27] and Bechle [25] uses DIC technology to obtain a full-field contours of the axial strain, where is possible to observe how the transformation actually propagates along the sample.

4.3.3 Study 3 – Influence of the grips

When analysing the local deformation on Figure 4.2 b), it was noticed that with the GL located closer to the grips, there was still some deformation of the wire that was not detected within the GL, suggesting the deformation was occurring somewhere around the grips. This comes from the fact that the grips that were used, fixed the sample on one side with the wire going around the grip, the test portion on the opposite side to the fixed region, meaning that some deformation is occurring around the grip that both the machine and the video extensometer are unable to detect. Therefore, a test was made using a generic tensile test grip, as seen in Figure 4.4 d).

To study the influence of the grips, two tests were performed. Both tests were conducted under the same conditions, with a total sample length of 130 mm, a GL of 110 mm and at a temperature of 37˚C, while the only change made was the grips. For test 1, the grips used previously were used while for test 2 the general tensile test grips were used, as detailed in Table 4.4 and illustrated in Figure 4.4 b) and Figure 4.4 d).

Table 4.4 – Detail of the influence of the grips test at 37˚C.

Test	Overall L (mm)	Gauge L (mm)	Temperature (°C)	Grip
1	130	110	37	Wire grip
2	130	110	37	Generic grip

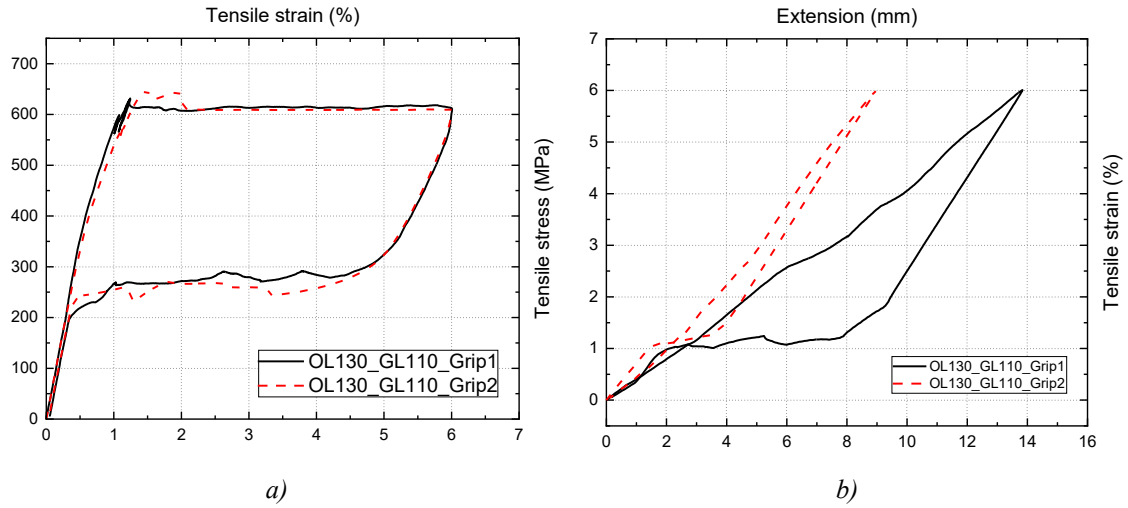

a) *b)*

Figure 4.9 –Tensile test results using different grips; a) Tensile stress-strain curve at 37˚C; b) Local strain versus global displacement plot for tensile loading using different grips.

Figure 4.9 shows the results obtained from study 3, where on Figure 4.9 a) is possible to see the stress-strain curve obtained from each test and on Figure 4.9 b) is it possible to see how the deformation evolved within the GL. Analysing the stress-strain curve, it appears that the grips do not have any great influence on the response. Nevertheless, when looking at the local deformation of each test, contrary to the stress-strain curve, it is possible to see that the grips have a significant influence on the response. It is possible to see that by

using the general tensile test grips, the static region during loading is much smaller when compared with the dedicated wire grip used in previous tests. This suggest that there is only a small portion of the wire that undergoes deformation which the GL does not detect. This length corresponds to the space between the GL and the grips, the 10 mm portions at the top bottom of the GL.

With this study it is possible to observe that although the grips do not influence the stress-stain curve (Figure 4.9 a)), it influences when studying the martensite nucleation. Both grips are pneumatic, so the pressure applied to the sample should be the same then using the same machine. The main different between the grips the that; the horn-like pneumatic cord grip the sample is tested opposite to the side where the sample is clamped, the wire is clamped and goes around the "horn". On the other hand, the generic "tweezers" grips clamp the sample with pneumatic tweezers and the sample is tested between the grips. Although the horn-like pneumatic grips are designs to test wires because it reduces the problem of jaw breaks, it is important to take in account that the nucleation of martensite initiates on the clamping are and not on the test area. In Figure 4.4 is possible to see an image of both grips.

4.4 Discussion and conclusions

In this chapter, several tensile tests were performed to study the localised deformation in nitinol wire under tensile loading. As mentioned on Chapter 3, this is a very particular characteristic of this material when subject to tensile loading. These tests focused on understanding how the deformation evolves within nitinol when using a slender specimen.

With the first study it was possible to identify the localised deformation in nitinol wire when under tensile loading. From the results presented on Figure 4.2, it was possible to conclude that with the increase in the GL, less deformation was detected by the extensometer, when subjected to the same overall deformation. With these results it was then possible to conduct further tests to understand where the deformation occurs and evolves along the wire, which lead to the second study.

For this second study, three tests were performed changing the position of the GL. This setup enabled the identification of where the deformation initiates and how it propagates subsequently. From the results obtained in Figure 4.5 and Figure 4.7, it is possible to conclude that the deformation starts at the top of the specimen, propagating towards the centre where it then meets with the deformation that subsequently initiated at the bottom of the specimen. These results are in agreement with the tests carried out by Bechle et al. [25] discussed in Chapter 3, where the deformation start at the ends of the specimen and propagates towards the centre. With the results obtained in this study it is also possible to have a better idea of how the martensitic transformation nucleates along the wire as presented on Figure 4.8, it is important to highlight that the scheme presented in this figure is based on the transformation obtained from Figure 4.5 and Figure 4.7 and based on the DIC image results published by Bechle [25] and Reedlunn [27]. Note that to have a better understanding of how the transformation propagates on nitinol wire, DIC techniques are important to use as future work since the studies presented on Section 3.1.2.1 are for nitinol tube and use a different type of grips. The current study uses horn-like pneumatic cord grips to fix the wire.

Finally, the third study focused on understanding the influence of the grips during the tensile test. From the results obtained in Figure 4.9, it is possible to see that although the overall stress-strain response was apparently the same when changing the grips, when looking at the local deformation is it possible to detect more localised deformation when using the general tensile test grips. This suggest that for future studies on the localised deformation, extra care needs to be taken when choosing the grips, where from this study it is possible to observe that the standard tensile grips capture a more accurate deformation than the horn-like grips.

As mentioned at the beginning of this chapter, the work described here served as an induction to the Terumo Aortic laboratories and their proceedings. It also served to gain experience on working experimentally with nitinol wire and understanding the importance of having a controlled temperature to obtain repeatable results. It is possible to observe from the results presented in this chapter, that the generic testing machine is suitable for

tensile testing, but it is not certain of the same machine will be suitable for compressive testing. The following chapters describe the different compressive test methods used to obtain repeatable compressive data from nitinol wire.

Chapter 5 Compression test method

5.1 Background

Understanding the behaviour of superelastic nitinol wire under tensile and compressive loading is important due to the high bending strains that the wire is subjected to when placed in the endovascular delivery system of the Anaconda stent graft. The response under tensile loading at high strain for nitinol has been thoroughly studied and now has a standard test method described in ASTM F2516-07 [1]. On the other hand, compressive testing of nitinol wire for high strains is not as extensively studied, contrary to tension, and there is no standard test method available at present.

Considering all the approaches described previously in Chapter 3, it has been decided to use the approach suggested by Brodie [3] and Boukis [2] to test nitinol wire under compressive loading. This is due to the fact that all the required equipment is readily available within the University laboratories, the past experience of the University technicians with the test method and the indication of potentially obtaining reproducible results for compression of wire up to 6% strains without buckling. Brodie [3] started studying nitinol wire under compression loading by using the Henderson et al. [28] test method where she initially intended to investigate compression in nitinol wire up to 6% compressive strain, the effect of cycling under compression and the temperature effect but he realised that the method used had associated difficulties due to friction effects in the holders and was thus forced to develop a new method based on using the Deben Microtest 2000 machine. Following this work, Boukis [2] studied nitinol wire under compressive loading in a single loading/unloading cycle testing displacement from 0.06 to 0.18 mm on a 3 mm sample length and 1 mm diameter, and a crosshead speed of 0.1 mm/min at room temperature.

Therefore, the Brodie [3] and Boukis [2] improved approach is used as the basis for this work which focuses on improving it to obtain repeatable results and therefore addresses the shortfall that still exists in compression testing. As described on the literature review,

compressing testing of nitinol has been reported using “bulk” samples; where the diameter of the sample is higher than 3 mm; or when using extra fixtures to support the wire. Brodie and Boukis’ approach uses no supports (reducing possible friction effects) and at the same time the samples have small diameter (1 mm) and have a ratio of Diameter/length of 3. This test method showed promising results and offers the potential to both load the sample and observe the full field deformation.

5.2 Objectives

Focusing on the main objective of obtaining compressive stress-strain data important for stent graft development, this work will be broken down into smaller objectives proposed under:

- Replicate the previous test of single loading/unloading up to 6% compressive strain;
- Identify the best technique to obtain the strain field during compression loading/unloading;
- Create a methodology of the compressive test method to be used by other researchers and/or to characterise different metal wire materials;

5.3 Equipment and method

Initially, a compressive test using the Deben Microtest 2kN tensile and compressive horizontal loading stage, which was available at the University of Strathclyde in the Advanced Materials Research Laboratory (AMRL), was considered. This module was specifically designed to be used inside an SEM for real time observation of the evolving sample deformation field. The SEM used to incorporate the compression test device was a Hitachi Scanning Electron Microscope S-3700N, also available at AMRL. The Deben system uses custom miniature load cells in the range of 660N to 2kN, with special jaws that were designed for the test with hardened and polished surfaces capable of resisting the compression load from the sample and avoiding indentation. These jaws were previously tested and validated to undertake this test without suffering indentation by

Brodie [3] and Boukis [2]. This device also has the ability to add a Peltier heating & cooling system with a temperature range of -20°C to +160°C in future. [78]

In the test method the sample was placed horizontally in the Deben device between the jaws using tweezers to hold the sample in place and lubricant was applied to both ends of the sample and on the surface of the jaws to decrease the friction effects during loading. Lubricant used for all the tests presented in this work was WD40. The samples were positioned and held in place using tweezers, with a pre-load applied before each test; pre-load used was around 10 N to maintain the sample in position. The tests were conducted inside the SEM and initially assumed to be at room temperature but the temperature effect inside the SEM will be detailed in the following paragraph. The test was controlled by the displacement being imposed on the Deben device and tested over three loading cycles (each cycle involves loading and unloading) up to 0.18 mm displacement (6% maximum nominal strain for samples of 3 mm length). The samples used in these compression tests have a diameter of 1 mm and are 3 mm long. In Figure 5.1 and Figure 5.2 it is possible to see the Deben Microtest setup within the SEM and the sample placed in between the jaws.

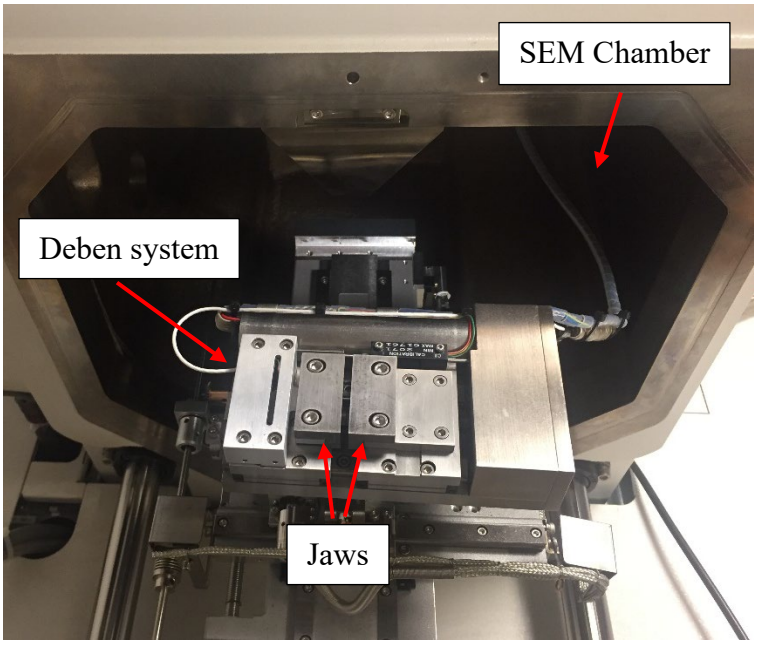

Figure 5.1 – Deben Microtest entering the SEM

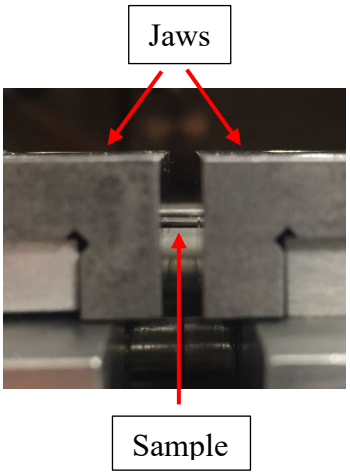

Figure 5.2 – Detail of the sample place between the compression jaws

One of the problems associated with using the SEM to test nitinol is controlling the temperature inside the SEM. The electron beam (EB) generated by the SEM that focuses on the sample causes a change in temperature of the sample. This temperature depends on the voltage and the electron beam current, where using high accelerating voltages or high current corresponds to an increase in the temperature irradiating the sample. To know the temperature inside the SEM during the compression test, extra equipment needed to be added to the setup, for example an infrared camera able to measure the temperature inside the SEM, such camera was not available in the current setup. [79]

5.3.1 Inclusion of Digital Image Correlation (DIC)

Digital image correlation is a non-contact optical method used to measure deformations or the strain field on a surface – either in plane (2D) or out of the plane (3D). It consists of obtaining several images of a surface marked with a random pattern, correlating the patterns in the images of the evolving deformation with the initial undeformed pattern and calculating the deformation of the pattern, assuming that the deformation of this pattern is

the same as that of the surface. The pattern usually consists of a white background with a black/grey speckle, where the size of the speckle determines the resolution of the field of view (FOV).

To apply DIC to the compression test described it was first necessary to identify the best technique for applying a suitable pattern. Due to the reduced sized of the samples used, the common method with a grey speckle printed on the surface was not viable and also there being no lenses available to obtain suitable images of sufficient resolution. Thus, the use of the live SEM full field image was the other option. Two different type of patterns were used on the sample surface. The first was based on the deposition of gold nanoparticles [80] on the surface and the second method was to use laser ablation.

The self-assembled gold nanoparticles were placed in the surface of the sample by Dr. Alastair Wark from department of Pure and Applied Chemistry from University of Strathclyde.

The inclusion of dots by laser ablation (with a MOPA pulse laser) was performed by Dr. André Cavaleiro and with guidance of Dr. Paulo Tavares at INEGI – Institute of Science and Innovation in Mechanical and Industrial Engineering in Portugal. The size of each dot was ±60 μm where two different samples were marked with different laser intensity (1xlaser and 10x laser).

5.4 Results

As mentioned in Section 2.3, the wire used was provided by Fort Wayne Metals to Terumo Aortic and the samples were cut by Glenhead Engineering with the size of 3 mm long and 1 mm diameter. Table 5.1 list all the compression tests made and the conditions for each test. This first list of tests has the aim of reproducing the previous results obtained by Brodie [3] and Boukis [2], to investigate the response at different strain rates, the effect of loading/unloading cycling and finally to study the best DIC technique to apply in the compression test.

Table 5.1 – List of compression tests performed on Deben + SEM system.

Test	Sample	Sample Ref_name	Strain (%)	Velocity (mm/min)	Cycles	Pre-Load (N)	Max Load (N)	Comments
1	S1	6_0.1_1_S1_1	6	0.1	1	34.27	676.17	Nanoparticle
2	S1	6_0.033_1_S1_2	6	0.033	1	20.6	387.98	Nanoparticle
3	S1	6_0.033_1_S1_3	6	0.033	1	2.21	561.6	Nanoparticle
4	S2	4_0.033_1_S2_4	4	0.033	1	36.56	473.16	1xlaser
5	S2	4_0.033_1_S2_5	4	0.033	1	3.65	473.65	1xlaser
6	S2	4_0.033_1_S2_6	4	0.033	1	3.47	471.11	1xlaser
7	S2	4_0.033_3_S2_7	4	0.033	3	3.45	606.44	1xlaser
8	S4	4_0.1_5_S4_8	4	0.1	5	25.14	485.79	No marks. Test end at the 1st cycle
9	S4	4_0.05_1_S4_9	4	0.05	1	3	509.71	No marks
10	S4	4_0.05_4_S4_10	4	0.05	4	0.51	509.08	No marks
11	S4	4_0.05_1_S4_11	4	0.05	1	25.12	523.91	No marks
12	S4	4_0.1_1_S4_12	4	0.1	1	8.44	524.41	No marks

13	S4	4_0.1_3_S4_13	4	0.1	3	7.5	524.46	No marks
14	S4	6_0.1_1_S4_14	6	0.1	1	6.74	627.13	No marks
15	S3	6_0.1_1_S3_15	6	0.1	1	40.07	741.63	10xlaser
16	S3	6_0.1_3_S3_16	6	0.1	3	2.34	757.61	10xlaser

For this first set of tests, four different samples were tested, referenced by naming as S1, S2, S3 and S4. During the discussion of the results, each sample will be referred to as the name of the sample for easier understanding and discussion of the results. Table 5.1 describes in detail how each sample was tested. In this table, the naming convention of the samples correspond to [Strain in %] _ [velocity of the test in mm/min] _ [sample name] _ [test number].

Figure 5.3 is an image of the nitinol wire compressive sample obtained from the SEM when placed between Deben jaws with a pre-load applied and ready to be tested. In the image it is possible to observe the majority of the sample. This sample does not contain any gold nanoparticals or laser marks.

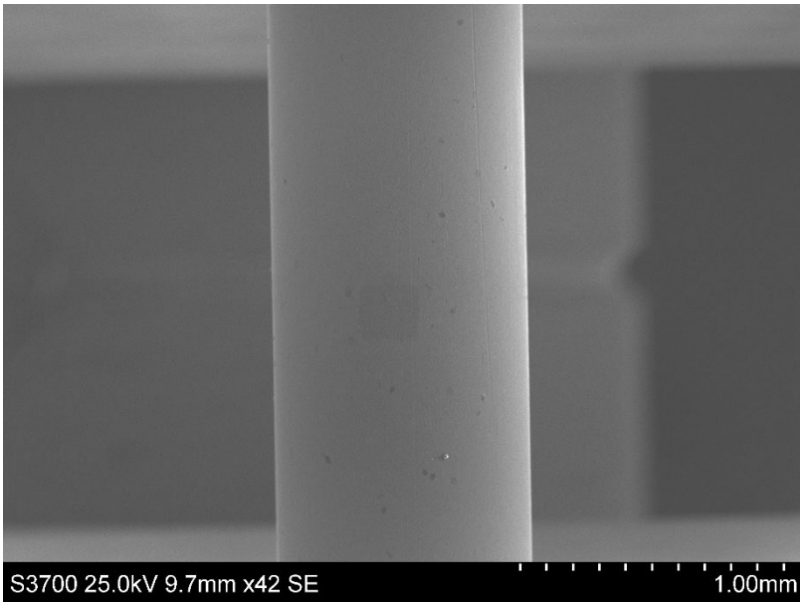

Figure 5.3 – SEM image of NiTi wire pre-loaded before the compression test.

The raw data from the Deben device is stored in a .csv file (comma-separated values) which contains the information of the jaws displacement (mm) and the force detected by the load cell (N). Test frequency as 0.5 Hz and no filter was added to the software when obtaining the raw data. The data is later transformed to True Stress (σ") and True Strain (ε') using the following equations,

$$\sigma'' = \sigma(1 + \epsilon) \tag{5.1}$$

$$\varepsilon' = \ln(1 + \varepsilon) \tag{5.2}$$

where,

$$\varepsilon = \frac{Elongation}{Original\ Length} \tag{5.3}$$

$$\sigma = \frac{Applied\ Force}{Cross\ Sectional\ Area} \tag{5.4}$$

[Note: In the reported results, true strain is calculated using the deformation along time detected by the load cell. True stress is calculated using nominal cross-sectional area. As the samples are very small assumption is made that the cross-sectional area is constant along the test.]

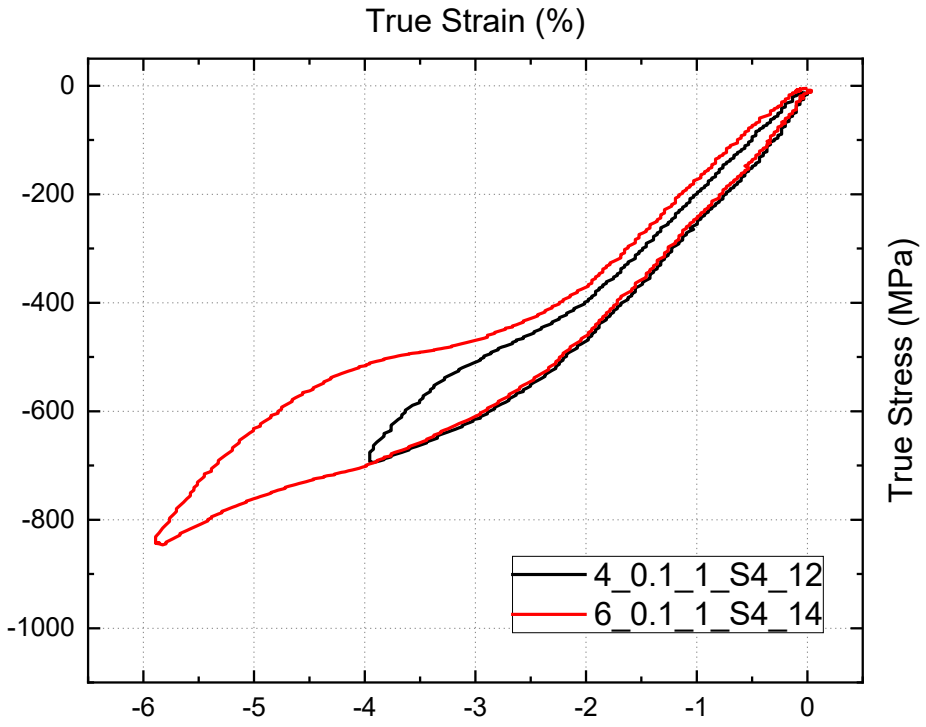

Figure 5.4 – Stress-strain response of single loading/unloading cycle for 4% and 6% compressive strain (sample S4)

Figure 5.4 shows the stress-strain response in compression for separate single loading/unloading cycles up to 4% (black line) and 6% (red line) maximum nominal strain, where it is possible to see:

- An initial linear elastic behaviour up to 2% strain and the loading path is similar for both responses until 4% strain;

- During loading to 4% strain (black line) the formation of a completed upper plateau region is not clear within the maximum compressive stress of 700 MPa. Since the stress-induced phase transformation from austenite to detwinned martensite occurs in the plateau, this figure suggests that this transformation is not complete at 4% compression strain. During unloading there is a small hysteresis visible that is equivalent to the reverse transformation where the phase changes again from detwinned martensite to austenite. The response cycle closes with linear elastic behaviour once more near to 0% strain suggesting that the sample did not suffer any permanent deformation;
- For 6% strain there is the formation of a small yet complete upper plateau at 4.5% strain approximately. As mentioned earlier in the literature review, the plateau in compression is not flat and has an increase in stress of approximately 200 MPa over a 2.5% strain increase. After this point the sample is fully transformed from austenite to detwinned martensite by the induced stress where it is possible to observe a near-linear elastic behaviour with a modulus equivalent to detwinned martensite deformation and at 6% strain it reaches a stress of around 850 MPa. During unloading there is a near-linear unloading from 6% strain down to the lower unload plateau at approximately 4% strain. This is associated with martensitic elasticity recovery of the deformation. During the lower plateau, the material progressively transforms back to austenite from detwinned martensite, similar to the response when strained to 4%, and again this plateau is not flat with a decreasing stress of approximately 100 MPa accompanying a 1% strain reduction. Contrary to the 4% straining test, the hysteresis is more evident in the 6% straining case. After the plateau, at 2.5% strain, the response shows linear elastic behaviour once more, where the material is mostly austenite, this linear response is equivalent to the deformation recovered from austenite. The hysteresis finishes when unloading reaches the value of zero stress, showing that there is no apparent residual strain since the cycle is closed at 0% strain and zero stress.

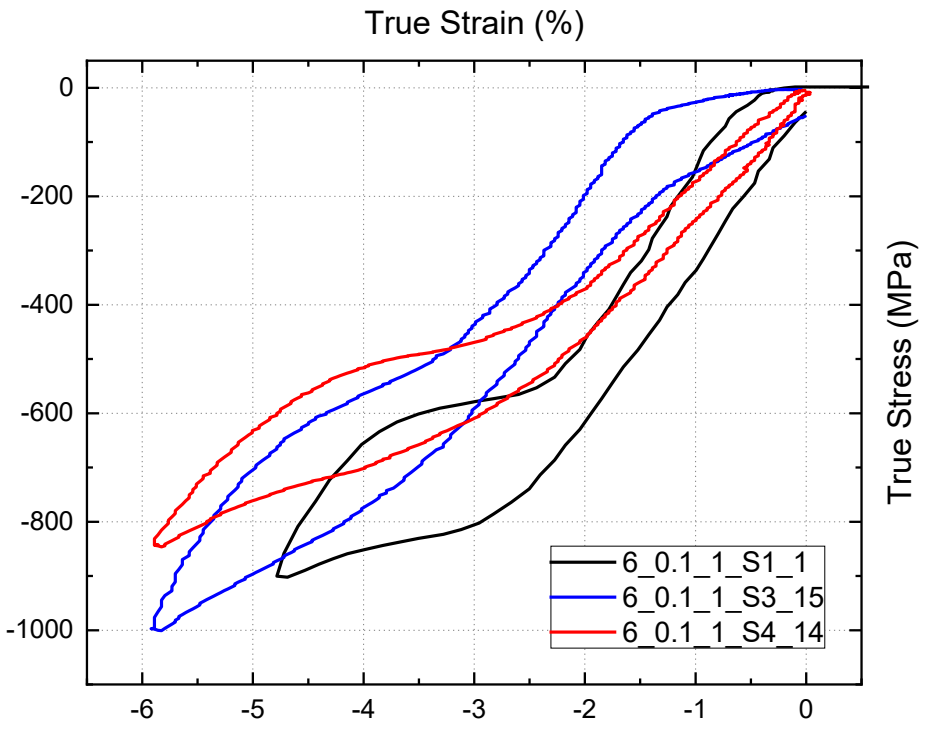

Figure 5.5 – Stress-strain response for single loading/unloading cycle at 6% compressive strain inside SEM (3 samples: S1, S3 and S4)

Figure 5.5 shows the stress-strain response of nitinol wire loaded to 6% compressive strain, tested in a single loading/unloading cycle. This figure shows the response of three different samples (S1, S3 and S4) and aims to compare the repeatability of this test. Comparing the three results is possible to observe:

- The responses are markedly different for each sample;
- Sample S1 (black line) shows a pre-load equivalent to approximately 300 MPa. Both upper and lower plateaux are more evident than sample S4 (red line). Also, the value of the stress at each plateau is also higher comparing to S4, with a maximum stress of 900 MPa. The response shows some initial unanticipated compliance from the system at the beginning of the test since the sample S1 does not reach 6% strain. Finally, S1 shows some residual strain of around 0.4%, suggesting some plastic deformation has occurred during loading;

- Sample S3 (blue line) also starts with a pre-load equivalent to 300 MPa. Contrary to S1 and S4, S3 does not display linear elastic behaviour during the austenitic phase both in loading and unloading. Both upper and lower plateaux are visible but not as clearly as S1, yet slightly higher than S4. At 6% strain S3 shows a stress value of 1000 MPa, which is higher when compared to the other responses. Finally, S3 shows a residual strain of almost 1%.

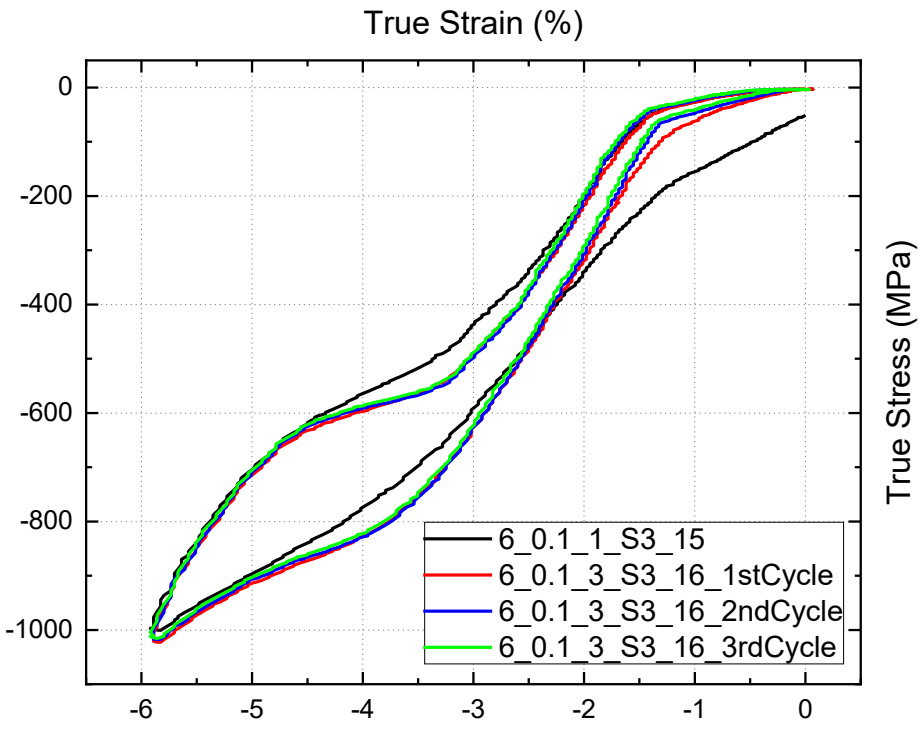

Figure 5.6 – Stress-strain response for single loading/unloading cycle at 6% compressive strain inside SEM versus three loading/unloading cycles (1 sample: S3)

Figure 5.6 compares the stress-strain response of a single nitinol wire sample when loaded through one cycle and then three cycles in compression.

- Both responses are similar when loading for three cycles, the plateaux are more evident than loading for just one cycle;

- The response from three cycles shows a good repeatability between the cycles with only a small deviation in the first cycle during the initial austenitic linear elastic deformation in loading;
- Both responses present nonlinear elastic behaviour both during loading and unloading in the austenite regime.

Figure 5.7 compares the compressive stress-strain response of nitinol wire when loaded up to 6% strain at different strain rates. The strain rate used during the tests was 5.5×10^{-4} s^{-1} equivalent to the loading stage velocity of 0.1 mm/min (black line) and 1.83×10^{-4} s^{-1} equivalent to a velocity of 0.033 mm/min (red line). The same sample, S1, was used during the tests at the different strain rates:

- Black line is the response at a strain rate of 5.5×10^{-4} s^{-1} which was already discussed previously in Figure 5.5, where it is possible to see more defined but not flat upper and lower plateaux, maximum stress of 900 MPa at 4.7% strain, a linear elastic loading and unloading relationship in the austenite phase and a residual strain of approximately 0.4%;
- Red line is the response at a strain of 1.83×10^{-4} s^{-1} and it shows both loading and unloading with a linear elastic response in the austenite phase that is less stiff compared to the black line. Also, both upper and lower plateaux are not as well defined, and the transformation stress values are lower compared with the higher strain rate response. Maximum stress at 5.5% strain is 750 MPa, 200 MPs lower than at the higher strain rate.

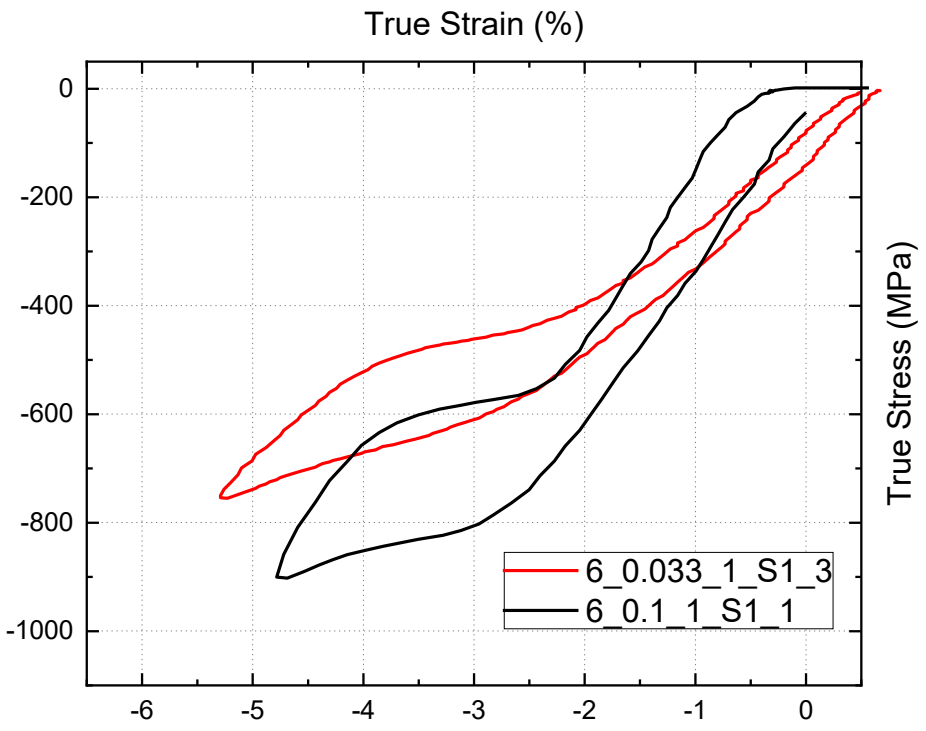

Figure 5.7 – Stress-strain response for single loading/unloading cycle at 6% compressive strain inside SEM at different strain rate (1 sample: S1)

Figure 5.8 shows the images obtained from the SEM of the nitinol wire with the self-assembled gold nanoparticles placed on the sample surface. In Figure 5.8 it is possible to observe the nanoparticles on the surface as white dots and the grey region is the surface of the wire, creating the speckle pattern required for the DIC. Since the nanoparticles are too small, when preforming DIC technique with SEM the field of view used thus corresponds to only a small area of the sample. To obtain the strain field throughout the full length of the sample, several tests of the same sample are needed while relocating the position of the FOV along the sample each time in order to provide a significant strain field area of the sample to analyse the full deformation throughout it (similar idea of the 2nd study presented on section 4.3.2 of this work).

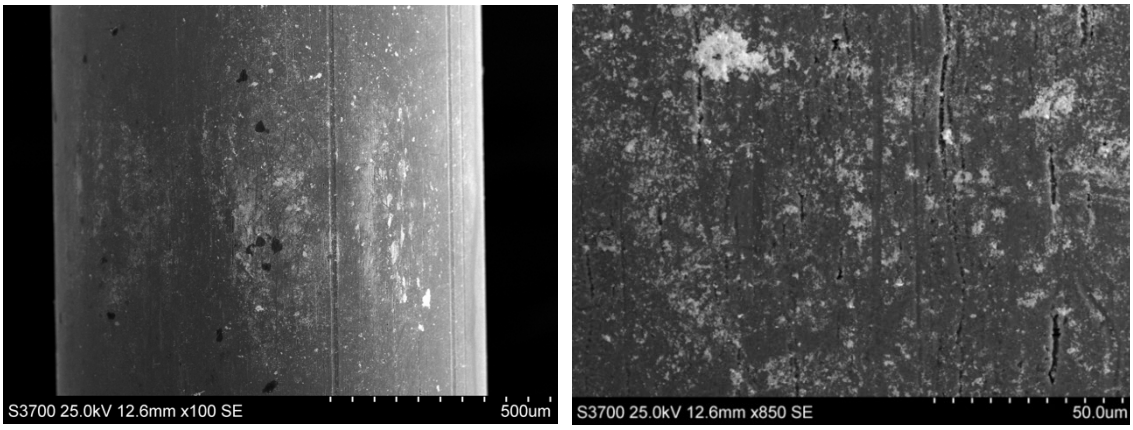

a) *b)*

Figure 5.8 – Images obtained from the SEM of S1 sample with gold nanoparticles with pre-load; a) Image of the sample at 500um scale; b) Image of the sample at 50um scale.

Figure 5.9 shows the images obtained from the SEM for the sample S2 with the laser marks made in the sample surface. It is possible to see some marks on Figure 5.9 a) that were not visible on Figure 5.3, the sample with no marks, although when magnified as in Figure 5.9 b) it is not clear if these marks are from the laser or if it is the surface that is damaged. The laser marks were made one by one, manually placed in a confined small area of the sample which suggests that these marks are not in fact the laser marks. Due to the difficulty of finding the laser marks in this sample, it was therefore not considered as a viable technique to implement DIC.

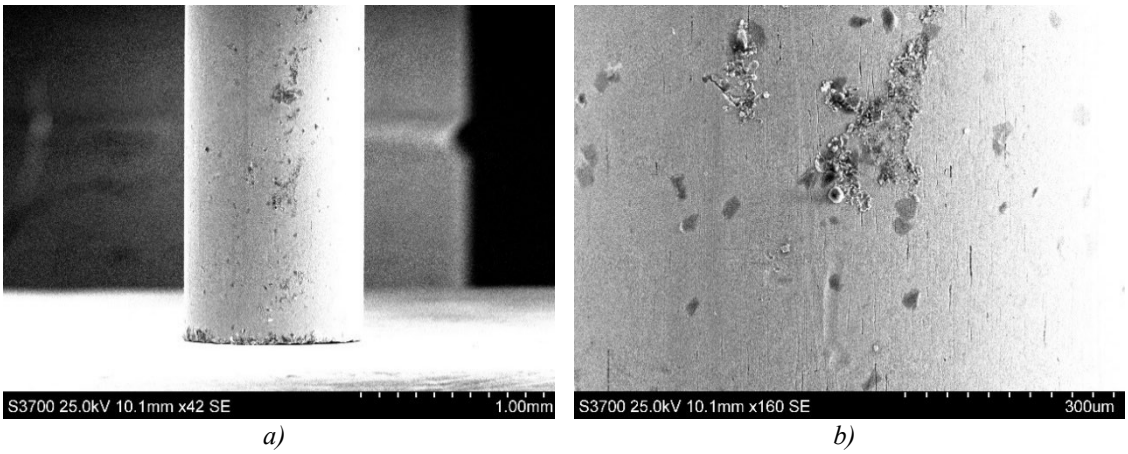

a) *b)*

Figure 5.9 – Images obtained from the SEM of S2 sample with laser marks with pre-load; a) Image of the sample at 1mm scale; b) Image of the sample at 300um scale.

5.5 Discussion / Conclusions

Analysing all the results obtained in this chapter it is possible to conclude that this method is not sufficiently reproducible enough when it comes to performing compression test on nitinol wire consistently and repeatedly.

Starting from the strain-stress responses obtained, when testing the same sample at different compressive strains (Figure 5.4), the responses follow the same path until 4% compressive strain, this suggest that the method is consistent with the stress-strain response when loading the same sample to different maximum strains. Comparing this figure with the stress-strain response obtained by Brodie [3] and Boukis [2], the stress values are not the same. For 4% maximum strain Boukis reached a maximum compressive stress of 900 MPa whereas in Figure 5.4 the maximum compressive stress at 4% strain is 700 MPa, and again for 6% strain here the maximum compressive stress was 900 MPa against the 1300 MPa obtained by Boukis. When trying to replicate the results for a single loading/unloading cycle for different samples all stress-strain responses obtained in Figure 5.5 give different results, thus it appears that it is not possible to replicate the results for different samples. This means that it is difficult to validate the repeatability of this test method. Nevertheless, when comparing single cycle with multiple loading/unloading cycles from Figure 5.6, the stress-strain response is similar for both tests as well as in the responses from the three cycle tests where the first cycle only shows a small difference during the linear elastic loading region associated with the austenitic phase. Finally, when studying the stress-strain response at different strain-rates as in Figure 5.7 there are no valid conclusions that can be obtained from this test, since according to the literature, it was anticipated that with increased strain-rate the stress-strain rate should also shift to a higher value of stress for a given strain. Therefore, in conclusion, it is not possible to validate the reliability of this test.

The DIC techniques used were also not conclusive. As already mentioned, the laser technique to mark the sample surface in order to create a speckle pattern necessary for DIC is not valid for use within the SEM during compression loading due to the difficulty

of locating the speckles through the SEM imaging system. A way to overcome this problem is to distribute the marks across the sample surface equally thereby eliminating the difficulty of finding the marks. The nanoparticles of gold created a good speckle pattern that can be captured through the SEM but only a small area of the surface is covered from which to create the strain field. When changing the settings of the SEM to record the image in real time during loading the quality of the image changes drastically, as seen in Figure 5.10, and it was also noticed that the sample moved as a rigid body during the compressive test by 'rotating'. It is not clear how the sample moves during the test but according to the videos obtained from the SEM and following the movement of the nanoparticles on the surface is possible see that they move from side to side suggesting there is some king of torsion during loading in compression. This 'rotation' might also be associated with the rotation of the machine, since the jaws are screw driven, making this 'rotation' a rotation of the system. From the videos obtained it is also possible to see that the sample is out of focus at some moments during the compressive loading, Figure 5.11, this also suggests some rigid body movement in the vertical direction.

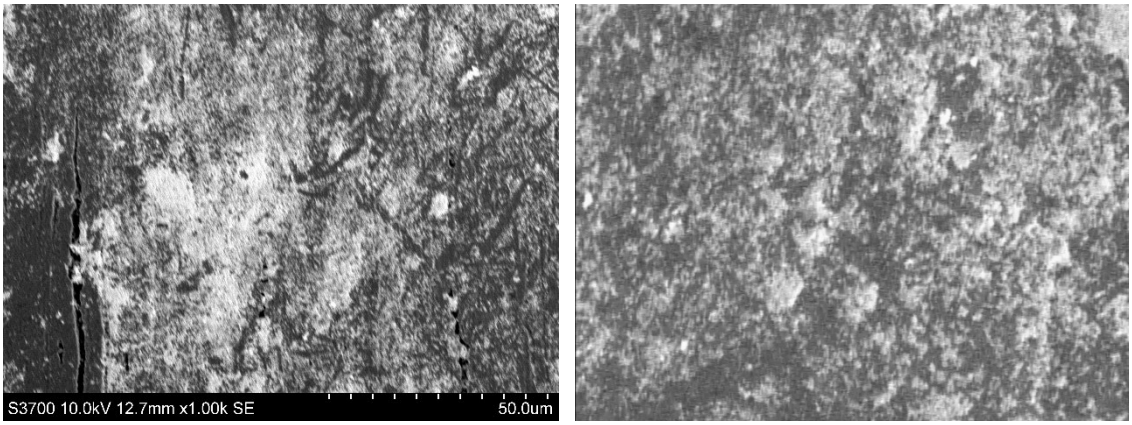

a) *b)*

Figure 5.10 – SEM image of the sample with nanoparticles at the surface; a) Image obtained from a stationary SEM setup image; b) Image obtained from the real time video SEM setup.

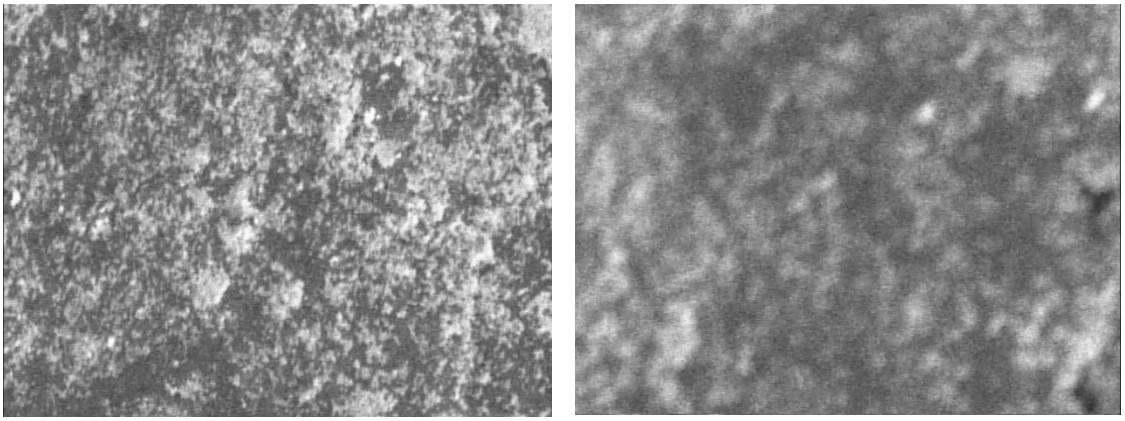

a) *b)*

Figure 5.11 – Screenshots of the SEM video obtained from the compression test with nanoparticles; a) Image at the beginning of the test; b) Image from the middle of the test.

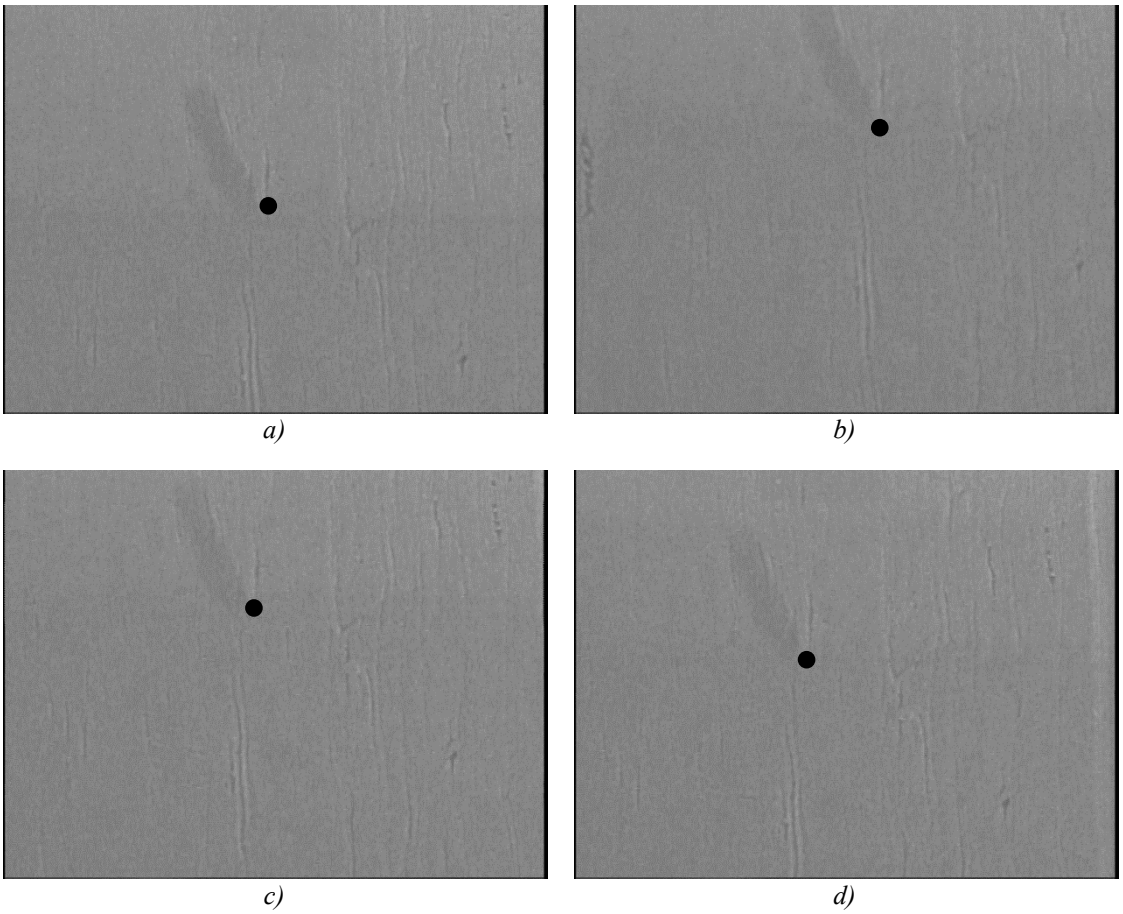

a) *b)*

c) *d)*

Figure 5.12 – Image frames from the SEM video of a sample during along one cycle of loading and unloading.

Looking in detail at the images in Figure 5.12 is possible to have a better understanding of how the sample moves as a rigid body during the compression test. This figure shows frames of the test during one cycle, where Figure 5.12 a) corresponds to first frame of the test and Figure 5.12 d) to the last frame of the test. Each figure has a black dot that was placed after, in the same place of the sample. From the dot is possible to see that during loading and unloading, the sample movements is not only axial but also lateral compared to the initial image of the test, showing that the body undergoes rotation during compression.

The fact that the temperature inside the SEM is unknown and the need to acquire new equipment to measure the temperature inside the SEM also discredited the compression test inside the SEM. Since nitinol is a material that is very sensitive to temperature changes, it is highly important to know the temperature at which the tests are being performed.

While trying to understand how the sample behaves during the compression test, it was noticed that some samples have defects caused by the cutting process. Figure 5.13 shows an image obtained from SEM of one of the samples ends in detail. From the image it is possible to see that the end is not flat.

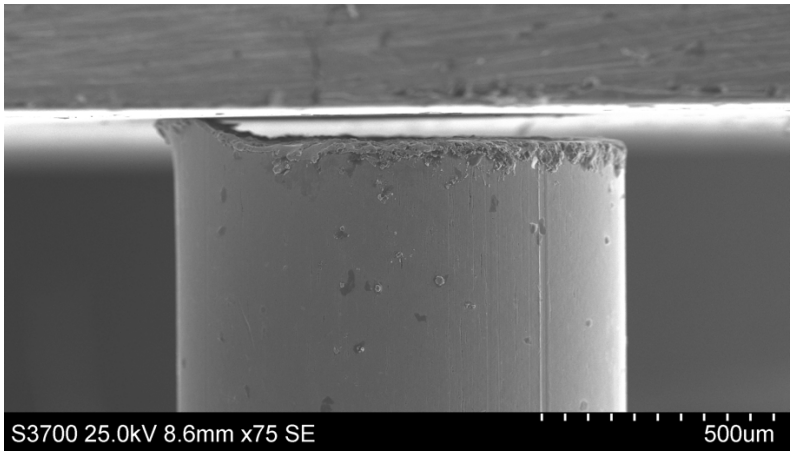

Figure 5.13 – SEM image: Detail of one end of the sample with defects caused by the cutting process.

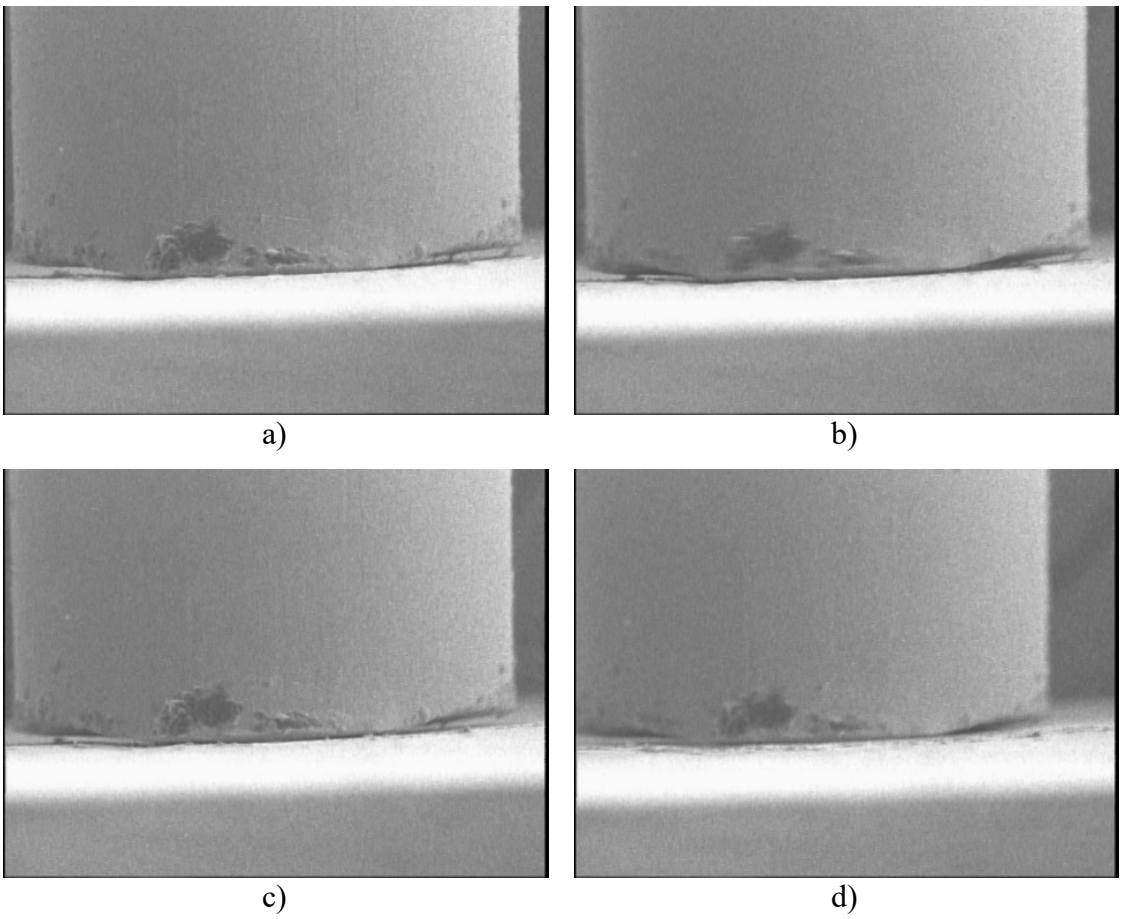

Figure 5.14 – Frames obtained from the SEM video showing the sample moving during the compression test inside the SEM.

Figure 5.14 shows a sequence of frames from the video obtained during a compression test inside the SEM. These image frames show how the sample behaves during the compression loading inside the SEM with detail from one of the ends of the sample. It is possible to confirm that the sample moves during the test where is possible to see a vertical and lateral rigid body displacement of the sample during unloading from image a) to d). Figure 5.14 a) shows the sample in the initial position. From this image it is also possible to see the presence of a bump at the end of the sample (defect from machining the sample), where the centre of the sample is in contact with the jaw surface but there is a visible gap at the sides of the sample. In Figure 5.14 b) it is possible to see, when comparing with the previous frame, that the sample is not in focus. Moving to Figure 5.14 c), both sides of the

sample are out of the focus, except the centre, meaning the sample has a lateral movement and the sample is being held by the defect caused by the cutting process as seen in Figure 5.13. Finally, from Figure 5.14 d) it is possible to see that the sample moved during the test because the sample is not centred in the frame, as seen in the previous frames.

In Appendix B: it is possible to see the full video recorded during the compression test where it is easily to visualise how the sample moves during the test, this video is only available on the digital version of this work.

Gathering all the information from the stress-strain responses and the images taken from the SEM it is possible to conclude that this method has several problems that influence the measured stress-strain response in compression. This highlights the necessity to develop a new method able to overcome the problems encountered in controlling the position of the sample during the test, the repeatability of the tests and that is capable of reliably measuring the strain during the test. This new method should be able to test at different temperatures. One of the great advantages in this method should be the ability to test different materials other than nitinol, where small samples of metallic wire are required to be tested, thus eliminating the current lack of compressive tests available for metallic wire. Therefore, this method should also be easy to reproduce by other researchers when testing fine wire samples of various metallic materials.

When using the loading stage available within the SEM initially investigated by Brodie [3] and Boukis [2], there are some errors associated with it, not being able to replicate their results or generate new results. The use of the Deben system presented problems related to positioning the sample during the test, high sensitivity to strain rate and compliance in the mechanism, questioning the reliability of this test method. Introducing the SEM to this setup also brought some problems, related to obtaining the temperature inside the SEM during the test as well as the implementation of DIC, where it was invalid due to the image quality provided by the SEM live video.

In conclusion, when analysing all the results presented in this chapter it is possible to affirm that the first method, although it presented promising opportunities, these does not

materialise due to the lack of repeatability in the load data, positioning of the sample during the test and unreliability in observing the deformation which precludes any image correlation approach.

This conclusion changes the main goals proposed at the beginning of this work, where the focus was to gather a comprehensive set of repeatable compression test data. The main goal of the next chapter therefore will focus on how to develop and validate a new compression test. A new method which uses the same type of sample, but an alternative means of loading was studied and validated. The development of this compressive method will be described in the following chapter.

Chapter 6
Development of a compressive test method

6.1 Background

As described on previous Chapter, the compression test method used by Brodie [3] and Boukis [2] proved to not be a reproducible test when loading nitinol wire under compression loading. With the previous test, it was not possible to validate the repeatability of the test, where the same results as the literature were not possible to obtain and it was identified that the method presented problems while holding the sample during the test, where it was verified that the sample moved from its initial position. Also, the fact that it is not possible to determine the exact temperature of the sample during the test, proved again that this method is not adequate to test nitinol wire.

In this chapter, a new compression test method is suggested to use while testing nitinol wire under compression loading that used the same samples and the equipment available on the University, such as the conventional testing machines.

6.2 Objectives

The main objectives proposed in this chapter are the following:

- Identify the most reproducible experimental setup for obtaining repeatable experimental results;
- Study the effect of length to diameter (L/D) ratio using the same diameter (1 mm) and changing the final length of the samples and identify the best sample length to use;
- Investigate the effect of three loading/unloading cycles up to 6% compressive strain;

- Characterise the stress-strain response at different temperatures, these being the in-service temperatures of room temperature (approx. 23°C), body temperature (37°C) and sterilization temperature (55° C).).

6.3 Development of the new compression test method and preliminary tests

An alternative method was investigated that aims to eliminate the problems described previously. In order to use the same samples from the previous method and to eliminate the problem of maintaining the sample at the same position during the test, the best solution was identified by changing the direction of the test using a universal testing machine and placing the sample vertically. Among the equipment available in the laboratory, the best option was to use the Instron 5969 series with a 50kN load cell. Table 6.1 compares the specifications of this machine with the Deben machine.

Table 6.1 – Specifications of each equipment used for compression testing.

Features	**Deben Microtest MT2000** [78]	**Instron 5969** [81]
Type of support	Electromechanical / placed horizontally	Electromechanical / placed vertically
Test type	(quasi) static	(quasi) static
Max force	2kN	50kN
Minimum speed	0.005 mm/min	0.001 mm/min
Operating temperature range	-20°C to +160°C with Peltier heating & cooling	-150 to +350°C with environment chambers

As presented on Table 5.1, the maximum load detected during a compression using the Deben system is close to 800 N. Although the load magnitude of the machines is changing from 2kN max force to 50kN max force, the Instron 5969 load cell has a sensitivity of

0.001 [82]. This indicates that the Instron machine is adequate to use to compress nitinol wire.

Figure 6.1 and Figure 6.2 shows the setup used during this method where in Figure 6.1 it is possible to see the Instron machine in a compression setup with the platens and in Figure 6.2 it is possible to see how the sample is placed between the platens. The platens used are generic platens available in the laboratory used for compressive loading, these platens are large in comparison to the sample size therefore the samples need to be placed in the centre of the platens to ensure the samples are under uniaxial compressive loading. All tests were performed at room temperature of 24±1˚C, temperature being measured with a thermometer placed near the platens, as seen in Figure 6.1.

The samples are placed at the bottom cell using tweezers until they are vertically stable, a pre-load is applied to the sample (between up to 5 N) to keep the sample secured. Lubricant (WD40) is applied at each end of the sample before each test. The raw data from the Instron machine is stored in a .csv file (comma-separated values) which contains the information of the time (s), displacement of the load cell (mm) and force measured by the load cell (kN). Test frequency as 50 Hz and no filter was added to the software when obtaining the raw data.

A first set of tests was preformed to test the new method and compare with the previous results. The same samples (S2 and S4) were used as well as new samples (S5, S6 and S8), thus it was possible to compare the stress-strain response of the same samples and also see if new samples provide the same response. In Table 6.2 the details of the first set of tests made using this arrangement are listed.

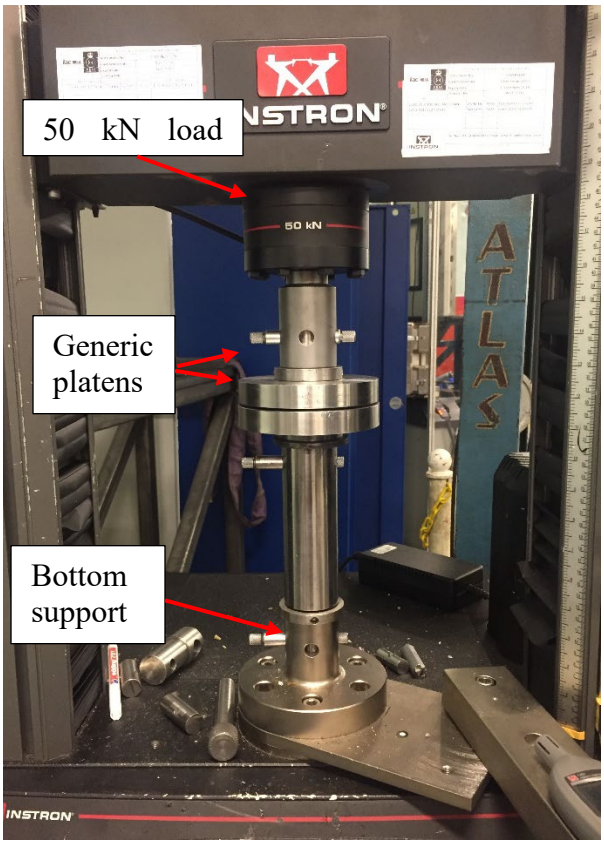

Figure 6.1 – New compressive test setup using Instron 5969 50kN

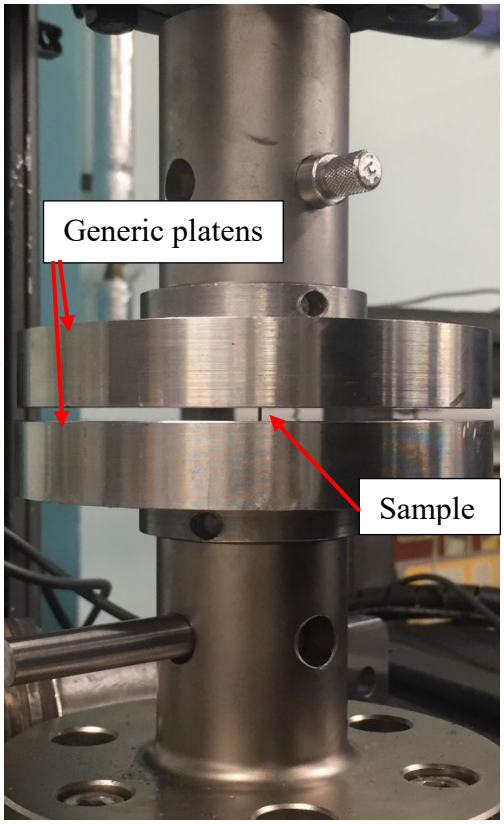

Figure 6.2 – Detail of the new compressive setup with the sample placed between the platens

Table 6.2 – Validation of the method: First set of tests at room temperature.

Test	Sample	Speed (mm/min)	Compressive strain (%)	Number of cycles
1	S2, S4, S5	0.05	4	3
2	S2, S4, S5, S6	0.1	4	3
3	S2, S4, S5	0.05	5	3
4	S2, S4, S5, S6	0.1	5	3
5	S2, S4, S5	0.05	6	3
6	S2, S4, S5, S6	0.1	6	3

For this first round of tests, samples S2 and S4 were loaded to 4% and 6% nominal maximum strain at two different crosshead velocities, 0.05 mm/min and 0.1 mm/min, to try to replicate the same conditions as in the previous tests. Samples S5 and S6 were tested in the same way as the previously used ones (S2 and S4) to provide a direct comparison of the results obtained using the same machine and thus compare how the stress-strain response might differ from previously tested and new samples.

When comparing the stress-strain responses from the different testing methods as in Figure 6.3 and Figure 6.4 it is possible to observe the difference between the responses obtained. On Figure 6.3 are the stress-strain responses for sample S4 when compressed to 4 % strain. The black line refers to the stress-strain response obtained from the Deben Microtest machine with test speed of 0.05 mm/min and the dotted line with the test speed of 0.1 mm/min. The red line refers to the stress-strain response obtained through the Instron machine with the test speed of 0.05 mm/min and the dotted line for a speed test of 0.1 mm/min. The first observation from this figure is the presence of a clear phase transformation, where an upper and a lower plateau are observed on both red lines obtained from the new method test. Also, it is possible to see the maximum compressive stresses obtained are significantly higher with the new test, rising to 950 MPa, this value being slightly higher than the value measured by Boukis [2].

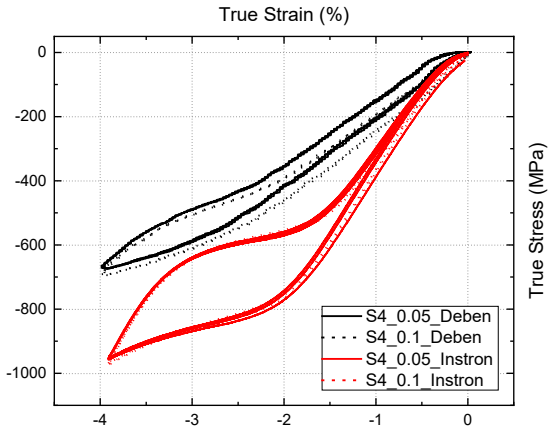

Figure 6.3 – Stress-strain curve comparing different methods for sample S4 at 4% compressive strain and different testing speeds

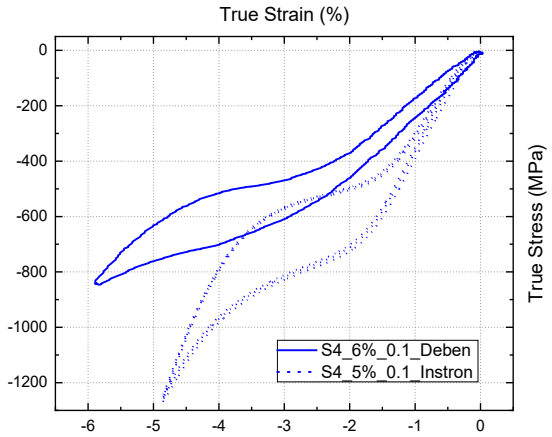

Figure 6.4 – Stress-strain curve comparing different methods from sample S4 at 6% strain (old method) vs 5% strain (new method).

Figure 6.4 shows the stress-strain response for sample S4 where the continuous blue line is the response obtained from the Deben device loaded up to 6% strain with a test speed of 0.1 mm/min and the dotted blue line is the response obtained from the Instron machine when the sample was loaded up to 5% strain at 0.1 mm/min. Comparing both responses it is possible to see again the maximum compressive stress is higher when tested with the new method with a maximum stress of approximately 1200 MPa when compressed up to 5% actual strain where with the previous test the maximum compressive stress obtained was approximately 900 MPa when compressed up to 6% strain. In the dotted blue line, it is also possible to see the emergence of linear elastic behaviour beyond approximately 3.5% strain, indicating that the material is mostly in the detwinned martensitic phase, whereas when the sample is loaded up to 6% strain using the previous method there is no evidence of the material being fully in this phase. With the results presented in Figure 6.3 and Figure 6.4 it is possible to see a significant improvement in the response obtained with the new method. After comparing the results from the two different methods, the responses obtained through the new method will be studied in more detail with the figures shown below to validate this method.

Figure 6.5 and Figure 6.6 that follow show in detail the stress-strain responses obtained using the new test method when comparing the results of the samples used previously with the virgin samples, showing consistency in the results from different samples with the new method.

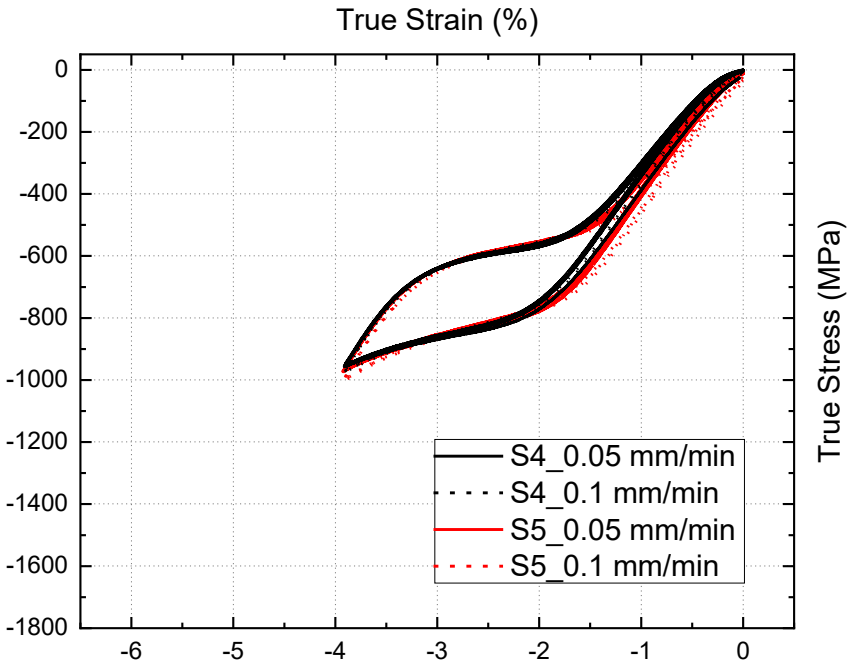

Figure 6.5 – Compressive stress-strain response of samples S4 and S5 for 4% strain at different speeds

Figure 6.5 compares the stress-strain response of samples S4 shown in black with sample S5 shown in red when compressed up to 4% strain. It also compares the stress-strain response at different loading rates, where the continuous lines correspond to 0.05 mm/min and the dotted lines correspond to 0.1 mm/min. From the responses is possible to see:

- The responses are not influenced by the change in loading rate, since both responses are almost the same. This suggest that the relatively small difference in the testing rate does not affect the stress-strain response in compressive loading, contrary to what was observed with the results from the Deben machine;

- The stress-strain responses are the same when looking at samples used previously and the virgin samples, demonstrating that the new method provides more consistent results;
- Looking at the responses it is possible to see linear elastic behaviour when loading up to 1.5% strain approximately and a corresponding compressive stress of 700 MPa. After this point the upper plateau commences where the forward transformation occurs, the phase change during this plateau transforming the austenitic crystals to detwinned martensite as caused by the induced stress. This plateau, as discussed previously, is not flat and it occurs over an increase of approximately 1.5% in strain and change in stress of 150 MPa. Just before the 4% maximum strain is reached it is possible to see the material entering a new linear elastic regime. During unloading, the creation of the lower plateau starts at 3.5% strain approximately and at 700 MPa stress. The plateau exists for a 1% change in strain approximately and a stress difference of 100 MPa. The reverse transformation finishes at 500 MPa and a corresponding strain of 1.5% thereafter a linear elastic response appears for unloading during the austenitic phase. The cycle finishes at zero stress and strain and no residual strain is shown.

In Figure 6.6 it is possible to compare the stress-strain response of sample S2 and S5 compressed up to 6% nominal strain at different rates. The black lines refer to sample S2 and the red lines to samples S5 where the continuous lines are from tests at a crosshead speed of 0.05 mm/min and the dotted lines from 0.1 mm/min. From these responses is possible to conclude that:

- Similar to the responses in Figure 6.5, here S2 and S5 have similar stress-strain responses with no difference in the responses again being observed as a result of any difference in the strain rate;
- On all four responses the first cycle shows some slight compliance when loading initially commences but the second and third cycles are consistent in all tests, with all samples being tested up to 3 cycles;

- Neglecting the first cycle from the cumulative response, it is possible to see the initial loading is linear elastic up to 1.5% strain and approximately 600 MPa. After this point it is observed that the upper plateau again emerges over a 1.5% strain range and an increase in stress of 150 MPa, with the phase transformation happening in this plateau. At 4.5% strain is possible to see a new linear elastic response associated with the detwinned martensitic phase, this linear response continues up to 6% strain with an associated maximum stress of 1600 MPa. The unloading starts with the linear elastic response continuing down to 4.5% strain and an equivalent stress of 700 MPa. The reverse transformation starts with the creation of the lower plateau between 3.5% and 2% strain approximately and with a change in stress of 100 MPa approximately. The material is then again fully austenite at 1.5% strain with the formation of the linear elastic unloading modulus. No residual strain is shown in the response.

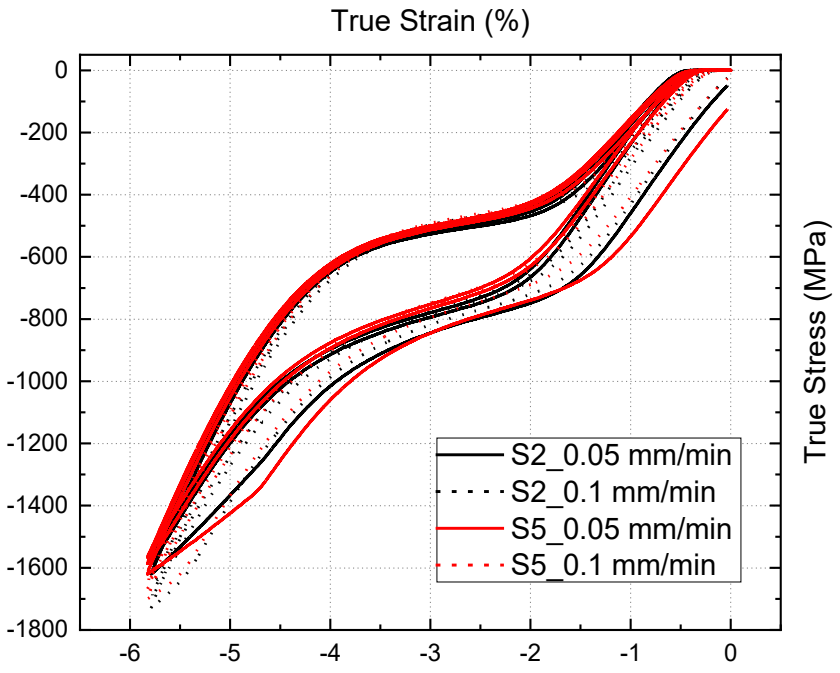

Figure 6.6 – Compressive stress-strain response of samples S2 and S5 for 6% strain at different speeds

With these results it is possible to verify the potential of the new method by obtaining better results than the previous SEM based method. Now it is necessary to validate the test for all ranges of maximum strains and for repeatability.

Sample S8 in Table 6.3 was tested from 2% up to 6% maximum nominal strain to study the compressive strain evolution with this method. For each strain, the sample was tested three times with 3 cycles on each test and the loading rate used is the same in all cases.

Table 6.3 – Validation of the method: Second set of tests using one sample for different compressive strain at room temperature.

Test	Sample	Speed (mm/min)	Compressive Strain (%)	Number of cycles
1	S8	0.1	2 to 6	3

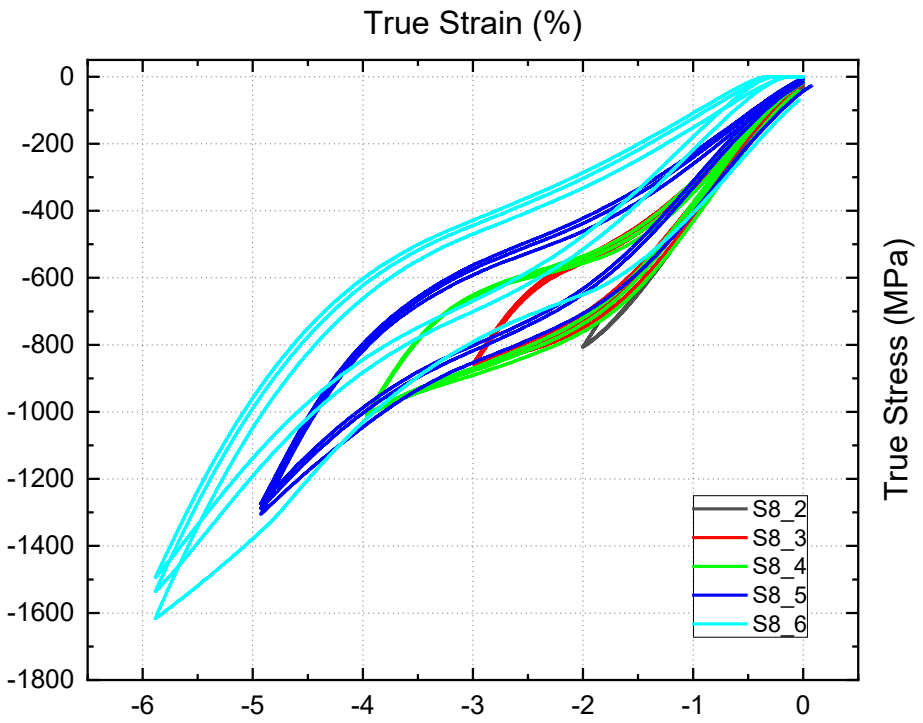

Figure 6.7 – Compressive stress-strain response evolution of the strain from 2% to 6% for sample S8 at room temperature.

After performing these tests, it is possible to understand the material response when subject to different maximum strains as well as the repeatability of the test. Figure 6.7 shows the strain evolution of sample S8 where the sample was tested to different maximum strain each time, and it is possible to see that:

- The loading path is consistent for all tests, with the exception of the test to 6% strain. Again, when loading up to 6% strain the first cycle appears to have some compliance when initially loaded but after shifting the second and third cycles towards the origin the stress-strain response lies on the same path as the previous cycle throughout loading. During unloading it is also possible to see the consistency of the response with increasing strain.

In Figure 6.8 it is possible to understand the repeatability of the response of the sample when compressed up to 4% strain. In this figure the stress-strain responses of the three tests are shown and is possible to verify the repeatability of this method.

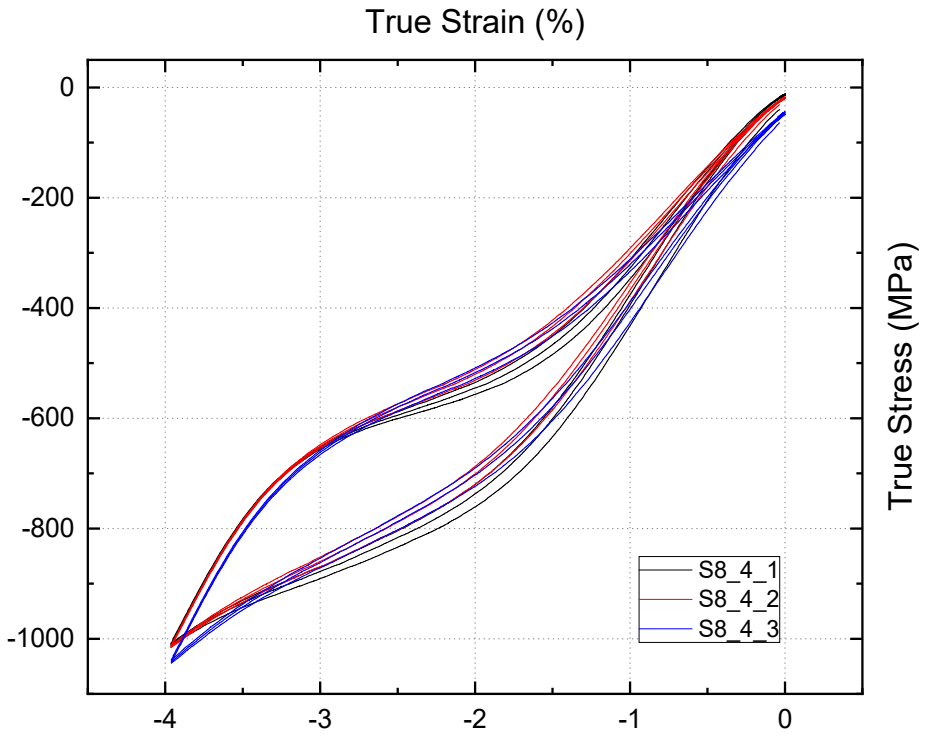

Figure 6.8 – Compressive stress-strain response of sample S8 when compressed up to 4% strain when tested three different times. Repeatability test.

Finally, still verifying the test for repeatability, Figure 6.9 shows the stress-strain response of all samples tested by the new method when compressed up to 4% strain. In this figure it is possible to see that the stress-strain response is the same for all the different samples tested. These results further reinforce the validity of the new method as a more reproducible approach for compressive testing of nitinol wire.

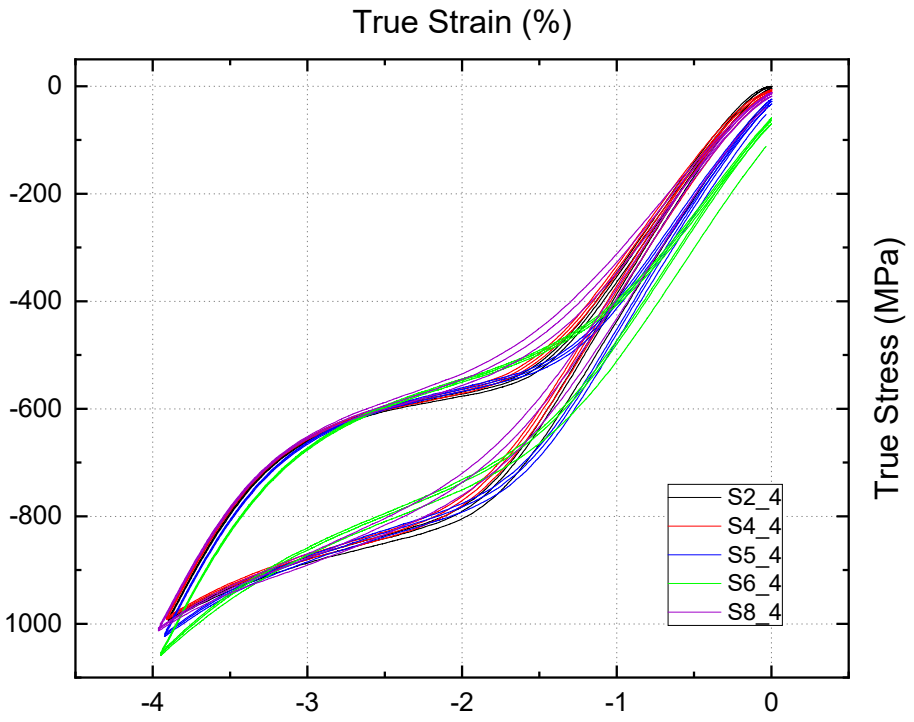

Figure 6.9 – Compressive stress-strain response comparison of all samples at 4% nominal strain.

6.4 Effect of sample length

The next step is to understand how the sample L/D ratio influences the stress-strain response in compressive loading. To make use of the samples that already exist, this set of tests included samples of 2 mm and 1.5 mm length and diameter of 1mm. The samples were cut the same way as previously and they were used as supplied. To minimise the misalignment caused during the cutting process, each sample was subjected to a pre-load

before being used. The new set of tests are detailed in Table 6.4. Following the same study as for sample S8, each of these samples was tested three times for each specified maximum strain and each test consisted of loading/unloading the sample three times (three cycles) at room temperature (25°C).

Table 6.4 – Validation of the method: Third set of tests

Test	Sample	Sample length (mm)	Speed (mm/min)	Compressive Strain (%)	Number of cycles
1	S9, S10, S11	2	0.1	2 to 6	3
2	S12, S13, S14	1.5	0.1	2 to 6	6

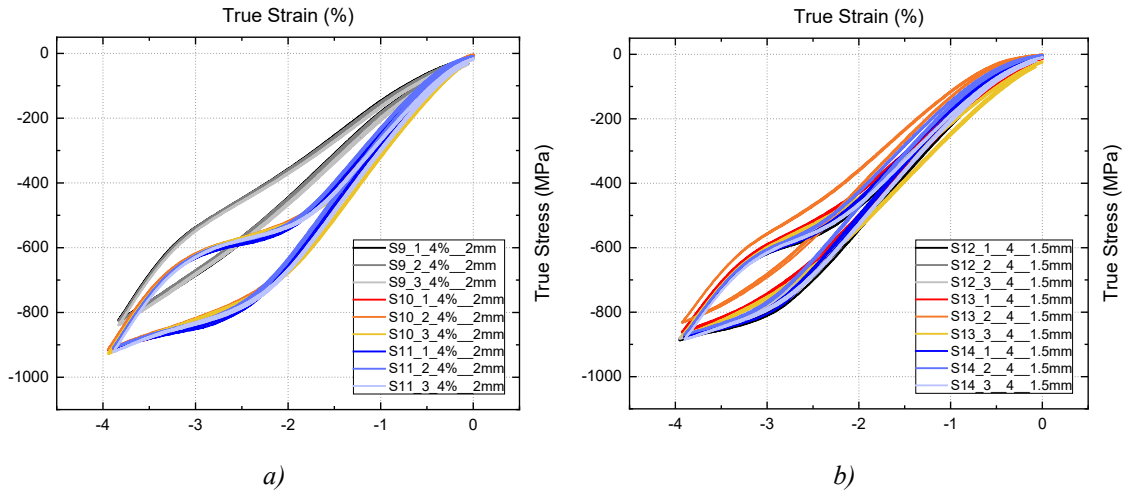

a) *b)*

Figure 6.10 – Compressive stress-strain response compressed up to 4% strain for a)2 mm sample length; b) 1.5 mm sample length.

Comparing the stress-strain responses of the 2 mm and 1.5 mm long samples in Figure 6.10 when loaded up to 4% maximum strain and tested three times, it is possible to see the maximum stress is slightly higher in the 2 mm sample than in the 1.5 mm one. Sample S9 of 2 mm length (grey colours) represents a defective response suggesting that it is a

faulty sample (assumption that the ends were not machined correctly), so will not be taken into consideration. When looking at the material phase change presented in the responses, it is possible to see for the 2 mm long sample the transformation is more advanced at 4% strain than for the 1.5 mm long sample, where both the upper and lower plateau are more distinct in the 2 mm long sample.

When comparing between the stress-strain response for compression up to 6% maximum strain for the 2 mm and 1.5 mm samples in Figure 6.11, the stress at maximum strain is higher for the 2 mm samples where a stress of approximately 1400 MPa was recorded against 1200 MPa for the 1.5 mm one, similar to the results for loading to 4 % maximum strain. Again, the sample S9 in Figure 6.11 a) (shaded grey) is not taken into account. Finally, the forward and reverse transformation is clearly visible in both sample lengths, the main difference observed suggests that in the 2 mm sample the accumulated elastic deformation in detwinned martensite is higher than for the 1.5 mm sample, the forward transformation starts first for the 2 mm sample where at 2 % strain it is possible to see the initiation of the upper plateau while in the 1.5 mm sample the upper plateau starts at 2.5 % strain.

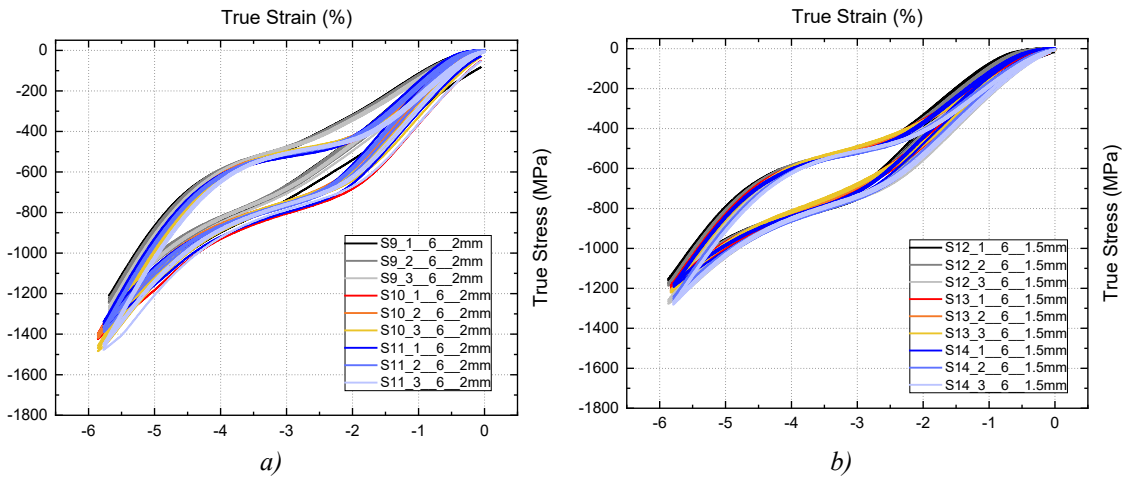

Figure 6.11 – Compressive stress-strain response compressed up to 6% strain for a)2 mm sample length; b) 1.5 mm sample length.

Finally, Figure 6.12 compares the stress-strain responses for the three different sample lengths tested to 6% maximum nominal strain, where it is possible to see the responses are similar, the main different being in the stress recorded at maximum strain. The difference between 1.5 mm and 2 mm is higher than between the 2 mm and 3 mm sample length. Also, during the austenitic phase, the response shows higher stiffness for 1.5 mm sample.

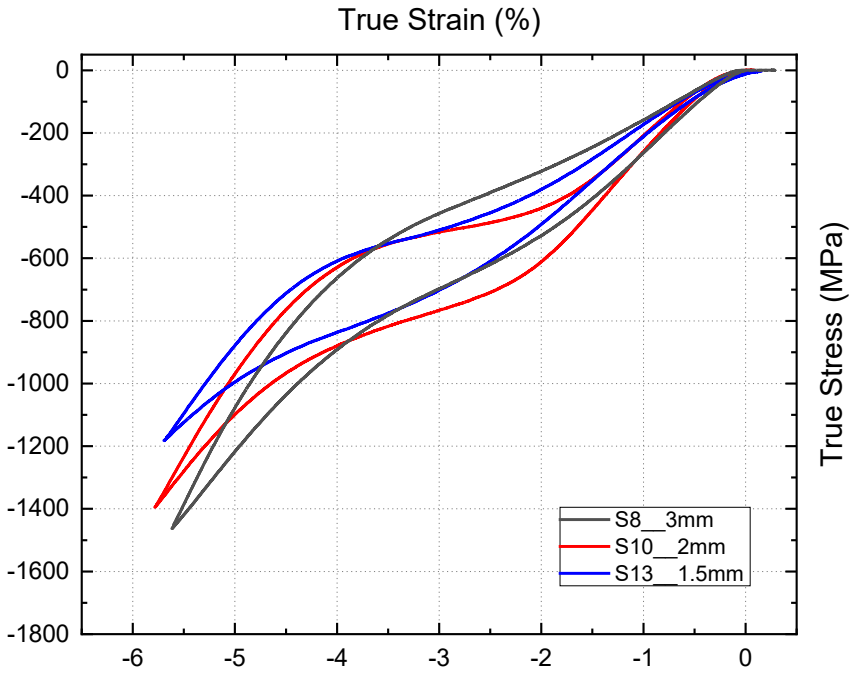

Figure 6.12 – Comparison of stress-strain response between 3 mm, 2 mm and 1.5 mm sample length when compressed up to 6% strain.

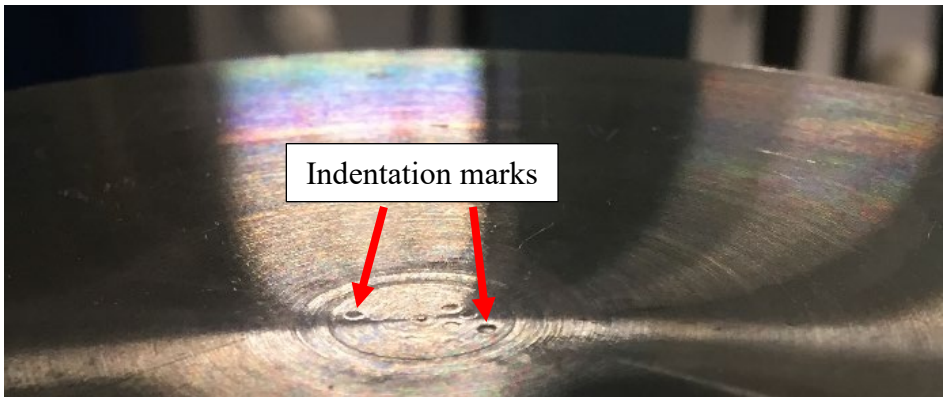

Figure 6.13 – Indentation in the platens cause by the samples.

During the compressive test, it was possible to observe indentation on both platens created by the samples, as seen clearly in Figure 6.13. Therefore, new platens were manufactured for this test with a hardener surface and with an overall size more appropriate to the samples used.

6.5 Improvement of the compressive test method

New platens were designed to support the compressive stress applied to the samples during the test, to implement strain measurement during the test and also to be used within Terumo Aortic laboratories, which are equipped with the same universal Instron mechanical testing machine but with a load cell of 2 kN capacity. The platens were manufactured in the workshop at the University of Strathclyde, made of tool steel, surface heat-treated and harden to 30 Rockwell to avoid sample indentation in the platens during testing. The platens were designed to attach directly to the 50 kN load cell of the AMRL Instron testing machine. A locking ring was also manufactured to attach to the platen. This locking ring screwed to the platen and located in the load cell, where it is then unscrewed against the load cell to prevent the platen moving. The platen is attached to the load cell through a central pin, so the locking ring is the crucial part in the platens because it gives more rigidity to the entire platen system.

In Figure 6.14 it is possible to see how the locking ring attaches to the platen. This figure is an image rendered from the software SolidWorks, used to design the parts, the image is

for illustrative purpose only. Appendix C:, shows the technical drawing of both the platen and the locking ring. The assembly of the platens to the load cell is shown in Figure 6.14 and Figure 6.15. Starting with Figure 6.14, the locking nut is screwed into the platen as follows in Figure 6.15 a). Then, the platen is attached to the load cell and fixed with a pin as seen in Figure 6.15 b), where at this point the locking nut is unscrewed until it reaches the load cell, locking the platen in this way and making a rigid system.

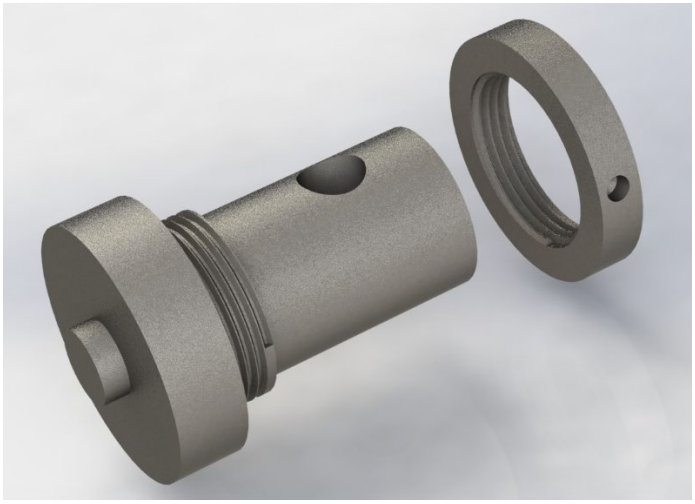

Figure 6.14 – Rendered image of the platen attaching to the locking nut.

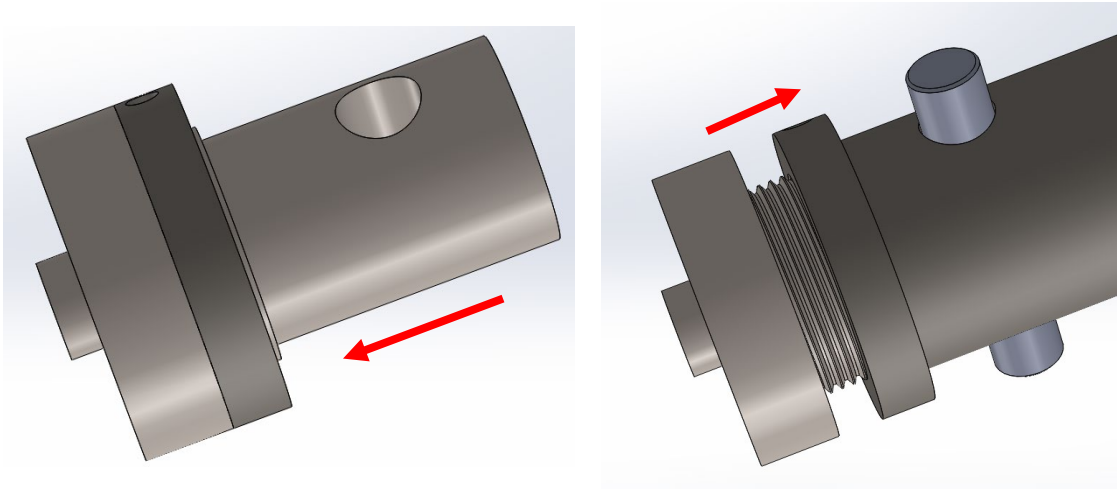

a) *b)*

Figure 6.15 – a) Locking nut screwed to the platen; b) Platen and locking nut attached to the load cell support with the locking nut unscrewed to the support to remove movements between the platen and the load cell support.

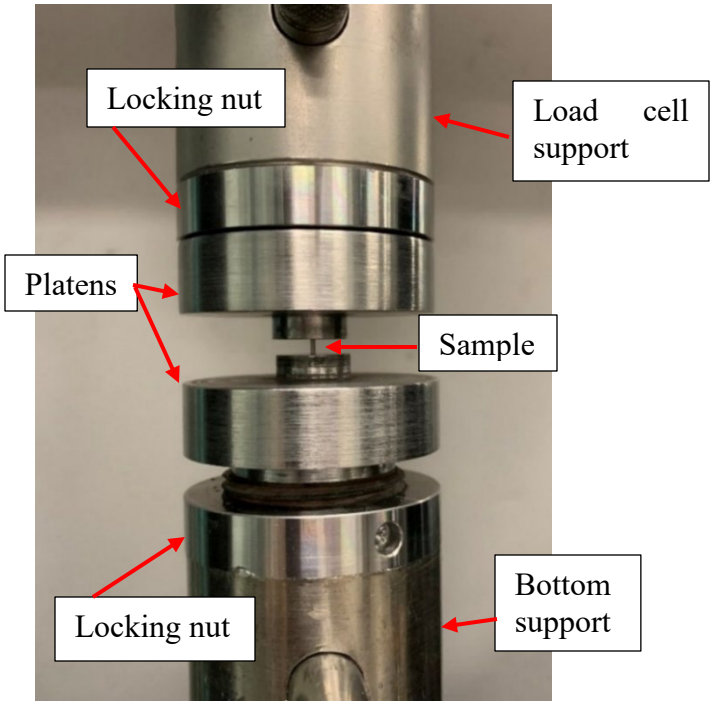

Figure 6.16 – Platens placed in the 50 kN machine with the locking nuts and sample between the platens.

From Figure 6.16 it is possible to see how the platens attach to the AMRL Instron 50 kN load cell with the central pin holding the platen into the load cell attachment. It is also possible to see how the locking rings are attached, where at the top load cell is almost fully screwed into the platen and for the bottom support it is possible to see a gap between the platen and the locking ring.

As mentioned previously, one of the aims of manufacturing the new platens is to be able to perform the compression tests at Terumo Aortic laboratory. The advantage of using the Terumo Aortic testing machine is due to the accessibility of an environmental chamber and also the fact that the available load cell at Terumo Aortic has a higher sensitivity than the 50 kN load cell available at AMRL. Finally, the availability of the machine at Terumo, where fewer people work on it when compared to with the machine available at the University, as well as the cost associated. To fit in the 2 kN load cell of the Terumo machine, adapters were designed to connect the new platens to the smaller load cell. This

adapter consisted of a sleeve that connected the platens to a small diameter load cell connector as seen in Figure 6.17.

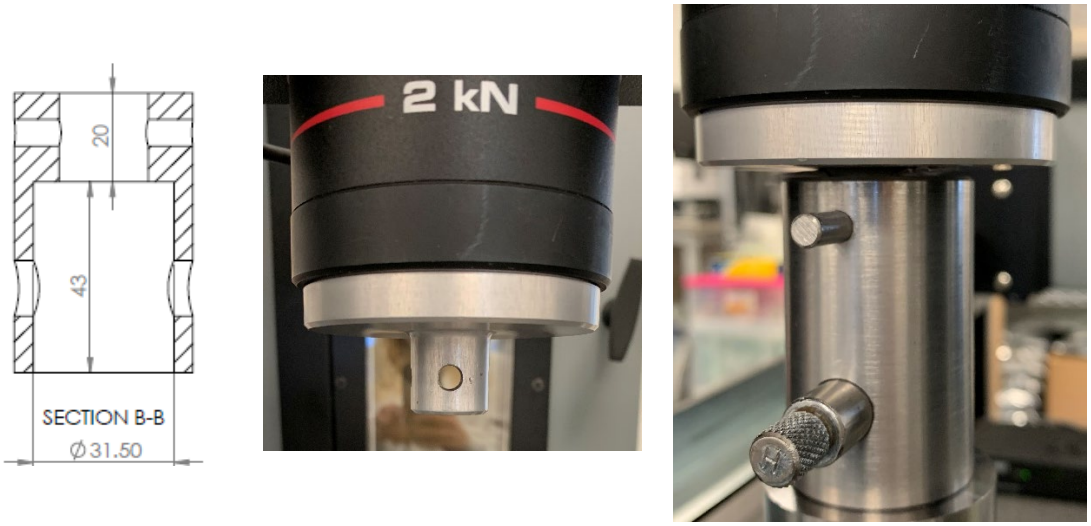

a) *b)* *c)*

Figure 6.17 – a) Technical drawing of the sleeve connector for 2 kN load cell; b) 2 kN load cell at Terumo Aortic laboratory; c) Sleeve connected to the 2 kN load cell.

From Figure 6.18 it is possible to understand how the sleeve connector attaches to the platen and the load cell. Figure 6.18 a) shows a rendered image, similar to Figure 6.14, where it is possible to see the sleeve connector attached to the platen and locking nut. It is also possible to see the pin in the centre that holds the sleeve connecter to the platen. Figure 6.18 b) shows a section view of the assembly to better understand how all the parts connect with each other. For this section view the colour of the platen was changed to red to better distinguish all components, and also the transparency of the pin was changed for the same reason. With this figure it is possible to see how the locking ring screws together with the platens and also the gap between the locking nut and the sleeve. During the test the locking nut needs to be completely unscrewed in such a way as to contact the sleeve connecter, as seen in Figure 6.19 b), to prevent any movement between the platen and the sleeve connector. From Figure 6.18 b) it is also possible to see at the top where the platen will attach to the 2 kN load cell shown in Figure 6.17 b).

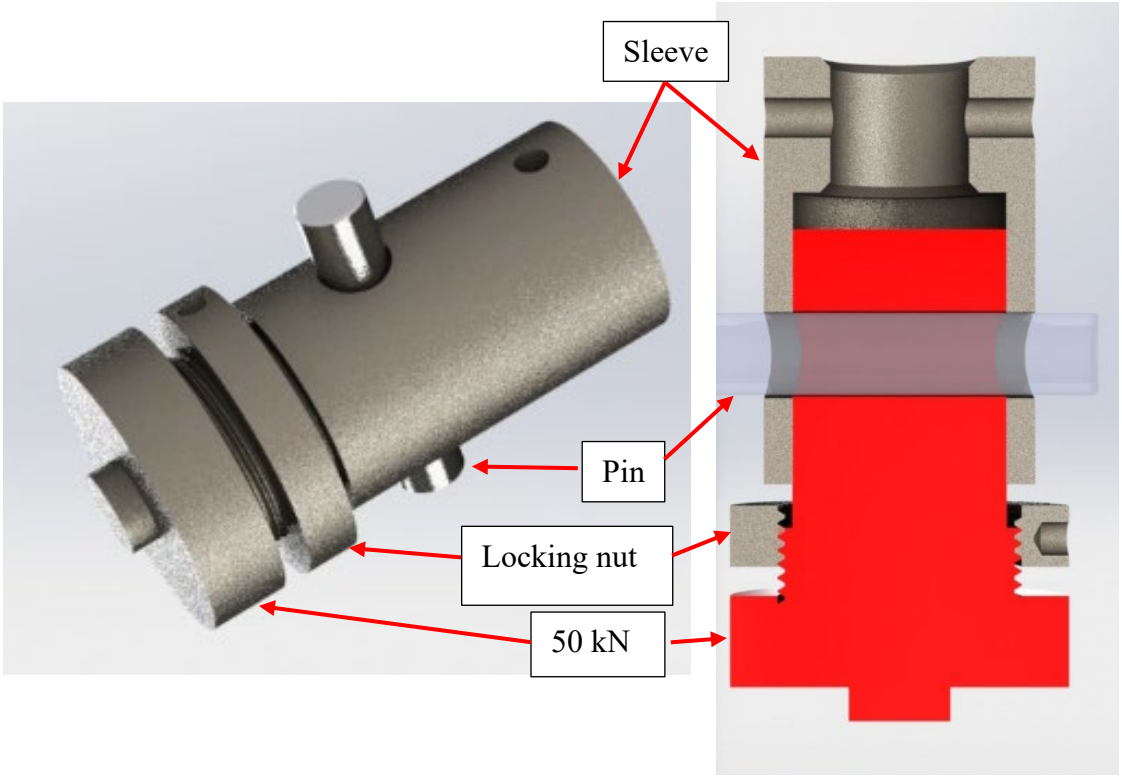

a) *b)*

Figure 6.18 – a) Rendered image of the final assembly of the platens with the sleeve connector; b) Section view of the platen.

6.5.1 First adaptation

The process to adapt the new platens for use in different testing machines was made in an iterative way. The first iteration was to adapt the platens for use inside the environmental chamber at Terumo, where specific connecters need to be added as seen in Figure 6.19.

For this first set of tests in the Terumo machine samples tested previously were used. The samples used were S2, S4, S5, S6 and S7 and the tests consisted of compressing each sample up to 6% maximum nominal strain first with one loading/unloading cycle and subsequently with multiple cycles. The tests were performed at room temperature inside the laboratory (approximately 18°C).

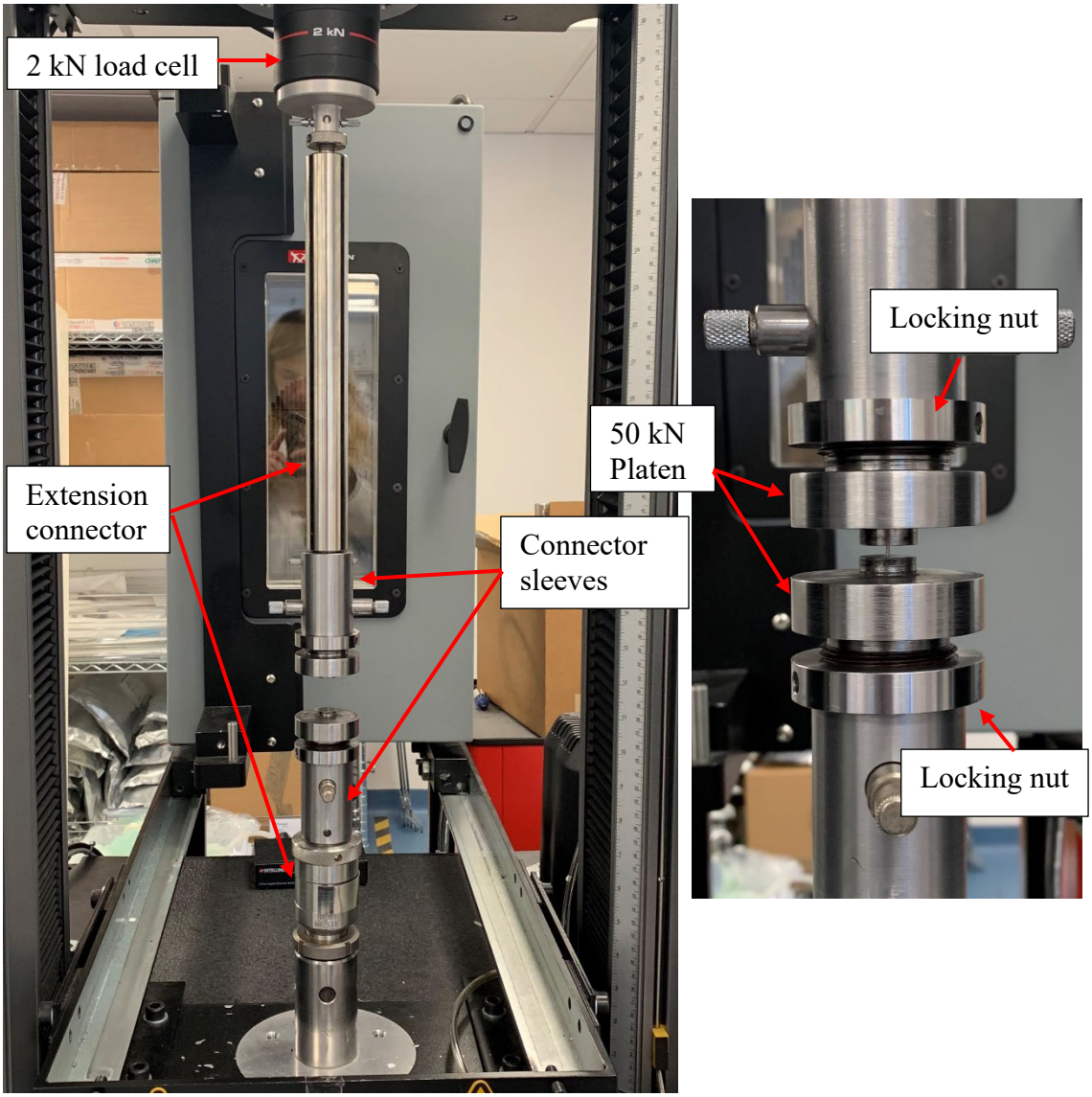

a) *b)*

Figure 6.19 – a) Compression test adaptation 1 at Terumo Aortic laboratories – 2 kN Load cell; b) detail of the sample placed between the platens.

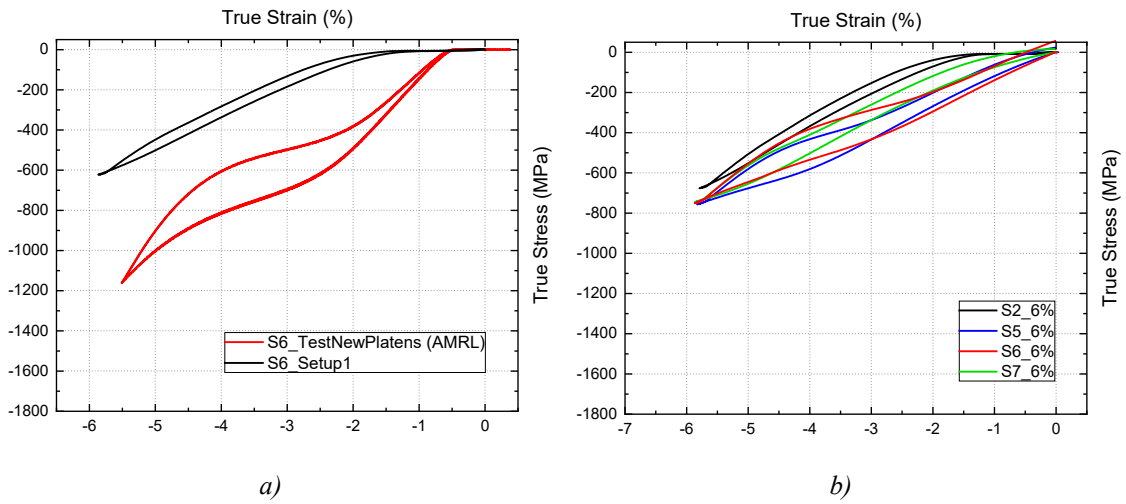

a) *b)*

Figure 6.20 – a) Comparison of stress-strain response for sample S6 at 6% strain in different machines using the same platens; b) Comparison of stress-strain response for different samples (S2, S5, S6 and S7) at 6% strain using the new platens in 2kN load cell.

Figure 6.20 show the first results obtained with the new platens attached to the 2 kN load cell. Figure 6.20 a) compares the stress-strain response of sample S6 tested obtained from the 50 kN load cell and the 2 kN load cell using the new platens. From this figure it is possible to see a big different between the two responses. When tested with the 2 kN load cell, the response shows significant compliance in the setup once the deformation actually starts to be recorded at supposedly 2% strain, and the material does not appear to go through any phase transformation. The figure also shows a discrepancy between the results obtained from the 50 kN and the 2 kN machine related to the stresses. From the response obtained from the 50 kN it is clear to see the upper and lower plateau between 600 and 800 MPa and 600 and 400 MPa respectively. It is also clear to see the linear elastic behaviours during loading and unloading for both austenite and detwinned martensite. By comparison with the response given by the 2 kN load cell, there is no formation of the upper and lower plateaux and the pre and post transformation linear elastic behaviours, are not as evident as in the response from 50 kN load cell.

Analysing the results in Figure 6.20 b), this figure shows the stress-strain response for different samples tested in the 2 kN load cell with the new platens and loaded up to 6%

strain, where it is possible to see that the responses follow similar paths where again no transformation is obviously visible in the response.

6.5.2 Second adaptation

In an attempt to obtain better results, the setup was changed, however this compromised the use of the environmental chamber. This change was made to understand if the problem from the previous adaptation is related to the extra compliance added to the system by the extra components used to place the platens at the middle of the Instron machine (Figure 6.19 a)). So, these changes went from removing one part of the connectors at a time to thereby understand the influence. Therefore, since the bottom support is universal for both testing machines, the first part to be removed was the bottom supports where the platen was placed directly in the machine with no extra supports or adaptors as seen now in Figure 6.21. For this test, the same samples were once again tested at the same conditions as previously.

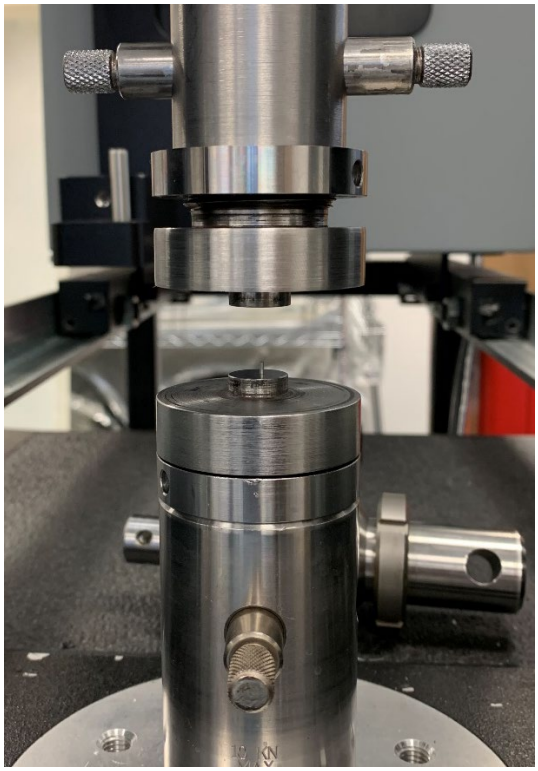

Figure 6.21 – Compression test adaptation 2 at Terumo Aortic with sample placed in the bottom platen, ready to be tested.

From Figure 6.22 it is possible to see that the stress-strain responses obtained by the second iteration are similar to the first iteration. This figure compares the stress-strain response of sample S4 obtained from the first iteration with the one obtained from the second iteration. As stated previously, both responses are similar, with no evidence of phase transformation having occurred and some erroneous compliance in the setup. It is also possible to see that the linear elastic moduli for austenite both during loading and unloading are lower than expected, indicating that this setup is unable to provide valid results.

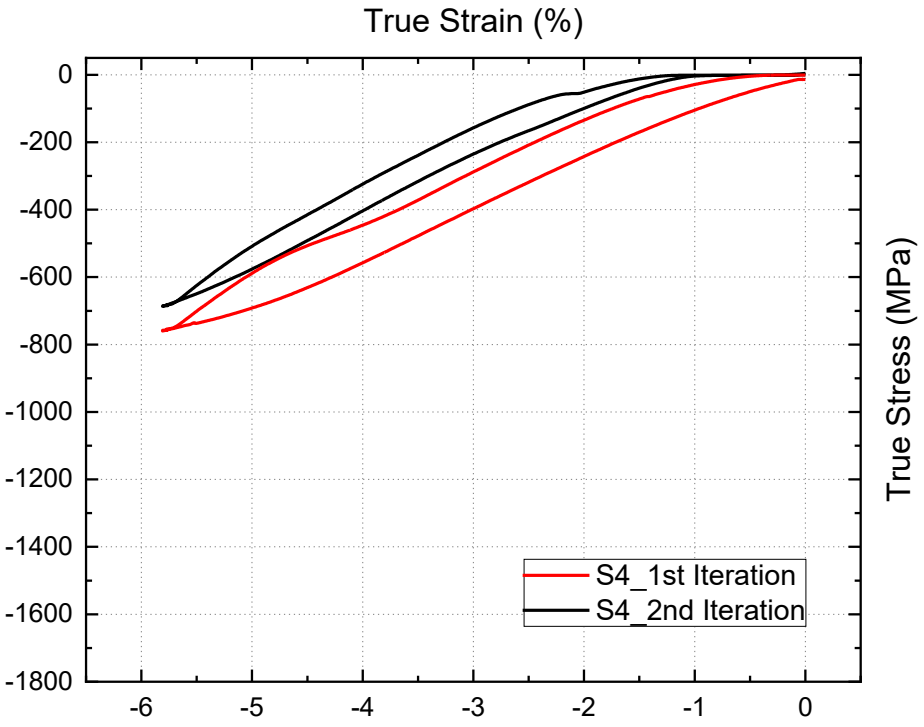

Figure 6.22 – Comparison of stress-strain response of sample S4 when compressed up to 6% strain in different setups.

One of the reasons for the stress-strain curves are not as expected might be due to the use of previously tested samples, so the same tests were performed using new samples. For this, 2 mm long samples were used due to the lack of availability of untested 3 mm long samples and the 2 mm response is known from previous tests on the AMRL machine

equipped with the 50 kN load cell. So, sample N15 was tested, using the same conditions of the previous test and both setup adaptations were investigated.

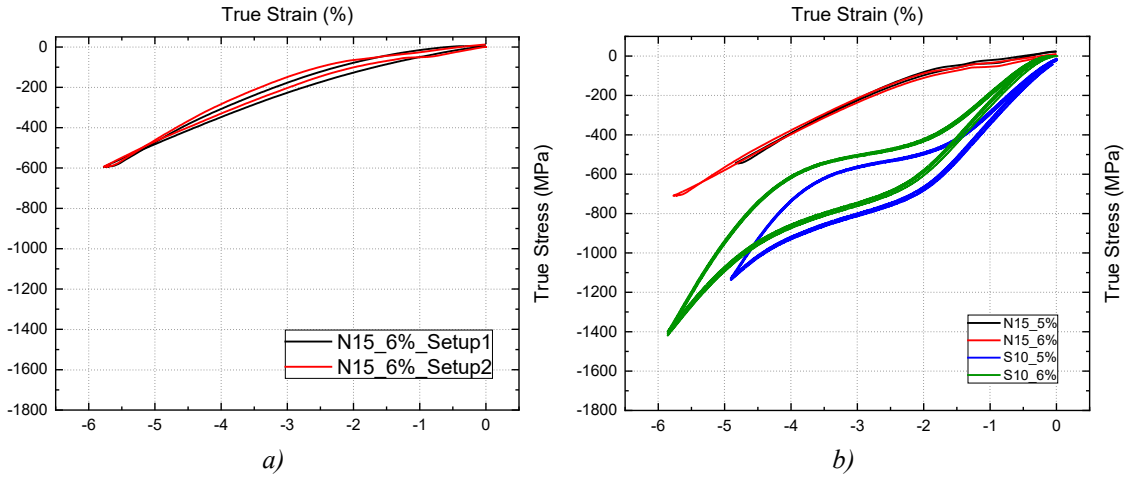

Figure 6.23 – Stress-strain response of a) Sample N15 for adaptation 1 and 2; b) Comparison of response of sample N15 and sample S10 for 5% strain and 6% strain.

From Figure 6.23 it is possible to see the results obtained from the new sample, where in Figure 6.23 a) the stress-strain curve for sample N15 is compared when it is tested in different setups (first and second iteration). Both responses are very similar to each other and there is no evidence of phase transformation in either response, indicating that the there is no erroneous compliance coming from the bottom of the setup/adaptors and that using virgin samples does not affect the results. Figure 6.23 b) compares the stress-strain response of sample N15 with the previous curve obtained for sample S10 tested with the old platens on the university laboratory (AMRL) machine. From this figure it is possible to compare the response when the samples are compressed up to 5% and 6% strain, where the difference between the responses is clearly visible. The black and red lines correspond to sample N15 whereas the blue and green lines correspond to sample S10. This demonstrates that the second adaptation of the test setup is still not able to provide valid results.

6.5.3 Third adaptation

As described in the previous section, it was established that removing the bottom adaptors does not change the measured stress-strain response, so in this latest adaptation, the connectors/extensions that are connected directly to the load cell will be removed, which potentially compromises the use of the environment chamber. In Figure 6.24 it is possible to see this third adaptation, using the new platens, where the bottom platen is connected directly to the machine and the platen at the top is connected to the load cell with the sleeve adapter that fits into the 2kN load cell. In this figure the sample is placed in between the platens ready to be tested. This test arrangement used previously tested samples to avoid wasting new samples.

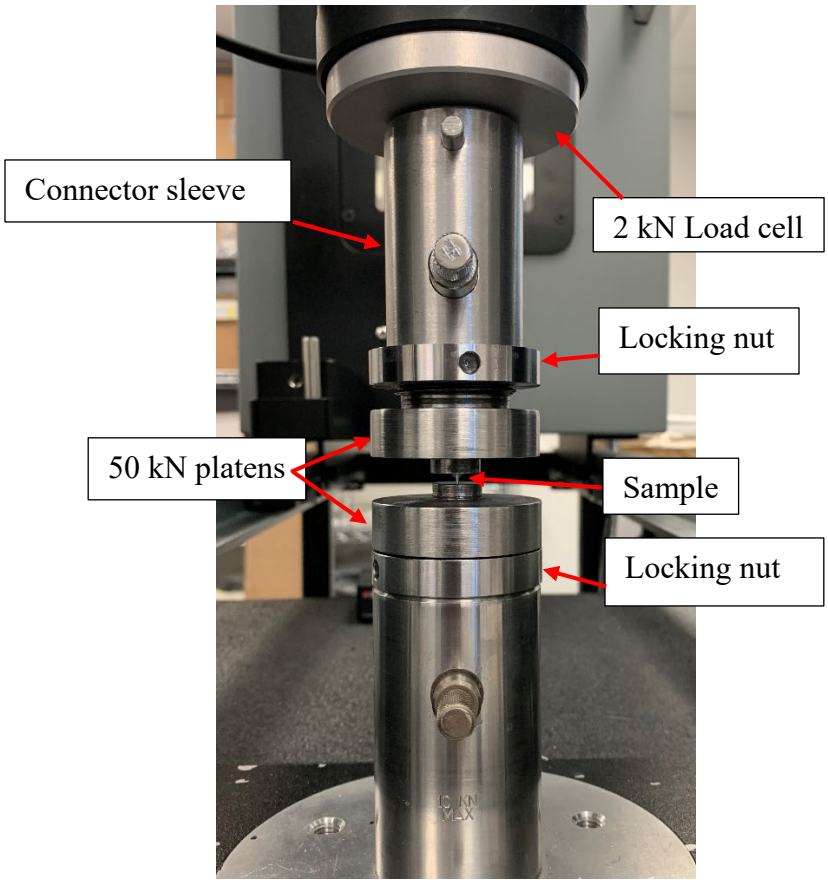

Figure 6.24 – Compression test adaptation 3 at Terumo Aortic with sample placed in the bottom platen, ready to be tested.

Samples S3 and S7 were used in this setup adaptation. These tests were performed at the same test conditions as previously, where the sample was compressed up to 6% maximum nominal strain at room temperature.

From the stress-strain curve obtained in Figure 6.25 for sample S7, it is possible to see that the response improved when compared with the previous adaptations, since in this figure it is now possible to see some hysteresis caused by the stress-induced phase transformation between austenite and detwinned martensite. Although some improvement is evident, this setup cannot be relied on yet, because the stresses recorded in this response are still lower than expected, the anticipated linear elastic response during the detwinned martensite phase is not evident and there is still some residual compliance in the setup.

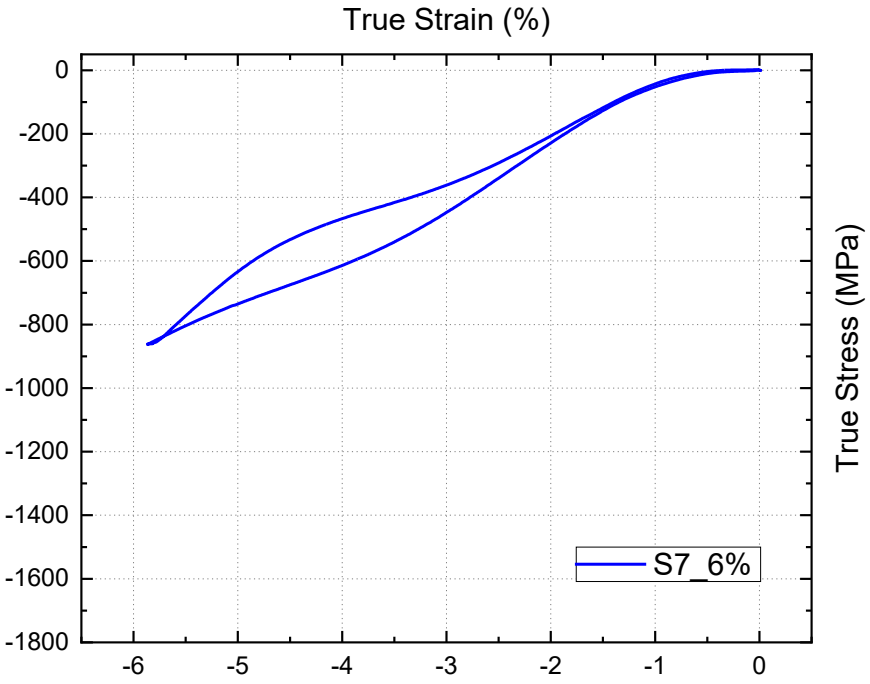

Figure 6.25 – Stress-strain response of sample S7 when compressed up to 65 strain in the third adaptation.

In an attempt to endorse this setup, different tests were performed, studying the influence of multiple cycles, the application of different pre-loads and increasing the machine displacement range. To study the influence of displacement, the sample was tested using

the normal displacement of 0.18 mm (6% nominal strain) and the displacement of 0.19 mm (≈ 6.5% nominal strain). To understand the influence of pre-load, two different pre-loads were applied in each test, a pre-load of 50 N and the second test at a pre-load of 103 N. As mentioned previously, with the vertical setup no pre-load is necessarily required to perform the compressive test. Finally, to study the influence of load cycling, three different tests were made, testing the sample over 3 cycles, 5 cycles and 20 cycles.

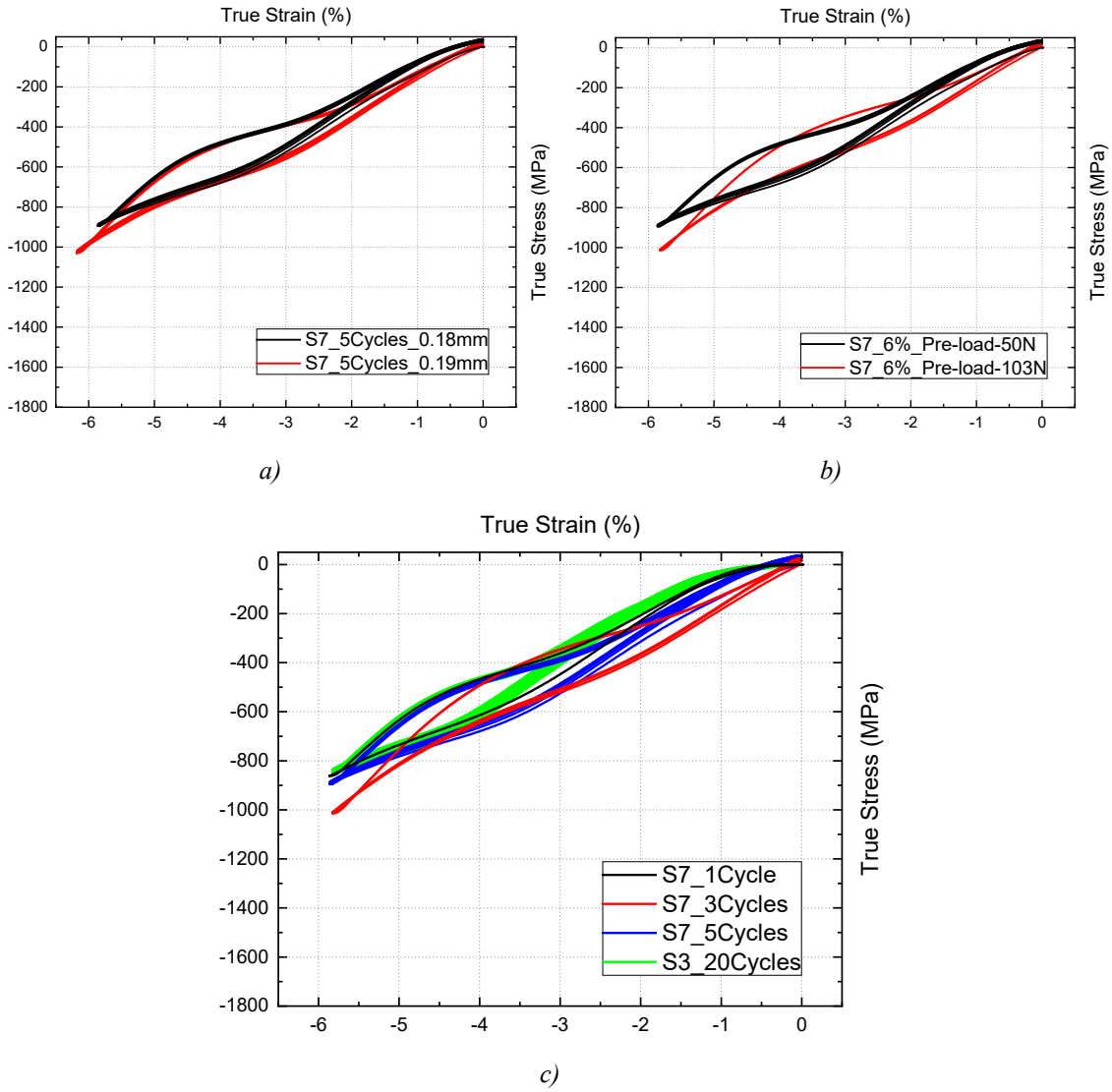

Figure 6.26 – a) Stress-strain response at different displacement; b) Stress-strain response applying different pre-loads; c) Stress-strain response at different cycles.

Figure 6.26 shows the stress-strain curves for all the additional tests made. In Figure 6.26 a) when increasing the displacement from 0.18 mm (equivalent to 6% strain) to 0.19 mm (equivalent to ≈ 6.5% strain) it is possible to identify the increase in strain in the red curve, the figure also suggests that the transformation finishes later than in the 6% strain case but the maximum stresses are still lower than expected, implying that increasing the displacement range does not improve the response significantly. The idea behind increasing the displacement range was to understand if the unanticipated compliance would be countered and 'shift' the transformation to higher strains.

For the second test, pre-loading was applied to the sample, again this process was based on the same idea as the previous test, to try to overcome the unexpected compliance present in the setup. As seen in Figure 6.26 b), the black line corresponds to a pre-load of 50 N and the red line to a pre-load of 103 N, where it is possible to see that when the higher pre-load is applied the phase transformation region appears to be longer and consequently the maximum stress is slightly higher but the parasitic compliance at lower strains is still present. Thus, in conclusion, pre-loading still does not endorse this adaptation. Finally, Figure 6.26 c) shows the stress-strain response when tested over different numbers of cycles. This test was designed to understand if the response stabilized to the expected one, similar to the method presented by Brodie [3] and Boukis [2]. Looking at the results obtained, it is possible to conclude that with 20 cycles (green line) the response is practically constant throughout the test, providing additional evidence for not adopting this particular adaptation of the test.

The third adaptation consisted of applying the platens directly to the machine supports. For the upper load cell, the sleeve adapter needs to be used to connect the platen to the smaller connection. At this point there are most likely two reasons that are preventing the test method being adapted to the Terumo machine these being:

- The sleeve connector made to adapt the 50kN fitting to a 2kN fitting is adding unwanted compliance to the machine setup;

- The machine is not suitable for NiTi under compressive loading due to the load cell having not been correctly calibrated for compression.

6.5.4 Fourth adaptation

This new adaptation consisted of eliminating the extra connectors in the system. This means that a new and smaller platen was designed, able to attach directly to the 2kN load cell. This platen was manufactured in the same way as the previous one with the new platen and the locking ring shown in Figure 6.27. The new setup is shown in Figure 6.28, where only one platen was made to fit directly in the load cell (upper platen) and the previous platen was used at the bottom, since the lower fixture is universal for this range of Instron machines.

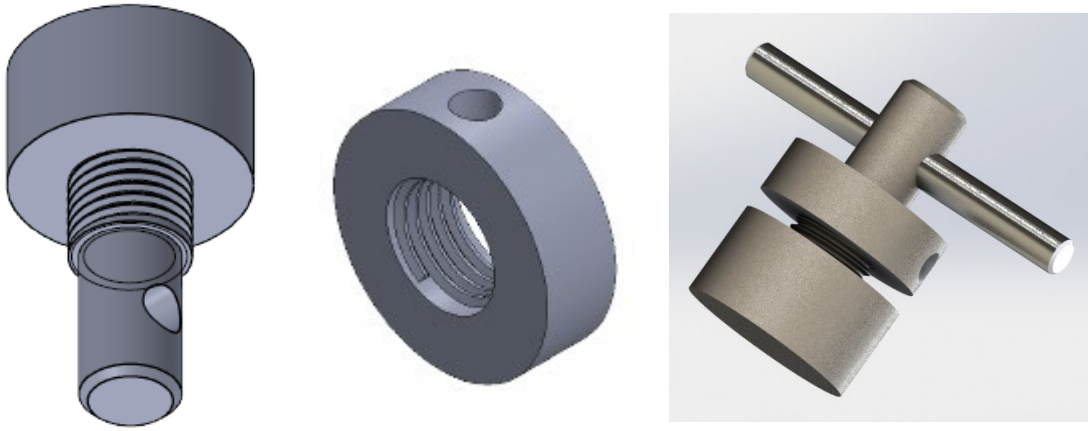

a) *b)* *c)*

Figure 6.27 – Illustration of the 2 kN platens; a) technical drawing of the platen; b) technical drawing of the locking nut; c) Rendered image of the platens and locking nut assembly with the pin that holds the platen to the load cell.

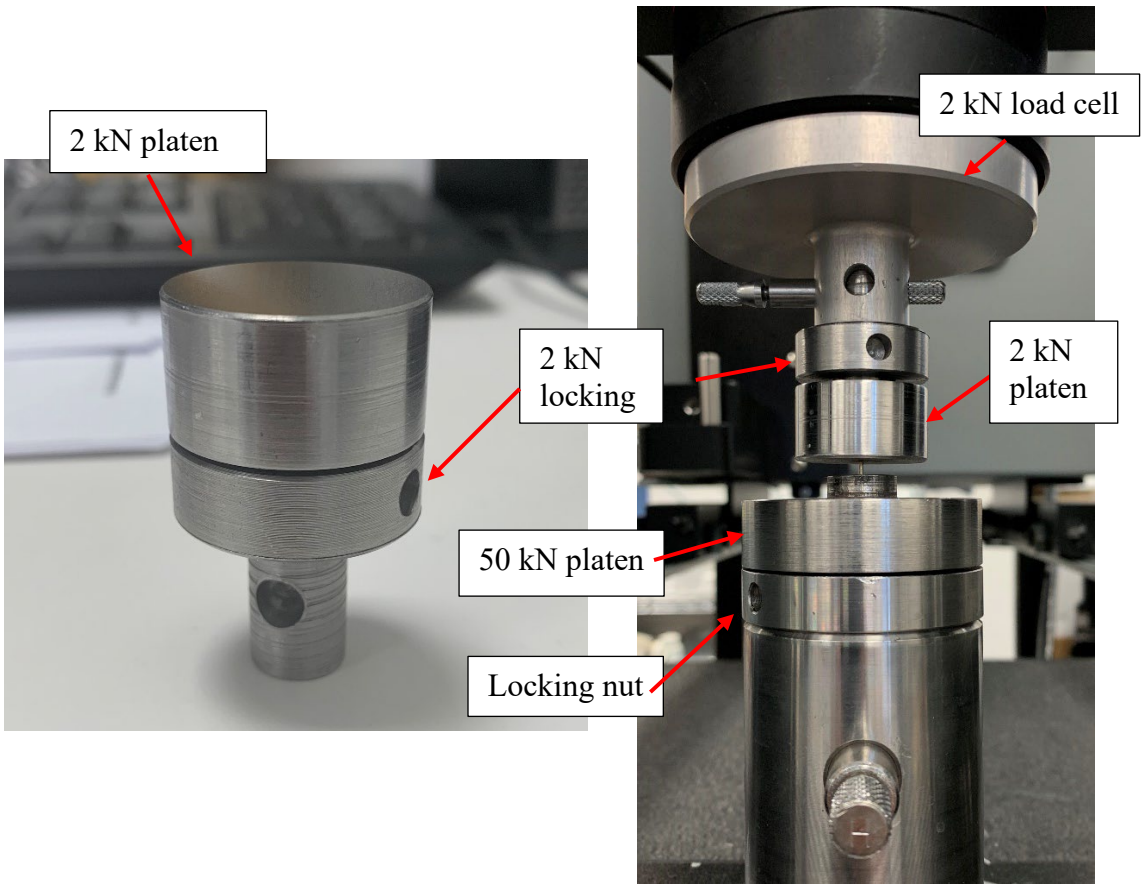

a) *b)*

Figure 6.28 – a) Smaller platen made for fourth adaption; b) Setup of the fourth adaptation with smaller platen attached directly to the 2kN load cell.

Sample S5 was used, and the same test was performed, where the sample was compressed up to 6% strain at room temperature. No pre-load was applied, and the test consisted of 3 loading cycles. In Figure 6.29 it is possible to see the stress-strain curve obtained for this test where it is compared with the first curve obtained for this sample when tested on the University AMRL machine with the first platens. From the results obtained it is possible to see that the material goes through a phase transformation but when compared with the first result (red line), the stresses obtained are still lower than expected. This setup still exhibits an elevated compliance seen in the stress-strain curve indicating that this adaptation will still not produce valid results.

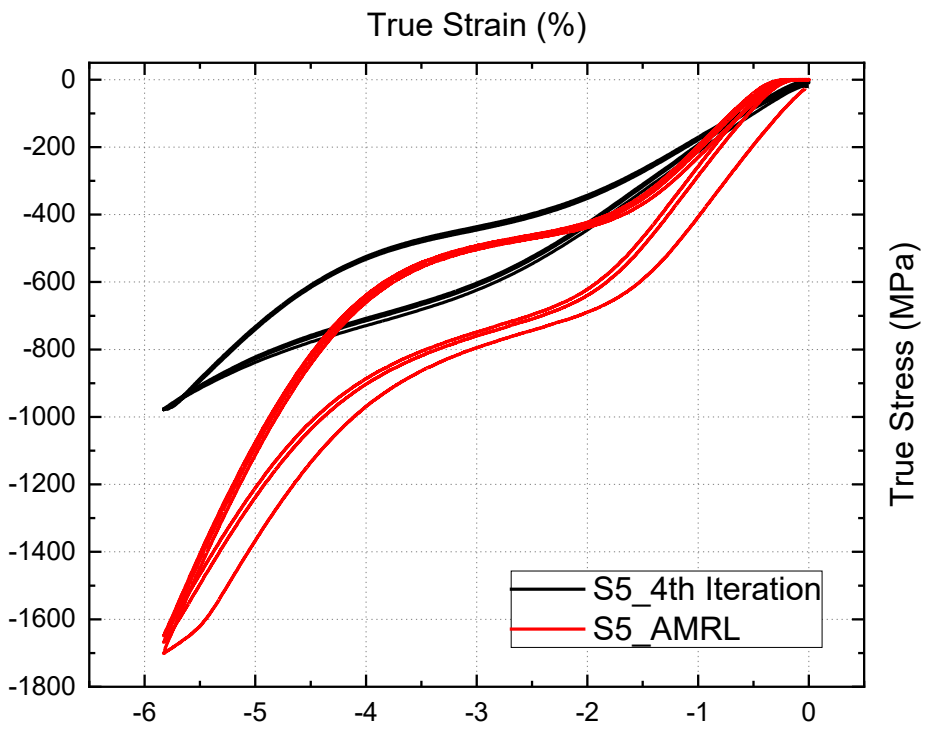

Figure 6.29 – Comparison of stress-strain curve of sample S5 from 4th adaptation and from AMRL.

When setting up the program in the machine, usually the test is displacement controlled and limited by strain. In other words, the displacement of the machine crosshead (vertically down for compression test) is controlled by the equivalent strain of the sample and the test ends when the inputted sample strain is detected and converted by the load cell. In these machines is possible to change these control configurations. When the machine crosshead displacement is controlled by the sample strain or the desired force and the test finishes when the load cell detects either the desired sample strain or the force inputted in the sample.

All previous tests were made by controlling the crosshead machine displacement by strain and the test finished when the desired sample strain was detected and converted by the load cell. Therefore, further tests were made by changing the configurations explained previously, in an attempt to understand the source of the unwanted compliance presented in this setup/machine. These tests consisted of:

- Control the machine displacement crosshead by sample strain and finish the test when a certain load is detected by the load cell;
- Control the machine displacement crosshead by force applied in the sample and finish the test when a certain load is detected by the load cell;
- Control the machine displacement crosshead by force applied in the sample and finish the test when a certain sample strain is detected and converted by the load cell.

The forces used to control these different configurations were obtained from the compression tests made previously with the 50 kN load cell. In this way it is possible to reduce the compliance of the setup, where the sample is compressed up to the equivalent force for the desired strain. Since these different control configurations did not improve the stress-strain responses, the results will not be presented in this work.

After testing all possible setups for this machine, it was finally concluded that this machine is not properly calibrated for compression loading.

6.5.5 Fifth adaptation

This last iteration consisted of using the platens design for the 50 kN load cell directly on the 50 kN load cell available at the laboratory in the University (AMRL). In Figure 6.30 a) it is possible to see the final setup attached directly to the 50 kN load cell while Figure 6.30 b) shows in detail the surface of the platens after the tests where no obvious post testing indentation is evident.

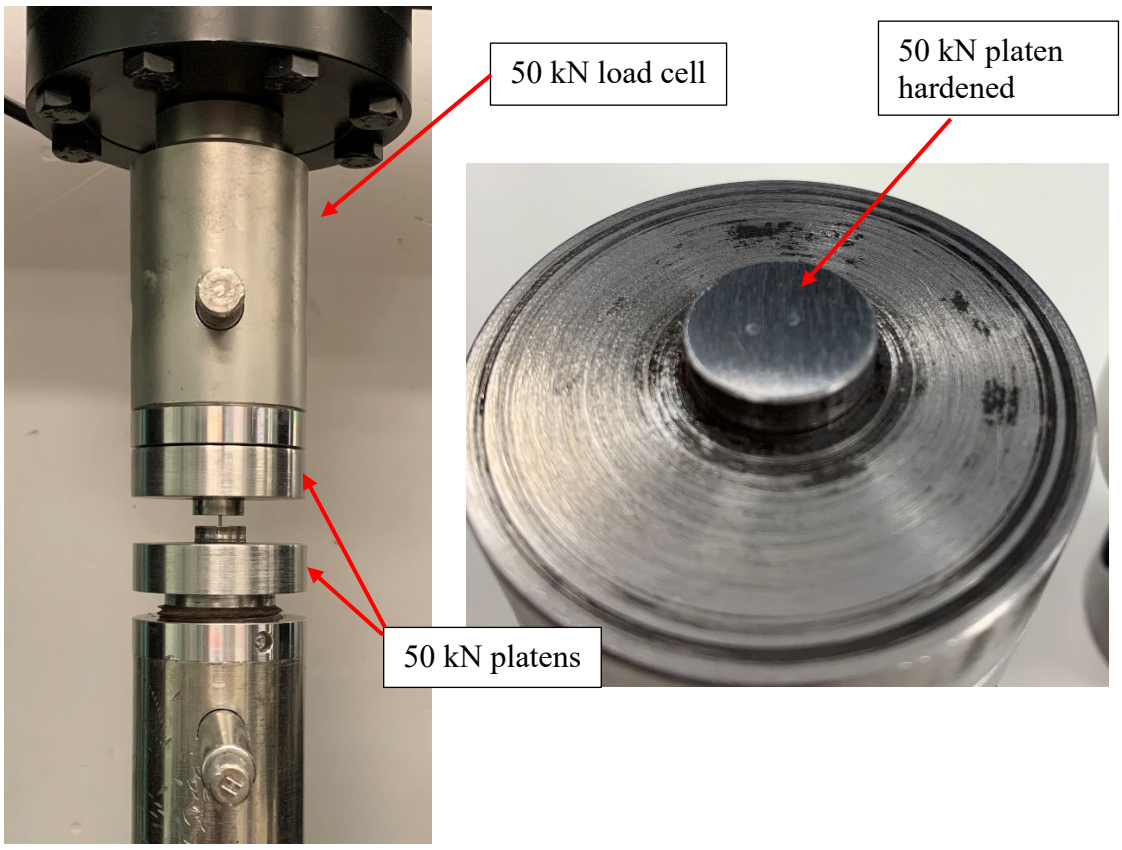

a) *b)*

Figure 6.30 – a) Final setup using the 50kN load cell; b) detail of the hardened surface of the platen after few compressive tests.

To validate this setup, sample S5 was tested once more using the same parameters as the previous test, loading the sample up to 6% strain at room temperature. The results obtained are presented in Figure 6.31 which compares the stress-strain curve obtained from this final setup with the curve obtained from the first tests using the original platens available within the laboratory.

From the results presented in Figure 6.31 it is possible to validate the results obtained using this setup. The red line refers to the curve obtained from this present setup and it is possible to clearly see the material phase change, the upper and lower plateaux are clearly

evident as well as the linear elastic response during both the austenitic and the detwinned martensitic phases for both loading and unloading.

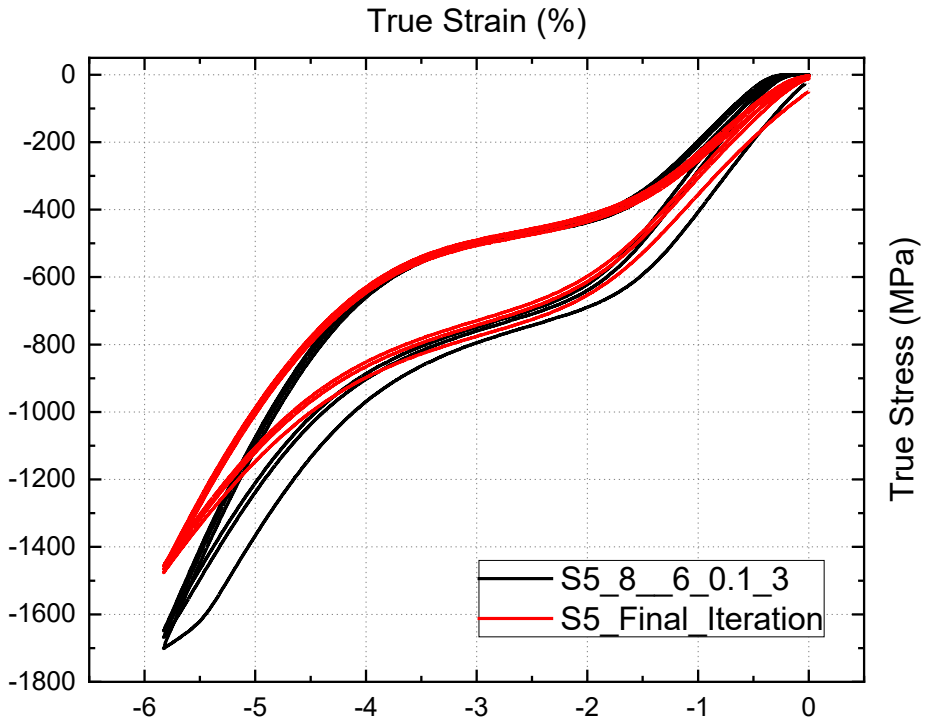

Figure 6.31 – Comparison of stress-strain curve of sample S5 using the new platens for 50kN load cell with the platens provided by AMRL.

6.6 Conclusions

This chapter describes all the steps for the development of a compressive test method after the method used in Chapter 5 proved not to be suitable to perform compressive testing for nitinol wire. The development of the method presented in this chapter started with an initial idea and the preliminary tests to validate the idea. After the validation of the idea the test method was improved by undergoing to several adaptations that are described in detail in the present chapter.

During the development of this method, the challenge of obtaining a reproducible method where several adaptations were made to arrive at the final setup is described. These

adaptations included the creation of different adaptors as well as different platens. It was also shown the importance of having the machines properly prepared to perform compression tests, by calibrating the load cells both for tension and compression loading.

This new method has been shown to provide more repeatable results when testing nitinol wire samples under compressive loading. Unlike the method used on previous chapter, in the new method tests the wire is in a vertical position, thus eliminating difficulties related to positioning the sample.

Considering the set of tests that studied the effect of the sample L/D ration in Figure 6.12, it is possible to conclude that increasing the sample length, the maximum stress apparently increases as well. But when comparing between different increases in sample length, this increase in maximum stress is greater for the increase between the 1.5 mm sample length and the 2 mm sample length that between the 2 mm sample length and the 3 mm sample length, despite this last increase in length being greater. This suggests that the stress strain response is dependent of the sample length. As mentioned on literature review, there is no study available that confirms any mechanical characteristic from nitinol that suggest a size dependency on the stress-strain response so at this stage it is assumed that this is size dependency is a consequence of the testing procedure and not a material effect. This way, a more extensive study of the effect of L/D ration is needed.

Despite all of the adaptations to the tests, it is concluded that using the test machine available at Terumo Aortic presented several difficulties when trying to replicate the tests. These difficulties are due to the additional compliance in the setup and the load cell calibration, suggesting the latter was not properly calibrated for compressive loading. Therefore, the final setup uses the 50 kN load cell available at the University of Strathclyde AMRL.

As for future tests it is suggested that a more extensive study of the L/R ratio is made to determine the best length to use when testing nitinol wire samples under compressive loading and the addition of an extensometer to the setup is important to validate the results which are currently based on machine displacement. Also, it is important to understand

the effect of temperature when testing nitinol wire under compressive loading. These studies will be presented in the following chapter, in attempting to fully validate the compressive testing method for nitinol wire.

Chapter 7
Experimental results of the compressive test method

7.1 Background

Chapter 5 presents a detailed study of the compressive test method proposed by Brodie [3] and Boukis [2]. The study identified that the method was unable to reproduce the previous results reliably and thus obtain new results. Also, it was discovered that the method has a problem associated with the positioning of the sample, since it was shown that the sample moves during the test. The application of a DIC based technique using the SEM was not viable for this test, since the resolution of the image decreased substantially when captured live, so it was not possible to use this technique for a test involving continuous sample movement. Therefore, the main objectives of present work were amended to include the development of a new, more reproducible compressive test method. This new method was developed in the previous chapter (Chapter 6), which describes all the stages needed to obtain a means of performing compressive test using small samples of nitinol wire.

This new method was demonstrated to provide repeatable results for compressive loading of nitinol wire with good repeatability. However, some improvements are still needed to this method such as implementing a strain measurement technique as well as studying the applicability of the test to nitinol wire at different temperatures, focusing on the working temperatures of 37˚C and 55˚C (working temperatures for nitinol wire when implemented in the Anaconda stent graft medical device). It is also important to further study the L/D ratio of the sample and understand what the ideal length is to use in compressive loading.

Apart from the improvement of the method, it is also important to understand the behaviour of nitinol wire under compressive loading to obtain the material parameters to be applied to the numerical models, these parameters will be obtained from experiments using the ideal L/D ratio.

This chapter will focus on some of the previous objectives that were initially considered in Chapter 5, like understanding the behaviour of nitinol under compressive load and understanding how the L/D ratio of the sample affects the stress-strain response, as well as further improvements to the method, including a method to directly measure the strain during the test rather than inferring it from the machine displacement, and testing at different temperatures.

7.2 Objectives

Focusing on improving the method developed in Chapter 5, this chapter will focus on:

- Further study the L/D ratio of the sample to understand which is the optimal length to test nitinol under compressive loading;
- Study the temperature dependence in compressive loading for the relevant working temperatures;
- Improvement of the method by measuring the strain directly during the test.

7.3 Study 1 – Length effect in the sample

From the results shown on Chapter 5, it was possible to see from Figure 6.7 that the value of the stress in the stress-strain response, when the samples were strained up to 6%, did not differ proportionally in relation to the change in length. In other words, looking at the stress-strain responses at 6% strain, the sample of 1.5 mm length presented a maximum stress value of approximately 1200 MPa, the 2 mm sample length presented a maximum stress value of 1400 MPa and the 3 mm sample length a maximum stress value just under 1500 MPa. This indicated that there was a bigger change in maximum measured stress between the samples with a length difference of 0.5 mm (1.5 and 2 mm sample) than between the samples with a difference of 1 mm length (2 mm and 3 mm sample). This suggests that the maximum stress in the stress-strain response does not increase directly with the increase in length, leading to the need to better understand how the L/D ratio influences this response when compressing nitinol wire.

The first study considered has the main goal of fully understanding how the ratio between sample length and radius influenced the stress-strain response of nitinol wire under compressive loading as well as identifying the ideal length to perform this test. A range of samples were manufactured with a constant diameter of 1 mm (D = 1 mm) and changing the length from 1 mm to 4 mm long in increments of 0.5 mm. Samples were manufactured following the same method as previously, using EDM technique to cut the samples. The samples were used as received, Figure 7.1 shows all sample sizes used in this study.

Figure 7.1 – Range of the samples used, from 1 mm length to 4 mm length with increments of 0.5 mm. Addition of £1 coin for size reference of the samples.

7.3.1 Alignment of the sample

One of the challenges associated with compressive testing is maintaining the sample under uniaxial compression throughout the test where it is very common for the sample to be under other modes of deformation like buckling or barrelling. For the 3 mm sample it was known already from Brodie [3] that the sample maintains the uniaxial loading during the test, from his work it was possible to see the sample being compressed to full strain (6 % nominal strain) inside the SEM from where it was possible to see that there were no other modes of deformation involved. With the increase in the sample length to 4 mm long, it was important to see if the sample remains under uniaxial compression during the test

therefore the Brodie methodology was adopted to ensure no other modes of deformation are present during the compression test of the longer sample.

Using the setup described in Section 4.3.1, with the Deben micromechanics system inside the SEM, samples of both 3.5 mm length and 4 mm length were compressed and measured using the SEM facilities when loaded and unloaded. The following Figure 7.2, Figure 7.3, Figure 7.4 and Figure 7.5 show the measurements for each sample.

Figure 7.2 shows the 3.5 mm sample with the pre-load applied, but otherwise undeformed. From this figure it was possible to obtain the initial measurements of the sample where it is seen that the sample has a total length of 3.62 mm and a diameter of 1.04 mm. These measures were located manually using the SEM facilities, but since it is a manual process there are possibly some slight errors associated with the measurements. Also, since the image was focused on the top centre of the sample and the sample was a cylinder, there is some slight image distortion when measuring out of the plane of focus. To measure the length of the sample, the cursor was placed in the centre of the sample, as seen in the figure, where the SEM was focused on. To measure the diameter, three cursors were placed along the sample length, at the top, centre, and bottom of the sample, to ensure the diameter was constant along the sample. These cursors were placed manually but it was hard to place them precisely at the same location along the sample. Therefore, these measurements are guidance to gain an idea of the deformation induced in the sample.

Figure 7.3 shows the 3.5 mm long sample when subjected a displacement of 0.09 mm, equivalent to a 2.6 % nominal compressive strain. From this figure it was possible to see that the final length was 3.53 mm and the diameter varied between 1.04 and 1.05 mm. This difference in diameter was assumed to be an error associated with the cursor measurement, indicating that the radial deformation appears to be approximately constant along the sample. Also noted was the compliance present in the Deben compression system itself since the input crosshead displacement was 0.21 mm, equivalent to 6% compressive strain, and the displacement measured by the SEM was only 0.09 mm.

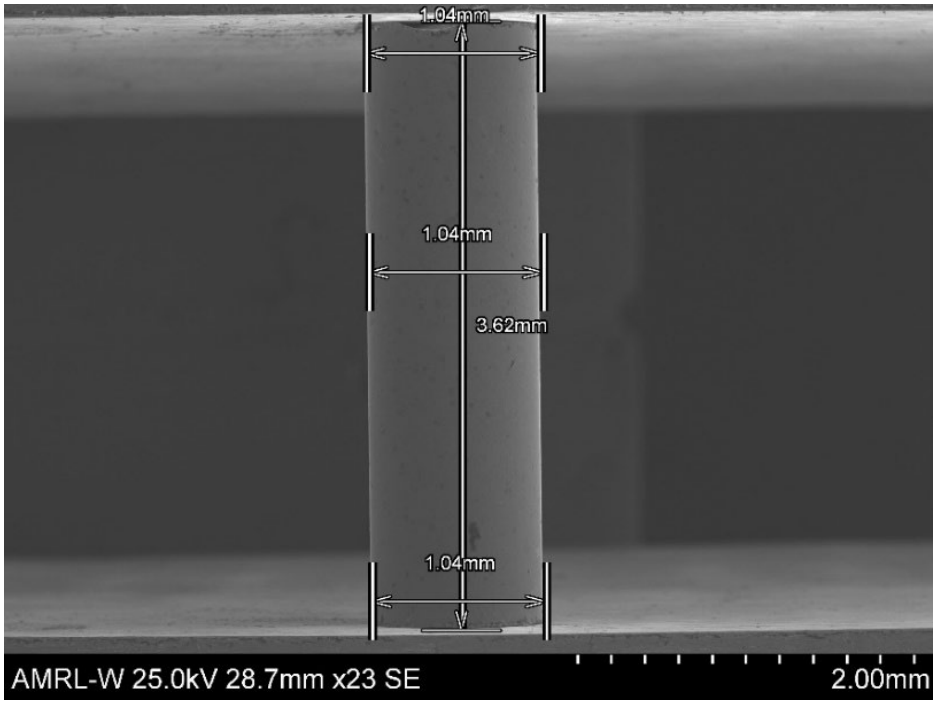

Figure 7.2 – SEM image of sample 3.5 mm with no displacement applied.

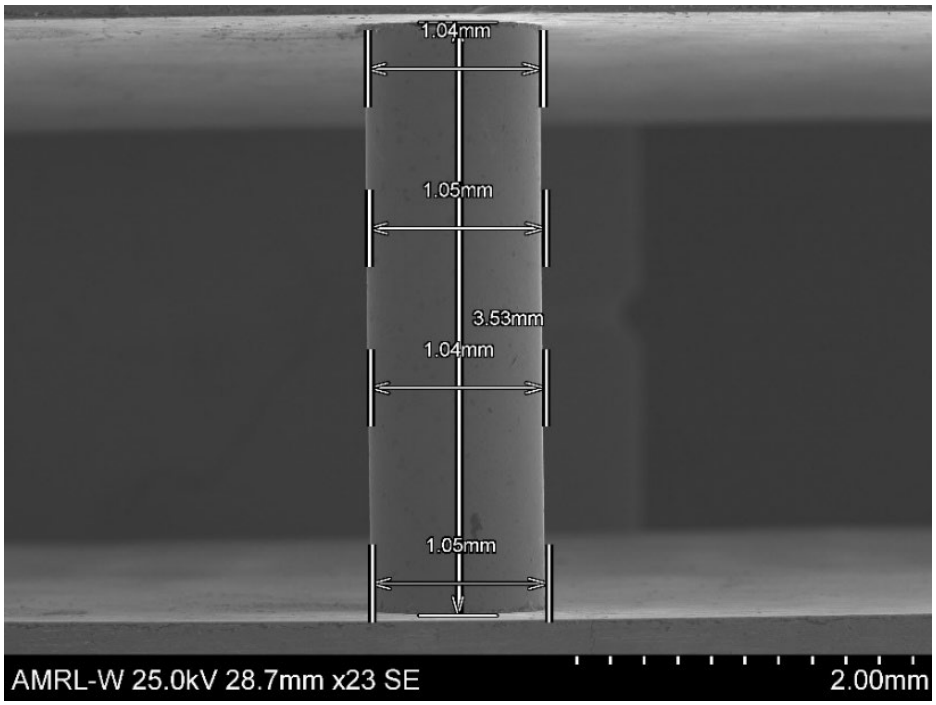

Figure 7.3 – SEM image of sample 3.5 mm with an imposed displacement of 0.09 mm (approximately 2.6 % strain)

Figure 7.4 shows the 4 mm long sample inside the SEM with the pre-load applied, but otherwise undeformed. From this image is possible to see that the length of the sample is 4.16 mm, and the diameter was 1.04 mm. Similar to the previous sample, the cursor was place in the centre of the wire to measure the sample length and for the diameter, several cursors were placed along the sample, as shown.

When loading the sample to a crosshead displacement of 0.24 mm (6% compressive strain), as in Figure 7.5, it was possible to see that the final displacement measured was 0.13 mm, this displacement is equivalent to approximately 3.25 % strain. Again, in this sample it was possible to see the compliance present in this system. When measuring the diameter, it increases at the ends of the sample by 0.01 mm and partway along the sample by 0.03 mm. These dimensions are not conclusive due to the associated errors, but it suggests the presence of friction at the ends of the sample since radial expansion is apparently suppressed. From the image it was possible to see that the sample was still under uniaxial deformation and there is no indication of other modes of deformation.

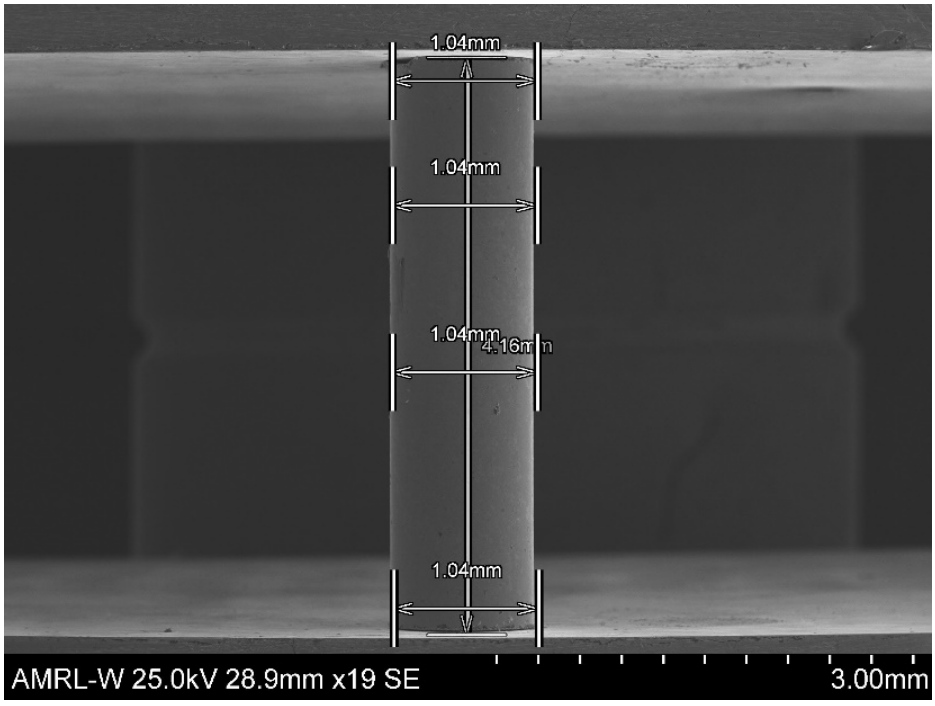

Figure 7.4 – SEM image of sample 4 mm with no displacement applied.

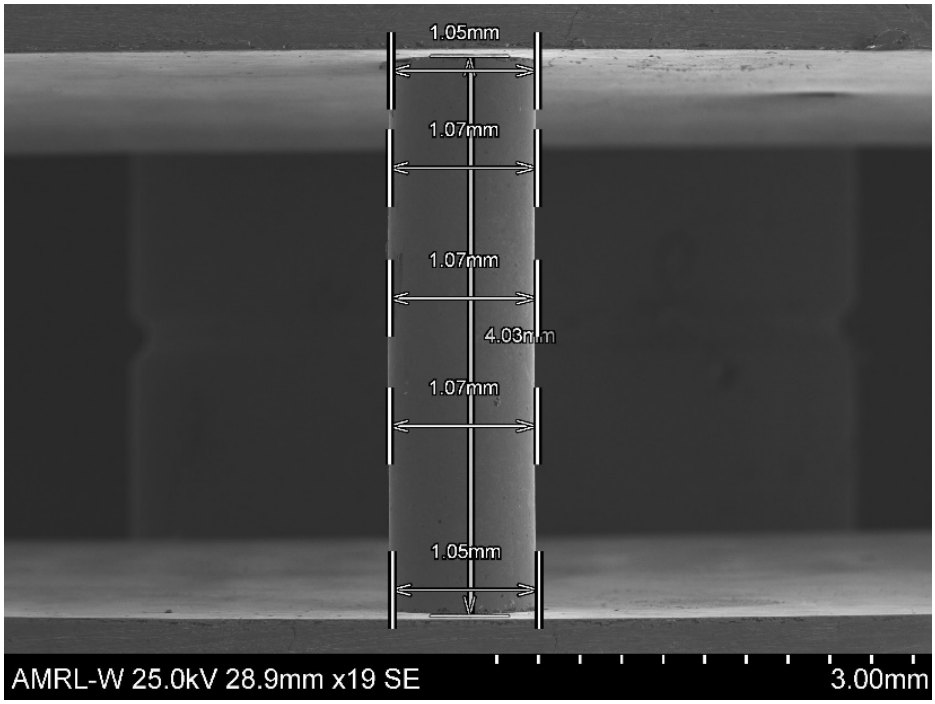

Figure 7.5 – SEM image of sample 4 mm with an imposed displacement of 0.13 mm (approximately 3.25 % strain)

In Figure 7.6 it is possible to see a permanently deformed 3.5mm long sample with no load applied after being subjected to an excessive deformation of 20 % nominal strain. This image is important in understanding how the samples are deformed during compression, since it is possible to see the behaviour of the sample when it displays other modes of deformation. After the sample is deformed to 20 % strain the permanent deformation, with the sample buckling, is clearly evident. When the sample is unloaded, the deformation is still visible along the sample length, as indicated by the white lines. This helps in validating the previous images, by understanding how the sample deforms under very high strain and is not seen in the previous images.

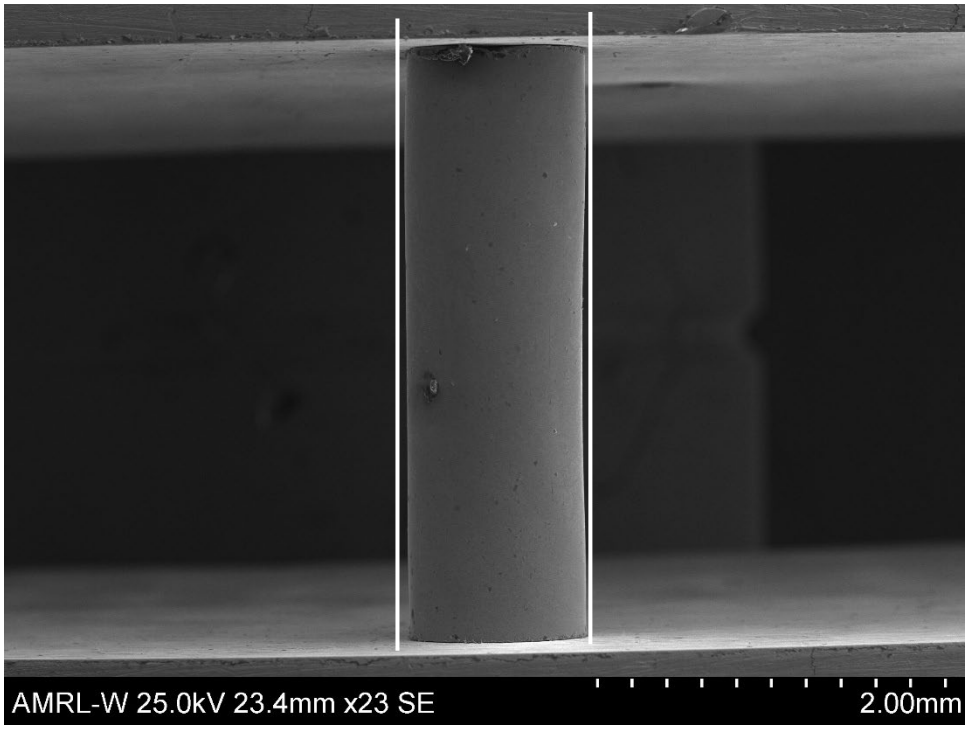

Figure 7.6 – SEM image of a 3.5 mm permanently deformed sample

To confirm the uniaxial deformation observed in the SEM, a quick estimation of the buckling load was calculated. Columns fail by buckling when their critical load is reached. The critical load is calculated using Euler's critical load (Eq. 7.1). Figure 7.7 shows the possible conditions of a compression test; with constrained ends (Figure 7.7 a)) and with pined ends (Figure 7.7 b)). In this case, because the ends of the sample remain parallel to the platens and do the sample do not rotate, it will be use the condition with both ends fixed as the more appropriate case.

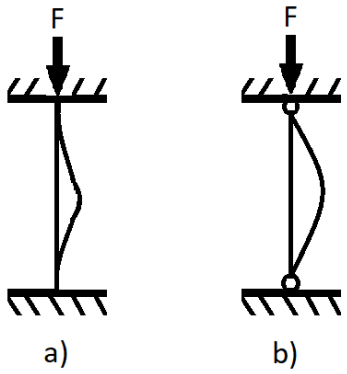

Figure 7.7 – Buckling shape of column; a) fixed in both ends b) pivoted in both ends.

$$P_{cr} = \frac{\pi^2 EI}{L_e^2} \tag{7.1}$$

$$L_e = \frac{1}{2}L \tag{7.2}$$

Where, L_e is the effective length obtained from the case in Figure 7.7 with both ends constrained. In Table 7.1 shows the value of the critic load calculated and the maximum force achieved for each sample length. Austenite elasticity was used as the elasticity modulus as it is the Martensite elasticity has a higher value, E_A=44900MPa.

Table 7.1 – Critic load for each sample length

L (mm)	Le (mm)	Pcr (N)	Fmax (N)
1	0.5	87011	470
1.5	0.75	38672	739
2	1	21753	820
2.5	1.25	13922	1020
3	1.5	9668	1050
3.5	1.75	7103	1140
4	2	5438	1200

Figure 7.8 compares the maximum load of each sample when subjected to 6% compressive strain (green line) with critical load calculated for each sample length using

equation 7.1 (blue line). From this figure it is possible to observe both curves converging but at 6% compressive strain the sample does not reach the buckling load.

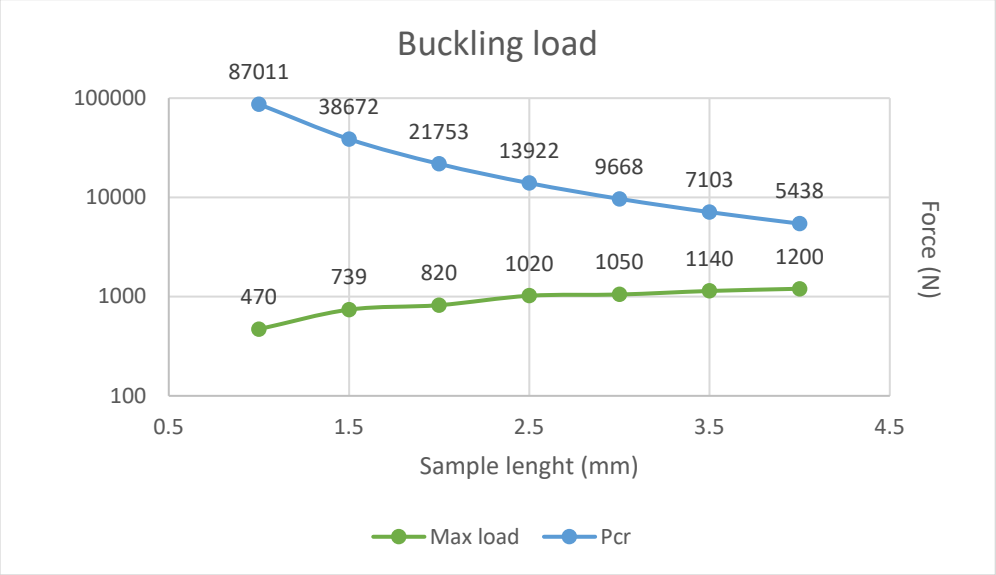

Figure 7.8 – Buckling load vs Maximum load for each sample length

Following the confirmation of the uniaxial mode of deformation in the SEM during the compressive test, it was possible to conclude that the new, longer samples of 3.5 mm and 4 mm length are also suitable for the further study of the effect of the L/D ratio.

7.3.2 Implementation of the video extensometer

During a compression test, not only the sample experience deformation. During any mechanical test, while the testing machine is subject to a force, the entire system experiences some degree of deformation, this includes the frame, load cell, couplings and specimen. This way, the raw displacement obtained from the load cell is the sum of total system deformation. [83]

The tests presented in this chapter were made using the method validated in the previous chapter, using the AMRL Instron 5969 and placing the sample vertically. To directly measure the strain during the compression test and remove machine compliance, a non-

contacting video extensometer was used. As mentioned before, the use of the extensometer is important to detect the real strain imposed on the sample during the compression loading, thus avoiding any compliance associated with the testing machine system. From Chapter 5 it was noted that the intrinsic compliance of the machine itself was adversely affecting the results, that were minimised by reducing the connectors and thus currently the strain derived from the machine displacement now should better match the displacement measured directly by the video extensometer.

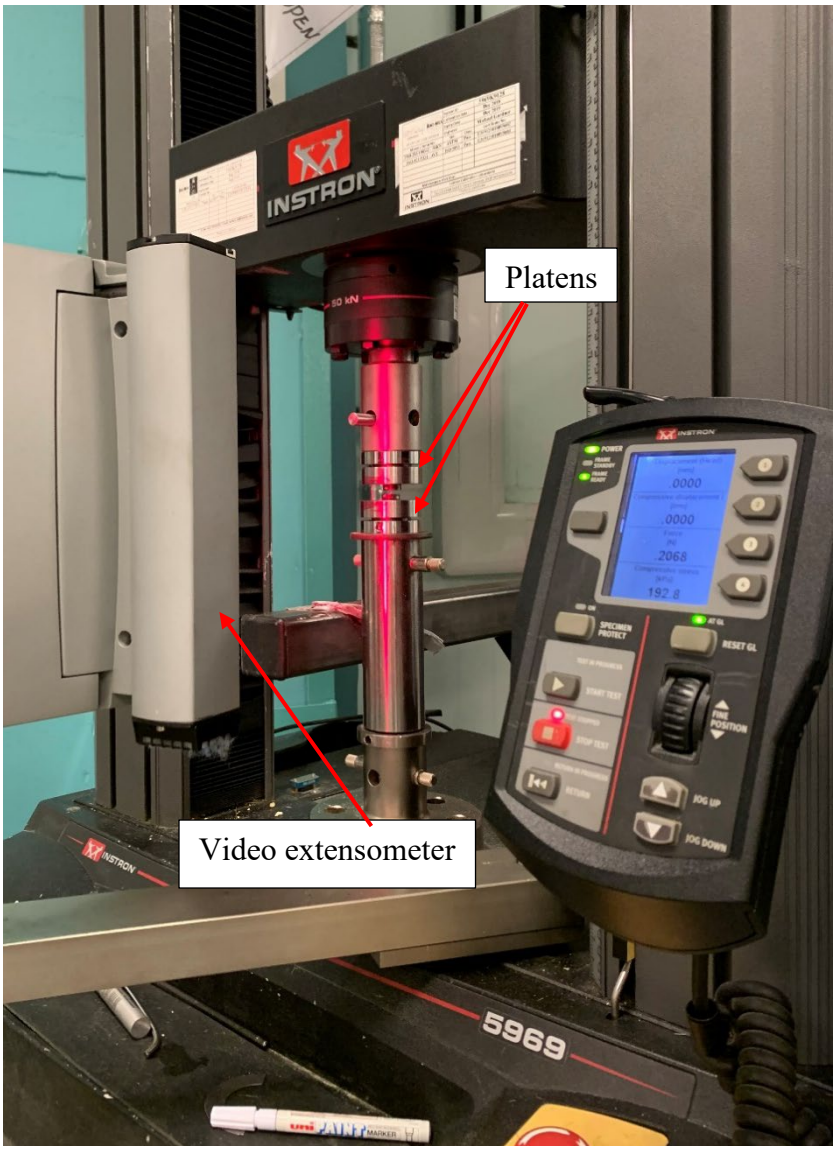

Figure 7.9 – Compression test method final setup with the video extensometer.

The video extensometer used was the Advance Video Extensometer (AVE 2) from Instron that attaches directly to the testing machine. This extensometer uses Digital Image Correlation (DIC) for strain measurement. In Figure 7.7 it is possible to see the final setup of the compression test with the video extensometer attached to the system.

To measure the strain, the extensometer follows the displacement of two white dots. Since the samples are too small to locate the dots, these were instead placed on the platens near the edge, as shown in Figure 7.10 a). The dots were placed on the platens using a white marker with a line width of 0.8 to 1.2 mm. Assuming the platens do not themselves incur any deformation during the test, the displacement of the platens is the same as the sample. Figure 7.10 b) shows how the extensometer identifies the dots and how the extensometer is calibrated for each test. From this calibration the gauge length (GL) is obtained for each sample. No filters were added to the software while obtaining the raw data from the video extensometer.

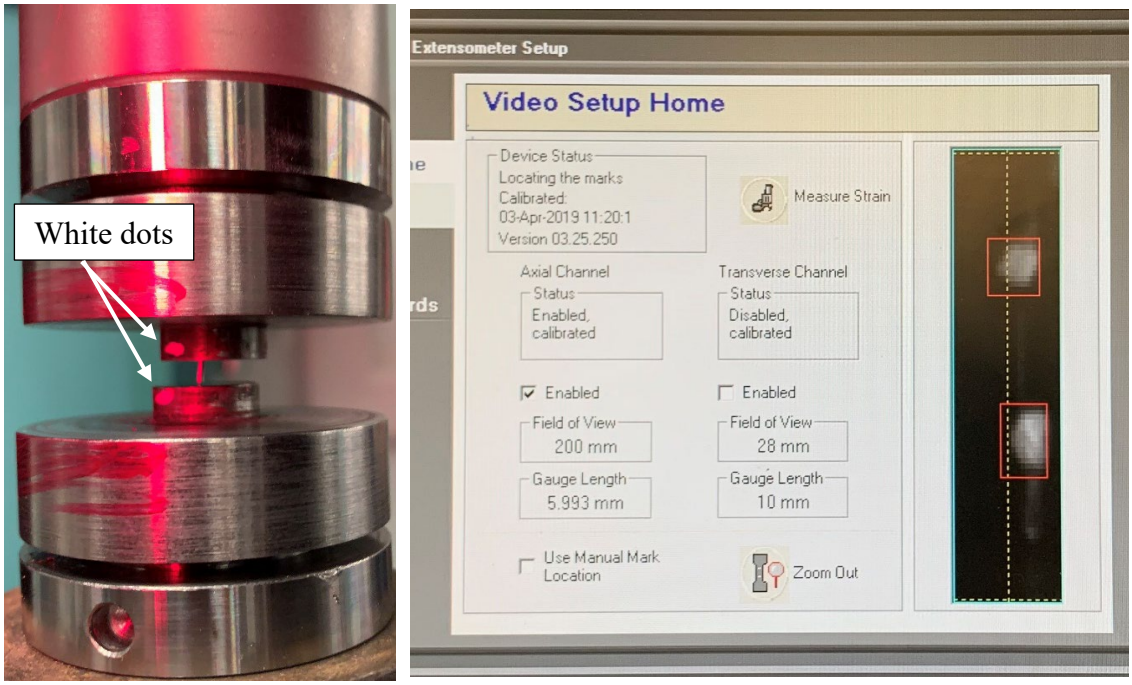

a) *b)*

Figure 7.10 – a) Detail of the compression setup with the sample placed between the platens, the red light focusing the sample from the video extensometer and with the white marks in the platens; b) software window of the video extensometer detecting the white marks in the platens and obtaining the GL for that sample.

Note that the sample shown on Figure 7.10 a) is not placed correctly. This image only serves to show the white dots on the platens and compare it with the sample.

7.3.3 Test plan

To study the effect of the sample L/D ratio, all sample sizes were tested, from 1 mm long to 4 mm long. Following the ASTM E691-19 – Standard Practice for Conducting an Interlaboratory Study to Determine the Precision of a Test Method [84], for each different length three different samples were tested. Table 7.2 lists the tests made during this study. The table shows that for each length, three different samples were tested. Also, for each sample, all different strain ranges were tested, in an ascending order, from 2% strain to 6% strain with a total of 5 tests for each sample. Finally, each test had 3 cycles, loading and unloading three times. Appendix D: has a detailed list of the tests performed at the prescribed conditions as well as the test pre-load and maximum load. To allow lateral expansion of the sample ends during the compression test, lubricant was applied to both the ends and the platens before each test.

Table 7.2 – Matrix of tests for L/D ratio study at room temperature, full list of test on Appendix C

Length (mm)	Number of Sample	Number of tests	Number of cycles
1	3	5	3
1.5	3	5	3
2	3	5	3
2.5	3	5	3
3	3	5	3
3.5	3	5	3
4	3	5	3

The samples were placed vertically between the platens with lubricant (WD40) at the sample ends. Before each test, a pre-load was applied to the sample to remove possible defects of the samples caused by the EDM cut. At the start of each test, it was necessary

to input the dimensions of each sample in the machine software to proceed with the internal calculations of strain and stress, although the raw values of the force and displacement were used to obtain the true stress and true strain during the analysis of the data, as explained later.

7.3.4 Validation of the strain measurement

Before analysing the effect of the L/D sample ratio, it was important to validate the measurements obtained from the video extensometer. In the same way as with the previous results from Chapter 5, the raw results exported from the machine are provided in a .CSV file. This file includes the information of the Time (s), Displacement (mm), applied Force (kN), Compressive Stress (MPa) and Video axial strain (%). The Time refers to each instant the machine acquired each measurement during the test. The displacement in mm refers to the distance in mm that the machine crosshead moved down, starting at the zero value at the beginning of the test. The force in kN is the force detected by the load cell at each instant of the test. Compressive stress is calculated by the machine based on the force and initial sample size inputted at the beginning of the test. Finally, Video axial strain is the strain measured by the video extensometer between the two white dots on the platens.

When comparing the stress-strain curve using the strain given by the machine displacement and video extensometer strain, two different curves are obtained. For both curves, the true stress (MPa) is calculated using equations (1) and (4) from Chapter 5. To calculate the true strain using the machine displacement, equations (2) and (3) from Chapter 5 are used as well. To obtain the true strain from the video extensometer, first it is important to understand how the strain is exported to the file containing the raw data.

Figure 7.9 shows a schematic representation of the sample between the platens with the marks (white dot) being tracked by the video extensometer, where c is the distance between the platens and v the distance between the white dots (measured by the video extensometer). Since the bottom platen is fixed in the support of the machine it does not undergo any displacement. Assuming also that the upper platen is not deformed during the test then:

$$\frac{\Delta v}{v} = \text{video strain (\%v)} \tag{7.3}$$

$$\frac{\Delta c}{c} = \text{machine strain (\%c)} \tag{7.4}$$

$$\Delta c = \Delta v \tag{7.5}$$

With the video extensometer it is possible to obtain the deformation between the white dots (eq. 7.3) and since it is assumed that the deformation measured by the video extensometer is equivalent to the deformation suffered by the sample (eq. 7.5), then it is possible to obtain the sample deformation using eq. 7.4.

The displacement measured from the video extensometer is actually exported to the file in normalised form as % strain (%v), which is equivalent to the displacement between the white marks shown in Figure 7.9 and in reference to the initial gauge length (GL) of the test (v). Initial GL of each test is known, so the required displacement was obtained by multiplying the % strain from the video extensometer by the GL to obtain the displacement in mm recorded from the video:

$$\frac{\Delta v}{v} = (\%v) \Leftrightarrow \Delta v = v \times (\%v)$$

$$\Delta v = \Delta c \Leftrightarrow (\%c) = \frac{\Delta v}{c}$$

Only at this point, can the true strain measured by the video extensometer be calculated using equations (2) and (3).

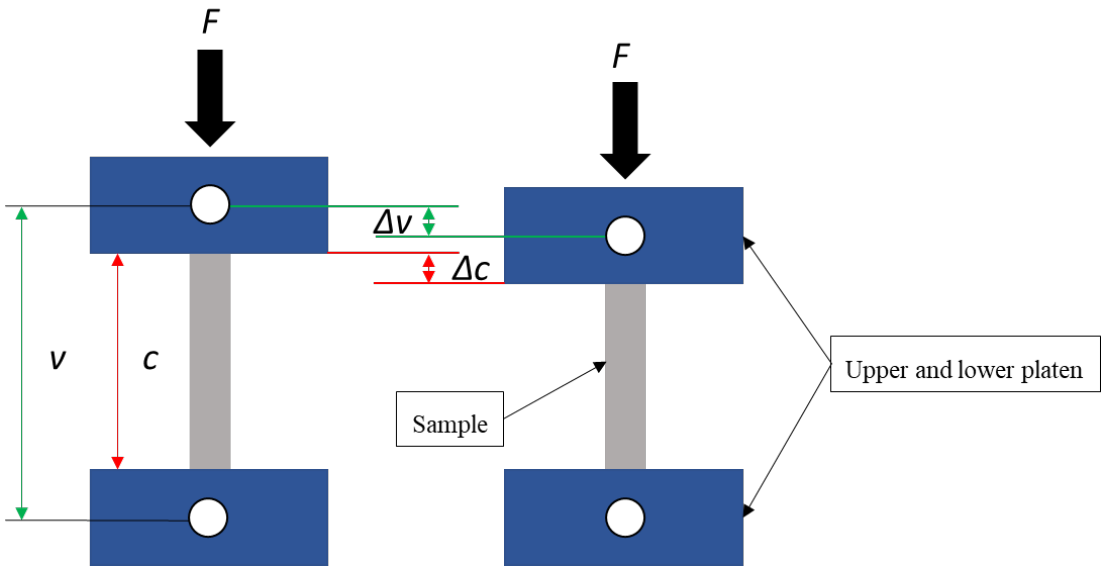

Figure 7.11 – Illustration of the compressive platens with the video extensometer marks.

The following Figure 7.12, Figure 7.13, Figure 7.14, Figure 7.15, Figure 7.16 and Figure 7.17 compare the stress-strain response obtained from a 3 mm long sample using the strain derived from machine displacement and that calculated from the video extensometer recording. This analysis compares the tested maximum strains of 2% to 6% using the same sample. For this analysis, only the last cycle of each test was considered, since it was shown in Chapter 5 that only the first cycle is slightly different from the subsequent two and also to simplify the visual representation of each response.

Figure 7.12 compares the stress-strain response at 2% strain between the strain calculated from the machine displacement and video extensometer. As explained in Chapter 5, when the 3 mm sample is loaded to 2 % strain, no transformation is visible in the stress-strain curve. Similarly, the stress-strain curve observed in Figure 7.12 also does not show any transformation using both the strains obtained from the machine and the video extensometer. Comparing now the two curves presented in the figure, the main difference observed is the initial stiffness seen in the curve. The response obtained from the video extensometer (blue line) shows a stiffer response than the machine (red line). In other words, at a nominal strain of 2%, the machine registers a maximum strain of

approximately 1.9%, whereas the video extensometer registers a maximum strain of 1.5%. The other significant difference refers to the quality of the response, where the one from the video extensometer the curve is affected by noise, unlike the response from the machine, where a well-defined line is observed.

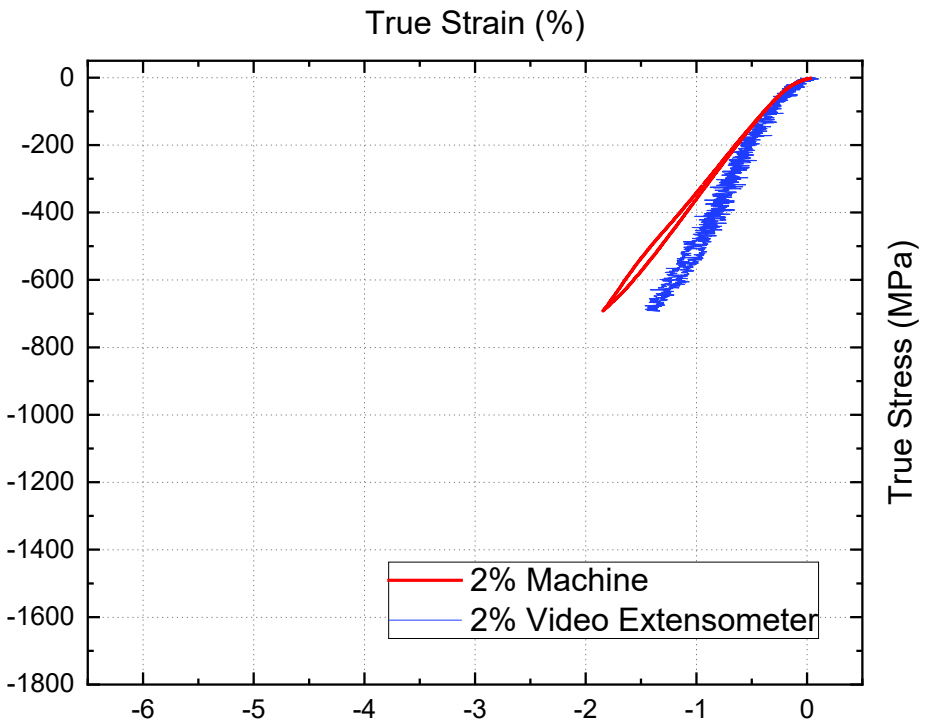

Figure 7.12 – Comparison of stress-strain response using the strain obtained from the load cell and the strain obtained from the video extensometer at 2% nominal strain.

Figure 7.13 compares the stress-strain response at 3% strain between the strain calculated from the machine (red interrupted line) and the video extensometer (blue line). At 3% strain it is possible to observe the beginning of phase change at approximately 700 MPa stress. Comparing both responses in this figure, the main difference is once more the stiffness between the two responses. Again, the response obtained from the video extensometer presents a stiffer curve from the beginning of the test, where the linear elastic behaviour shows a steeper gradient leading to a maximum strain of 2.5% when a nominal strain of 3% is imagined. Similar to the response at 2% nominal strain, the machine shows a maximum strain of approximately 2.9%, and a difference between the video extensometer and load cell of approximately 0.4% strain.

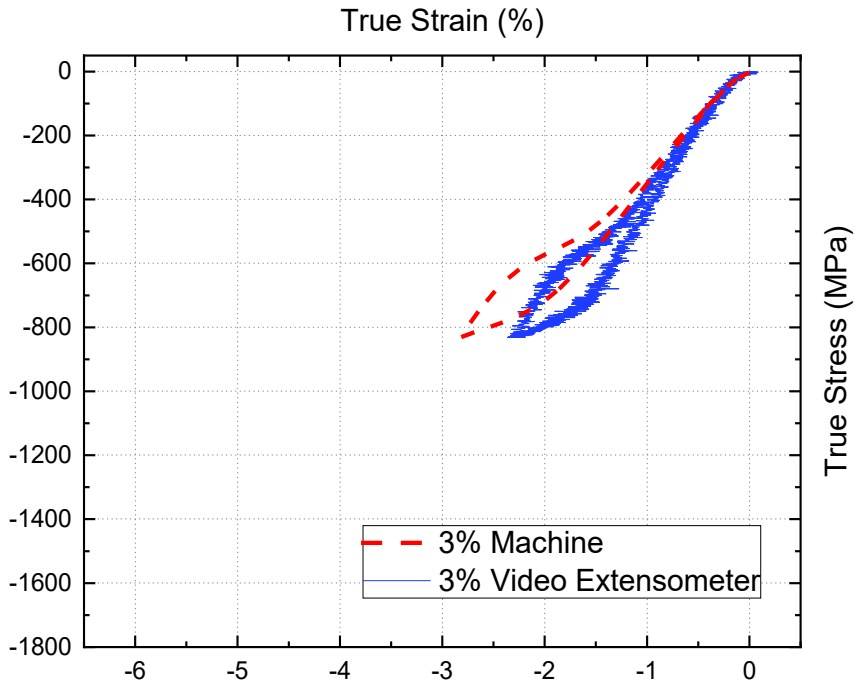

Figure 7.13 – Comparison of stress-strain response using the strain obtained from the load cell and the strain obtained from the video extensometer at 3% nominal strain.

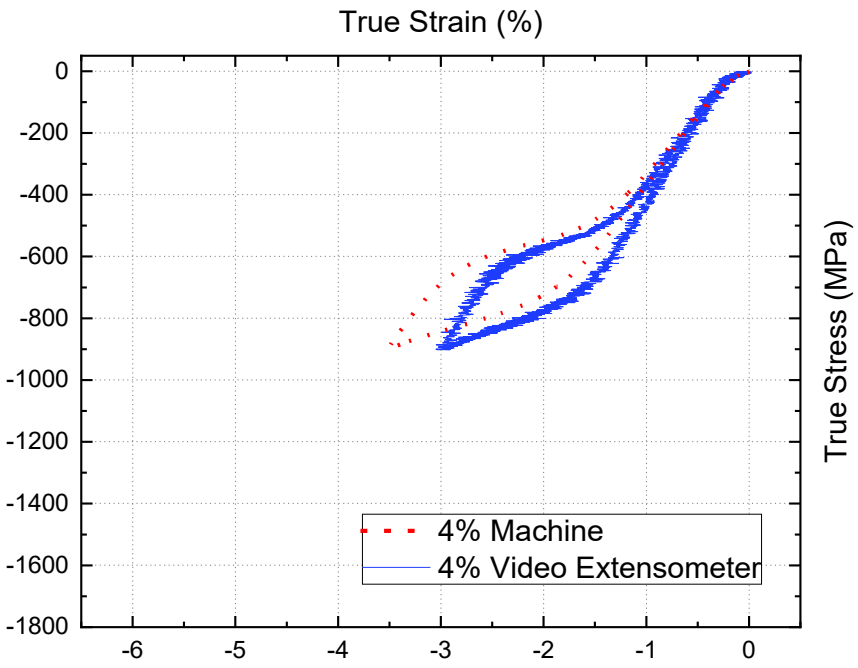

Figure 7.14 – Comparison of stress-strain response using the strain obtained from the load cell and the strain obtained from the video extensometer at 4% nominal strain.

Now looking at the stress-strain curve at 4% maximum nominal strain in Figure 7.14, which compares the stress-strain curve using the true strain calculated from the video extensometer (blue line) and from the machine displacement (red dotted line), it is possible to see that both responses exhibit similar behaviour. The main difference identified is the initial stiffness shown by the curves. The response obtained from the video extensometer presents a stiffer response that it is possible to see at the beginning of the curve. For a nominal strain of 4%, the machine detects a maximum strain of approximately 3.5% strain and the video extensometer detects a maximum strain of 3% strain. In both responses the onset of phase change is clearly visible.

Like the previous results, when comparing the response obtained from the machine displacement (red dash-dot line) in Figure 7.15 with the strain from the video extensometer (blue line) both responses are similar. Both curves present an almost complete phase transformation while the only difference is the shift to the right side of the red line, showing that the blue line, from the video extensometer, presents a stiffer response from the beginning of the curve. At a 5% nominal strain, the maximum strain induced by the machine it is approximately 4.8% strain, whereas maximum strain detected by the video extensometer is 4.2% approximately.

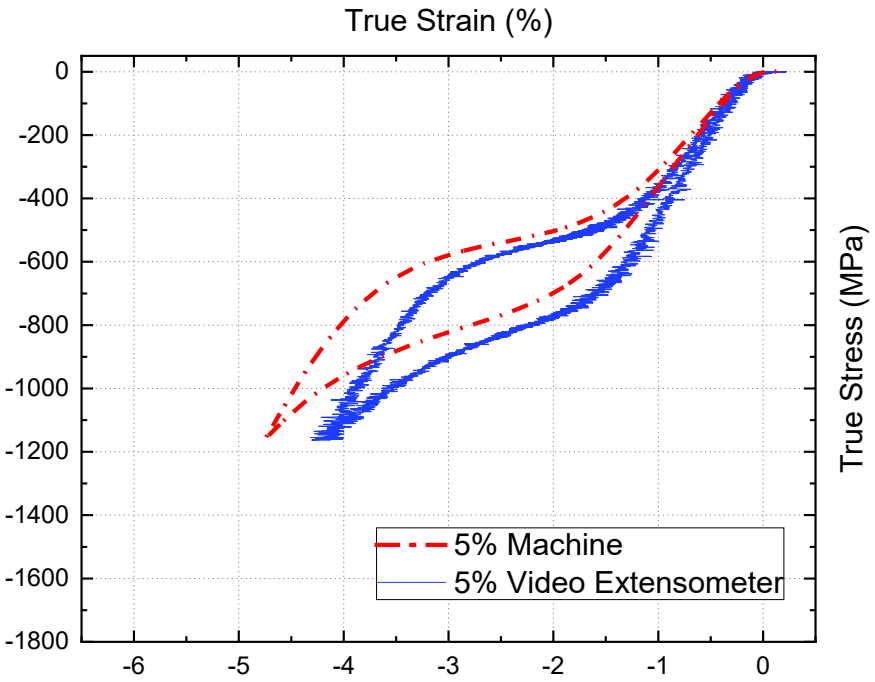

Figure 7.15 – Comparison of stress-strain response using the strain obtained from the load cell and the strain obtained from the video extensometer at 5% nominal strain.

Finally, when looking at the 6% maximum nominal strain response in Figure 7.16, the same behaviour is shown when comparing the responses obtained from the machine (red dash-dot-dot line) and the video extensometer (blue line). A complete phase transformation is detected on both responses, as well as linear elastic behaviour both during the austenite and martensite phases. The stiffness is higher when looking at the curve from the video extensometer, where for a nominal strain of 6%, the maximum strain detected is approximately 5.1%, as opposed to the curve from the machine, where the maximum strain detected is approximately 5.6%.

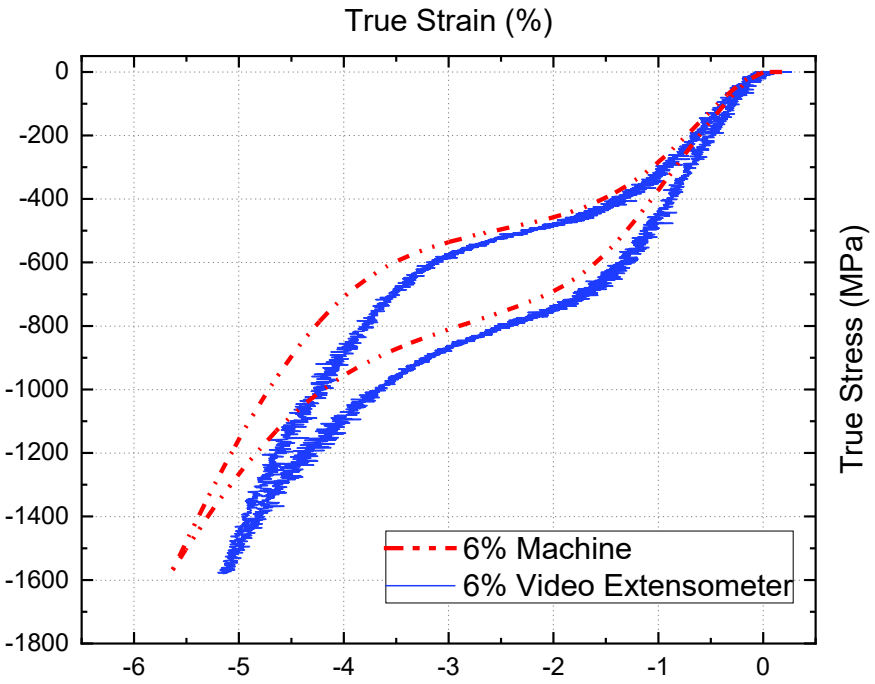

Figure 7.16 – Comparison of stress-strain response using the strain obtained from the load cell and the strain obtained from the video extensometer at 6% nominal strain.

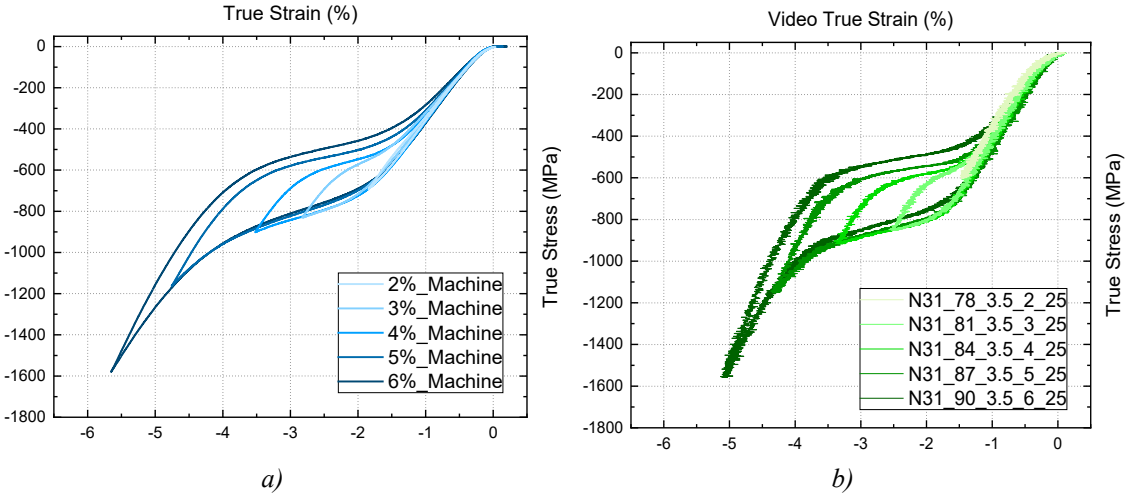

a) *b)*

Figure 7.17 – Comparison of stress-strain curve during strain evolution for a) true strain calculated from the machine displacement; b) true strain calculated from the video extensometer.

Figure 7.17 compares the strain evolution for the 3 mm sample length of the strain obtained from the machine displacement, Figure 7.17 a), and the strain obtained from the video extensometer, in Figure 7.17 b). From this figure it is possible to observe a consisting loading path using both strain measures, with the video extensometer showing a stiffer response initially along the strain evolution.

When comparing the strain-stress measurements using the machine load cell and the video extensometer, it is possible to observe that the response obtained from the video extensometer is associated with noise, this noise is associated with possible ambient light changes or reflections on the measurement marks, as the test set up was not in a close environment.

From the previous analysis it is possible to assume the results obtained from the machine as valid results by comparing with the results obtained from the video extensometer. When measuring the strain field during the compressive loading, a similar response is obtained for each maximum strain. The main difference detected is the initial stiffness of the sample, which is higher than the one based on the machine displacement. This stiffness remains constant with the increase in maximum applied strain, albeit with an approximate constant difference of 0.5% in maximum strain between the machine and the video extensometer-based responses.

Although the video extensometer an accurate measure of the strain deformation because it removes the machine compliance, throughout the following studies, the response obtained from the machine will be used due to it being a smoother response with reduced noise. All tests were performed using video extensometer, when using the stress-strain curve for the numerical models, the raw data obtained from the video extensometer will be used.

7.3.5 Results from L/D ratio study

After validating the use of machine displacement with the use of the video extensometer during the compression tests, it is possible to start analysing the results for the effect of the L/D ratio and understand how it affects the results. As mentioned previously, for each

sample, the test is finished after 3 cycles, each cycle equals complete loading and unloading the sample. For this study, the temperature used was the laboratory room temperature that ranged from 24˚C to 25˚C and for each test, lubricant was placed at the ends of the sample to avoid friction forces throughout. The complete list of the tests performed is presented in 9.4 Appendix D:

Due to the great quantity of the results obtained, only some will be shown in this work, also only the last cycle of each test will be presented to simplify the presentation of the results. Finally, the results presented in this section were obtained using the true strain calculated from the recorded machine displacement. This is due to the response obtained from the machine showing very little noise compared to the curve obtained from the video extensometer, thus, easier qualitative interpretation of the responses.

The results shown in this section will look in detail at the repeatability of the test, will compare the sample length influence for each level of nominal strain applied and finally will look at the strain evolution.

Starting with Figure 7.18, this shows the stress-strain curve for the 4 mm long sample tested to 6% nominal strain. The figure compares the three different samples of length 4 mm tested, where it is possible to see that the test still shows good repeatability when testing these longer samples. The stress-strain responses shown in this figure have only minor differences between the 3 samples, sample 2 (red dash line) shows a small delay at the starting of the transformation both during the loading and unloading elastic behaviour in the austenite phase. On the other hand, sample 3 (blue dot line) presents a higher maximum stress than the other samples, with an increase of approximately 100 MPa. Nevertheless, looking at all curves, both upper and lower plateaux have similar duration as well as the same slope of the linear elastic behaviour during the martensite phase.

In general, all samples of each particular length investigated exhibit similar consistency as the curves presented in Figure 7.18. This demonstrated the repeatability of the test during the L/D ratio study.

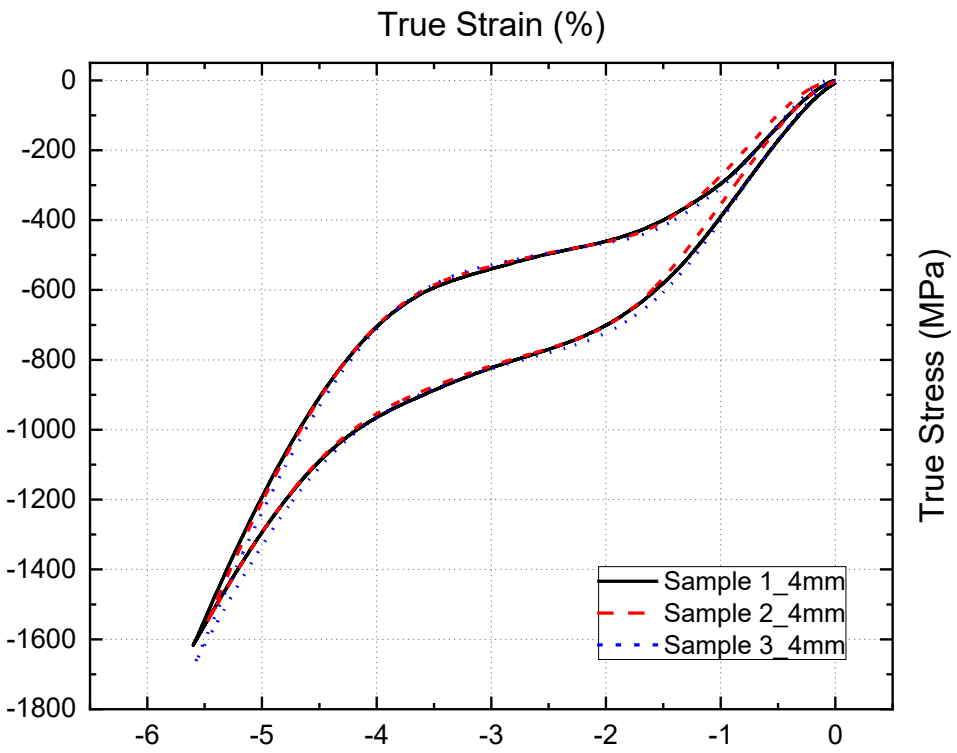

Figure 7.18 – Stress-strain curve of three different 4 mm sample long compressed to 6% nominal strain

Analysing now the strain evolution for a 4 mm sample length, only the response of one sample is shown here since repeatability was already demonstrated in Figure 7.18.

Figure 7.19 it shows the stress-strain response of the strain evolution for the 4 mm long sample, with an L/D ratio of 4. The strain evolution follows the same loading and unloading path while increasing the strain. For 2% nominal strain (continuous line) the stress-strain curve does not show any phase transformation. The maximum stress at 2% strain is 800 MPa and an equivalent maximum force of 600 N. For 3% nominal strain (dashed line) the phase transformation starts but only the initiation of the upper plateau is visible, and the maximum stress reaches 900 MPa approximately (maximum force of 660 N). During loading the 3% strain curve follows the same loading path as the previous test, until 2% strain beyond which the transformation is visible, starting at 2.5% strain approximately. For 4% nominal strain (dash-dot line) it is possible to observe the

continuation of the 3% strain curve. The hysteresis from the phase transformation is shown in the curve but it is not clear that the full transformation from austenite to martensite has occurred. The upper plateau starts at 2.5% approximately and finishes at the maximum strain of 4% with a maximum stress of 1000 MPa, with a maximum force of 730 N. At 5% nominal strain (dash-dot-dot line) it is possible to observe the beginning of the linear elastic behaviour during the martensite phase, indicating that the material is fully transformed at 5% strain. The curve follows the same loading path as the previous strains with the upper plateau starting at 2.5% strain and finishing at 4% strain. The maximum stress at 5% strain is 1200 MPa with a maximum force of 900 N.

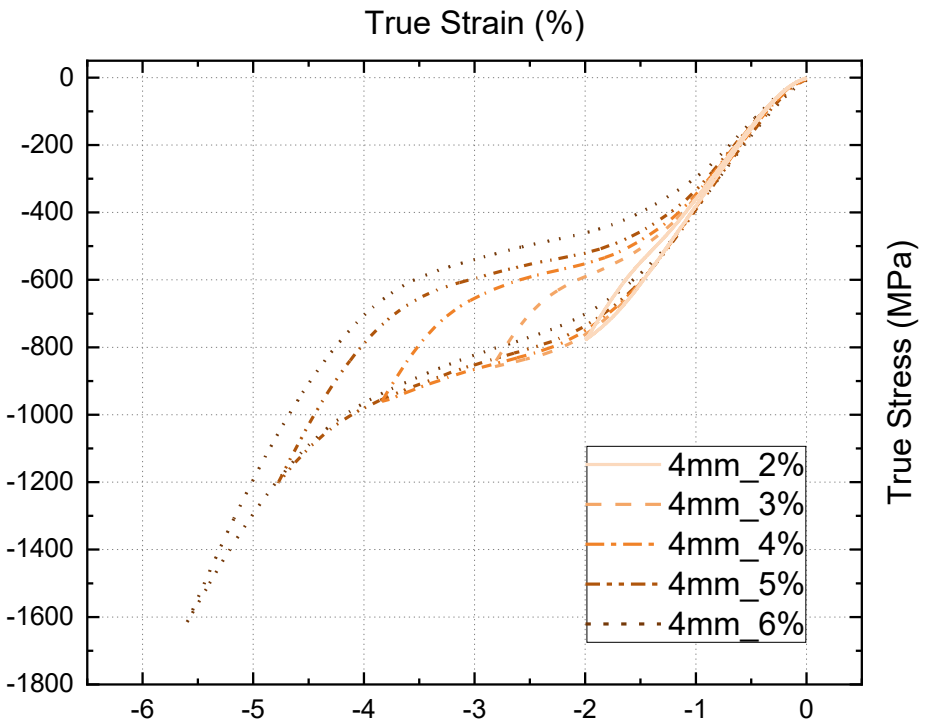

Figure 7.19 – Stress-strain response of strain evolution for 4 mm sample long

The lower plateau starts at approximately 3% strain, at 600 MPa and finishes at 2% strain with a corresponding decrease in stress in 100 MPa, followed by the linear elastic behaviour in austenite. For 6% nominal strain (dotted line) the curve follows the same loading path as the previous strain until 5% strain. At this point the material displays linear

elastic behaviour in the martensite phase, meaning the sample is fully transformed from austenite to martensite. The upper plateau starts at 2.5% strain with a stress of 800 MPa and finishes at 4% strain, with an equivalent stress of 1000 MPa. The maximum stress at 6% strain is 1600 MPa with an equivalent maximum force of 1200 N. The lower plateau during unloading follows the linear elastic behaviour upon unloading during the martensitic phase. The lower plateau starts at 3.5% strain approximately and at 600 MPa, it finishes at 2% strain approximately with a decrease in stress of 200 MPa. The response finishes with the linear elastic behaviour during unloading during the austenitic phase reaching 0% strain indicating that the sample does not incur any residual strain during this compressive test.

After analysing the strain evolution of 4 mm sample length, the same analysis was made for all different sample length, and it was possible to observe the strain evolution in all different sample length. To avoid repetition of the results, the analysis of the strain evolution for all sample length are reported in Appendix D.

After analysing how the strain evolution behaves for the different sample lengths, it is possible to see that it follows the same loading path at any given sample length. However, looking at an L/D ratio of 1, it is obviously not possible to obtain valid results when loading the sample up to 6% strain. For ratios higher than 1 it is possible to obtain more valid results with the main difference between them being the stress values.

Looking now at specific strain it is possible to understand and compare how the stress-strain response changes by varying the L/D ratio of the sample. In this section, the effect of L/D for each maximum nominal strain will be studied in detail where in each figure the scale is now adjusted appropriately for each different strain so that the curves are more readily visualised.

Figure 7.20 compares the stress-strain response at 2% strain for all the different sample lengths. From the previously presented results, it is expected that at 2% strain no transformation is visible and Figure 7.24 confirms this. Nevertheless, it is possible to see that with the increase in the L/D ratio, the linear elastic behaviour is more evident. For the

1 mm long (simple line) sample, the curve is almost a flat line, suggesting that the sample behaves in an excessively compliant manner. For the 1.5 mm long sample (line with square) it is visible that the sample is responding more consistently and exhibiting a more evident linear elastic behaviour but still overly compliant, and the stress-strain response also presents some curvature, but the sample only reaches a maximum stress of 200 MPa. A similar response is visible for the 2 mm long sample, where more consistent linear elastic behaviour is visible but with an unexpectedly low maximum stress value. Looking at the response given for the 2.5 mm long sample, the curve shows clear linear elastic behaviour during the austenite phase with a maximum stress of approximately 450 MPa. Finally, for 3, 3.5 and 4 mm sample long, the stress-strain response is almost identical for all. Here the curves now show a consistent response with higher slope and the three samples reach the same maximum stress of 700 MPa.

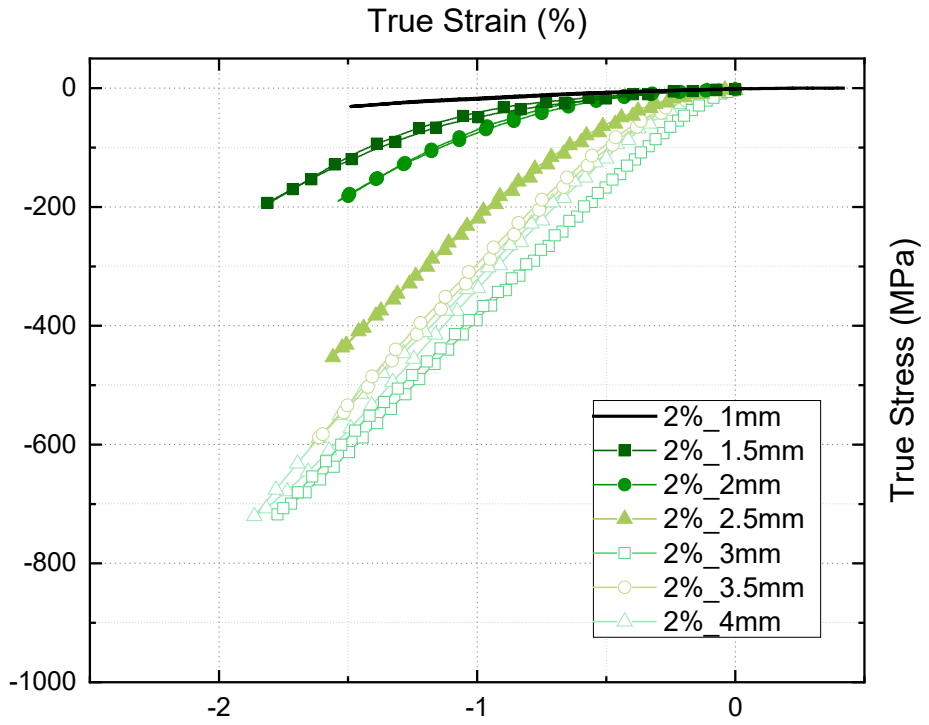

Figure 7.20 – Stress-strain response of the sample length evolution at 2% nominal strain.

Figure 7.21 and Figure 7.22 compares the stress-strain response for 3% nominal strain and 4% nominal strain for all of the different sample lengths respectively. Comparing both figures, it is possible to observe immediately that in both cases the phase transformation is initiated at longer sample lengths, albeit with the transformation response being progressed more at 4% strain than at 3%. For the sample with an aspect ratio of 1 (single line) both figures show an unexpectedly high compliance with a maximum stress of 150 MPa at 3% and 300 MPa at 4% strain. For 3% strain, both 1.5 and 2 mm sample lengths present similar stress-strain responses with overly compliant linear elastic behaviour being shown in both curves. For the 1.5 mm long sample the maximum stress at 3% strain is 350 MPa approximately and for the 2 mm long sample the maximum stress at 3% strain is 600 MPa. The same is observed at 4% strain, where both 1.5 and 2 mm long samples have similar curves but the maximum stresses are closer to each other, where for 1.5 mm sample a stress of 700 MPa is registered and for 2 mm it is 800 MPa.

Analysing the stress-strain curves for 2.5 mm to 4 mm long samples at both 3% and 4% nominal strain it is evident that the curves follow a similar path. The 2.5 mm sample long is the only curve that shows slight differences when compared with the higher sample aspect ratios.

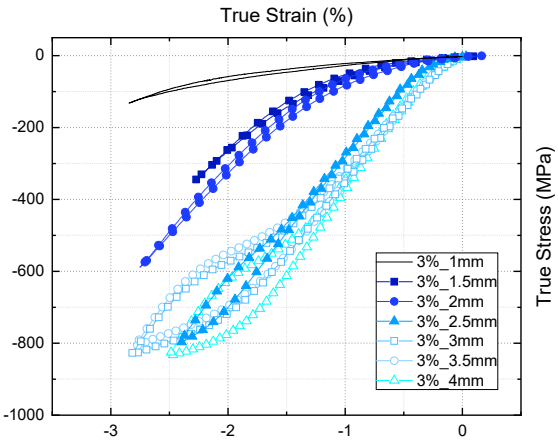

Figure 7.21 – Stress-strain response of the sample length evolution at 3% nominal strain

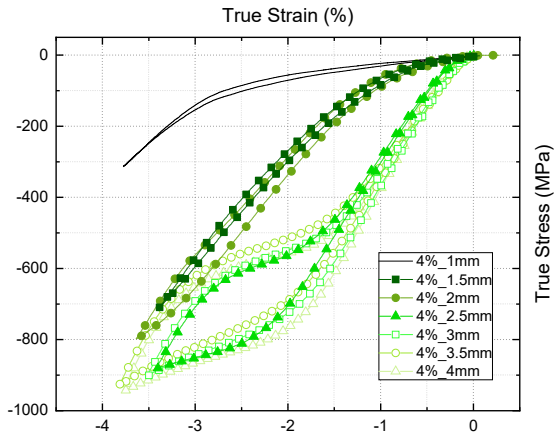

Figure 7.22 – Stress-strain response of the sample length evolution at 4% nominal strain

From the results shown in Figure 7.21 and Figure 7.22 it is thus possible to see a tendency for the stress-strain curve to converge as the L/D ratio increases. Furthermore, looking at higher maximum strains in Figure 7.23 and Figure 7.24 it is possible to confirm the tendency of the stress-strain curves to converge with the increase of the sample length. Visually, it is possible to classify 3 different groups of tests with the same curve. For the 1 mm long sample, the curve is different from all other lengths, where only an overly compliant response in the elastic region of austenite is visible, this is the first group. The second group is formed by samples 1.5 and 2 mm long. With the increase in strain, it is possible to see that the response is very similar for the two lengths. Finally, the last group is formed by samples from 2.5 to 4 mm long. With the increase in strain, it is evident that these samples display the same curve. In this way, it is possible to say that in this group are presented the best sample length ratio to use in compression loading of nitinol wire. It is evident that the accuracy of the strain measures increases as the samples get longer since they become more compliant and the associated displacements greater.

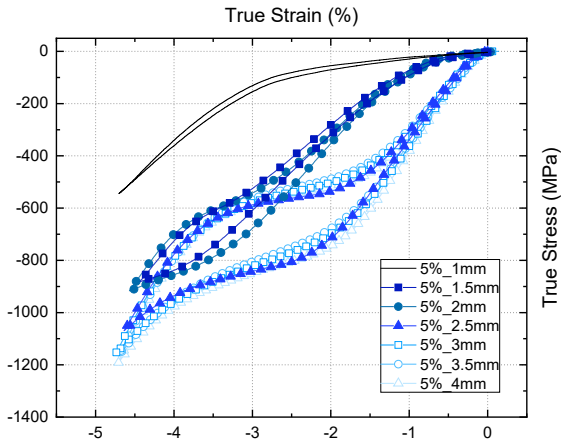

Figure 7.23 – Stress-strain response of the sample length evolution at 5% nominal strain

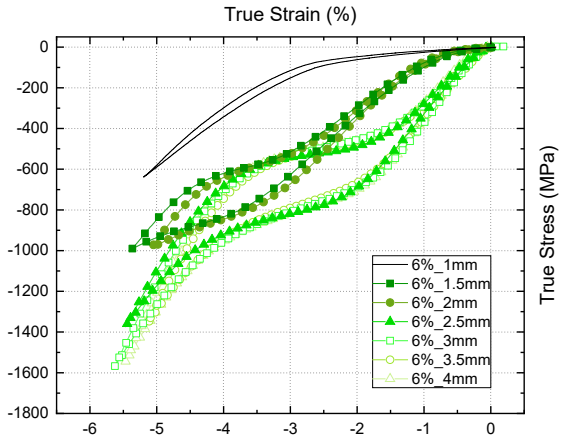

Figure 7.24 – Stress-strain response of the sample length evolution at 6% nominal strain

From this study it is possible to confirm that the effect of the L/D in the stress-strain response is a consequence of the test method. When looking at material stiffness, as shorten the sample is the stiffer the material gets, and this is due to a geometry consequence as the stiffness is inversely proportional to the sample length (1/L). During the compression test, the machine presents a fixed stiffness, intrinsic to every test machine,

this way, when testing nitinol wire under compressive loading, as the sample gets shorter, the material stiffness increases and the increase is not a linear increase, so when testing very short samples (1 mm length), the machine is not able to determine the stress-strain response. The machine stiffness was not calculated in this work, but analysing Figure 7.20, Figure 7.21, Figure 7.22, Figure 7.23, Figure 7.24 it is possible to see the results converging with the increase of the sample length and this increase is not linear as well, due to the inverse proportionality of the material stiffness to the sample length.

7.4 Study 2 – Temperature effect

For the temperature effect the same setup was used as previously with the addition of the environmental chamber. The chamber used was the one available at the University's advanced materials research laboratory (AMRL). As seen in Figure 7.25, to adapt the environmental chamber to the compression test setup, new supports needed to be added to fit the platens inside the chamber, this is due to the size of the chamber, where the load cell is outside of the environmental chamber. These new connecters made it possible to perform the test within the environmental chamber, ensuring the test was performed in a controlled temperature environment. The temperature used in this study was 37˚C – human body temperature and thereby the in-service temperature of the stent graft medical device. The samples used to test nitinol wire under compression loading at elevated temperature had a length of 2.5 mm and 4 mm. These particular lengths were chosen based on the conclusions from the L/D sample ratio since they represented the shortest and longest lengths of the third sample group.

Figure 7.25 shows the final setup of the compression test with the inclusion of the environmental chamber. Due to the limitation of the available connectors, the sample is not placed in the middle of the environmental chamber. This prevents the use of the video extensometer because the sample is covered by the chamber's door during the test. For this study, three samples of 2.5 mm length and two samples of 4 mm length were tested. Due to the lack of relevant information when testing the samples up to 3% nominal strain

under compressive loading, this study only considered the maximum nominal strains of 4%, 5% and 6%. Table 7.2 details all the tests performed at a temperature of 37˚C.

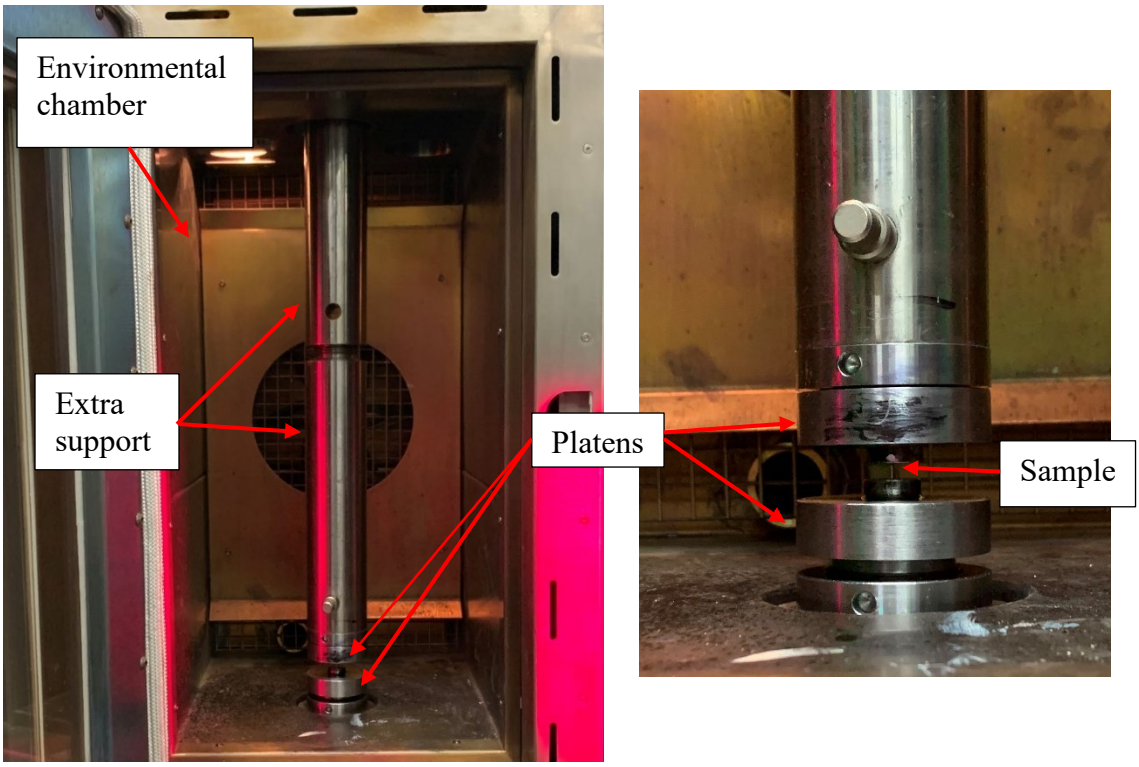

Figure 7.25 – a) Setup of the compression test inside of the environmental chamber with the extra supports; b) detail of the sample between the platens inside the environmental chamber.

7.4.1 Results

The data for the following responses were obtained in the same way as before. As mentioned previously, the video extensometer was not used during the compression tests at higher temperatures, 37˚C. These results aim to understand the behaviour of the nitinol wire under compression loading at 37˚C with emphasis on the strain evolution and repeatability of the test and will also compare responses at both temperatures of 25˚C and 37˚C when other test conditions are the same.

Table 7.3 – List of compression tests for temperature of 37˚C

Test	Sample	Name	Strain (%)/(mm)		L_S (mm)	T (°C)	Li (mm)
1	T22	T22_108_2.5_4_37	4%	0.1	2.5	37	2.49
2	T22	T22_109_2.5_5_37	5%	0.125	2.5	37	2.49
3	T22	T22_110_2.5_6_37	6%	0.15	2.5	37	2.49
4	T25	T25_114_2.5_4_37	4%	0.1	2.5	37	2.49
5	T25	T25_115_2.5_5_37	5%	0.125	2.5	37	2.49
6	T25	T25_116_2.5_6_37	6%	0.15	2.5	37	2.49
7	T26	T26_117_2.5_4_37	4%	0.1	2.5	37	2.49
8	T26	T26_118_2.5_5_37	5%	0.125	2.5	37	2.49
9	T26	T26_119_2.5_6_37	6%	0.15	2.5	37	2.49
10	T26	T26_120_2.5_7_37	7%	0.175	4	37	2.49
11	T50	T50_121_4_4_37	4%	0.16	4	37	4.00
12	T50	T50_122_4_5_37	5%	0.2	4	37	4.00
13	T50	T50_123_4_6_37	6%	0.24	4	37	4.00
14	T50	T50_124_4_7_37	7%	0.28	4	37	4.00
15	T51	T51_125_4_4_37	4%	0.16	4	37	4.00
16	T51	T51_126_4_5_37	5%	0.2	4	37	4.00
17	T51	T51_127_4_6_37	6%	0.24	4	37	4.00

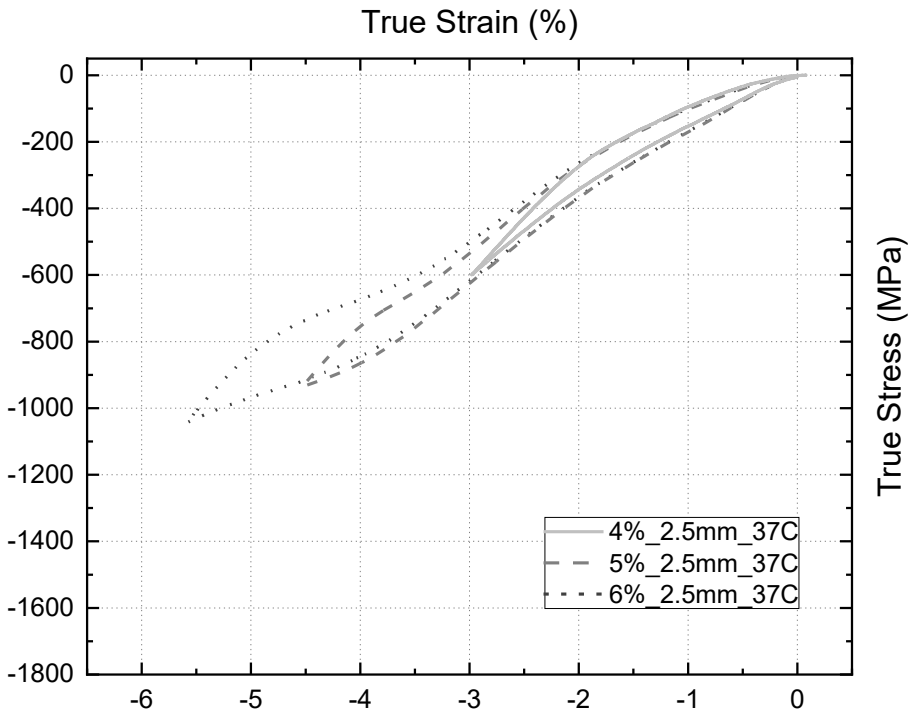

Figure 7.26 – Strain evolution of 2.5 mm sample long at 37˚C

Starting with the results presented in Figure 7.26, it shows the response for strain evolution using the 2.5 mm long sample at 37˚C. At 4% nominal strain (continuous line), the curve does not present any phase transformation, just the linear elastic behaviour during the austenitic phase both during loading and unloading. From this response it is possible to see that during unloading the path is different from the loading path, re-joining the loading path only at 0.5% approximately. The maximum stress obtained at 4% strain is 600 MPa. At 5% nominal strain (dashed line) the loading path of the stress-strain curve is the same as for the previous maximum strain. At this strain value it is possible to see the start of the phase transformation where it commences at approximately 4% strain. At maximum strain, the sample registers a stress of approximately 900 MPa, from where it starts unloading. The unloading path from 5% nominal strain is almost linear but having a different path from loading. This unloading path joins the same path as the 4% nominal strain, where the curve again closes at approximately 0.5% strain. For the last test, the 6% nominal strain (dotted line) response shows the phase transformation more advanced. The

curve follows the same loading path as the previous maximum strains and a small upper plateau is visible after 4% strain. At 6% strain the curve does not display a fully transformed martensitic phase and the maximum stress obtained is approximately 1050 MPa. During unloading, the lower plateau is barely identifiable between 4.5% strain and 4% strain. At this point the unloading path starts following the same as the previous nominal strains, again with the loading and unloading path joining at 0.5%.

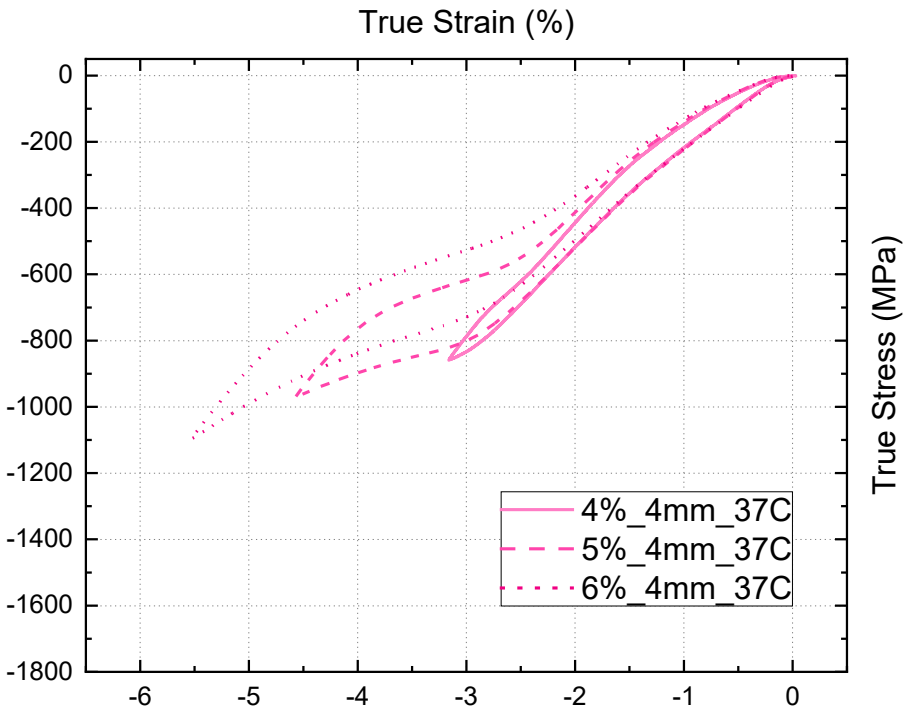

Figure 7.27 – Strain evolution of 4 mm sample long at 37˚C

When analysing the strain evolution of the 4 mm long sample in Figure 7.27 it is possible to see that for 4% nominal strain (continuous line), the stress-strain curve is similar to that obtained for the 2.5 mm long samples, where no phase transformation is visible and the loading and unloading paths are different. The maximum stress at 4% strain for the 4 mm long sample is approximately 900 MPa. At 5% nominal strain (dashed line), the stress-strain curve follows the same loading path as the previous curve. The phase transformation starts with the creation of the upper plateau at 3% strain until the maximum measured

strain of 4.5%. The plateau has a corresponding increase in stress of almost 200 MPa and the curve reaches a maximum stress of 1000 MPa. During unloading the lower plateau starts at 3.5% strain approximately and finishes at 3% strain with an accompanying decrease in stress of 100 MPa. After this point the unloading path follows the same unloading path of the 4% strain curve. At 6% nominal strain (dotted line) it is possible to observe a more developed phase transformation, but it is not clear that linear elastic behaviour during the fully martensitic phase is reached. The curve follows the same loading path as the previous strains until 2% strain. At this point it is possible to see the initiation of the phase transformation, where the upper plateau starts at approximately 3% strain and continues until the end of the test at 6% nominal strain with an increase in stress of 300 MPa. The maximum stress at 6% nominal strain is 1100 MPa. During unloading the lower plateau goes from 4% strain to 3% strain with a decrease in stress of approximately 200 MPa. Similar to the previous curves, at 2% strain the curve follows the same unloading path as the previous curves, this being different to the loading path.

Figure 7.28 compares the stress-strain curve between the 2.5 mm sample long and the 4 mm long sample, at 6% nominal strain. From this figure is possible to analyse the repeatability of the test and compare the responses for the different sample lengths. From the figure it is possible to see that for 2.5 mm long the responses of the three different tests are identical (continuous line, dashed line and dash-dot line). The same behaviour is visible for the 4 mm long sample (dash-dot-dot line and dotted line), when analysing the responses of the two different samples at 6% strain the curves follow similar loading and unloading paths. Although the repeatability is evident for each sample when compressed up to 6% nominal strain, the similarity of the curves between the two different sample lengths it is not visible, as mentioned in the results from L/D ratio study section in Figure 7.24.

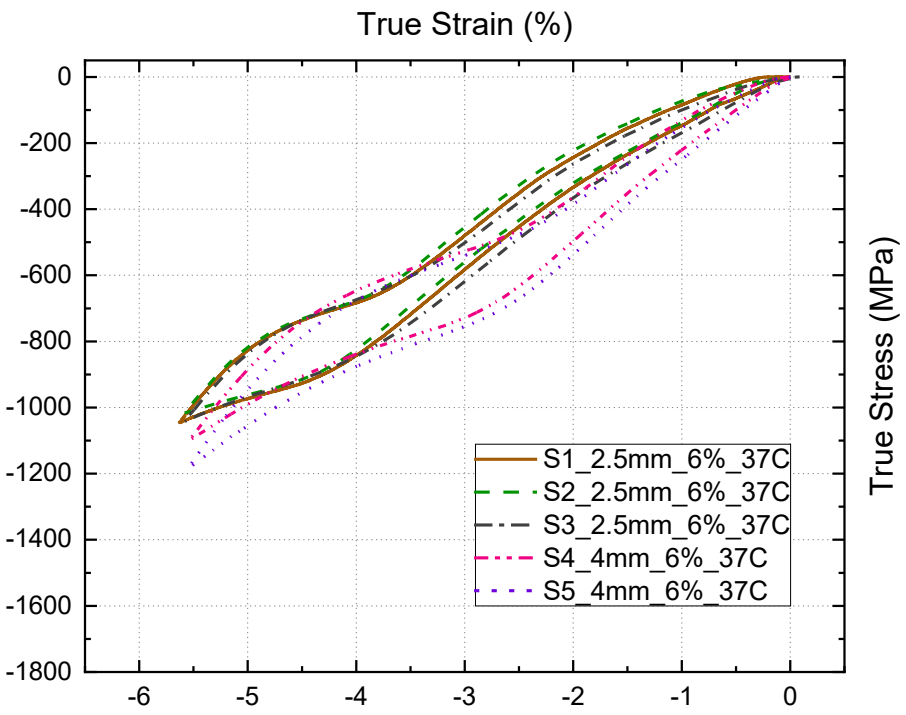

Figure 7.28 – Comparison of the stress-strain response of 2.5 mm and 4 mm sample long at 6% strain and 37˚C temperature.

Comparing now the stress-strain curves between the two different temperatures it is possible to conclude that the responses differ considerably when changing the setup to test at different temperatures. Figure 7.28 compares the stress-strain response at different temperatures for the 2.5 mm long sample. At 37˚C (dotted line) it is possible to see the initiation of the phase transformation, where the upper and lower plateaux are visible, but the linear elastic behaviour during the martensitic phase it is not seen in the same way as the response obtained for 25˚C (continuous line). Comparing both responses, it is also possible to see that at 25˚C the material response is stiffer and registers higher values of the stress throughout the curve. This is contrary to what was expected when increasing the temperature during compression. According to Brodie [3], when increasing the temperature, the material was expected to exhibit increased stiffness and achieve higher values of stress for the upper and lower plateaux.

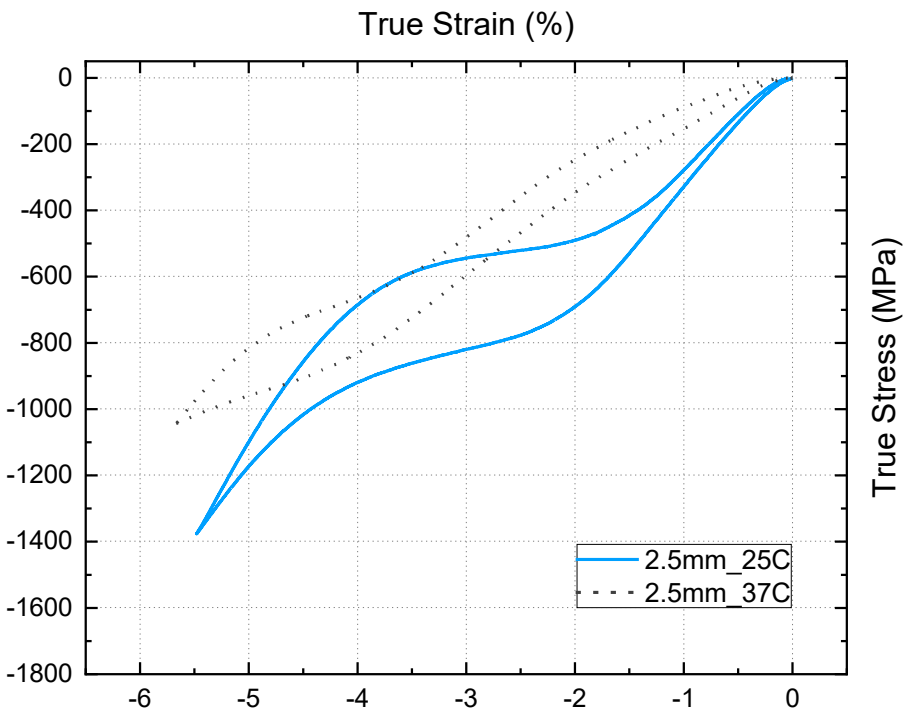

Figure 7.29 – Comparison of the stress-strain curve of the 2.5 mm sample long at different temperatures (25˚C and 37˚C) at 6% strain.

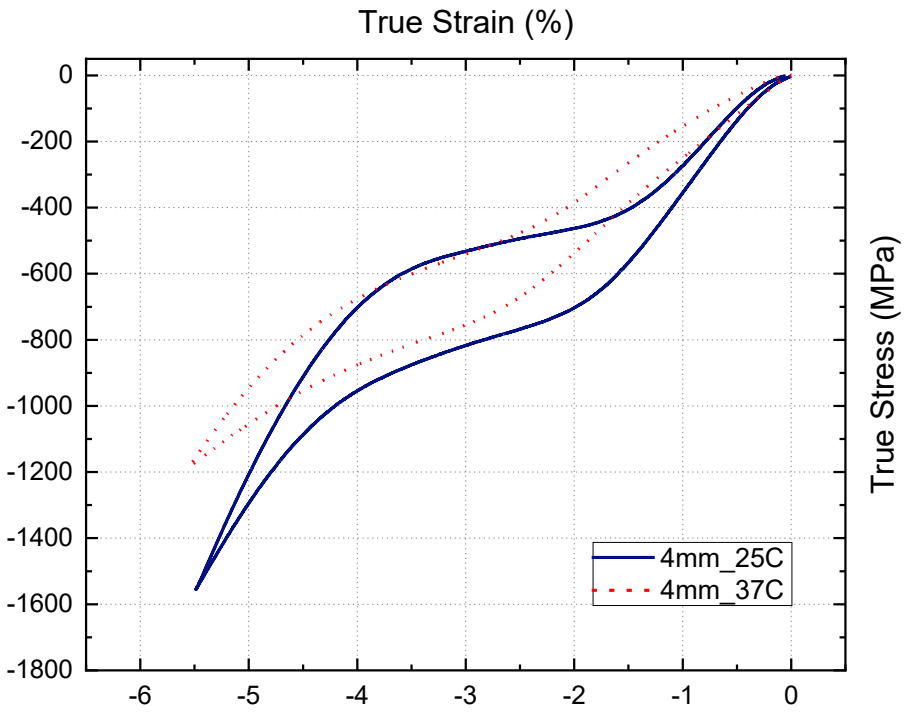

Figure 7.30 – Comparison of the stress-strain curve of the 4 mm sample long at different temperatures (25˚C and 37˚C) at 6% strain.

Analysing the stress-strain response for the 4 mm long sample at different temperatures in Figure 7.30, the same conclusions are obtained. For 37˚C (dotted line) the stress-strain curve shows lower values of stress when comparing with the response obtained at 25˚C (continuous line), the plateaux at 37˚C are also not as distinctive as the observed for 25˚C. This suggest that the change in the setup has a significant influence in the response at 37˚C by adding more compliance to the setup, thus invalidating the tests performed at 37˚C.

In an attempt to overcome the additional compliance encountered in the setup with the extension of the supports, the samples were compressed up to 7% strain to see if the response would shift to the expected values. Figure 7.31 compares the stress-strain response at 7% nominal strain for both 2.5 mm and 4 mm long sample at 37˚C with the stress-strain response obtained at 25˚C for the 4 mm long sample at 6% nominal strain. From this figure it is possible to conclude that when compressing the samples to 7% nominal strain at 37˚C the response is still not as expected, with the stress values throughout being higher than at 25˚C.

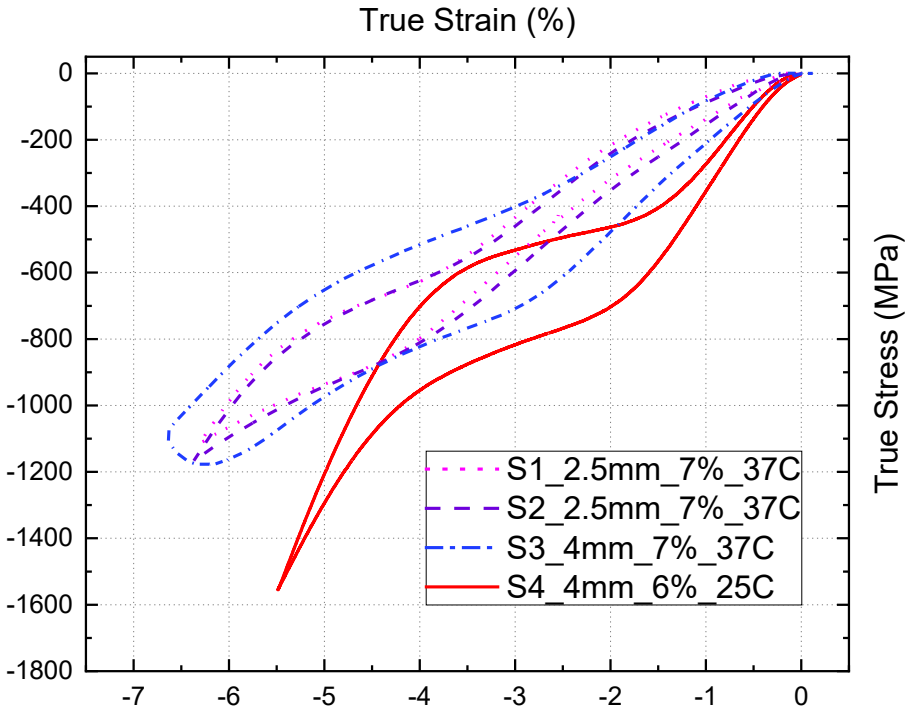

Figure 7.31 – Comparison of the stress-strain curve of the 2.5 mm and 4 mm sample long at 7% strain and 37˚C with the 4 mm sample long at 6% strain at 25˚C.

7.5 Discussion and Conclusions

After analysing the proposed studies of the L/D ratio and the influence of the temperature, it is possible to draw some conclusions. Firstly, for the study of the ratio between the sample length and the diameter of the sample, when comparing how the stress-strain curves for each nominal strain change with the increase in length, from Figure 7.24 to Figure 7.28 it is possible to see a tendency for the curves to create three different responses. The first group contains the sample of 1 mm length, with a ratio of 1. In this sample, the material is not able to transform from austenite to martensite when compressed to 6% strain. In this way it is possible to conclude that when using a "squat" sample of very small dimensions, it was not possible to obtain any repeatable results when submitted to compressive loading.

The second group is composed of the samples 1.5 mm and 2 mm long. With the increase in strain, it is possible to see the initiation of the phase transformation when subjected to higher strain. With the increase in strain, it is also possible to see the tendency of the responses obtained from these lengths to converge with increasing sample length. Although the transformation is visible in both sample lengths, the stress-strain curves never reach the fully martensitic phase since the associated linear elastic behaviour is not detected.

Finally, the third group is composed by the samples of 2.5 mm, 3 mm, 3.5 mm and 4 mm length. With the increase in strain, it is possible to see the response of the 2.5 mm long sample converging toward those of the longer samples. Also, from the responses obtained for this group it is clearer to identify the different stages of the transformation such as upper and lower plateaux and linear elastic behaviour both for austenite and martensite. In this way it is possible to conclude that 3mm to 4 mm are the best sample lengths to use for compression loading of fine wire. Due to the difficulty in producing such small samples and due to the observation that the strain measure's accuracy increases as the samples get longer, the 4 mm sample long is concluded to be the optimum choice.

In general, all the tests performed during the L/D ratio study, presented similar stress-strain curves but some exceptions were detected. For example, with the 2 mm long sample, the stress-strain curve obtained from one of the samples registered lower values of stress at the maximum strain. This suggests that the specific sample was defective. Therefore, some samples were further analysed under a microscopic to observe the ends of the samples. In Figure 7.36 and Figure 7.37 it is possible to identify some defects from the EDM machining. Figure 7.36 shows the detail of the edges of the sample. On Figure 7.36 a) it is possible to see a bump on the edge when it should be flat, as detailed in the rectangular frame. In Figure 7.36 b) it is possible to see the edge of the sample damaged, with an unclean cut, detailed in the rectangular frame. Figure 7.37 shows the detail of the sample end surface. In Figure 7.37 a) as detailed in the elliptic frame, it is possible to see the extra material equivalent to the bump identified in Figure 7.36 a). This bump precludes the sample from valid uniaxial compression testing. Small defects are also identified in Figure 7.37 b), where it is possible to see again that the end surface is not flat and perpendicular to the wire axis.

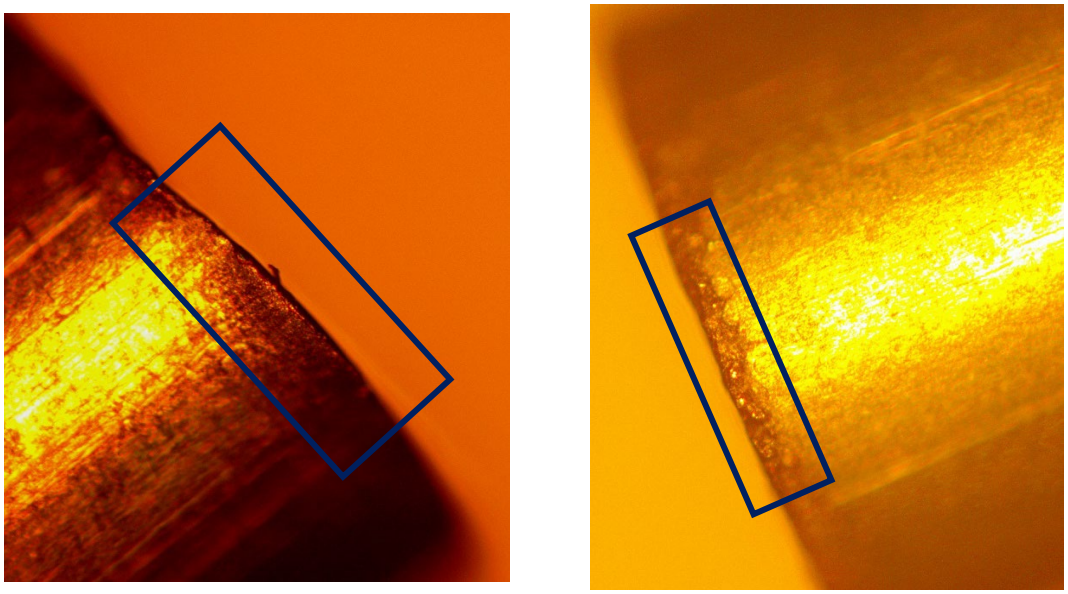

a) b)

Figure 7.32 – Detail of the edge of the samples used during the compression test; a) sample with a bump in the edge; b) different sample with defects in the edge.

With Figure 7.36 and Figure 7.37 is it possible to conclude that in future tests is important to prepare the samples before each test by abrading the surface to remove the imperfections from the EDM machining or other type of surface treatment.

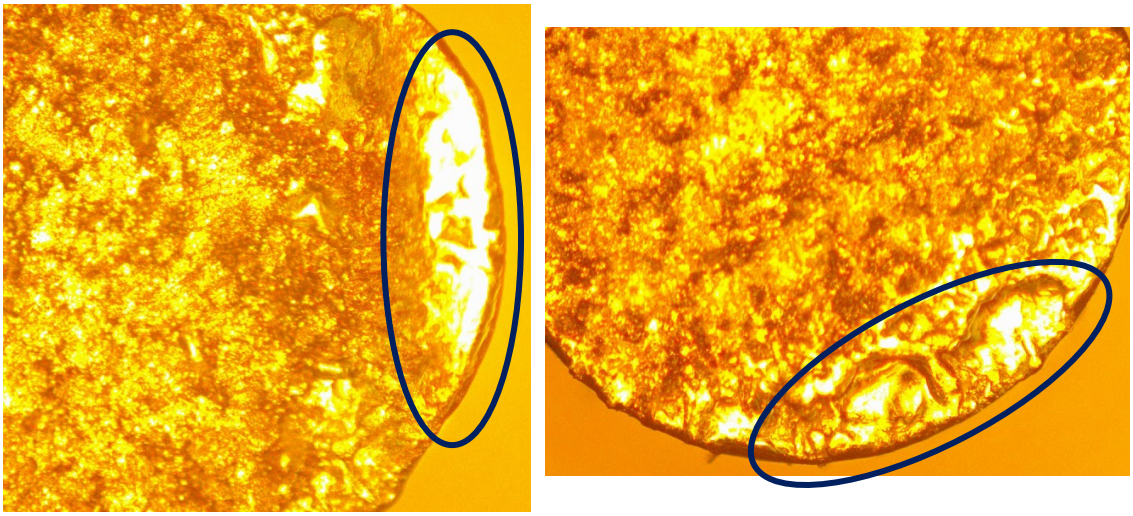

a) b)

Figure 7.33 – a) End surface of the sample with the bump; b) End surface of the sample with defects.

Chapter 6 shows that the intrinsic compliance of the machine itself was affecting the results, which was minimised by reducing the connectors attached both to upper and lower grips used during the compression test. So, when the setup needed to be changed to fit the compression test within the environmental chamber, no valid conclusions were possible from the second study that aimed to understand the effect of the temperature on nitinol wire under compressive loading. The results obtained at 37˚C show that when adding the connectors necessary to permit the environmental chamber, additional compliance is unavoidably included in the setup and hence no valid results were obtained during the tests described in section 7.4 . According to the literature, when increasing the temperature for compressive loading, the stress-strain curve is expected to have higher values of stress throughout the strain range. This was clearly not seen when compressing the nitinol wire at temperature of 37˚C.

As an alternative to performing the compression test at other temperatures, it is suggested to use a temperature-controlled water bath. This is suggested as future work since such a facility was not available for the present work.

The next chapter focuses on the numerical work performed. In this chapter two numerical models are studied by simulating the setup presented in this chapter. Both numerical models are supplied with the compressive parameters obtained during the compression tests in an attempt to replicate the results presented in this chapter.

8.1 Background

A compression testing method for metallic wires was developed and compressive tests were performed using superelastic nitinol wire used for stent graft devices. The mechanical response of nitinol was characterised under compression loading at different conditions. Results and analysis of these tests are previously detailed in Chapter 7. An important aim of the experimental work was to provide enough data for reproducible parameter input to a constitutive model of the nitinol material used in Finite Element Analysis (FEA). The experimental results will provide useful data to validate the numerical model by comparing with the FEA simulations of compression. The experimental results will in this way, allow an assessment of the FEA material model for compression loading, with the ultimate aim of improving the model used in bending simulations of stent graft components.

As mention on Chapter 3, this work will follow that of Brodie [3] and Boukis [2] in FEA, where both focused on the constitutive model developed by Aurrichio and Taylor [56] that is available in the Abaqus FEA software as a built-in user material subroutine 'ABQ_SUPER_ELASTIC' UMAT [85].

Boukis [2] presented a model for compressive loading based on 'ABQ_SUPER_ELASTIC' UMAT where the input parameters where obtained mainly from tensile testing and only one input value from compression testing. Brodie [3], on the other hand, using the same constitutive model, presented a model using more inputs obtained from compression testing by changing the symmetry mode for the model.

Taking in consideration the work presented by Brodie and Boukis, this chapter focuses on understanding the response of FEA simulations of nitinol under compression loading, where different approaches are taken to understand the different responses. This work also

compares the response obtained from the ABQ_SUPER_ELASTIC' UMAT with a different constitutive model developed by Kelly and Stebner [4].

8.2 Objectives

The aim of the present work regarding the numerical modelling centres on understanding how the commercially available constitutive model responds to compressive loading and compare with a different constitutive model. Therefore, to achieve this, the following objectives were pursued:

- Obtain the experimental material properties to implement in the numerical models;
- Calibrate a representative UMAT 'at room temperature' material model using uniaxial compressive data inputs from the experimental data presented in Chapter 7;
- Understand how the UMAT responds, by changing the model conditions;
- Compare the UMAT response with a different constitutive model.

8.3 Methods

This section considers the numerical model available within the commercially available finite element Abaqus software. The software version used was Abaqus 6.14 with the built-in user material model (UMAT) for superelastic nitinol calibrated for a specific material using parameters obtained from the uniaxial tensile test results. This material model is based on the phenomenological constitutive model developed by Aurrichio and Taylor [56]. In the present work, the parameters used were obtained from uniaxial compressive stress-strain data described in Chapter 7, and compared with previous results from Brodie [3] and Boukis' [2] earlier work.

The 'ABQ_SUPER_ELASTIC' UMAT built-in constitutive model is calibrated by the user for the specific material to be modelled by inputting 15 parameters obtained from the experimental results. These inputs include:

- Definition of different elastic properties both for austenite and martensite phases;

- Tension-compression asymmetry;
- Definition of the uniaxial tensile and compressive stress-strain curves;

8.3.1 UMAT parameters

Figure 8.1 (obtained from Dassault Systems 'UMAT for Superelasticity and Plasticity of Shape Memory Alloys) describes the 15 parameters used to calibrate the material model from the experimentally measured uniaxial stress-strain curves for nitinol. Looking at the figure it is possible to see that the majority of the inputs are obtained from the uniaxial tensile stress-strain response and only two from the uniaxial compressive stress-strain response.

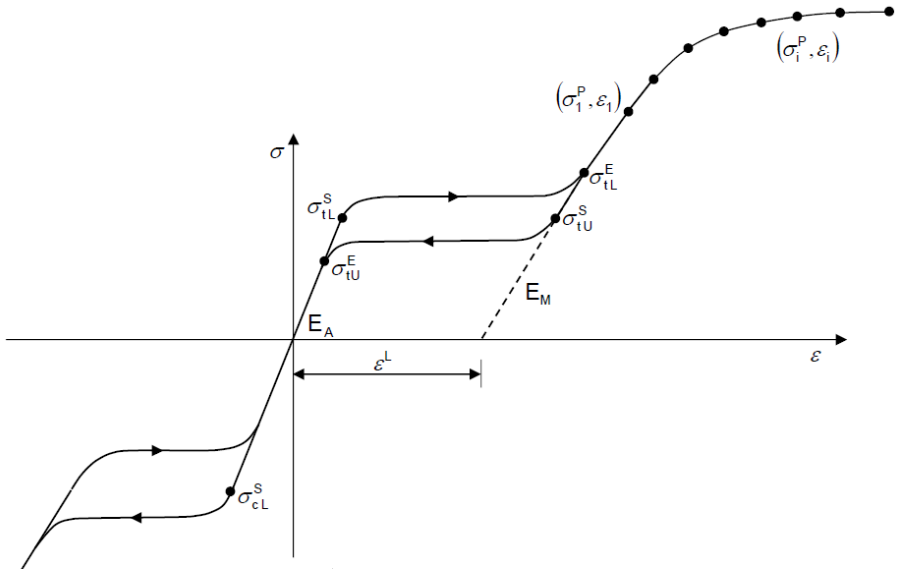

Figure 8.1 – Input parameters for nitinol UMAT model [85]

Table 8.1 describes the parameters in Figure 8.1. The values describing the elasticity in austenite and martensite (parameters 1 and 3 respectively) are obtained by calculating the slope of the respective linear elastic behaviour part of the uniaxial stress-strain response. Although the Poisson's ration, both for austenite and martensite phases, can be calculated by using the equation (1) where v is the Poisson's ratio, E the elastic modulus and G the shear or torsional modulus, since the shear or torsional modulus was not obtained

experimentally in this work, the value of ν used will be 0.45, as obtained from the reference [27] Reedlunn et al, for both austenite and martensite phases.

$$\nu = \left(\frac{E}{2G}\right) - 1 \tag{8.1}$$

The transformation strain (parameter 5) is obtained by projecting the E_M gradient from the end of the loading plateau down to the strain-axis, as indicated in Figure 8.1. Reference temperature (parameter 9) is set to 0 for isothermal simulations, therefore, parameters 6 and 10 are not used in this work and are set to 0 as well.

Start and end of transformation loading parameters (parameters 7 and 8) are obtained from the stress level at the start and end of the loading plateau, respectively. In the same way, start and end of transformation unloading parameters (parameters 11 and 12) are the stress value point obtained from the start and end of the unloading plateau, respectively.

The start of transformation stress during loading in compression (parameter 13), similar to parameters 7 and 11, is obtained using the stress value point at the beginning of the loading plateau during compression. This value needs to be inputted as a positive value. Note that in the Abaqus UMAT, if this value is set to 0 then the symmetrical model is used.

The volumetric transformation strain (parameter 14) is set to be equal to the transformation strain (parameter 5), this allows the UMAT to create an algorithm where the ε_V^L value is computed based on σ_L^S and σ_{CL}^S.

In this work, no annealing simulations are needed, so parameter 15 is set to 0 and consequently parameter 16 is as well. In addition, in this work the plastic behaviour in compression will not be studied, so stress-strain points from the yield curve will not be added (parameter 17 set to 0).

Table 8.1 – Input parameters of the Superelasticity UMAT [85]

No.	Symbol	Description	Units
1	E_A	Austenite elasticity	MPa
2	ν_A	Austenite Poisson's ratio	
3	E_M	Martensite elasticity	MPa
4	ν_M	Martensite Poisson's ratio	
5	ε^A	Transformation strain	
6	$\left(\frac{\delta\sigma}{\delta T}\right)_L$	δσ/δT loading	MPa/˚C
7	σ_L^S	Start of transformation loading	MPa
8	σ_L^E	End of transformation loading	MPa
9	T_O	Reference temperature	˚C
10	$\left(\frac{\delta\sigma}{\delta T}\right)_U$	δσ/δT unloading	MPa/˚C
11	σ_U^S	Start of transformation unloading	MPa
12	σ_U^E	End of transformation unloading	MPa
13	σ_{CL}^S	Start of transformation stress during loading in compression, as a positive value	MPa
14	ε_V^L	Volumetric transformation strain	
15	N_A	Number of annealings to be performed during the analysis	
16	N_P	Number of stress-strain pairs to define the plastic curve	
17	σ_{NP}^P, ε_{NP}	Stress-strain points in the yield curve	

Now looking at the previous work of Boukis [2] and Brodie [3][86], Boukis simulated compressive loading using only parameter 13, start of transformation stress in

compression. On the other hand, Brodie used a different approach to simulate the compressive loading, where he used the model in symmetric form by setting the start of transformation stress in compression (parameter 13) to 0. Also, for both start and end of transformation during loading and unloading (parameters 7, 8, 11 and 12) Brodie used the compressive values obtained from the experimental stress-strain response results. In other words, Brodie's approach [86] inverted the UMAT curve in Figure 8.1 to the compressive response. Since this work will focus only on the numerical compressive response, it will follow a similar approach to the one presented by Brodie, where instead of the tensile parameters described from Figure 8.1, the compressive values will be used but with the main difference being that the start of transformation stress during loading in compression will be obtained from the experimental work performed by Boukis, using the start of transformation stress identified during loading in tension.

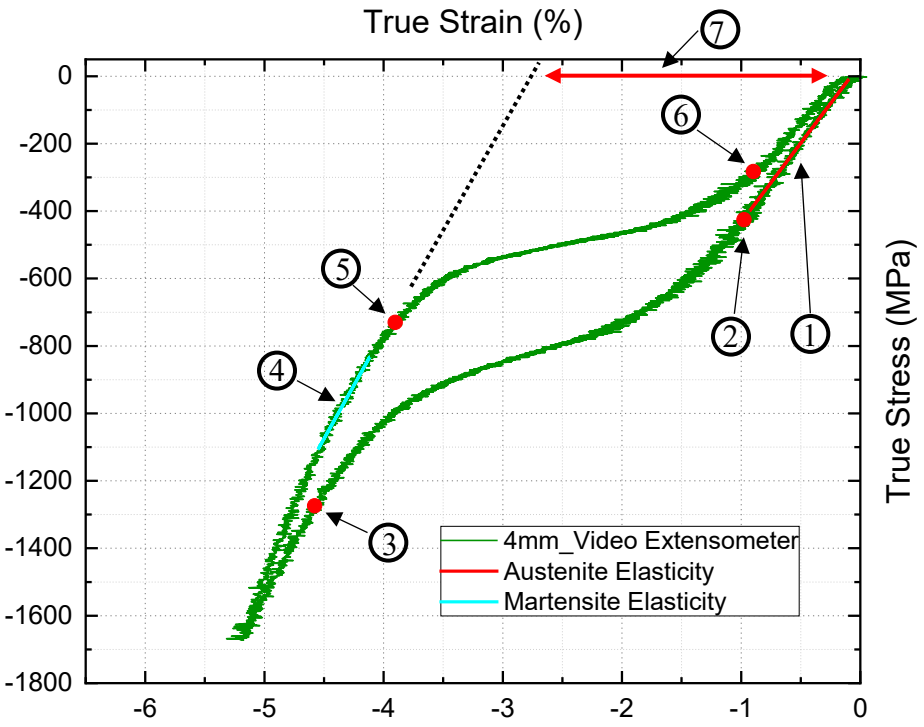

Figure 8.2 –Obtaining of the Superelasticity UMAT parameters from the experimental compressive stress-strain response of 4mm sample long.

Table 8.2 – Parameters used in UMAT for different sample length.

No.	Symbol	2.5 mm	3 mm	3.5 mm	4 mm	4mm_N35
1	E_A	40367	47899	54067	46179	44900
2	ν_A	0.45	0.45	0.45	0.45	0.45
3	E_M	38367	44610	47433	57890	54700
4	ν_M	0.45	0.45	0.45	0.45	0.45
5	ε^A	0.0275	0.024	0.026666667	0.027833333	0.028
6	$\left(\frac{\delta\sigma}{\delta T}\right)_L$	0	0	0	0	0
7	σ_L^S	565	519	478	484	546
8	σ_L^E	1152	1190	1122	1203	1198
9	T_O	0	0	0	0	0
10	$\left(\frac{\delta\sigma}{\delta T}\right)_U$	0	0	0	0	0
11	σ_U^S	703	773	724	783	813
12	σ_U^E	345	284	259	259	255
13	σ_{CL}^S	540	540	540	540	540
14	ε_V^L	0.0275	0.024	0.026666667	0.027833333	0.028

From Figure 8.2 it is possible to see how the required parameters were obtained from a compressive stress-strain experimental response. Figure 8.2 corresponds to the stress-strain response obtained from the experimental method described in Chapter 7, for 4 mm long sample compressed to 6% strain. The strain in this figure was obtained from the video extensometer. Austenite elasticity (E_A – parameter 1) was obtained from the slope of the

linear elastic behaviour seen during the austenite phase as indicated by point ① in Figure 8.2. Following the same method, the martensite elasticity modulus (E_M – parameter 3) was obtained from the slope of the linear elastic behaviour during the martensite phase shown by point ④ in Figure 8.2. The start of transformation loading (σ_L^S) and unloading (σ_U^S) and end of transformation loading (σ_L^E) and unloading (σ_U^E) were obtained from the stress values identified from the respective points ②, ⑤, ③, ⑥ shown in Figure 8.2 and are equivalent to parameters 7, 11, 8 and 12 in Table 8.1. Finally, the transformation strain (ε^L), explained previously, is obtained by tracing a line from the E_M gradient to the x-axis, as shown in Figure 8.2 correspondent to point ⑦ in the figure.

The parameters used in this work were obtained from sample lengths of 4 mm, 3.5 mm, 3 mm, and 2.5 mm, from the experimental work described in Chapter 7 using the strain obtained from the video extensometer. Since 3 samples were tested for each length, the parameters used correspond to the average of the values obtained from the experimentally measured stress-strain response as described previously. Table 8.2 lists the parameters obtained from experimental measures for each sample length that were then inserted in the UMAT to simulate the stress-strain response of nitinol under compressive loading.

8.3.2 Compression Modelling

The model created in Abaqus to simulate the compressive loading of nitinol wire, used a 3D deformable cylinder with 1 mm diameter and the length ranging from 2.5 to 4 mm long, to simulate the actual specimens tested experimentally. The two compressive platens were represented as 3D analytical rigid surfaces as seen in Figure 8.4. To replicate the experimental conditions, the contact used between the platens and the wire was surface-to-surface with finite sliding. Also, a low friction coefficient was used in the analysis to simulate the lubricant applied on both ends of the wire during the compression test.

To mesh the geometry, 20-node quadratic brick, reduced integration elements (C3D20R) were used. Generally, this type of element is the best choice for most simulations due to combining the capabilities of the fully integrated elements while being less computational

demanding. (mesh with a total number of 576 quadratic hexahedral elements of type C3D20R)

From Figure 8.3 it is possible to see the boundary conditions imposed on the model. The behaviour of the platens was controlled by two reference points (RP) constrained in all directions. The central axis on the geometry, as visible in the figure, was constrained on both x and y-axes. The compressive loading cycle was defined by 2 steps, loading and unloading movement. The loading movement was controlled by displacement, where a known displacement was applied to the left RP, causing the left platen to move in the negative z-axis direction (compressive movement). The unloading movement was controlled in the same way, where the displacement is set to zero upon returning to the initial position in this case the platen moves in the positive z-axis direction.

After the simulations, force-displacement data was recorded for each simulation and then the same process as for the experimental data was used to convert the force-displacement to stress-strain, as explained in Chapter 7. Using the same approach to obtain the stress-strain curve both for experimental and numerical results, provided as basis for accurate comparison between both responses.

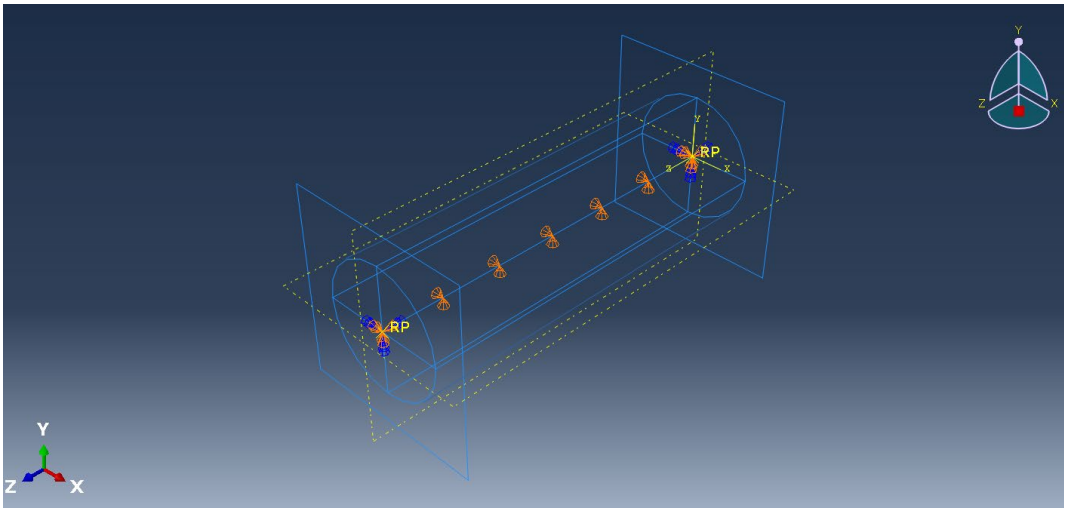

Figure 8.3 – Boundary conditions of the Abaqus compression model

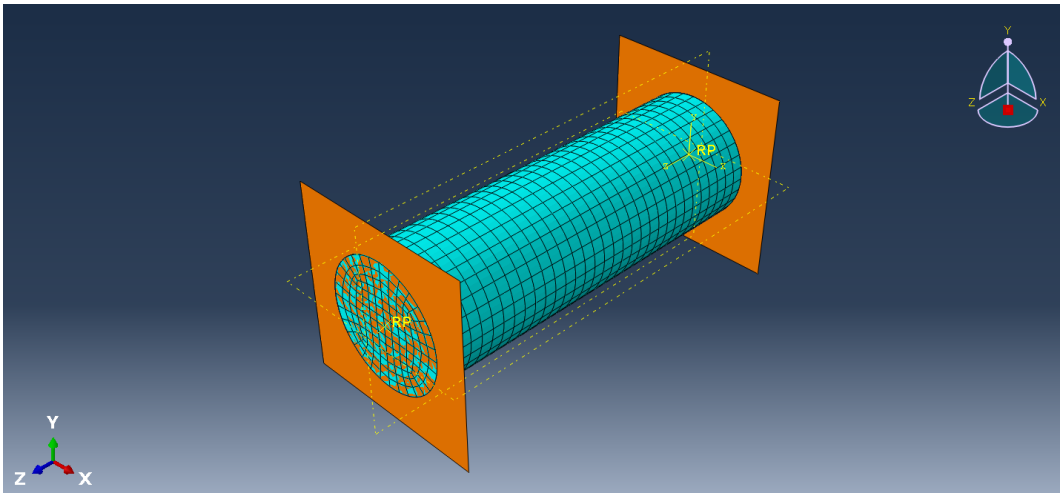

Figure 8.4 – Meshed geometry of the Abaqus compression model

8.4 Superelasticity UMAT results

This section presents the stress-strain curves obtained from the simulations which are then compared with the experimental curves. The simulations performed include compression at 6% strain for each sample length, 2.5 mm, 3 mm, 3.5 mm and 4 mm using the parameters from Table 8.2 for each length respectively. Using the parameters from the 4 mm long sample, comparison is made between the parameters obtained from one sample and from the average of the three samples tested. Comparisons with the previous results obtained from Boukis and Brodie are also presented, using the parameters of the 3 mm long sample. The influence of the constrains used at the ends of the sample was also studied. Different simulations were made where the ends were fully constrained with no radial expansion and fixed just at the centre of the cross section allowing radial expansion. Finally, simulation of a 4 mm long sample using the parameters obtained from tests on other sample lengths is also presented. However, when simulating alternative sample lengths with parameters derived from 4 mm sample test, the simulation failed to converge.

Figure 8.5 compares the experimental stress-strain curve (black continuous line) against the simulated stress-strain curve for the 4 mm long sample. Two numerical curves are compared as well, where different parameters were used, the parameters obtained from a

specific 4 mm sample (red dashed line) and the mean values obtained from the three 4 mm sample long tested (blue dotted line). Analysing both numerical responses, it is possible to see that the linear elastic behaviour during austenite for loading and unloading follow the same stress-strain path. The beginning of the transformation and upper plateau is coincident in all curves, showing that the simulation curves are matching with the experimental one. At this point the simulation curves start to diverge. Focusing on the response obtained using the parameters from a specific sample, the upper plateau presented follows the same loading path as the experimental curve, while the deviation starts at the end of the plateau, showing a longer plateau that the experimental result. The red dashed line presents an upper plateau that starts at 2% true strain and finishes at 5% true strain, with an increase in stress of 400 MPa over the transformation. This is succeeded by linear elastic behaviour in martensite with lower stress values when compared to the experimental results. At 6% strain, the stress-strain curve forecasts a maximum stress of 1800 MPa, with the curve more extended during the martensitic phase compared to the experimental stress-strain curve. During unloading, the lower plateau is longer than the plateau presented by the experimental curve. At approximately 4% strain, both the experimental and numerical curve for the one specific sample present the same stress-strain path until the end of the test.

Analysing now the numerical response using the mean values from all 4 mm samples, at the beginning of the phase transformation during loading, the curve predicts an upper plateau with a higher slope when compared with the experimental curve. The plateau starts at 2% strain and finishes at 4.5% strain approximately. For the linear elastic behaviour during the martensitic phase, the curve predicts the same loading path as the experimental curve until a stress of 1600 MPa approximately is reached. At this point, the linear elastic behaviour is extended up to 2100 MPa approximately, when the prescribed 6% strain is reached. During unloading, at 1600 MPa, the curve forecasts the same unloading path as the experimental curve, until 1400 MPa approximately, where the lower plateau starts.

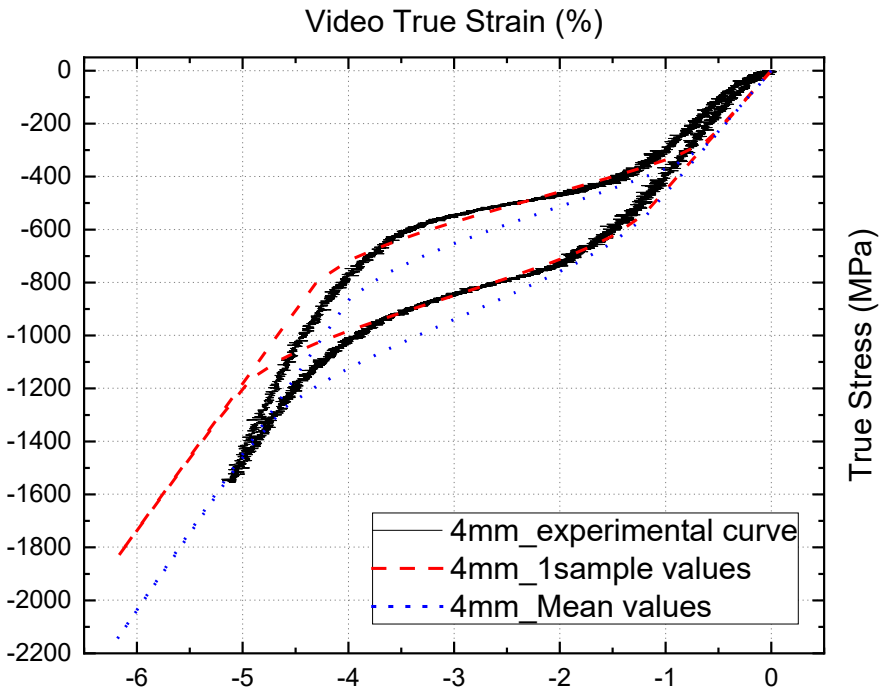

Figure 8.5 – Compressive stress-strain curve for 4mm sample long comparing the results from experimental and numerical using the 4 mm parameters from a specific sample and using the 4 mm parameters mean values.

Comparing the results from Figure 8.5, using the parameters for the 4 mm sample length, with the results obtained by Boukis [2] and Brodie [3] from the 3 mm sample length, presented in Chapter 3 in Figure 3.17 and Figure 3.18, it is possible to see some improvements using both the parameters from a single sample and the average of all tests from the 4 mm sample length. As Boukis previously stated, the plateaux presented for compression during simulation are similar to the plateaux expected from tensile tests. The transformation plateaux presented by Boukis are flat with no gradient, with a maximum stress at the end of the transformation of approximately 800 MPa, the same as at the beginning of the transformation during compression. This previous result is explained by the fact that in his simulations he used the UMAT with the parameters obtained from tensile tests, thus demonstrating that the model is not able to accurately reproduce the stress-strain behaviour in compression of the nitinol wire. On the other hand, Brodie, using a similar approach as the one presented in this work, manage to obtain a compressive

stress-strain curve more similar to the experimental results. Brodie applied a UMAT model using the compression parameters instead of the tensile, with the parameter 13 set to 0 to use the model in a symmetrical manner. Comparing his results in Figure 3.18 with those presented in Figure 8.5, the main difference is at the beginning and end of transformation both in loading and unloading, where Brodie presented a curve with distinct discontinuity in slope at the beginning and end to the transformations. However, the results obtained experimentally, where both beginning and end of transformation is represented by a more continuous curve in which it is more difficult to precisely distinguish the beginning and end of the plateaux.

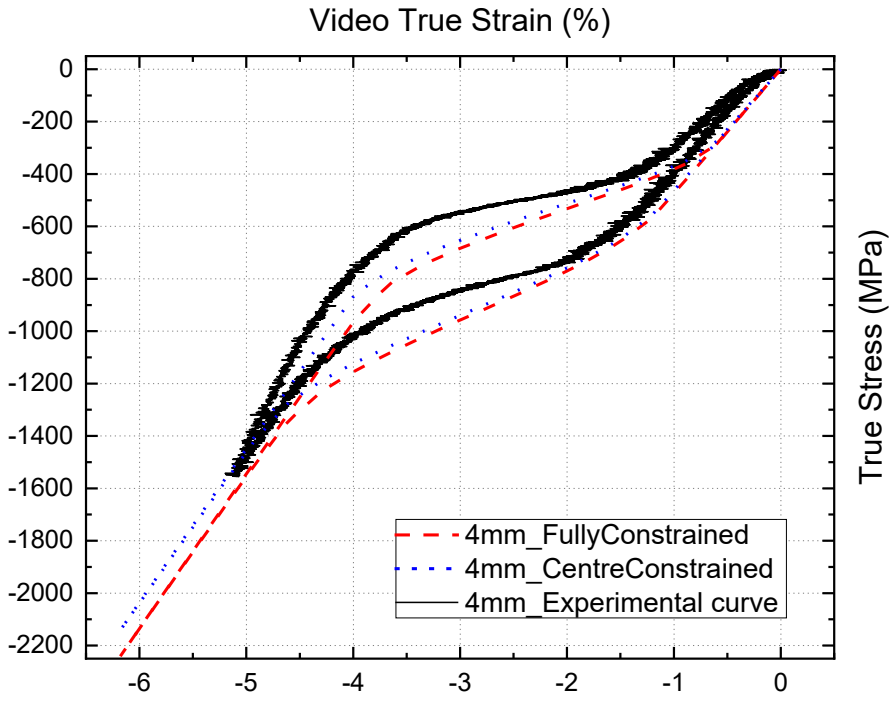

Figure 8.6 – Comparison of the compressive stress-strain curves using different constraint against the experimental stress-strain curve.

Figure 8.6 studies the influence of the constraints applied in numerically forecasting the response for the 4 mm long sample using the mean parameter values. This figure compares the experimental results (continuous line) with the results obtained numerically, constraining only the ends through the centre line (blue dotted line) and fully constraining

both ends to the platens (red dashed line) thereby not allowing the sample to displace in the radial direction at the ends. The fully constrained ends analysis allowed understand how the sample interacts with the platens without adding lubricant (friction coefficient = 1 – all nodes on the in surface are fully constrained). On the other hand, by constraining the centre node at the surface ends allowed the sample to freely expand radially (friction coefficient = 0 – all nodes on the in surface are unconstrained. This comparison is manly compare Abaqus response using a low friction coefficient, friction coefficient = 0 and friction coefficient = 1.

The stress-strain response presented in Figure 8.6 only presents the response using friction coefficient = 1, friction coefficient = 0 and the experimental stress-strain curve avoid confusion in the analysis and from the response is possible to see that although it is visible a slight influence of the friction coefficient, the gap is very small, therefore the stress-strain numerical response with low a low friction coefficient sits in between the presented curves. It is possible to see that when the sample is fully constrained at both ends, the stress-strain curves present slightly higher values of stress, suggesting a stiffer material behaviour. This is according to what was observed in reality, where the lubricant used at the ends of the sample permitted less constrained radial deformation throughout the sample length, and thus a less stiff material response. This comparison allowed the model to have a coarse mesh, maintaining a reduced computational time for each analysis.

After analysing how the parameters specified in the model and the constraints influenced the simulation, it is important to see the stress-strain response at different sample lengths. The following figures present the predicted stress-train curve for each sample length using the respective sample length experimental mean values and compares the prediction with the experimental response.

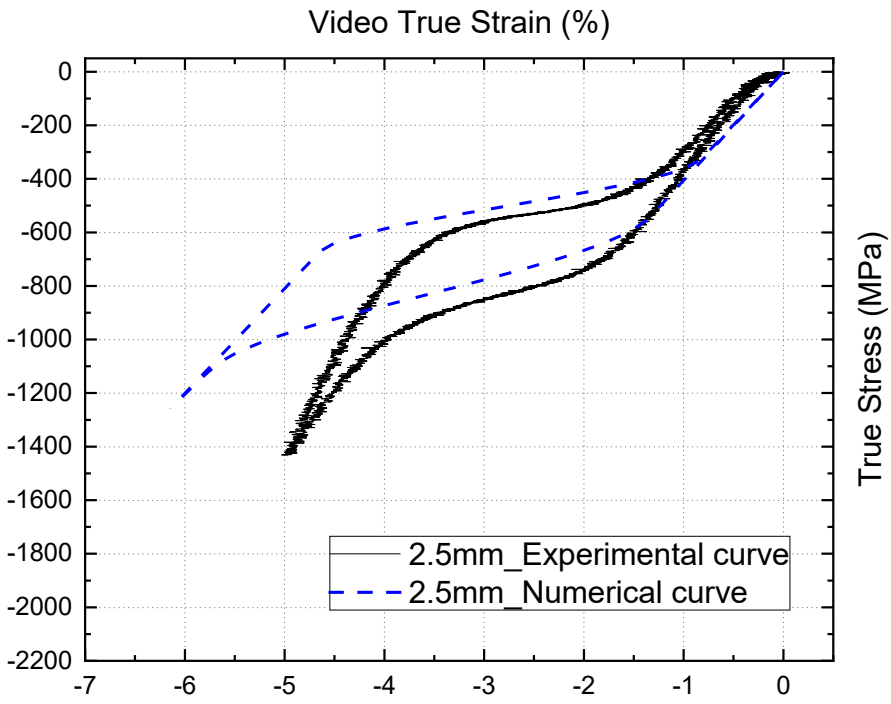

Figure 8.7 – Comparison between the experimental and numerical compressive stress-strain response in compression of 2.5 mm sample long.

Figure 8.7 compares the stress-strain response obtained numerically (dashed blue line) for 2.5 mm long sample with the one obtained experimentally (continuous black line) for 2.5 mm long sample. For the numerical prediction, the FE model described previously was used but with the change in the length of the sample from 4 mm to 2.5 mm long and the input parameters used are as presented in Table 8.2 for 2.5 mm sample length mean values. Comparing both curves, is it possible to see the slope of both loading and unloading during the linear elastic behaviour in austenite is similar. After this point, in loading, the numerical curve starts the transformation at lower stress values, when compared with the experimental curve. The forecast plateau is longer than for the presented experimental curve, where it starts at 1.5% approximately and finishes at 5.5% strain at 1000 MPa. The maximum stress at 6% is 1200 MPa, lower than the experimental curve. The unloading path is also at lower stress when compared with the experimental curve. Both numerical

and experimental unloading paths converge again at 1.5% strain and 400 MPa approximately.

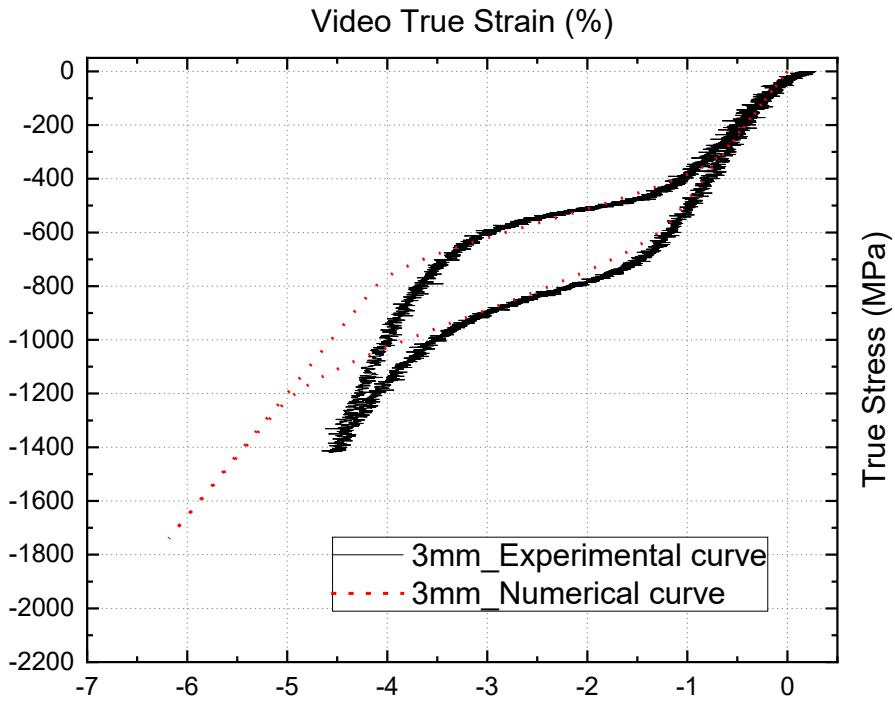

Figure 8.8 – Comparison between the experimental and numerical compressive stress-strain response in compression of 3 mm sample long.

Figure 8.8 compares the numerically forecast stress-strain curve from 3 mm long sample with the experimental response for the same length. The FE model used is the same as described in section 8.3.2 , but with the sample length changed to 3 mm. The parameters used is this model are listed in Table 8.2 for 3 mm long sample mean values. The numerical response for 3 mm long is very similar to the experimental response until 3% strain during loading and after 3% strain during unloading. The upper plateau from the numerical response is longer than the experimental plateau, starting at 1.5% and finishing at 5% strain approximately. The maximum stress obtained from the numerical response is higher than the experimental response, with a maximum of 1800 MPa at 6% strain. During unloading the lower plateau starts at 4% strain and 700 MPa, but still exhibits a longer plateau than that obtained experimentally.

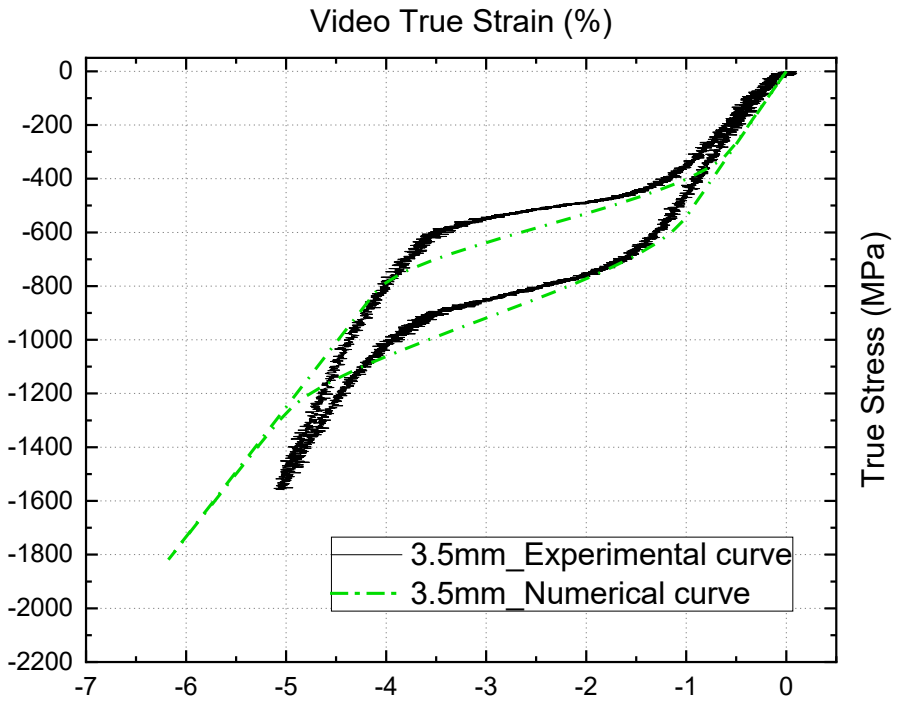

Figure 8.9 – Comparison between the experimental and numerical compressive stress-strain response in compression of 3.5 mm sample long.

The same procedure was used to obtain the numerical response for the 3.5 mm long sample, where the FE model used was once again the same but with the change in length of the sample as prescribed. The parameters used in the UMAT are specified in Table 8.2 for 3.5 mm long sample mean values.

From Figure 8.9, is possible to compare the numerical and experimental stress-strain curve for 3.5 mm long sample. From the figure is possible to see that both curves are similar. The main differences appear in upper and lower plateaux, where the gradient is higher for the numerical response. Both plateaux have an associated increase in stress of 400 MPa in the numerical case, whereas in the experimental response, the plateaux have an increase of only 200 MPa. The slope throughout the linear elastic behaviour during the austenite phase is lower for the numerical response. The maximum stress obtained numerically is higher than the experimental response, with a maximum stress of 1800 MPa at 6% strain.

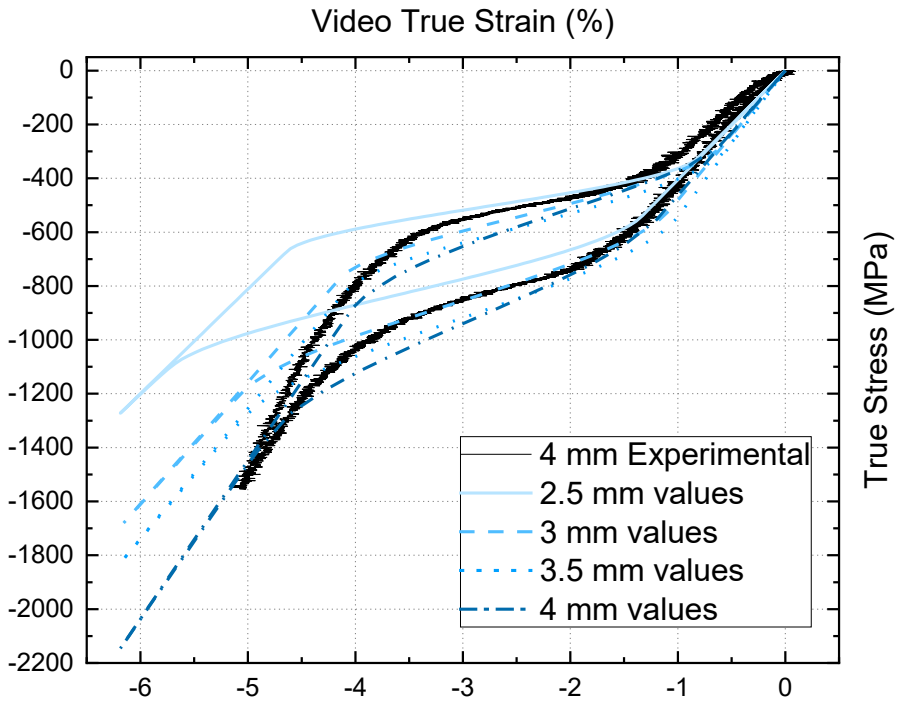

Figure 8.10 – Comparison of the numerical compressive stress-strain curves using different input values for 4 mm sample length.

Figure 8.10 compares the numerical stress-strain curve for 4 mm long samples while using the parameters of different sample lengths. For this simulation, the model used was the same as described in section 8.3.2 with 4 mm long sample but for each simulation, the UMAT parameters were different, using the parameters of 2.5, 3 and 3.5 mm average values to simulate the 4 mm sample. From this figure is possible to see a convergence of the numerical responses towards the martensite elasticity of the experimental result. On the other hand, it is also possible to see the increasing plateaux stress values, with the numerical response, using the parameters for 4 mm giving higher than measured values in these stresses.

Although the simulated stress-strain curved give a good approximation to the experimental stress-strain response of nitinol wire under compressive loading, it is clear to observe the limitations of the UMAT when simulating compressive response. As mentioned at the beginning of this chapter, the input parameters for the nitinol UMAT

model are based on the tensile response. When trying to invert the UMAT parameters in a tensile response to a compressive response, it is possible to obtain a stress-strain curve closer to the experimental but it is evident the limitation on the UMAT model to reproduce the asymmetric characteristic of nitinol.

8.5 Kelly and Stebner model

In this section an alternative model to the UMAT is tested. A description of this model is previously provided in Chapter 3 section 3.2.2 . This model was developed by Kelly and Stebner and all the results presented in this section were provided by Professor Aaron Stebner from Colorado School of Mines, USA. Stebner analysed the behaviour of nitinol wire both under compression and tension loading, using the experimental curves from the 4 mm long sample during compression loading presented in this work and the experimental curves from tensile tests performed and provided by Boukis [2].

The parameters selected for the constitutive model used to simulate the behaviour of nitinol under tension and compression were selected in two different ways. Firstly, accurately matching the compressive response took precedence (Case 1) then secondly matching the tensile response took priority (Case 2). Figure 8.11 and Figure 8.12 present the results using both approaches, where it is possible to understand how the model performs for each case. In both cases, for the compression data, only the last cycle of the experimental results under compression and three different samples were used. For the tensile data, the experimental results were used as given, two cycles in total with one full cycle and the second the sample goes up to rupture, again from three different samples.

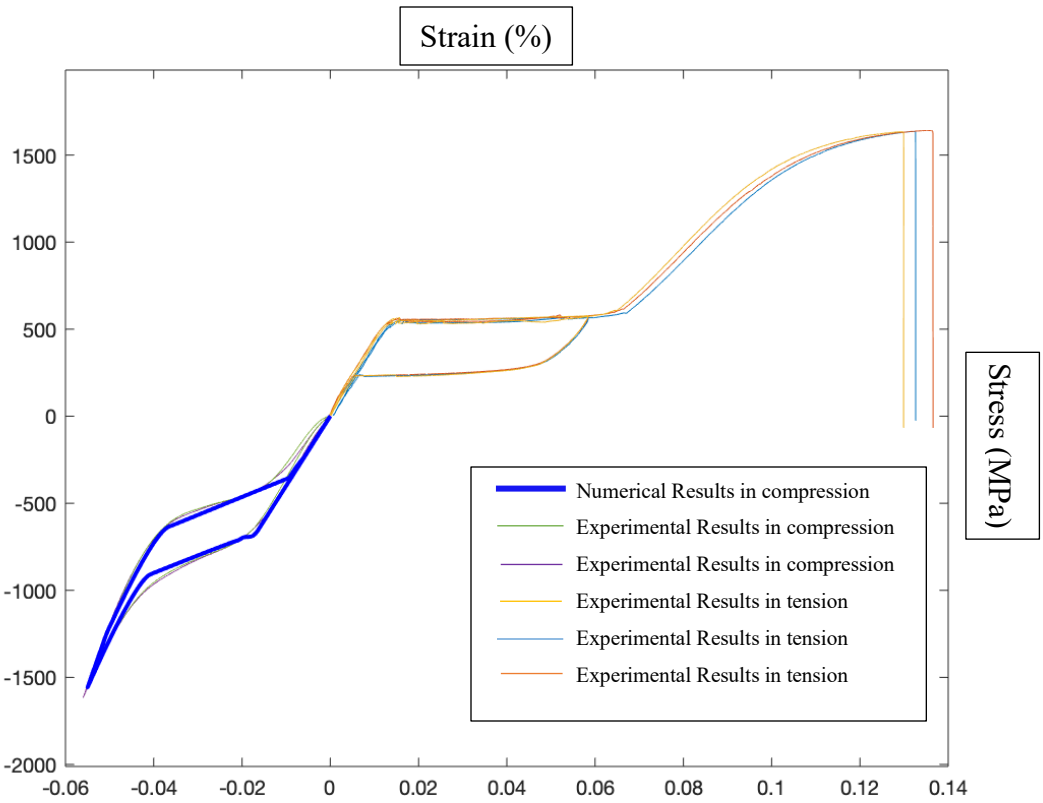

Figure 8.11 – Tension-compression stress-strain numerical response fitting the compression response as the most important (case 1) – Image provided by Stebner.

Figure 8.11 and Figure 8.12 shows that the constitutive model developed by Stebner can be fitted with different parameters, depending on their perceived significance the user prefers, although as it is unknown how this data was analysed, it is not possible to take any conclusions from this work. Further analysis using this method are necessary to directly compare this model with the UMAT model.

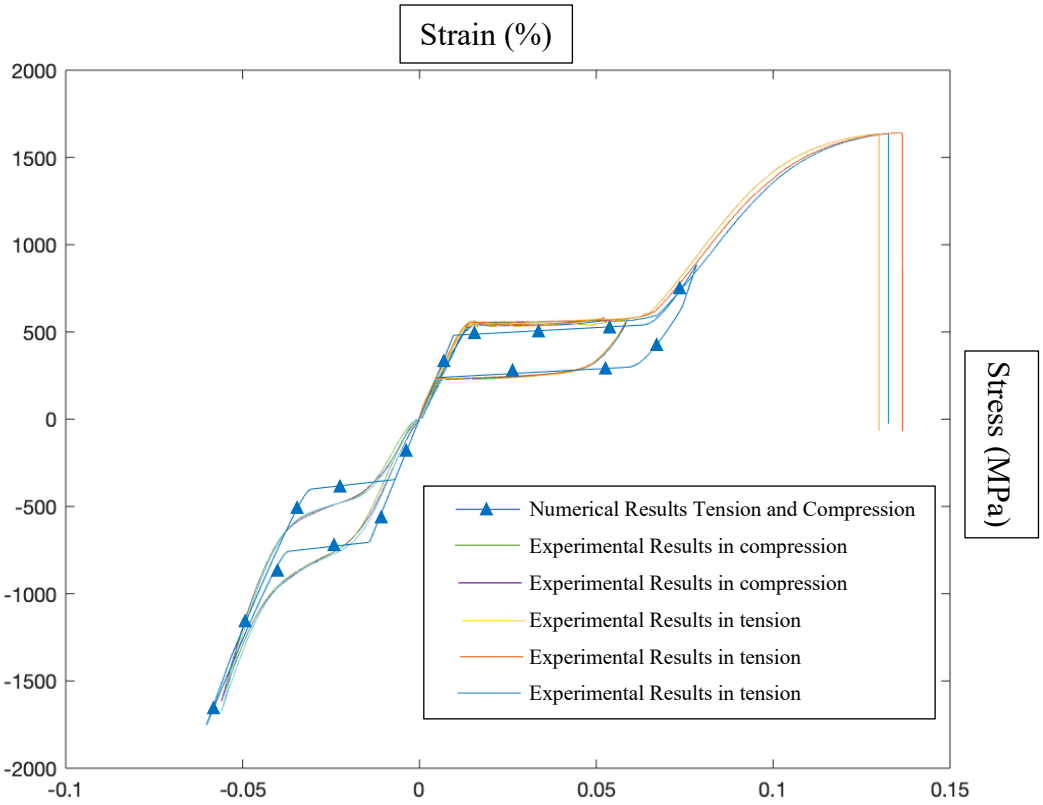

Figure 8.12 – Tension-compression stress-strain numerical response fitting the tension response as the most important (Case 2) – Image provided by Professor Stebner.

8.6 Conclusions

In this chapter, uniaxial compressive test results from Chapter 7 were used to calibrate different material constitutive models deployed in FE simulations. The constitutive models used are the Abaqus Superelasticity UMAT, based on the Auricchio Taylor model, for nitinol and the Kelly and Stebner proposed constitutive model.

From previous works, it is known that the Superelasticity UMAT constitutive model has some limitations when simulating the nitinol wire under compressive loading. To overcome these limitations, an unconventional approach was presented that consisted of calibrating the UMAT using the compressive values presented in Chapter 7. To have more consistent results, the parameters used for each sample length were obtained from the mean values of all experimental tests. This solution provided a good comparison between experimental and simulated stress-strain response, where the loading path during

austenitic and martensitic phases are very similar. However, during the transformation phases the model was unable to follow the experimental loading and unloading paths precisely.

It is also shown in this chapter that with increasing sample length, the stress-strain curve more closely matches the experimental curve. This is similar to what was observed with the experimental results, where the stress-strain curve converges to the same response with the increase in sample length.

When modelling uniaxial compression loading, although the Abaqus UMAT model is able to give a reasonable prediction of the experimental curves, there are still some limitations of the model. With this model is it possible to obtain the austenite modulus, start and end loading stresses, and martensite modulus. The limitation is seen during the hysteresis, between the martensite loading and unloading slopes (phase transformation). This leads to a major limitation in simulating bending because the model will be unable to use an asymmetric model, giving a poor representation of the compressive curve in this case. The model available in Abaqus takes into consideration only one parameter to control compressive loading, as described at the beginning of this chapter.

This limitation also seen by other authors of the Abaqus UMAT model for bending loading, comes from the fact that the model is not able to accurately represent a single asymmetric material when simulating both tension and compression. Nevertheless, modelling bending loading is very important in stent design, due to the bending deflections that the stent is subject to during packaging and deployment of the stent in-situ.

Analysing the stress-strain curve obtained by Stebner and comparing with the UMAT stress-strain curve, this model predicts better results than the Abaqus Superelasticity UMAT although as these results were provided by Stebner himself, it is not possible to conclude anything and there are very unknowns related to this work. The results presented by Stebner indicate a good approximation to the experimental response but it is important to understand how the parameters are set in this model to directly compare with the UMAT model.

Chapter 9 Conclusions and Recommendations

9.1 Conclusions

This project originated within the longstanding collaboration between Terumo Aortic and the University of Strathclyde with the main goal of studying the behaviour of superelastic nitinol wire used to manufacture the medical device, the Anaconda stent graft, and further improve its design. Initially, this project had the main goal to extend and develop previous experimental work of Brodie and Boukis on preliminary compression testing and improve their test method by identifying and implementing a suitable specimen strain measurement with full field strain measurements of nitinol wire under compression as well as testing at different temperatures. On the FEA modelling work, the aim was to improve the commercially available constitutive models taking in account the experimental work and on this basis simulate both compression and bending behaviour as well as study the model capabilities under fatigue. Due to the many complications encountered when reproducing the preliminary compression test method, the main objective changed to focus on developing a new compression method and validate it by testing fine nitinol wire at high strain deformation. The present work thus centres on an iterative way of developing a new experimental compression test method.

This project had the main goal to experimentally characterized the nitinol wire under compressive loading by developing a repeatable compressive test method for fine nitinol wire able to achieve up to 6% strain. The importance of this work is work is described in Chapter 2, where it explains the need to improve the design of Anaconda stent graft design using numerical model to have a better understanding of the Anaconda devise in all different size ranges. Currently the numerical model commercially available and used in the industry present limitations when simulating the nitinol asymmetry, since during the cycle life of the Anaconda stent graft device the nitinol rings suffer high strains deformation under tension, compression, bending and torsion, it is important to have a good characterisation of nitinol wire under these deformations. The literature presented in Chapter 3, focus mainly on the compressive behaviour of nitinol, where little information

of nitinol is available in compression. When focusing on the behaviour of nitinol wire, only a few studies are available. This indicates a big gap in the literature of characterization of nitinol wire in compression. This way, the work presented in this thesis focus on the development of a compressive test method for nitinol wire with the aim to reduce the gap in the literature as well as gain more understanding of the behaviour of nitinol wire under compression loading. Before the characterisation of nitinol in compressive loading, a small test of nitinol wire in tensile test is presented in Chapter 4. The work started by studying the nitinol wire under tension, with the assistance of Boukis, to fully understand the tensile test method and the protocol used at Terumo Aortic laboratories. These tensile tests focused on replicate some of the localised transformation described in section 3.1.2.1 and previously reported by other authors, as well as understand the influence that the grips have on the tensile response of nitinol wire. From this study it was possible to demonstrate the localised deformation of nitinol wire under tension, understanding and verifying where the phase transformation initiates on the wire. The literature mention that the grips influence the initiation of the martensite nucleation due to the apparent stress concentration caused by the grips. This way, the work presented in this thesis looks also how different type of grips influence the martensite nucleation. It was verified that the grips do have an influence when looking at the localised deformation of the nitinol wire. The results presented in Chapter 3 of other authors, used the generic tensile grips to fix the samples contrary to the horn-like pneumatic grips used in this study. When using the horn-like pneumatic grips to test nitinol wire in tension, the wire is fixed opposite to the side where the test occurs, as seen in Figure 4.4. These grips prove to be good when testing the wire as explained by Boukis, but when studying the localised deformation of the nitinol wire, the part of the wire that goes around the grip is incurring deformation that is not detected by the video extensometer of the machine displacement. In Chapter 4 it was possible to replicate the strain localization of nitinol wire method presented by Shaw [19] using video extensometer with the GL placed at different areas of the wire and have a better understanding of the strain localisation presented in nitinol during tensile loading. Chapter 5 initiates the characterization of nitinol wire in compressive loading. The test method used in this chapter was developed by Brodie and

Boukis with the aim to improve the test methos by adding DIC to obtain the strain field of the sample surface along the test. When trying to replicate the compression testing, the test method used initially proved not to be viable for testing nitinol wire. As described in Chapter 4, it was very challenging to reproduce previous results, the application of DIC to obtain a full field strain of the sample was not successful and finally, it was shown that the sample moved while the test was occurring. The fact that the sample in this test method is placed horizontally, makes it harder to fix the sample during the test. A new test method was therefore developed to test nitinol wire.

Chapter 6 describe all the adaptations made to this new test until it was possible to obtain a repeatable stress-strain response. This test method was developed to use the same nitinol samples of 1 mm diameter wire, to have the same material processing history used in the Anaconda stent graft device. This method consists in placing the small sample vertically in the bottom compressive platen using tweezers to hold the sample. The sample is fixed by placing the upper platen on the top surface of the sample creating a pre-load to hold the sample in place. This test proved to be viable for obtaining repeatable compression test data.

Chapter 7 focus on validating the test method. A video extensometer was also added to the test to obtain the deformation between the platens. The test was validated through an extensive repetition of compression tests using different sample lengths, ranging from 1 mm to 4 mm long with increments of 0.5 mm. Since 3.5 mm and 4 mm sample length was not tested before, a buckling study is also presented in this chapter to guarantee both sample length does not reach the critical buckling force during the compression test. After the validation of the results, with the verification that the samples do not suffer unwanted modes of deformation when longer samples are used, two studies are presented to give a better understanding of the test method and samples used. The first of these consisted of studying the ratio between the sample length and diameter. From this study it was verified that the stress-strain response in compression did not change according to the sample length, instead the tendency for the creation of three different groups of responses was observed. The L/D ratio of 1 formed one group. The L/D ratio of 1.5 and 2 formed a

second group and finally the last group was composed by the L/D ratio of 2.5, 3, 3.5 and 4. The formation of these groups is proven to be a consequence of the test, where when testing samples of 1 mm long, the material stiffness of the sample appears to be higher than the machine stiffness. With the study of the L/D ration it is possible to conclude that the ideal sample length to use is between 2.5 mm and 4 mm, being the latest the preferred length due to being easier to use the samples. The second study consisted of testing the method in a temperature-controlled environment. No conclusions were obtained with this study due to limitations of the equipment used.

The FEA model presented in this work, follows a different approach from previous work. The Auricchio constitutive model available in the commercial software Abaqus is used because it is the software used at Terumo Aortic on the design of stent grafts. The approach presented in this work uses the parameters obtained from compression tests instead of tension parameters, similar to that which Brodie presented in his work, where the main difference is the symmetry of the model, which is not used in this work, as explained in Chapter 8. The results obtained shown a slight improvement of the compression stress-strain response where the model was able to reproduce some non-linearity during the martensite transformation, but this approach, although not tested, is not suitable for in-service bending tests because it only takes in account the compression parameters and not the tension parameters. A different alternative, non-commercial, model was also tested in the present work. The model was developed by Kelly and Stebner and the stress-strain results of this model, presented in Chapter 8, were performed by Stebner. Looking at the stress-strain curves presented by Stebner, this model caused some curiosity within the Terumo Aortic engineers due to the apparent ability to simulate the asymmetry of nitinol. Although Stebner results looks promising, no conclusions are possible to obtain from this work due to the unknown assumptions associated to this analysis. A deeper understanding of this model is necessary to be able to reproduce the stress-strain curves withing Terumo Aortic research team to validate the model and implement it in the finite element software Abaqus. To validate the assumptions made in Chapter 7 regarding the size dependency observed between the sample length and diameter during the compressive test, a different

model should be use, for example, a micromechanical model to study the grain structure/microstructure of the nitinol wire. This study is out of the scope of the design of the stent graft medical device; therefore, it was not taken in consideration for this work.

In conclusion, the work described in this thesis present a very extensive experimental work, both in tensile and mainly in compression that will be used to improve the current simulation models of the Anaconda stent graft device. It can be concluded that the main objective of this project has been met, as a new compression test method has been demonstrated as reproducible for testing nitinol wire as well as the characterization of the compressive behaviour of nitinol wire presented here. The compressive method presented in this work is also intended to be applied to different materials, surpassing this way the goals initially proposed for this work, where it was achieved a method able to compress nitinol wire at high strains and characterise the material for medical applications as well as reducing some of the gap currently available in characterising metal wires for different final applications. Furthermore, the experimental testing provided useful input data to validate the existing Abaqus FEA-based material model for compression behaviour.

9.2 Recommendations for tensile testing

Although tensile testing is not part of the main scope for this project, some recommendations will be described here for future work to conclude the work presented here.

The recommendations suggested in this work is to improve tensile testing focus on the future work of localised deformation. It is recommended to perform the study 2 presented in section 4.3.2 using DIC technology to obtain the full field strain of the nitinol wire during the tensile test as well as obtain the tensile stress-strain response using the generic pneumatic tensile grips and later compare the results with the literature review presented in Chapter 3.

9.3 Recommendations for compression testing

The compression test method presented in this work proved to be reproducible when testing nitinol wire at high strain deformation, but some extra studies would benefit the method.

For future work it is important to test different techniques to control the temperature during the compression tests, where a temperature-controlled water bath is suggested as next step. Also, a full field strain measurement of the nitinol wire during compression is suggested to confirm the absence of any localised deformation in the compressive behaviour.

Regarding the samples, extra care needs to be taken when obtaining new sample, where it is important to make sure that both edges of the sample are polish and flat. It would also be interesting to continue increasing the sample length and reach a limit length to understand how the stress-strain response evolves during compression behaviour.

Finally, as mentioned at the beginning of Chapter 5, this compression test method was developed to later be able to test different metallic wire samples, therefore would be interesting to see if this test method can be adapted to different metal materials.

9.4 Recommendation for the numerical models

The recommendation for the numerical models is to focus on the model presented by Kelly and Stebner, where it is important to apply the model to bending deformation and understand any improvements in the prediction when compared with the work already published by Brodie regarding the numerical models that focused on the bending behaviour of superelastic nitinol wire.

References

[1] American Society for Testing and Materials, "ASTM F2516−14: Standard Test Method for Tension Testing of Nickel-Titanium Superelastic Materials," *ASTM Int.*, p. 6, 2015, doi: 10.1520/F2516-14.2.

[2] A. Boukis, "A comprehensive methodology for the experimental characterisation and numerical modelling of nickel-titanium wires used in medical devices," University of Strathclyde, 2019.

[3] R. Brodie, "Characterization of Superelastic Nitinol Wire for Application to Aortic Stent Graft Design," University of Strathclyde, 2018.

[4] A. Kelly, A. P. Stebner, and K. Bhattacharya, "A micromechanics-inspired constitutive model for shape-memory alloys that accounts for initiation and saturation of phase transformation," *J. Mech. Phys. Solids*, vol. 97, pp. 197–224, 2016, doi: 10.1016/j.jmps.2016.02.007.

[5] "Abdominal aortic aneurysm - NHS." [Online]. Available: https://www.nhs.uk/conditions/abdominal-aortic-aneurysm/. [Accessed: 25-Apr-2020].

[6] "Abdominal aortic aneurysm screening - Screening - Health topics - Public Health Scotland." [Online]. Available: http://www.healthscotland.scot/health-topics/screening/abdominal-aortic-aneurysm-screening. [Accessed: 26-Apr-2020].

[7] M. L. Dijkstra *et al.*, "Dutch experience with the fenestrated Anaconda endograft for short-neck infrarenal and juxtarenal abdominal aortic aneurysm repair," *J. Vasc. Surg.*, vol. 60, no. 2, pp. 301–307, 2014, doi: 10.1016/j.jvs.2014.02.011.

[8] "Anaconda™ AAA Stent Graft System for Challenging AAA Anatomy - Endovascular Today." [Online]. Available: https://evtoday.com/articles/2016-nov-supplement2/anaconda-aaa-stent-graft-system-for-challenging-aaa-anatomy. [Accessed: 25-Apr-2020].

[9] S. G. J. Rödel, R. H. Geelkerken, R. J. Prescott, H. J. Florek, P. Kasprzak, and J. Brunkwall, "The Anaconda™ AAA Stent Graft System: 2-Year Clinical and Technical Results of a Multicentre Clinical Evaluation," *Eur. J. Vasc. Endovasc. Surg.*, vol. 38, no. 6, pp. 732–740, 2009, doi: 10.1016/j.ejvs.2009.08.007.

[10] "Aortic Aneurysms | BSIR." [Online]. Available: https://www.bsir.org/patients/aortic-aneurysms/. [Accessed: 26-Apr-2020].

[11] T. Duerig, A. Pelton, and D. Sto, "An overview of nitinol medical applications," vol. 275, no. Materials Science and Engineering, pp. 149–160, 1999, doi: 10.1016/S0921-5093(99)00294-4.

[12] *Shape memory alloy engineering : for aerospace, structural and biomedical applications*. Kidlington, Oxford: Butterworth-Heinemann, 2015.

[13] A. Ziolkowski, *Pseudoelasticity of shape memory alloys : theory and experimental studies*. Elsevier, 2015.

[14] H. U. Schuerch, “Certain Physical Properties and Applications of Nitinol,” Washington, D.C., 1968.

[15] Q. Sun, R. Matsui, K. Takeda, and E. A. Pieczyska, Eds., *Advances in Shape Memory Materials*. Springer Nature, 2017.

[16] G. B. Kauffman and I. Mayo, “The Story of Nitinol: The Serendipitous Discovery of the Memory Metal and Its Applications,” vol. 2, no. 2, pp. 1–21, 1996.

[17] J. Mohd Jani, M. Leary, A. Subic, and M. A. Gibson, “A review of shape memory alloy research, applications and opportunities,” *Mater. Des.*, vol. 56, pp. 1078–1113, 2014, doi: 10.1016/j.matdes.2013.11.084.

[18] T. W. Duerig, K. N. Melton, D. Stöckel, and C. M. Wayman, *Engineering Aspects of Shape Memory Alloys*, vol. 1. Butterworth-Heinemann, 1990.

[19] J. A. Shaw and S. Kyriakides, “Thermomechanical aspects of NiTi,” *J. Mech. Phys. Solids*, vol. 43, no. 8, pp. 1243–1281, 1995, doi: 10.1016/0022-5096(95)00024-D.

[20] D. C. Lagoudas, Ed., *Shape Memory Alloys: Modelling and Engineering Applications*. Springer International Publishing, 2008.

[21] J. A. Shaw, C. B. Churchill, and M. A. Iadicola, “TIPS AND TRICKS FOR CHARACTERIZING SHAPE MEMORY ALLOY WIRE: PART 1-DIFFERENTIAL SCANNING CALORIMETRY AND BASIC PHENOMENA,” *Exp. Tech.*, vol. 32, no. 5, pp. 55–62, Sep. 2008, doi: 10.1111/j.1747-1567.2008.00410.x.

[22] D. Jiang, S. Kyriakides, C. M. Landis, and K. Kazinakis, “Modeling of propagation of phase transformation fronts in NiTi under uniaxial tension,” *Eur. J. Mech. A/Solids*, vol. 64, pp. 131–142, 2017, doi: 10.1016/j.euromechsol.2017.02.004.

[23] L. Orgeas and D. Favier, “Non-symmetric tension-compression behaviour of NiTi alloy,” *J. Phys. IV*, vol. C8, no. December, pp. 605–610, 1995, doi: 10.1051/jp4/199558605.

[24] L. Orgéas and D. Favier, “Stress-induced martensitic transformation of a NiTi alloy in isothermal shear, tension and compression,” *Acta Mater.*, vol. 46, no. 15, pp. 5579–5591, 1998, doi: 10.1016/S1359-6454(98)00167-0.

[25] N. J. Bechle and S. Kyriakides, “Localization in NiTi tubes under bending,” *Int. J. Solids Struct.*, vol. 51, no. 5, pp. 967–980, 2014, doi: 10.1016/j.ijsolstr.2013.11.023.

[26] D. Siddons and R. J. Moon, “Tensile and compression performance of superelastic NiTi tubing,” *Mater. Sci. Technol.*, vol. 17, no. September, pp. 1073–1078, 2001, doi: 10.1179/026708301101511202.

[27] B. Reedlunn, C. B. Churchill, E. E. Nelson, J. A. Shaw, and S. H. Daly, “Tension, compression, and bending of superelastic shape memory alloy tubes,” *J. Mech. Phys. Solids*, vol. 63, no. 1, pp. 506–537, 2014, doi: 10.1016/j.jmps.2012.12.012.

[28] E. Henderson, D. H. Nash, and W. M. Dempster, “On the experimental testing of fine Nitinol wires for medical devices,” *J. Mech. Behav. Biomed. Mater.*, vol. 4, no. 3, pp. 261–

268, 2011, doi: 10.1016/j.jmbbm.2010.10.004.

[29] C. Elibol and M. F.-X. Wagner, “Investigation of the stress-induced martensitic transformation in pseudoelastic NiTi under uniaxial tension, compression and compression–shear,” *Mater. Sci. Eng. A*, vol. 621, pp. 76–81, 2015, doi: 10.1016/j.msea.2014.10.054.

[30] A. Jalaeefar and B. Asgarian, “Experimental Investigation of Mechanical Properties of Nitinol , Structural Steel , and Their Hybrid Component,” vol. 09, no. October, pp. 1498–1505, 2013, doi: 10.1061/(ASCE)MT.1943-5533.0000701.

[31] Z. Xie, Y. Liu, and J. Van Humbeeck, “Microstructure of NiTi shape memory alloy due to tension–compression cyclic deformation,” *Acta Mater.*, vol. 46, no. 6, pp. 1989–2000, 1998, doi: 10.1016/S1359-6454(97)00379-0.

[32] Y. Liu, Z. Xie, J. Van Humbeeck, and L. Delaey, “Asymmetry of stress–strain curves under tension and compression for NiTi shape memory alloys,” *Acta Mater.*, vol. 46, no. 12, pp. 4325–4338, 1998, doi: 10.1016/S1359-6454(98)00112-8.

[33] A. Saigal and M. Fonte, “Solid, shape recovered ‘bulk’ Nitinol: Part I-Tension-compression asymmetry,” *Mater. Sci. Eng. A*, vol. 528, no. 16–17, pp. 5536–5550, 2011, doi: 10.1016/j.msea.2011.03.060.

[34] W. W. Chen, Q. P. Wu, J. H. Kang, and N. A. Winfree, “Compressive superelastic behavior of a NiTi shape memory alloy at strain rates of 0.001-750 s-1,” *Int. J. Solids Struct.*, vol. 38, no. 50–51, pp. 8989–8998, 2001, doi: 10.1016/S0020-7683(01)00165-2.

[35] S. Nemat-Nasser and J. Y. Choi, “Strain rate dependence of deformation mechanisms in a Ni-Ti-Cr shape-memory alloy,” *Acta Mater.*, vol. 53, no. 2, pp. 449–454, 2005, doi: 10.1016/j.actamat.2004.10.001.

[36] S. Nemat-Nasser, J. Y. Choi, W. G. Guo, and J. B. Isaacs, “Very high strain-rate response of a NiTi shape-memory alloy,” *Mech. Mater.*, vol. 37, no. 2-3 SPEC. ISS., pp. 287–298, 2005, doi: 10.1016/j.mechmat.2004.03.007.

[37] S. Nemat-Nasser and W. G. Guo, “Superelastic and cyclic response of NiTi SMA at various strain rates and temperatures,” *Mech. Mater.*, vol. 38, no. 5–6, pp. 463–474, 2006, doi: 10.1016/j.mechmat.2005.07.004.

[38] R. R. Adharapurapu, F. Jiang, K. S. Vecchio, and G. T. Gray, “Response of NiTi shape memory alloy at high strain rate: A systematic investigation of temperature effects on tension-compression asymmetry,” *Acta Mater.*, vol. 54, no. 17, pp. 4609–4620, 2006, doi: 10.1016/j.actamat.2006.05.047.

[39] K. Zhang and Q. Sun, “Cyclic Compressive Responses of NiTi Shape Memory Alloy---Effects of Loading Frequency,” in *Advances in Shape Memory Materials: In Commemoration of the Retirement of Professor Hisaaki Tobushi*, Q. Sun, R. Matsui, K. Takeda, and E. A. Pieczyska, Eds. Cham: Springer International Publishing, 2017, pp. 231–241.

[40] P. Šittner, L. Heller, J. Pilch, C. Curfs, T. Alonso, and D. Favier, “Young’s modulus of austenite and martensite phases in superelastic NiTi wires,” *J. Mater. Eng. Perform.*, vol.

23, no. 7, pp. 2303–2314, 2014, doi: 10.1007/s11665-014-0976-x.

[41] A. N. Bucsek, H. M. Paranjape, and A. P. Stebner, “Myths and Truths of Nitinol Mechanics: Elasticity and Tension–Compression Asymmetry,” *Shape Mem. Superelasticity*, vol. 2, no. 3, pp. 264–271, 2016, doi: 10.1007/s40830-016-0074-z.

[42] S. C. Mao, J. F. Luo, Z. Zhang, M. H. Wu, Y. Liu, and X. D. Han, “EBSD studies of the stress-induced B2-B19′ martensitic transformation in NiTi tubes under uniaxial tension and compression,” *Acta Mater.*, vol. 58, no. 9, pp. 3357–3366, May 2010, doi: 10.1016/J.ACTAMAT.2010.02.009.

[43] T. W. Duerig, A. R. Pelton, and K. Bhattacharya, “The Measurement and Interpretation of Transformation Temperatures in Nitinol,” *Shape Mem. Superelasticity*, vol. 3, no. 4, pp. 485–498, 2017, doi: 10.1007/s40830-017-0133-0.

[44] Pelton, Duerig, and Wick, “We are Nitinol. ™ Experimental and FEM Analysis of the Bending Behaviour of Superelastic Tubing,” 1994.

[45] S. De la Flor, C. Urbina, and F. Ferrando, “Asymmetrical Bending Model for NiTi Shape Memory Wires: Numerical Simulations and Experimental Analysis,” *Strain*, vol. 47, no. 3, pp. 255–267, Jun. 2011, doi: 10.1111/j.1475-1305.2009.00679.x.

[46] K. Runesson, *CONSTITUTIVE MODELING OF ENGINEERING MATERIALS - THEORY AND COMPUTATION - The Primer*, 7th ed. 2006.

[47] C. Cisse, W. Zaki, and T. Ben Zineb, “A review of constitutive models and modeling techniques for shape memory alloys,” *Int. J. Plast.*, vol. 76, pp. 244–284, 2016, doi: 10.1016/j.ijplas.2015.08.006.

[48] F. Falk, “Model free energy, mechanics, and thermodynamics of shape memory alloys,” *Acta Metall.*, vol. 28, no. 12, pp. 1773–1780, Dec. 1980, doi: 10.1016/0001-6160(80)90030-9.

[49] F. Falk, “Ginzburg-Landau Theory of Static Domain Walls in Shape-Memory Alloys,” 1983.

[50] Q. P. Sun and K. C. Hwang, “Micromechanics modelling for the constitutive behavior of polycrystalline shape memory alloys-I. Derivation of general relations,” *J. Mech. Phys. Solids*, vol. 41, no. 1, pp. 1–17, Jan. 1993, doi: 10.1016/0022-5096(93)90060-S.

[51] M. Huang, X. Gao, and L. C. Brinson, “Multivariant micromechanical model for SMAs. Part 2. Polycrystal model,” *Int. J. Plast.*, vol. 16, no. 10, pp. 1371–1390, Jan. 2000, doi: 10.1016/S0749-6419(00)00014-0.

[52] P. Blanc and C. Lexcellent, “Micromechanical modelling of a CuAlNi shape memory alloy behaviour,” *Mater. Sci. Eng. A*, vol. 378, no. 1-2 SPEC. ISS., pp. 465–469, Jul. 2004, doi: 10.1016/j.msea.2003.11.065.

[53] A. Sadjadpour and K. Bhattacharya, “A micromechanics-inspired constitutive model for shape-memory alloys,” *Smart Mater. Struct.*, vol. 16, no. 5, pp. 1751–1765, 2007, doi: 10.1088/0964-1726/16/5/030.

[54] V. I. Levitas and I. B. Ozsoy, “Micromechanical modeling of stress-induced phase transformations. Part 1. Thermodynamics and kinetics of coupled interface propagation and reorientation,” *Int. J. Plast.*, vol. 25, no. 2, pp. 239–280, Feb. 2009, doi: 10.1016/j.ijplas.2008.02.004.

[55] F. Auricchio, R. L. Taylor, and J. Lubliner, “Shape-memory alloys: Macromodelling and numerical simulations of the superelastic behavior,” *Comput. Methods Appl. Mech. Eng.*, vol. 146, no. 3–4, pp. 281–312, 1997, doi: 10.1016/S0045-7825(96)01232-7.

[56] F. Auricchio and R. L. Taylor, “Shape-memory alloys: modelling and numerical simulations of the finite-strain superelastic behavior,” *Comput. Methods Appl. Mech. Eng.*, vol. 143, no. 1–2, pp. 175–194, 1997, doi: 10.1016/S0045-7825(96)01147-4.

[57] J. G. Boyd and D. C. Lagoudas, “a Thermodynamical Constitutive Model for Shape Memory Materials,” *Int. J. Plast.*, pp. 1–40, 1996.

[58] X. Gong and A. Pelton, “Finite element analysis and experimental evaluation of superelastic Nitinol stent,” *SMST 2003 Int. Conf. Shape Mem. Superelastic Technol.*, pp. 453–462, 2004.

[59] F. Nematzadeh and S. K. Sadrnezhaad, “Effects of material properties on mechanical performance of Nitinol stent designed for femoral artery: Finite element analysis,” *Sci. Iran.*, vol. 19, no. 6, pp. 1564–1571, Dec. 2012, doi: 10.1016/J.SCIENT.2012.10.024.

[60] J. Lubliner, “A simple model of generalized plasticity,” *Int. J. Solids Struct.*, vol. 28, no. 6, pp. 769–778, 1991, doi: 10.1016/0020-7683(91)90155-9.

[61] J. Lubliner and F. Auricchio, “Generalized plasticity and shape-memory alloys,” *Int. J. Solids Struct.*, vol. 33, no. 7, pp. 991–1003, 1996, doi: 10.1016/0020-7683(95)00082-8.

[62] F. Auricchio and E. Sacco, “A one-dimensional model for superelastic shape-memory alloys with different elastic properties between austenite and martensite,” *Int. J. Non. Linear. Mech.*, vol. 32, no. 6, pp. 1101–1114, 1997, doi: 10.1016/s0020-7462(96)00130-8.

[63] F. Auricchio, “A robust integration-algorithm for a finite-strain shape-memory-alloy superelastic model,” *Int. J. Plast.*, vol. 17, no. 7, pp. 971–990, 2001, doi: 10.1016/S0749-6419(00)00050-4.

[64] N. Rebelo, N. Walker, and H. Foadian, “Simulation of Implantable Stents,” in *Abaqus Users Conference*, 2001, pp. 421–434.

[65] Dassault Systèmes Simulia Corp., “Abaqus Technology Brief: Simulation of Implantable Nitinol Stents,” *Abaqus Technol. Br.*, no. April, pp. 3–5, 2007.

[66] “Plasticity model for superelastic materials.” [Online]. Available: https://abaqus-docs.mit.edu/2017/English/SIMACAEMATRefMap/simamat-c-plastsuperelastic.htm. [Accessed: 25-Apr-2020].

[67] F. Auricchio and L. Petrini, “Improvements and algorithmical considerations on a recent three-dimensional model describing stress-induced solid phase transformations,” *Int. J. Numer. Methods Eng.*, vol. 55, no. 11, pp. 1255–1284, 2002, doi: 10.1002/nme.619.

[68] F. Auricchio, S. Marfia, and E. Sacco, “Modelling of SMA materials: Training and two way memory effects,” *Comput. Struct.*, vol. 81, no. 24–25, pp. 2301–2317, 2003, doi: 10.1016/S0045-7949(03)00319-5.

[69] F. Auricchio and A. Reali, “A phenomenological one-dimensional model describing stress-induced solid phase transformation with permanent inelasticity,” *Mech. Adv. Mater. Struct.*, vol. 14, no. 1, pp. 43–55, 2007, doi: 10.1080/15376490600864570.

[70] F. Auricchio, A. Reali, and U. Stefanelli, “A three-dimensional model describing stress-induced solid phase transformation with permanent inelasticity,” *Int. J. Plast.*, vol. 23, no. 2, pp. 207–226, 2007, doi: 10.1016/j.ijplas.2006.02.012.

[71] F. Auricchio, A. Reali, and U. Stefanelli, “A macroscopic 1D model for shape memory alloys including asymmetric behaviors and transformation-dependent elastic properties,” *Comput. Methods Appl. Mech. Eng.*, vol. 198, no. 17–20, pp. 1631–1637, 2009, doi: 10.1016/j.cma.2009.01.019.

[72] F. Auricchio and E. Bonetti, “A new ‘flexible’ 3D macroscopic model for shape memory alloys,” *Discret. Contin. Dyn. Syst. - Ser. S*, vol. 6, no. 2, pp. 277–291, 2013, doi: 10.3934/dcdss.2013.6.277.

[73] F. Auricchio, E. Bonetti, G. Scalet, and F. Ubertini, “Theoretical and numerical modeling of shape memory alloys accounting for multiple phase transformations and martensite reorientation,” *Int. J. Plast.*, vol. 59, pp. 30–54, 2014, doi: 10.1016/j.ijplas.2014.03.008.

[74] A. Sadjadpour and K. Bhattacharya, “A micromechanics inspired constitutive model for shape-memory alloys: The one-dimensional case,” *Smart Mater. Struct.*, vol. 16, no. 1, 2007, doi: 10.1088/0964-1726/16/1/S06.

[75] O. Cazacu, B. Plunkett, and F. Barlat, “Orthotropic yield criterion for hexagonal closed packed metals,” *Int. J. Plast.*, vol. 22, no. 7, pp. 1171–1194, 2006, doi: 10.1016/j.ijplas.2005.06.001.

[76] M. Panico and L. C. Brinson, “A three-dimensional phenomenological model for martensite reorientation in shape memory alloys,” *J. Mech. Phys. Solids*, vol. 55, no. 11, pp. 2491–2511, 2007, doi: 10.1016/j.jmps.2007.03.010.

[77] Y. Chemisky, A. Duval, E. Patoor, and T. Ben Zineb, “Constitutive model for shape memory alloys including phase transformation, martensitic reorientation and twins accommodation,” *Mech. Mater.*, vol. 43, no. 7, pp. 361–376, 2011, doi: 10.1016/j.mechmat.2011.04.003.

[78] “2kN & 5kN Tensile compression and horizontal bending stage - Deben UK – SEM accessories & tensile testing.” [Online]. Available: https://deben.co.uk/tensile-testing/sem/2kn-5kn-tensile-compression-and-horizontal-bending-stage/. [Accessed: 01-May-2020].

[79] T. Tokunaga *et al.*, “Temperature distributions of electron beam-irradiated samples by scanning electron microscopy,” *J. Microsc.*, vol. 248, no. 3, pp. 228–233, 2012, doi: 10.1111/j.1365-2818.2012.03666.x.

[80] A. D. Kammers and S. Daly, “Self-Assembled Nanoparticle Surface Patterning for Improved Digital Image Correlation in a Scanning Electron Microscope,” pp. 1333–1341, 2013, doi: 10.1007/s11340-013-9734-5.

[81] Instron, “5960 Series Universal Testing Systems - Instron.” [Online]. Available: https://www.instron.us/en/products/testing-systems/universal-testing-systems/electromechanical/5900-series/5960-dual-column. [Accessed: 02-Mar-2020].

[82] “No Title.” [Online]. Available: https://www.instron.us/en-us/our-company/library/test-types/compression-test. [Accessed: 13-Jan-2020].

[83] Instron, “Universal Testing Machine Compliance.” [Online]. Available: https://www.instron.com/-/media/literature-library/whitepapers/2010/12/compliance-correction.pdf. [Accessed: 08-May-2022].

[84] ASTM International, “E691-19 Standard Practice for Conducting an Interlaboratory Study to Determine the Precision of a Test Method.” ASTM International, West Conshohocken, PA, 2019, doi: https://doi.org/10.1520/E0691-19.

[85] Dassault Systèmes Simulia Corp., “UMAT for Superelasticity and Plasticity of Shape Memory Alloys.” .

[86] R. C. Brodie, W. M. Dempster, D. Bow, M. C. Van Zyl, and D. H. Nash, “ANALYSIS, DESIGN AND PRODUCTION OF PRODUCTS COMPRISING SUPERELASTIC MATERIALS,” WO 2014/184591 Al, 2014.

Appendix A: Image sequence of deployment of the Anaconda device

Images obtained from an institutional video disseminated by Terumo Aortic.

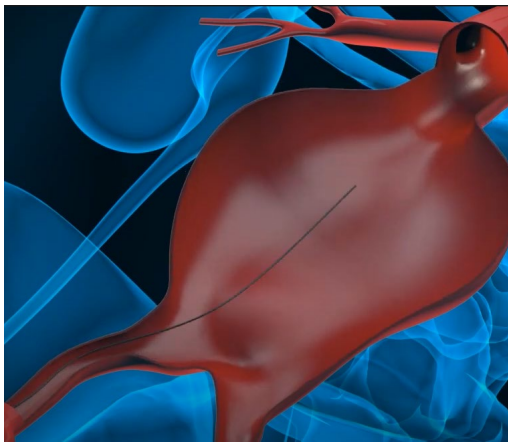

a)

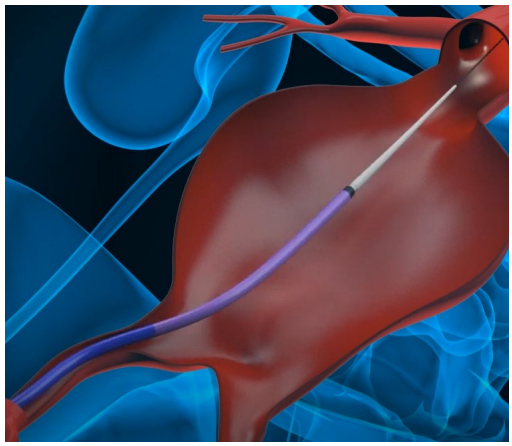

b)

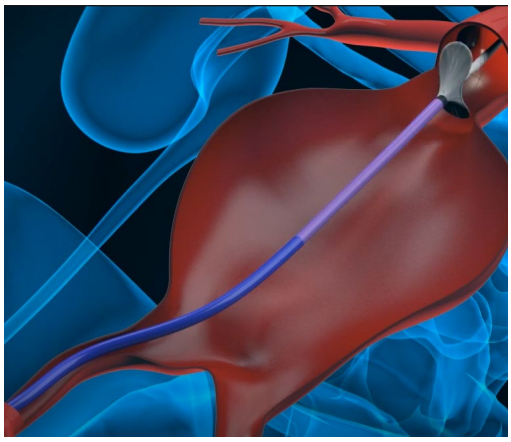

c)

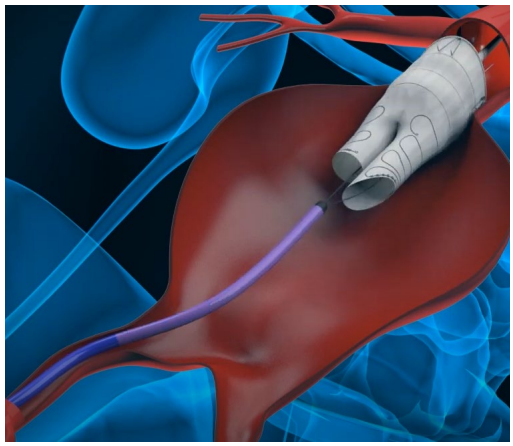

d)

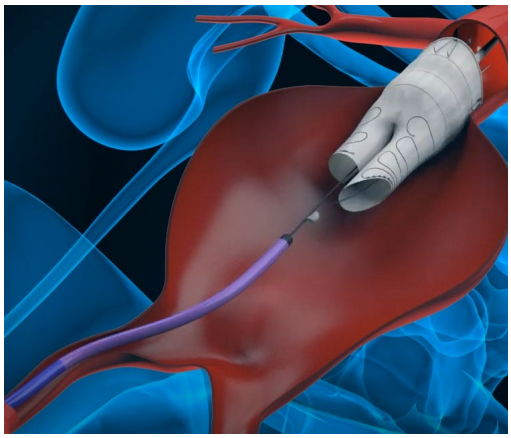

e)

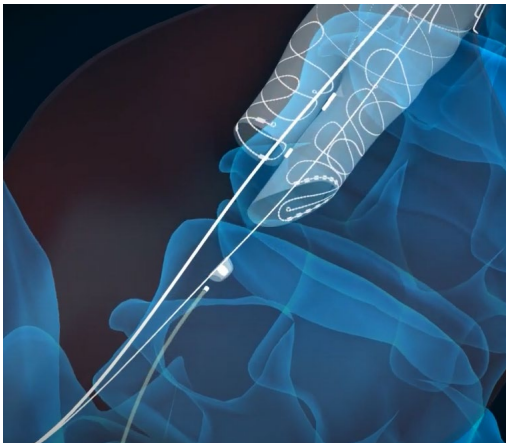

f)

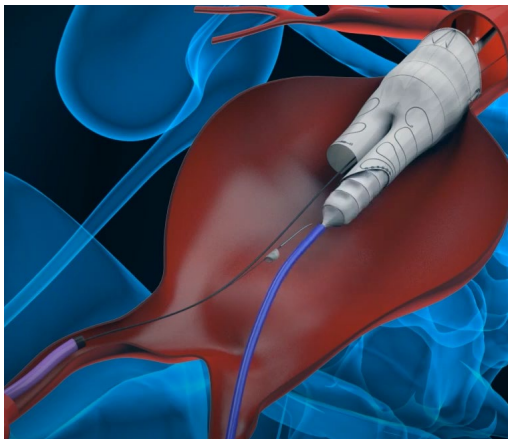

g)

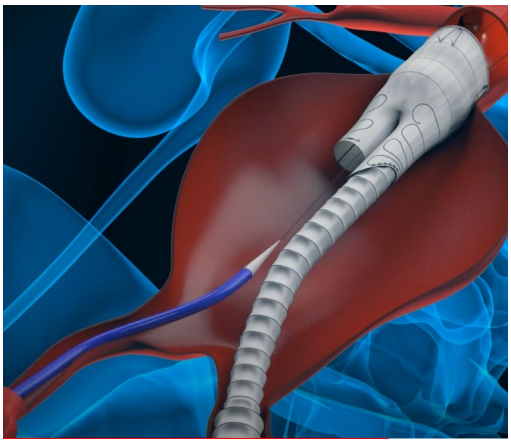

h)

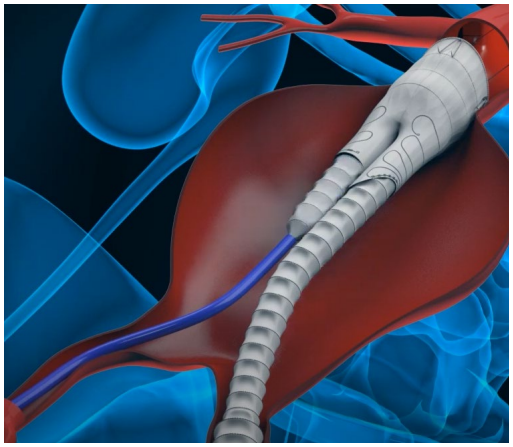

i)

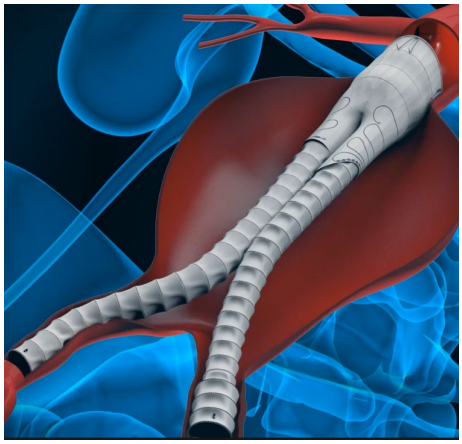

j)

Figure A.1 – Image sequence of Anaconda device deployment

Appendix B: Video during a compression test

Figure B-1 – Video of a compression test performed inside the SEM.

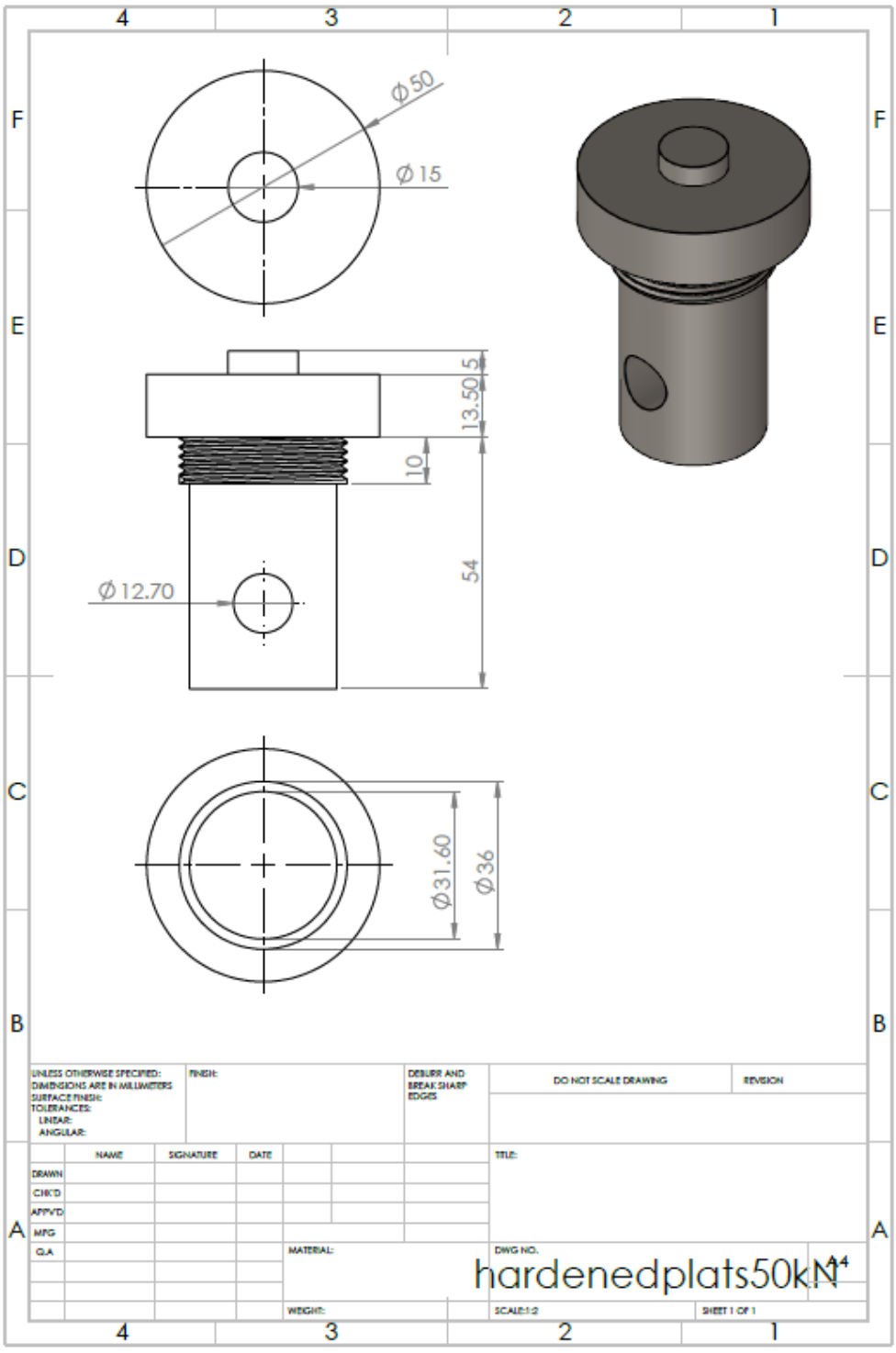

Figure C-1 – Technical drawing of the 50 kN platens

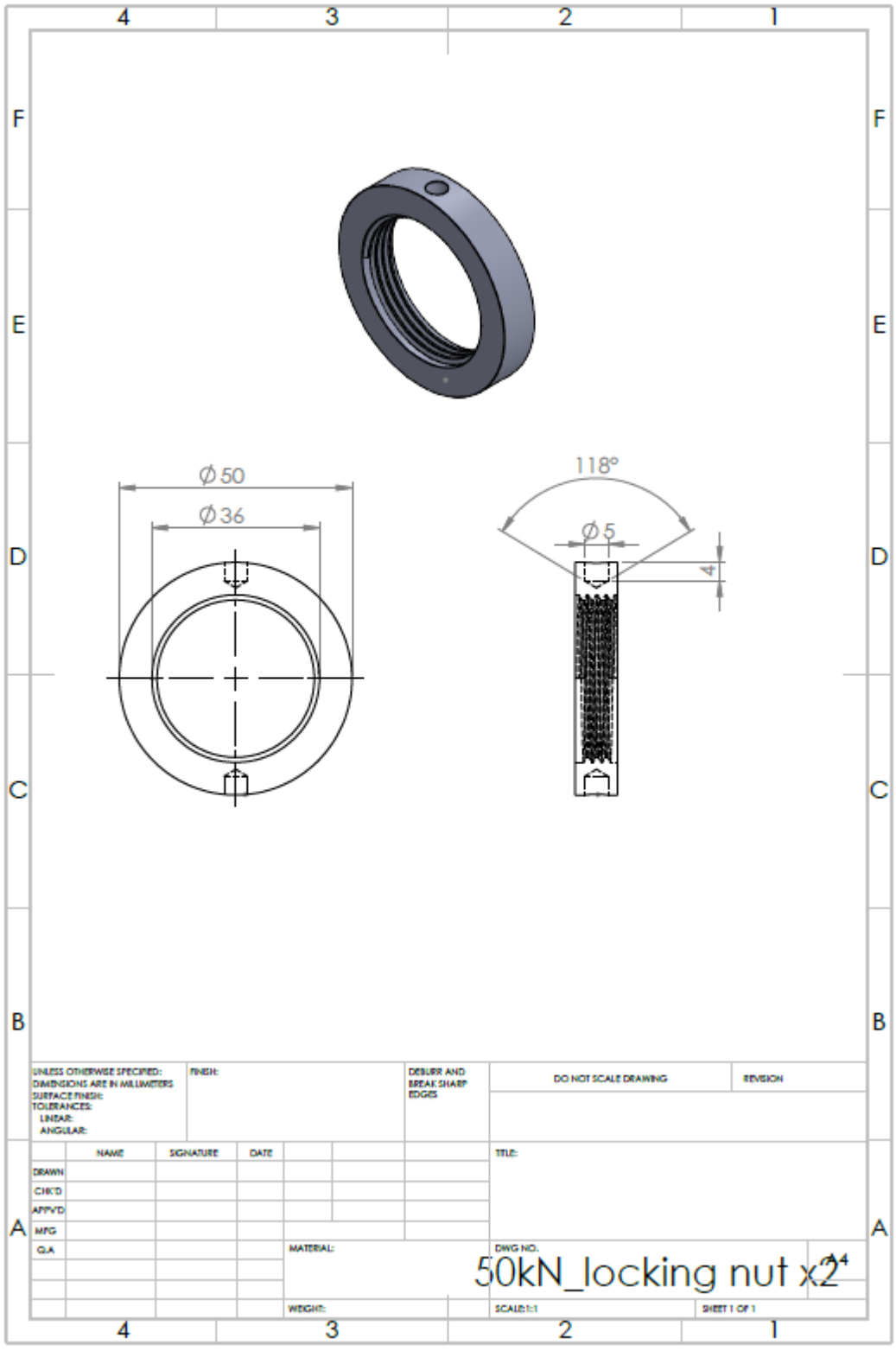

Figure C-2 – Technical drawing of the locking nut for the 50 kN platens

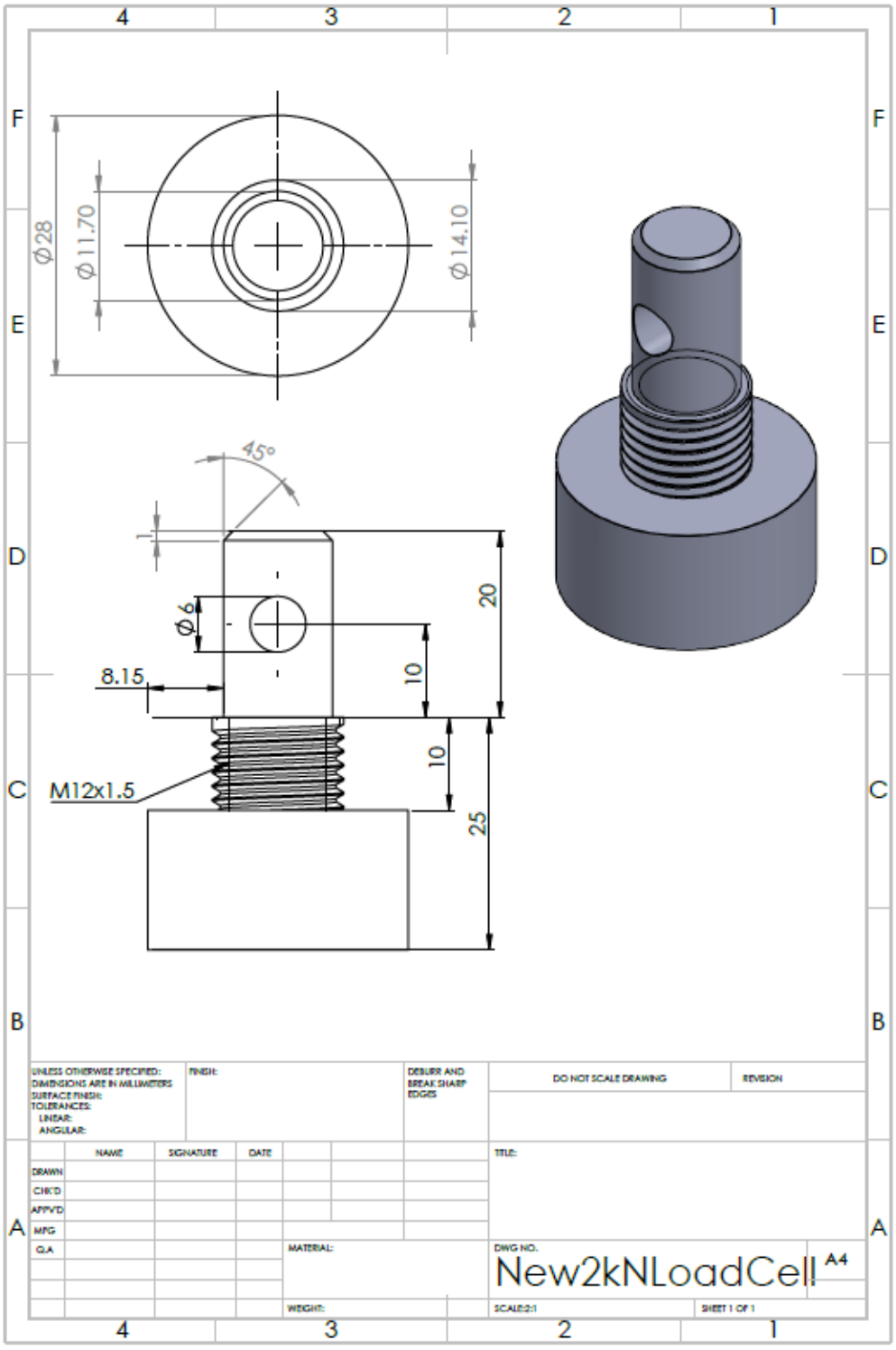

Figure C-3 – Technical drawing of the 2 kN platens

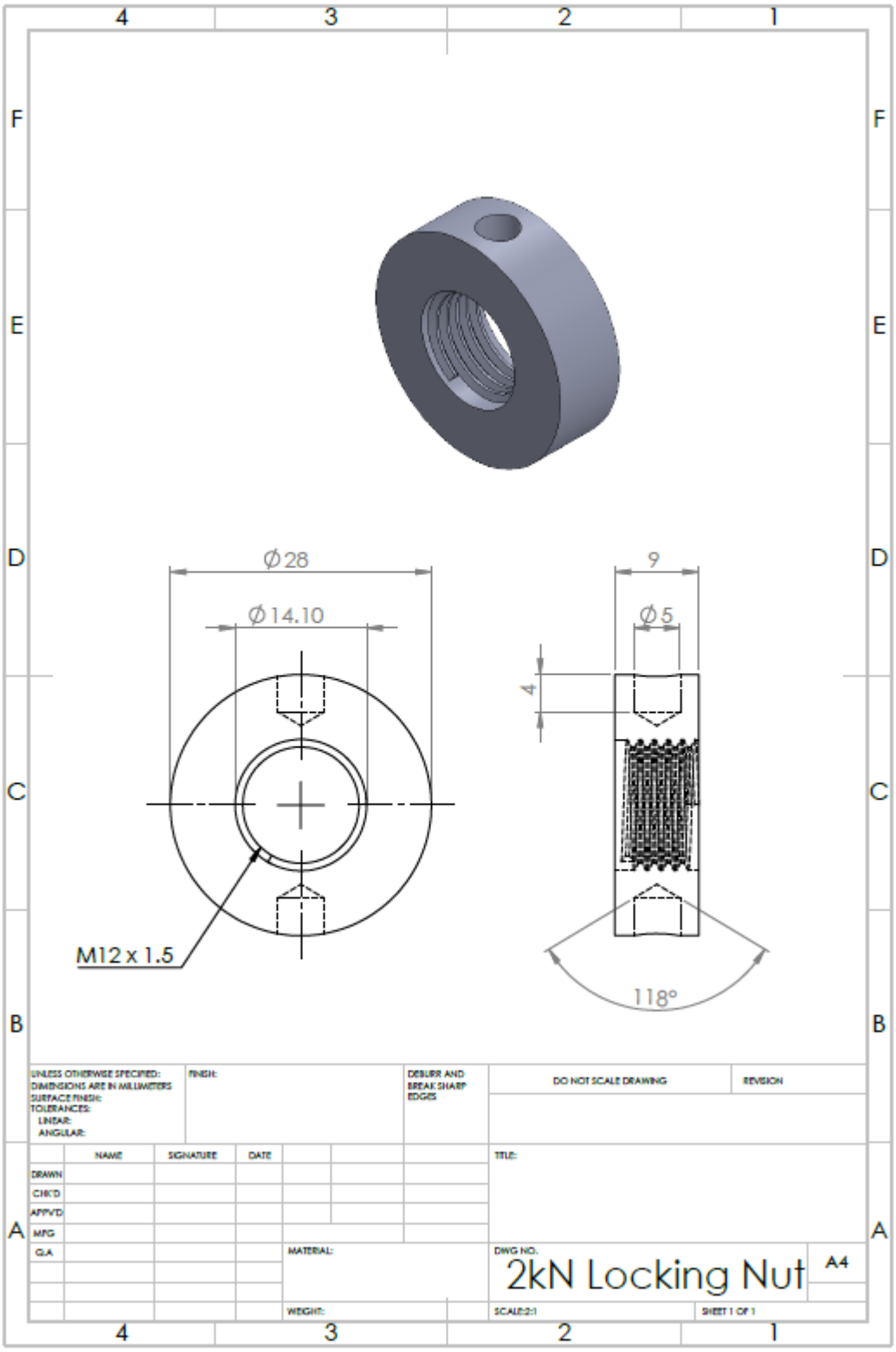

Figure C-4 – Technical drawing of the locking nut for the 2 kN platen

Appendix D: List of the compression tests

Table D-1 – List of the compression tests performed for the study of L/D ratio.

Test	Sample	Name	Strain (%)/(mm)		L_S (mm)	T (°C)	Li (mm)	Gage Length	Pre-load (N)	Max load (N)
1	N1	N1_1_1_2%_25	2	0.02	1	25	1.06	3.851	2	25
2	N2	N2_2_1_2%_25	2	0.02	1	25	1.04	3.663	3.2	47.8
3	N5	N5_3_1_2%_25	2	0.02	1	25	1.04	3.670	1.1	23.9
4	N1	N1_4_1_3%_25	3	0.03	1	25	1.06	3.85	2	40.6
5	N2	N2_5_1_3%_25	3	0.03	1	25	1.04	3.663	2.2	100.7
6	N5	N5_6_1_3%_25	3	0.03	1	25	1.04	3.661	2.5	78.9
7	N1	N1_7_1_4%_25	4	0.04	1	25	1.06	3.845	1	58.3
8	N2	N2_8_1_4%_25	4	0.04	1	25	1.04	3.663	3.1	236.6
9	N5	N5_9_1_4%_25	4	0.04	1	25	1.04	3.659	1	190.2
10	N1	N1_10_1_5%_25	5	0.05	1	25	1.06	3.839	1	100.2
11	N2	N2_11_1_5%_25	5	0.05	1	25	1.04	3.663	3.3	407
12	N5	N5_12_1_5%_25	5	0.05	1	25	1.04	-	0.3	244.7

13	N1	N1_13_1_6%_25	6	0.06	1	25	1.06	3.815	1	312.1
14	N2	N2_14_1_6%_25	6	0.06	1	25	1.04	3.675	3	474.8
15	N5	N5_15_1_6%_25	6	0.06	1	25	1.04	-	2.5	433.5
16	N8	N8_16_1.5_2%_25	2	0.03	1.5	25	1.51	4.251	4	152.7
17	N9	N9_17_1.5_2%_25	2	0.03	1.5	25	1.52	4.180	2	294.3
18	N12	N12_18_1.5_2%_25	2	0.03	1.5	25	1.52	4.184	2	136.4
19	N8	N8_19_1.5_3%_25	3	0.045	1.5	25	1.51	4.254	6	268.9
20	N9	N9_20_1.5_3%_25	3	0.045	1.5	25	1.52	4.177	1	560
21	N12	N12_21_1.5_3%_25	3	0.045	1.5	25	1.52	4.204	2	496.5
22	N8	N8_22_1.5_4%_25	4	0.06	1.5	25	1.51	4.246	5	540.4
23	N9	N9_23_1.5_4%_25	4	0.06	1.5	25	1.52	4.173	1	653.4
24	N12	N12_24_1.5_4%_25	4	0.06	1.5	25	1.52	4.183	1	635.3
25	N8	N8_25_1.5_5%_25	5	0.075	1.5	25	1.51	4.242	3	661
26	N9	N9_26_1.5_5%_25	5	0.075	1.5	25	1.52	4.172	1.2	722

27	N12	N12_27_1.5_5%_25	5	0.075	1.5	25	1.52	4.175	2	680.7
28	N8	N8_28_1.5_6%_25	6	0.09	1.5	25	1.51	4.24	3	737.5
29	N9	N9_29_1.5_6%_25	6	0.09	1.5	25	1.52	4.166	1	891.5
30	N12	N12_30_1.5_6%_25	6	0.09	1.5	25	1.52	4.177	3.1	834.1
31	N15	N15_31_2_2%_25	2	0.04	2	25	2.02	4.787	1.2	147
32	N16	N16_32_2_2%_25	2	0.04	2	25	2.01	4.663	4.5	206.6
33	N19	N19_33_2_2%_25	2	0.04	2	25	2.04	4.704	1	70.8
34	N15	N15_34_2_3%_25	3	0.06	2	25	2.02	4.785	2	384.4
35	N16	N16_35_2_3%_25	3	0.06	2	25	2.01	4.663	4	448.6
36	N19	N19_36_2_3%_25	3	0.06	2	25	2.04	4.692	2	280.2
37	N15	N15_37_2_4%_25	4	0.08	2	25	2.02	4.778	2	621.6
38	N16	N16_38_2_4%_25	4	0.08	2	25	2.01	4.669	1	603.1
39	N19	N19_39_2_4%_25	4	0.08	2	25	2.04	4.690	2.9	542.5
40	N15	N15_40_2_5%_25	5	0.1	2	25	2.02	4.778	3	687.3
41	N16	N16_41_2_5%_25	5	0.1	2	25	2.01	4.661	1	685.3

42	N19	N19_42_2_5%_25	5	0.1	2	25	2.04	4.686	2	663.6
43	N15	N15_43_2_6%_25	6	0.12	2	25	2.02	4.785	3	736.8
44	N16	N16_44_2_6%_25	6	0.12	2	25	2.01	4.657	1	819.2
45	N19	N19_45_2_6%_25	6	0.12	2	25	2.04	4.683	2	730.4
46	N20	N20_46_2.5_2%_25	2	0.05	2.5	25	2.49	5.525	2	452.4
47	N21	N21_47_2.5_2%_25	2	0.05	2.5	25	2.5	5.242	3	292.1
48	N24	N24_48_2.5_2%_25	2	0.05	2.5	25	2.49	5.122	2	353.2
49	N20	N20_49_2.5_3%_25	3	0.075	2.5	25	2.49	5.517	2.1	651.4
50	N21	N21_50_2.5_3%_25	3	0.075	2.5	25	2.5	5.236	2	612.4
51	N24	N24_51_2.5_3%_25	3	0.075	2.5	25	2.49	5.126	3	615.8
52	N20	N20_52_2.5_4%_25	4	0.1	2.5	25	2.49	5.52	1.1	686.8
53	N21	N21_53_2.5_4%_25	4	0.1	2.5	25	2.5	5.240	0.6	667.3

54	N24	N24_54_2.5_4%_25	4	0.1	2.5	25	2.49	5.125	1.1	665.5
55	N20	N20_55_2.5_5%_25	5	0.125	2.5	25	2.49	5.516	2	807.4
56	N21	N21_56_2.5_5%_25	5	0.125	2.5	25	2.5	5.125	1	800.7
57	N24	N24_57_2.5_5%_25	5	0.125	2.5	25	2.49	5.110	2	800.6
58	N20	N20_58_2.5_6%_25	6	0.15	2.5	25	2.49	5.512	2	1060.3
59	N21	N21_59_2.5_6%_25	6	0.15	2.5	25	2.5	5.245	1.4	1021.5
60	N24	N24_60_2.5_6%_25	6	0.15	2.5	25	2.49	5.105	2	1060.1
61	S8	S8_61_3_2%_25	2	0.06	3	25	2.94	-	3.1	393.7
62	N41	N41_62_3_2%_25	2	0.06	3	25	2.99	5.537	3	532.8
63	N42	N42_63_3_2%_25	2	0.06	3	25	2.98	5.534	2	554.7
64	S8	S8_64_3_3%_25	3	0.09	3	25	2.94	-	8.7	536.8
65	N41	N41_65_3_3%_25	3	0.09	3	25	2.99	5.548	2.1	633.9

66	N42	N42_66_3_3%_25	3	0.09	3	25	2.98	5.53	2	657.4
67	S8	S8_67_3_4%_25	4	0.12	3	25	2.94	-	1	655.3
68	N41	N41_68_3_4%_25	4	0.12	3	25	2.99	5.557	2	682.7
69	N42	N42_69_3_4%_25	4	0.12	3	25	2.98	5.532	2.1	716.7
70	S8	S8_70_3_5%_25	5	0.15	3	25	2.94	-	7.1	850
71	N41	N41_71_3_5%_25	5	0.15	3	25	2.99	5.545	2	869.7
72	N42	N42_72_3_5%_25	5	0.15	3	25	2.98	5.532	1	855.2
73	S8	S8_73_3_6%_25	6	0.18	3	25	2.94	-	7.1	1058.7
74	N41	N41_74_3_6%_25	6	0.18	3	25	2.99	5.55	1	1170.3
75	N42	N42_75_3_6%_25	6	0.18	3	25	2.98	5.683	7	1053.4
76	N27	N27_76_3.5_2%_25	2	0.07	3.5	25	3.49	6.261	2	507.7
77	N28	N28_77_3.5_2%_25	2	0.07	3.5	25	3.49	6.003	1.1	500.8
78	N31	N31_78_3.5_2%_25	2	0.07	3.5	25	3.49	6.14	2	465.3
79	N27	N27_79_3.5_3%_25	3	0.105	3.5	25	3.49	6.25	2	655.8

80	N28	N28_80_3.5_3%_25	3	0.105	3.5	25	3.49	5.995	2	616.1
81	N31	N31_81_3.5_3%_25	3	0.105	3.5	25	3.49	6.141	3	648.4
82	N27	N27_82_3.5_4%_25	4	0.14	3.5	25	3.49	6.242	2.1	720.3
83	N28	N28_83_3.5_4%_25	4	0.14	3.5	25	3.49	5.99	2	702.1
84	N31	N31_84_3.5_4%_25	4	0.14	3.5	25	3.49	6.157	2	693
85	N27	N27_85_3.5_5%_25	5	0.175	3.5	25	3.49	6.241	2	877.6
86	N28	N28_86_3.5_5%_25	5	0.175	3.5	25	3.49	5.989	2	872.9
87	N31	N31_87_3.5_5%_25	5	0.175	3.5	25	3.49	6.158	2	861.6
88	N27	N27_88_3.5_6%_25	6	0.21	3.5	25	3.49	6.24	1.1	1143.6
89	N28	N28_89_3.5_6%_25	6	0.21	3.5	25	3.49	5.966	2	1015.7

90	N31	N31_90_3.5_6%_25	6	0.21	3.5	25	3.49	6.167	2	1156
91	N34	N34_91_4_2%_25	2	0.08	4	25	3.98	6.752	2.5	596.9
92	N35	N35_92_4_2%_25	2	0.08	4	25	4.01	6.683	3	491.5
93	N38	N38_93_4_2%_25	2	0.08	4	25	4	6.633	1.1	558.5
94	N34	N34_94_4_3%_25	3	0.12	4	25	3.98	6.755	2	655.7
95	N35	N35_95_4_3%_25	3	0.12	4	25	4.01	6.684	2	637.7
96	N38	N38_96_4_3%_25	3	0.12	4	25	4	6.553	1	656.7
97	N34	N34_97_4_4%_25	4	0.16	4	25	3.98	6.751	3	727.2
98	N35	N35_98_4_4%_25	4	0.16	4	25	4.01	6.67	1	713.7
99	N38	N38_99_4_4%_25	4	0.16	4	25	4	6.55	1	724.8
100	N34	N34_100_4_5%_25	5	0.2	4	25	3.98	6.747	4	899.8
101	N35	N35_101_4_5%_25	5	0.2	4	25	4.01	6.67	2.1	891.1
102	N38	N38_102_4_5%_25	5	0.2	4	25	4	6.554	1	869.1

103	N34	N34_103_4_6%_25	6	0.24	4	25	3.98	6.743	6.1	1198.7
104	N35	N35_104_4_6%_25	6	0.24	4	25	4.01	6.673	2.1	1154
105	N38	N38_105_4_6%_25	6	0.24	4	25	4	6.543	1	1239.7

Appendix E: Stress-strain evolution response for 1 mm to 3.5 mm sample length

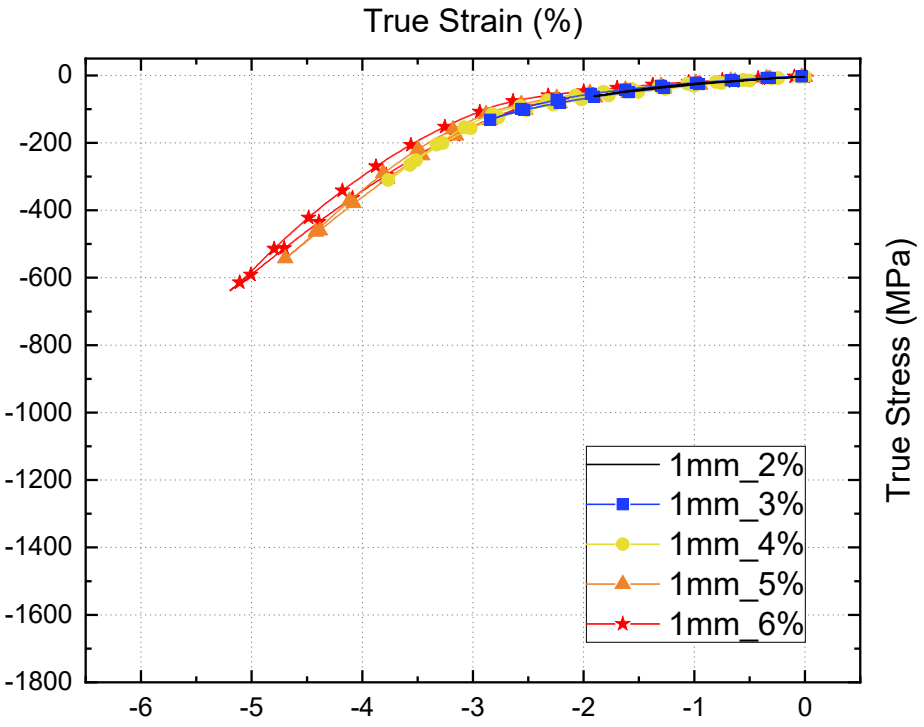

Figure E.1 – Stress-strain response of strain evolution for 1 mm sample long

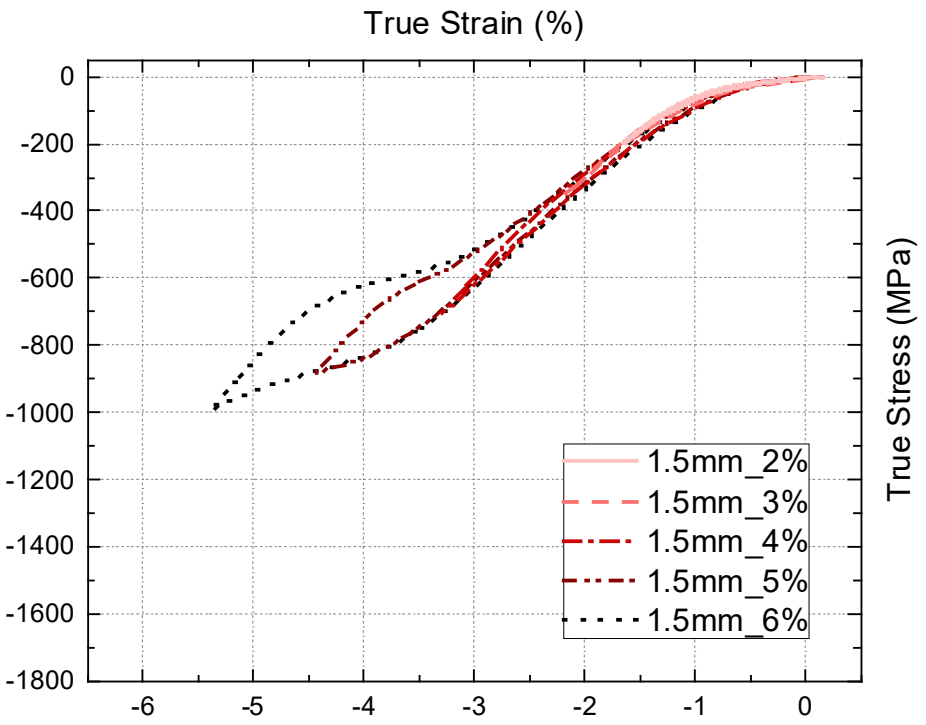

Figure E.2 – Stress-strain response of strain evolution for 1.5 mm sample long

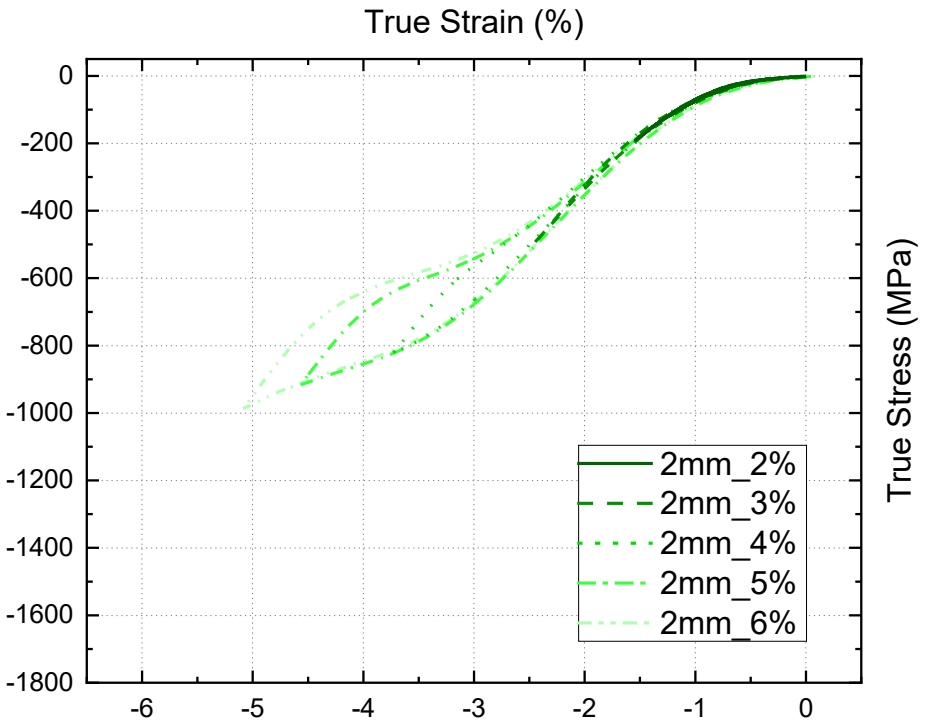

Figure E.3 – Stress-strain response of strain evolution for 2 mm sample long

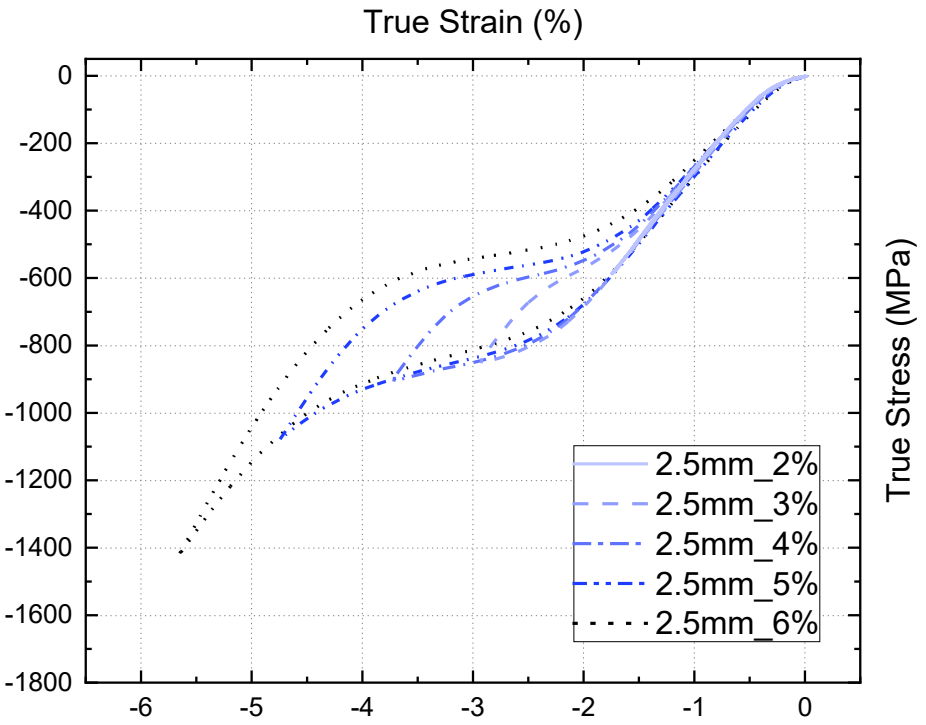

Figure E.4 – Stress-strain response of strain evolution for 2.5 mm sample long

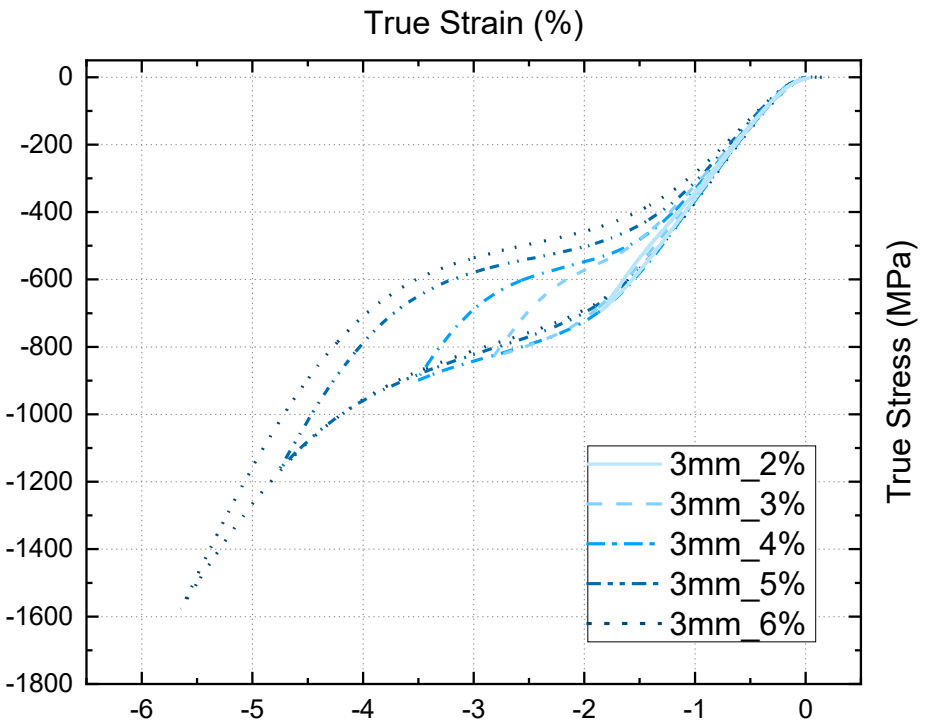

Figure E.5 – Stress-strain response of strain evolution for 3 mm sample long

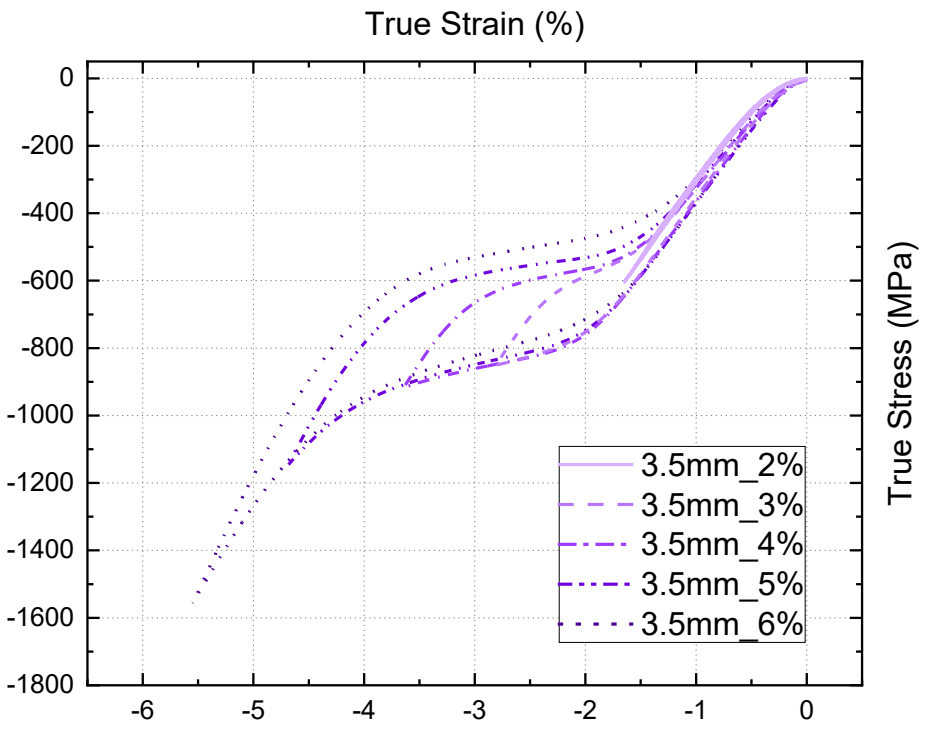

Figure E.6 – Stress-strain response of strain evolution for 3.5 mm sample long